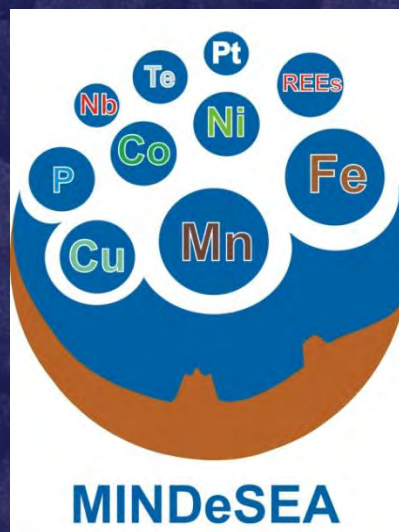


# MINDeSEA

## Seabed Mineral Deposits in European Seas: Metallogeny and Geological Potential for Strategic and Critical Raw Materials



### Deliverable 2.3-2: Workshop #2

<b>WP2 leader:</b> <b>Geological Survey of Spain (IGME) - Spain</b>		
 <b>Instituto Geológico y Minero de España</b>	<b>Address:</b> C/ Ríos Rosas, 23 28003 Madrid Spain	<b>Telephone:</b> +34 91 349 58 61 (T. Medialdea)
		<b>Email:</b> t.medialdea@igme.es
<b>WP2 IGME:</b> Teresa Medialdea (WP Lead)		



<b>Deliverable number</b>		<b>Short Title</b>	
2.3		Workshop Report	
<b>Long Title</b>			
Deliverable 2.3 – Workshops dedicated to the main themes of the work packages			
<b>Short Description</b>			
This document is intended as a summary of the presentations and activities of the MINDeSEA Workshop, held in Trondheim on November 27 <sup>th</sup> , 2019			
<b>Keywords</b>			
GeoERA Raw Materials, Consortium activities, workshop			
<b>Presenters / Organisation</b>		<b>Organiser / Organisation</b>	
Ben Snook / NTNU Javier González / IGME Marco Brønner / NGU Florent Szitkar / NGU Ketil Hokstad / Equinor Anna Lim / NTNU Visit to Automated Underwater Robotics (AUR) Laboratory, NTNU, hosted by Øystein Sture / Martin Ludvigsen		Henrik Schiellerup / NGU	
<b>File name</b>			
MINDeSEA_D2-3-2_WP2-Workshop Report.doc			
<b>Deliverable due date</b>		<b>Deliverable submitted date (WP leader)</b>	
October 2019 (M16)		December 2019 (M18)	
<b>Comments</b>			
Workshop was delayed due to calendar challenges among key participants.			

<b>History</b>				
<b>Version</b>	<b>Author</b>	<b>Status</b>	<b>Date</b>	<b>Comments</b>
01	Henrik Schiellerup, NGU	Final	09 December 2019	

<b>Dissemination level</b>		
<b>PU</b>	Public	X
<b>CO</b>	Confidential, for project partners, GeoERA and the European Commission only	



### **D.2.3. Report on the MINDeSEA Workshop, hosted by the Geological Survey of Norway, November 27<sup>th</sup>, 2019, in Trondheim, Norway**

#### **Project Overview**

The project “Seabed Mineral Deposits in European Seas: Metallogeny and Geological Potential for Strategic and Critical Raw Materials” (MINDeSEA) results from the collaboration between eight GeoERA Partners and four Non-funded Organizations at various points of common interest for exploration and investigation into seafloor mineral deposits. The project MINDeSEA is sponsored by the European Commission as an ERA-NET action under Horizon 2020 and is designed with the following objectives:

1) Characterise deposit types; 2) Characterise the trace element content of the deposit types, including CRM; 3) Identify the principal metallogenic provinces; 4) Develop harmonised mineral maps and datasets of seabed deposits incorporating GSO datasets, along with mineral-potential and prospectivity maps; 5) Demonstrate how the case study results can be used in off-shore mineral exploration; 6) Analyse present-day exploration and exploitation status in terms of regulation, legislation, environmental impacts, exploitation and future directions. 7) Demonstrate the efficiency of a pan-European research approach to understanding seabed minerals and modes of exploration.

A workshop was organised in connection with the 3<sup>rd</sup> MINDeSEA project meeting on November 27<sup>th</sup>, 2019, to establish an arena where participants and other stakeholders can exchange knowledge and views concerning relevant issues within deep-sea mining. Key stakeholders present at the workshop included GeoERA partners, The Norwegian University of Science and Technology (NTNU), and the Norwegian energy company Equinor. The meeting was organised by the Geological Survey of Norway (NGU).

#### **Objectives of the Workshop**

The objectives of the workshop were:

1. To introduce external stakeholders and partners to the content and progress of the MINDeSEA project.
2. To further expand the MINDeSEA stakeholder network to relevant universities and industries, and to explore new working relationships beyond the project partners.
3. To connect the MINDeSEA project with on-going activities at the Norwegian University of Science and Technology (NTNU) within deep sea mineral deposits and underwater technology development.
4. To improve the awareness and understanding of geophysical tools, signals and surveys in deep sea mineral exploration.
5. To explore the possible symbiosis between exploration and model understanding for off-shore oil and sea bed minerals

#### **Workshop Framework and Deliverable**

The workshop started with an opening statement by NGU followed six keynote talks by experts in marine mineralisations, marine mineral characterisation, exploration models and geophysics from hydrocarbons to minerals. The oral programme had allocated time for discussions among the 18-20 participants. After the main workshop session, 12 delegates visited the Automated Underwater Robotics (AUR) lab at NTNU for a lecture and display of underwater tools and technologies in use in Norwegian underwater surveys.

The deliverable includes the current workshop summary and pdf-versions of the presentations now available from the MINDeSEA project website: <https://geoeramindesea.wixsite.com/mindesea/>



MEETING

**GeoERA-MINDeSEA Workshop**

DATE

27.11.2019

MEETING ORGANISER

**NGU**

VENUE

Geological Survey of Norway  
Leiv Eirikssons vei 39, Trondheim,  
Norway

08h45	09h00	Registration	All
09h00	09h10	Opening by NGU	Henrik Schiellerup (NGU)
09h10	09h35	MarMine - investigations into sulphide mineralisation on the Arctic Mid-Ocean Ridge	Ben Snook (NTNU)
09h35	10h00	Deep sea mineral resources – the MINDeSEA project	Javier González (IGME)
10h00	10h25	Geophysical exploration techniques on mid-oceanic ridges: Old methods and new challenges	Marco Brønner (NGU)
10h25	10h45	<b>Coffee Break</b>	<b>All</b>
10h45	11h10	Exploration methodology from petroleum to mineral resources	Ketil Hokstad (Equinor)
11h10	11h35	Magnetic response of hydrothermal systems	Florent Szitkar (NGU)
11h35	12h00	Hydrothermal activity at the ultraslow-spreading Mohn's Ridge: new insights from near-seafloor geophysics	Anna Lim (NTNU)
12h00	12h45	<b>Lunch Break</b>	<b>All</b>
12h45	13h15	Transport to AUR-Lab (NTNU)	All
13h15	14h30	Tour of the AUR (Automated Underwater Robotics) lab at NTNU ( <a href="https://www.ntnu.edu/aur-lab">https://www.ntnu.edu/aur-lab</a> )	Martin Ludvigsen/Øystein Sture





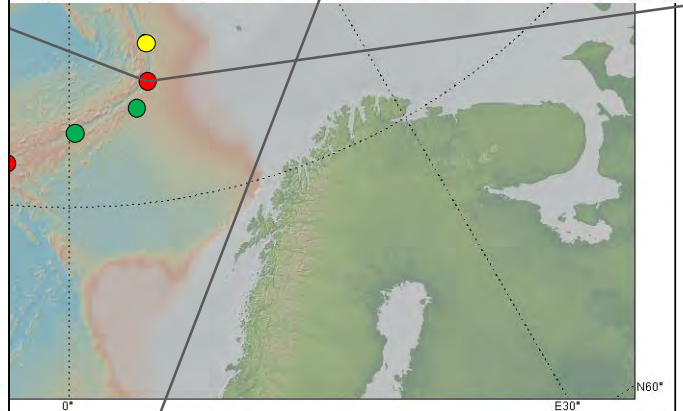
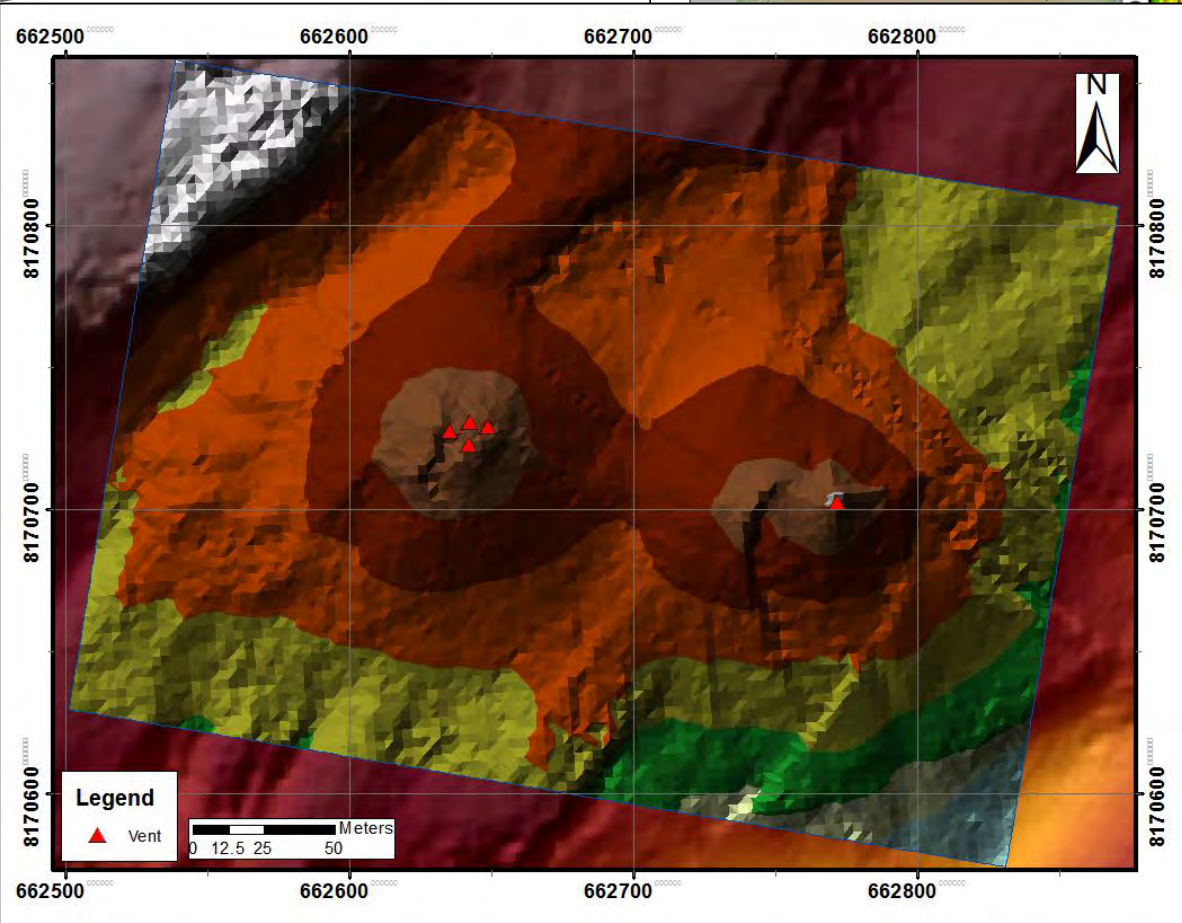
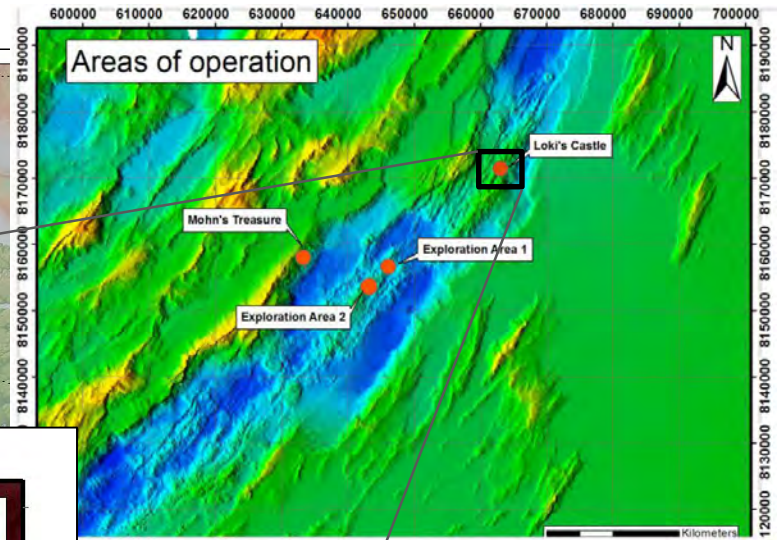
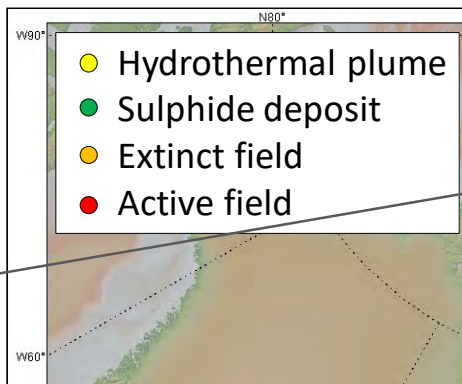
# MARMI<sup>NE</sup>

## WP4 Characterisation

Ben Snook, Kurt Aasly



# Setting



Data after Pedersen et al. 2010

Data after Ludvigsen et al. 2016

## WP1

Sample  
identification  
and collection

## WP2

Mineral  
processing  
options

## WP3

Deep sea  
mining pilot  
feasibility study

## WP4

Characterisation

**WP5** Environmental impacts

**WP6** Project management/dissemination

# MarMine, WP4 Characterisation

## Initial workpackage aims:

- Description of ore samples – *composition and chemistry, grain size, mineral associations, liberation potential*
- Contrast of ore material pre- and post-processing to assess the efficiency of extraction methods
- Rock mass characterisation



# WP1

Sample identification and collection

# WP2

Mineral processing options

# WP3

Deep sea mining pilot feasibility study

# WP4

Characterisation

Contrast of pre- and post-processing material

Contrast of pre- and post-processing material

Rock mass characterisation

Rock mass characterisation

Creation of a spatial and grade distribution model

Creation of a spatial and grade distribution model

Development of the UHI technique

Development of the UHI technique

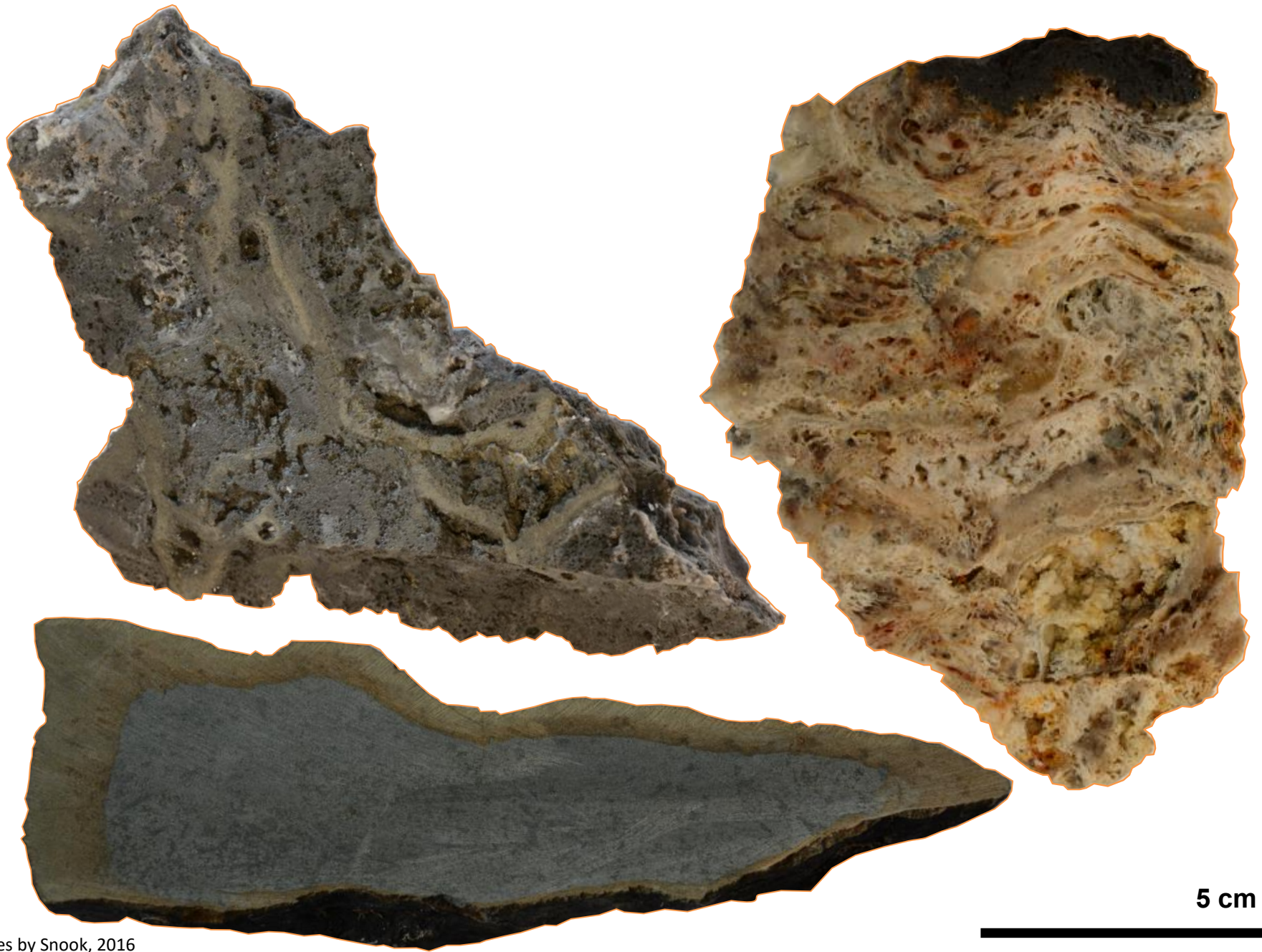
**WP5** Environmental impacts

**WP6** Project management/dissemination

# Work achieved

- Initial mineralogical classification;
- Petrographical investigation of smoker and Min Pro material;
- CT scanning of gravity cores and seafloor sulphide boulder cores;
- Sediment gravity core analyses (X-ray imaging, density measurements, magnetic susceptibility, XRF transect);
- XRD, ICP-ES/MS and FA of a large seafloor sulphide sample suite;
- Collaboration with WP2 to inform Mineral Processing experiments;
- QEMSCAN mineralogical assessment of black smoker material;
- Experiments to collect UHI spectra from mineralised material and host lithologies, and processing of data;
- Mineralogical/petrographic contribution to Mn nodules experiments.

# Hand samples

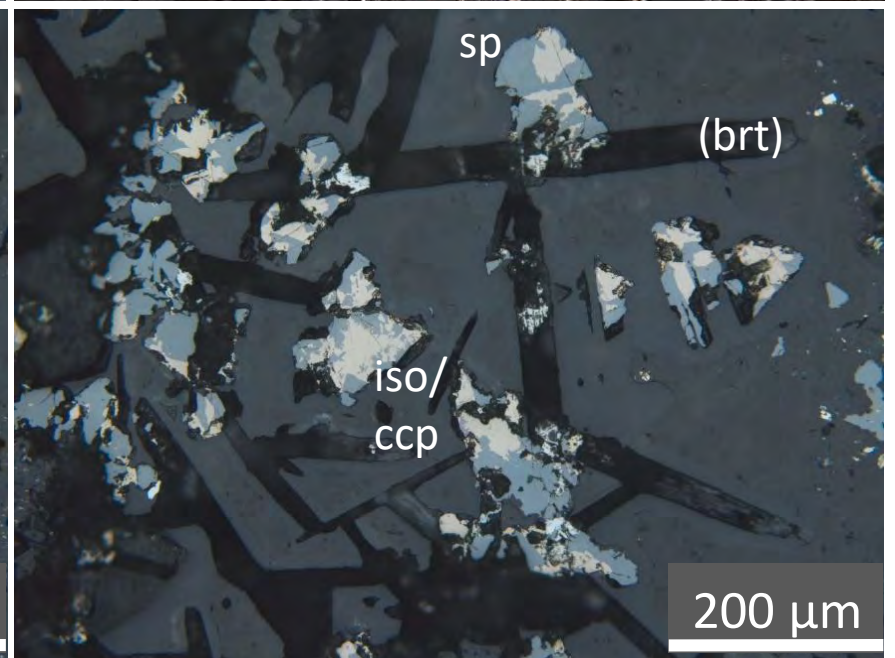
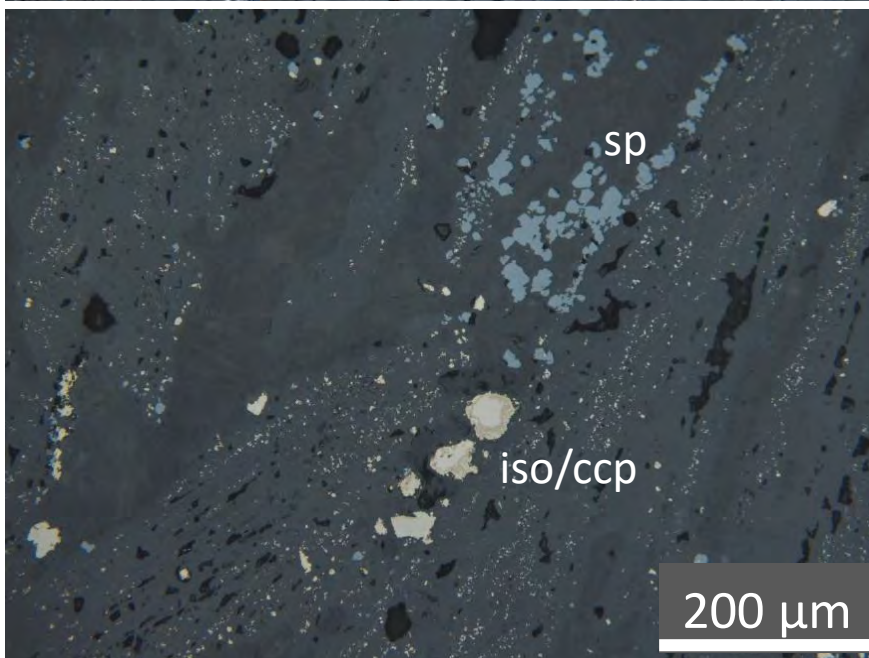
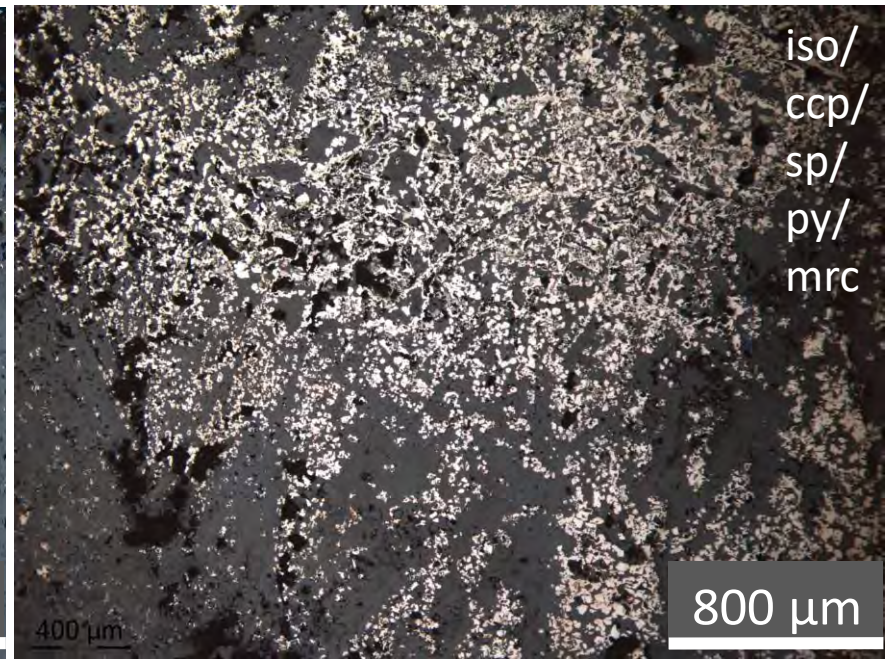
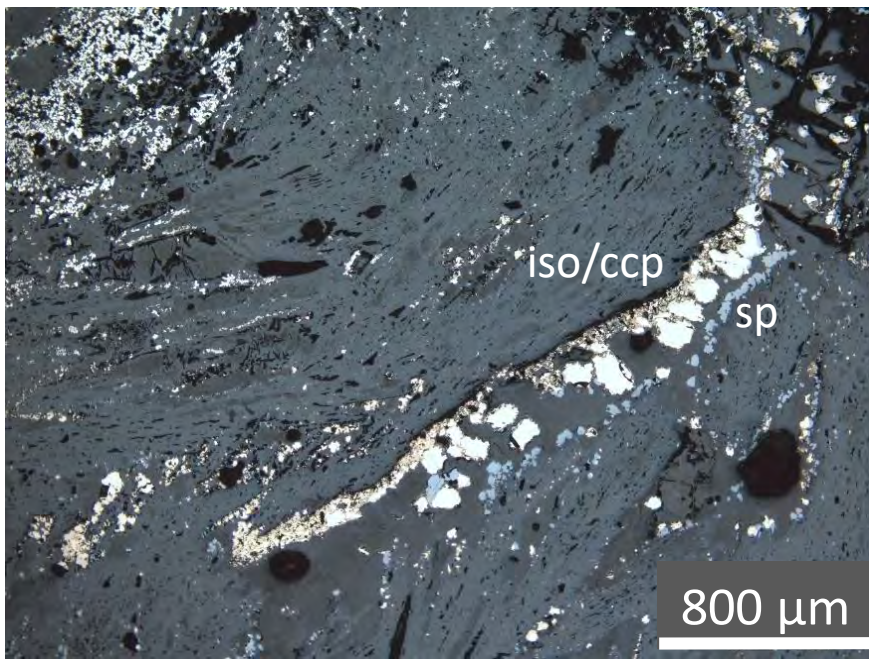


5 cm

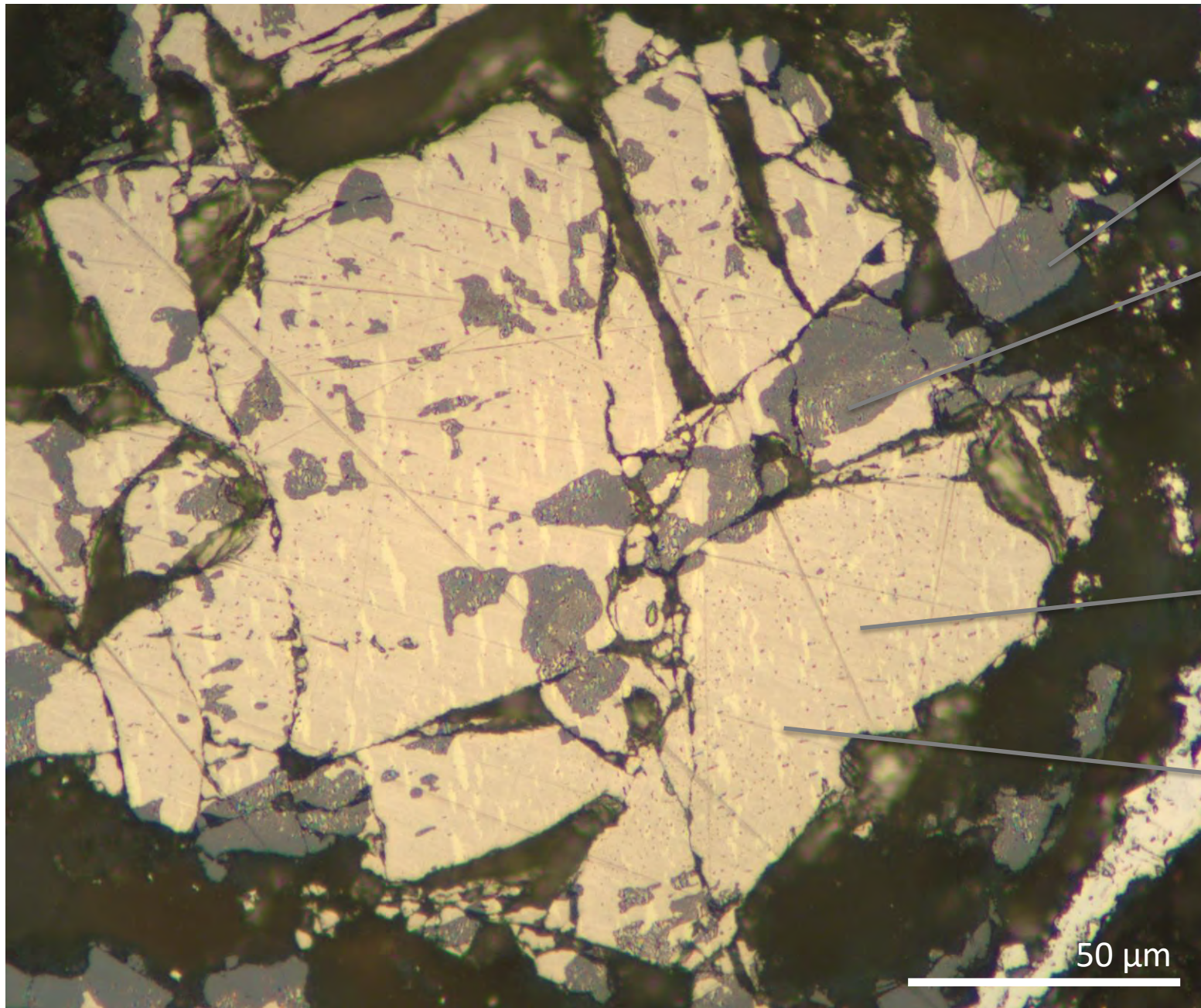
Images by Snook, 2016



# Reflected light microscopy







sphalerite...  
(Zn)

...variably  
with  
chalcopyrite  
disease

isocubanite  
(Cu)

chalcopyrite  
exsolutions  
(Cu)

Images by Snook, 2016

sphalerite...  
(Zn)

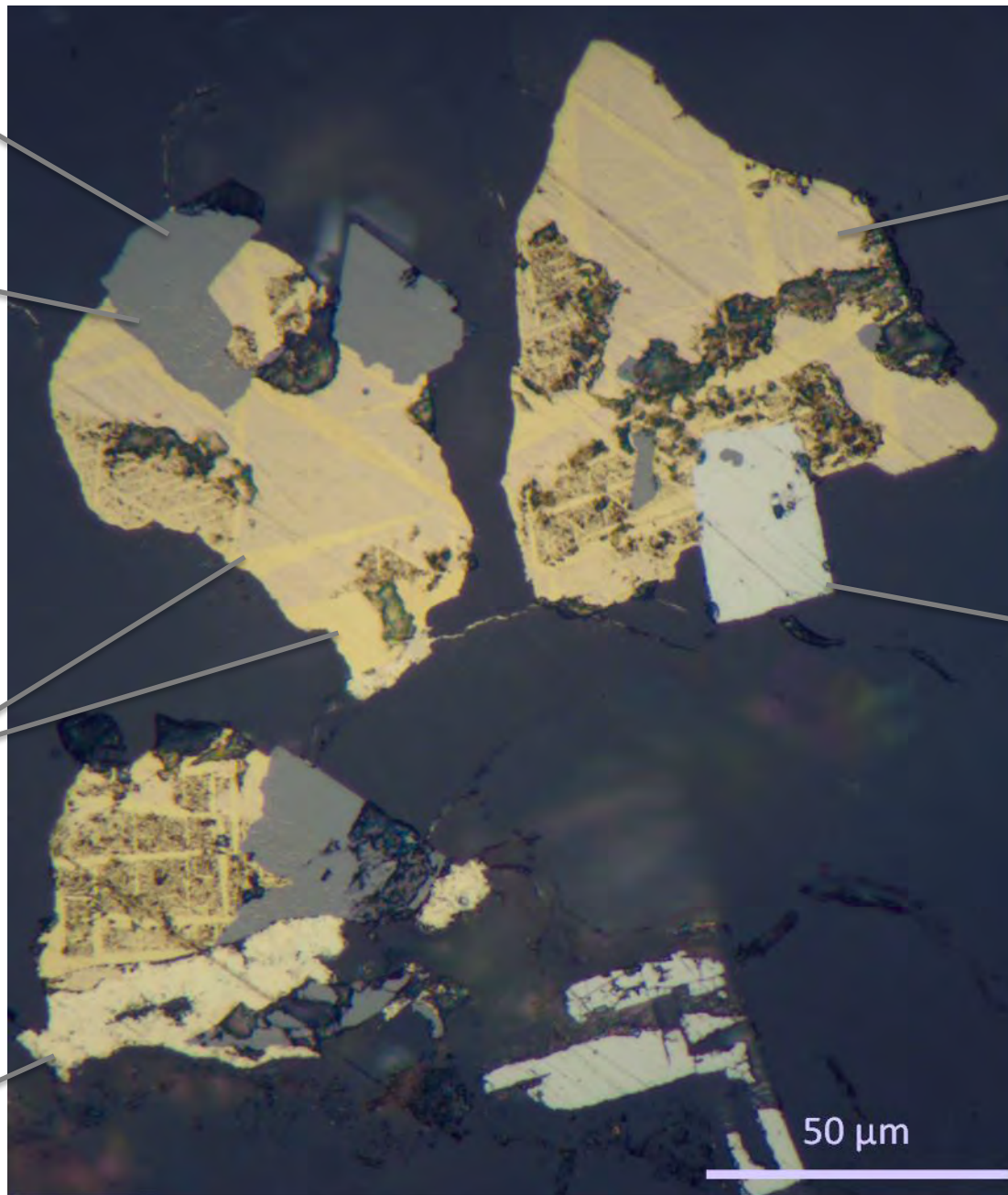
...variably  
with  
chalcopyrite  
dissolve

larger  
chalcopyrite  
lamination (Cu)

pyrite

isocubanite with  
chalcopyrite  
exsolution  
(Cu)

galena (Pb)



Snook et al., 2018

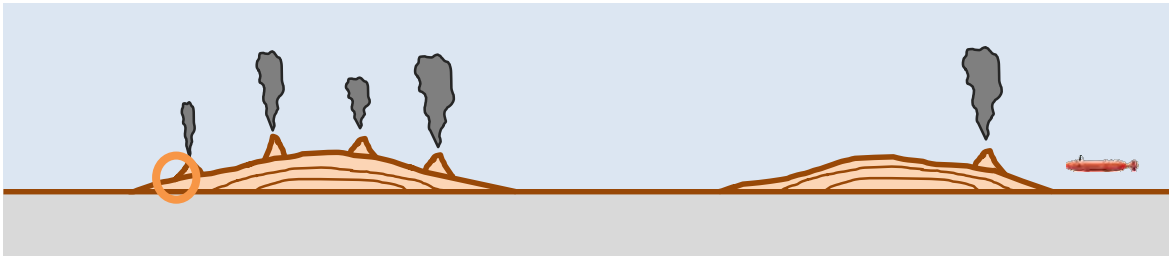
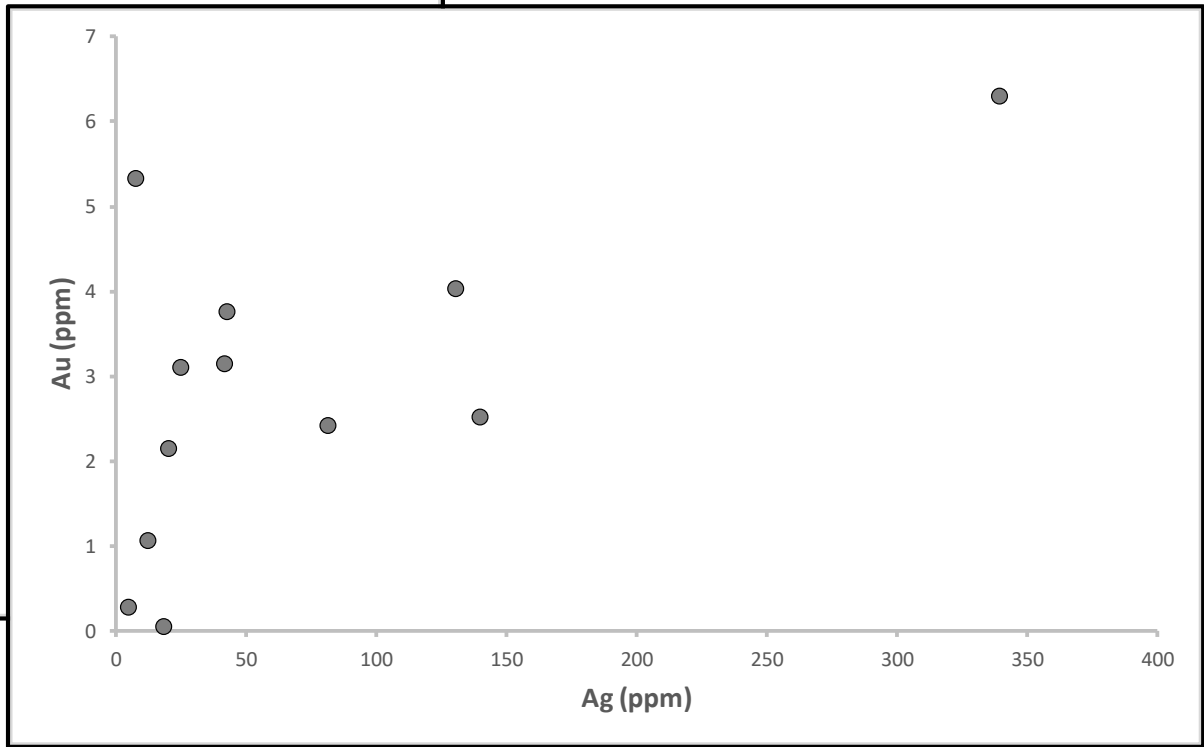
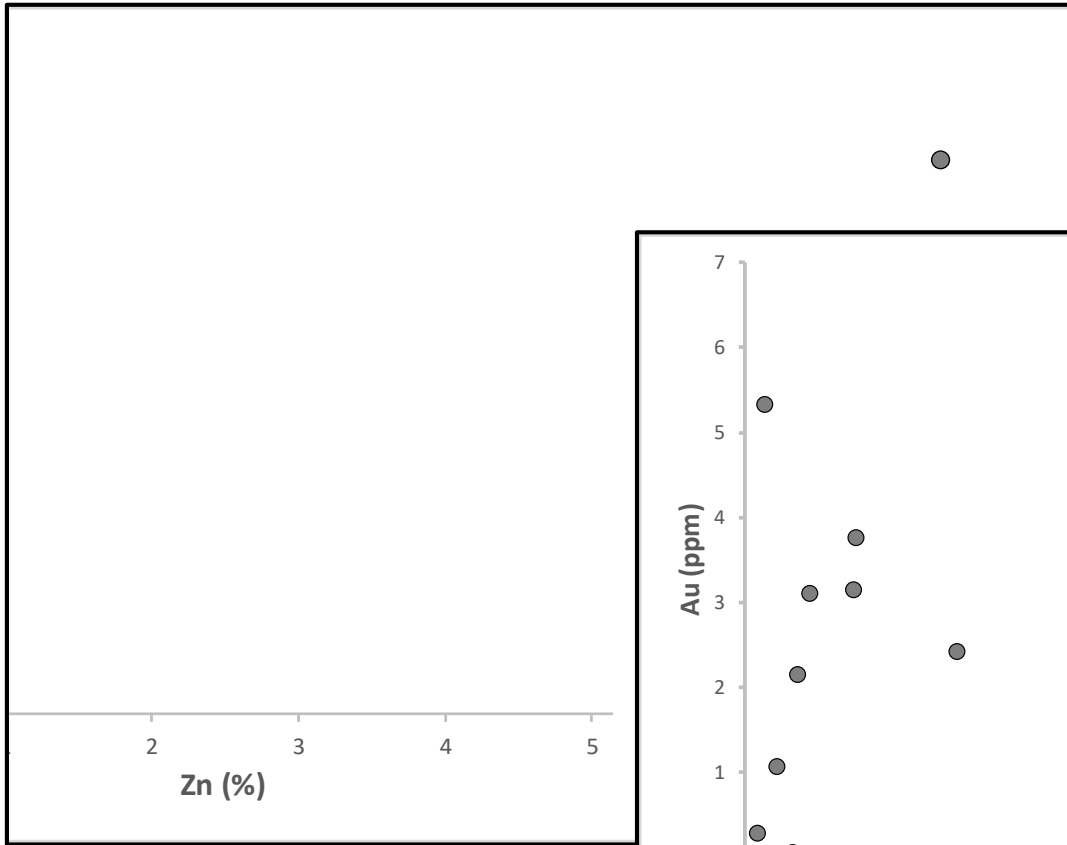


# XRD mineralogy

? is uncertain, + is 0 – 5% , ++ is 5 – 15%, +++ is 15% and over

	<i>brt</i>	<i>qtz</i>	<i>amo</i>	<i>py</i>	<i>mrc</i>	<i>sp</i>	<i>iso</i>	<i>ccp</i>	<i>gn</i>	<i>po</i>	<i>anh</i>	<i>gp</i>	<i>tlc</i>	<i>hl</i>
<b>4-01</b>	++		++	++	+++	++	+	+	?	+				
<b>6-03</b>	+++		+	+++	+++	+	+	+						
<b>6-11</b>	+++		+											
<b>6-13(w)</b>	+++		+											
<b>6-13(b)</b>	+++		++	+	+	++	+	++	+	+				
<b>6-20</b>	+++		+											
<b>14-4</b>	+++	+++	+											
<b>14-14</b>	++	+++	+	+	+	+	+	+	+					
<b>14-16</b>	+	+++	+	+	++	+++	++	+	+					
<b>14-18</b>	+++	+++	+			?								
<b>14-21</b>	+++	+++	+			?			+					
<b>14-22</b>	+	+++	+	+		+								
<b>15-4</b>			+			+					+++	++	+++	+
<b>17-1</b>			+++	?				+					+++	++
<b>17-01</b>			+++	?				+					+++	++
<b>18-01</b>			+			+					+++	+++		

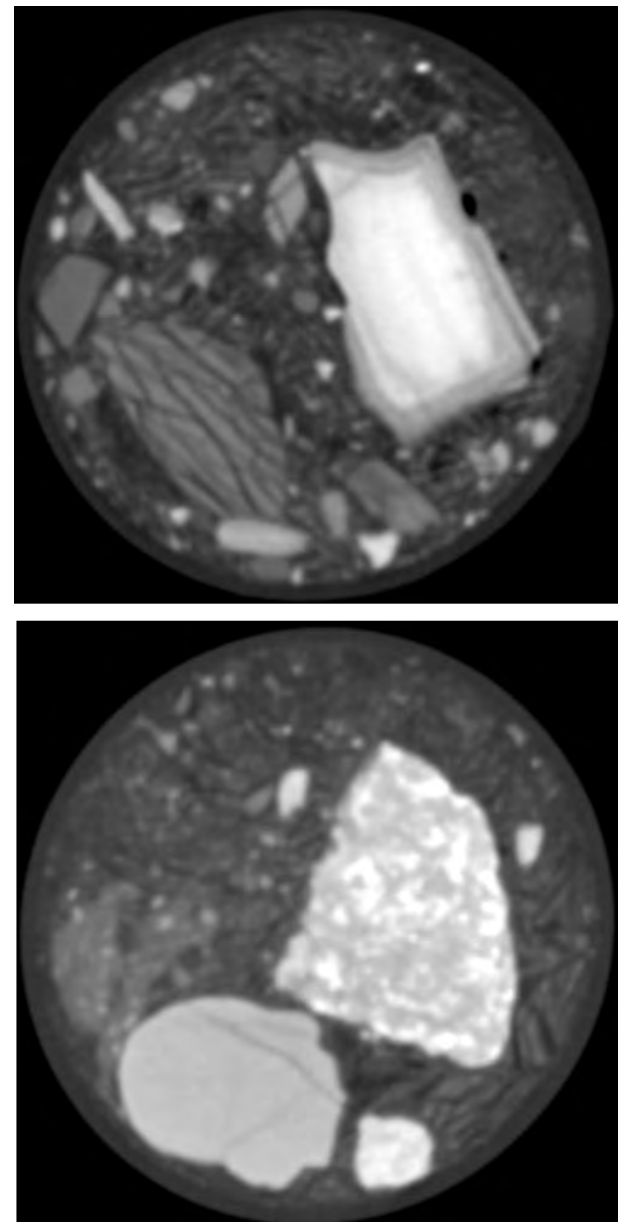
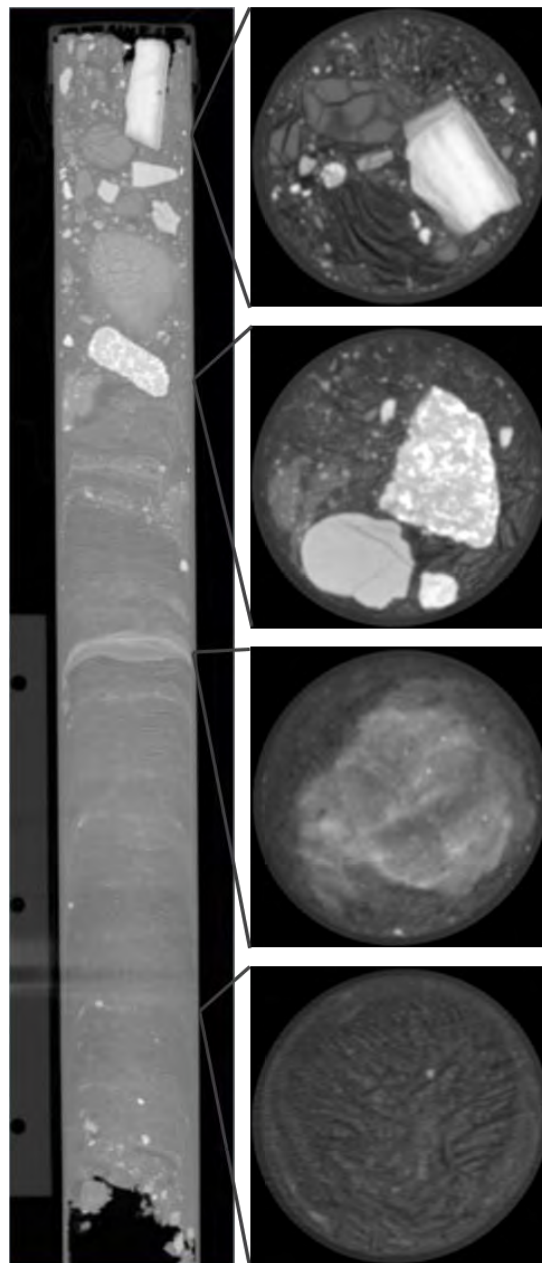
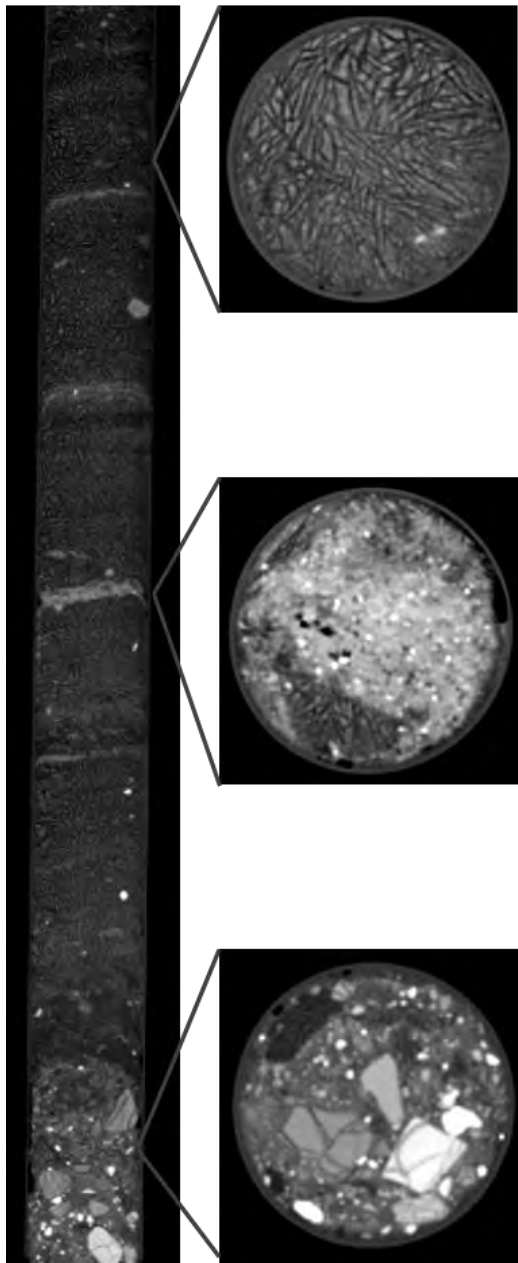
# ICP-ES/MS and fire assay geochemistry

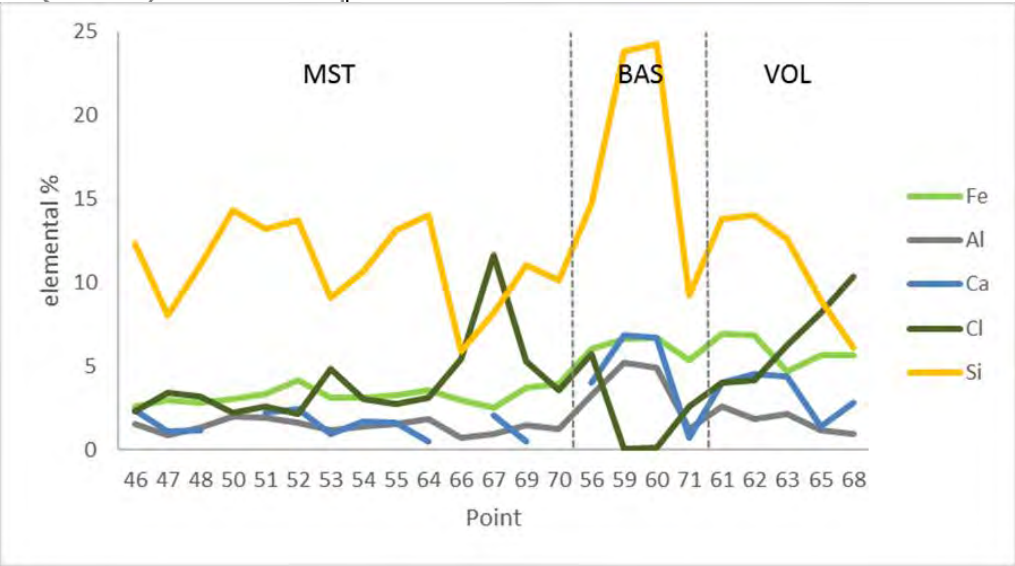
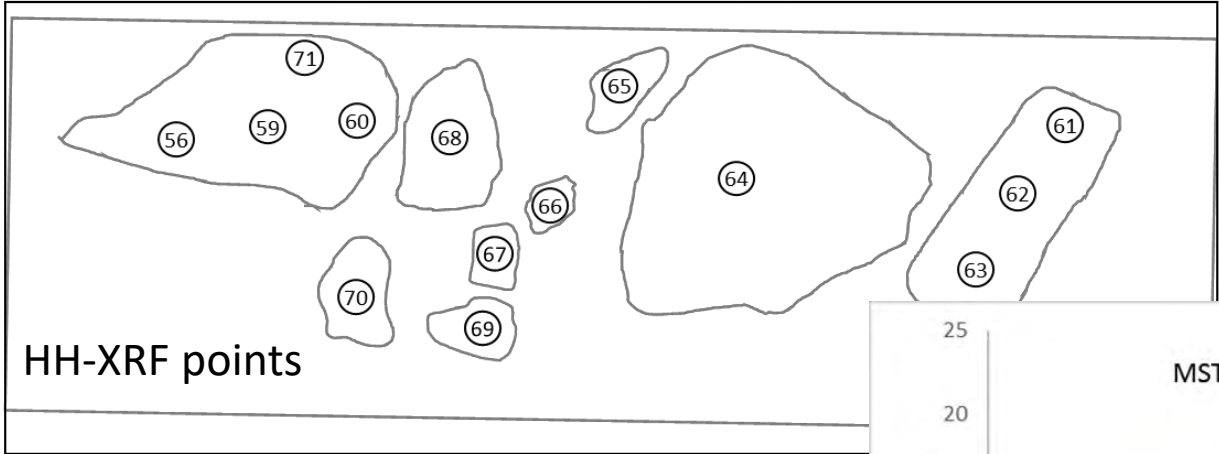
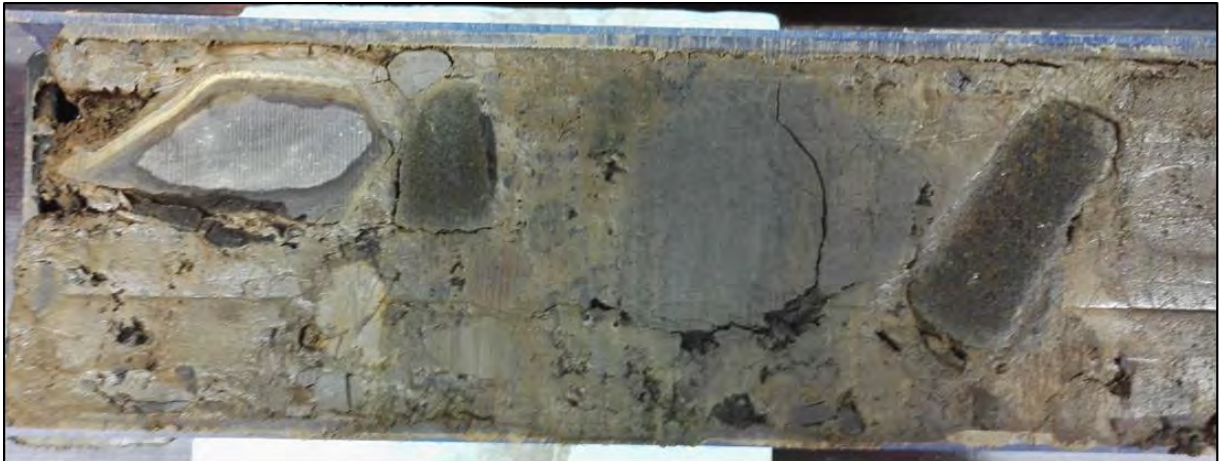


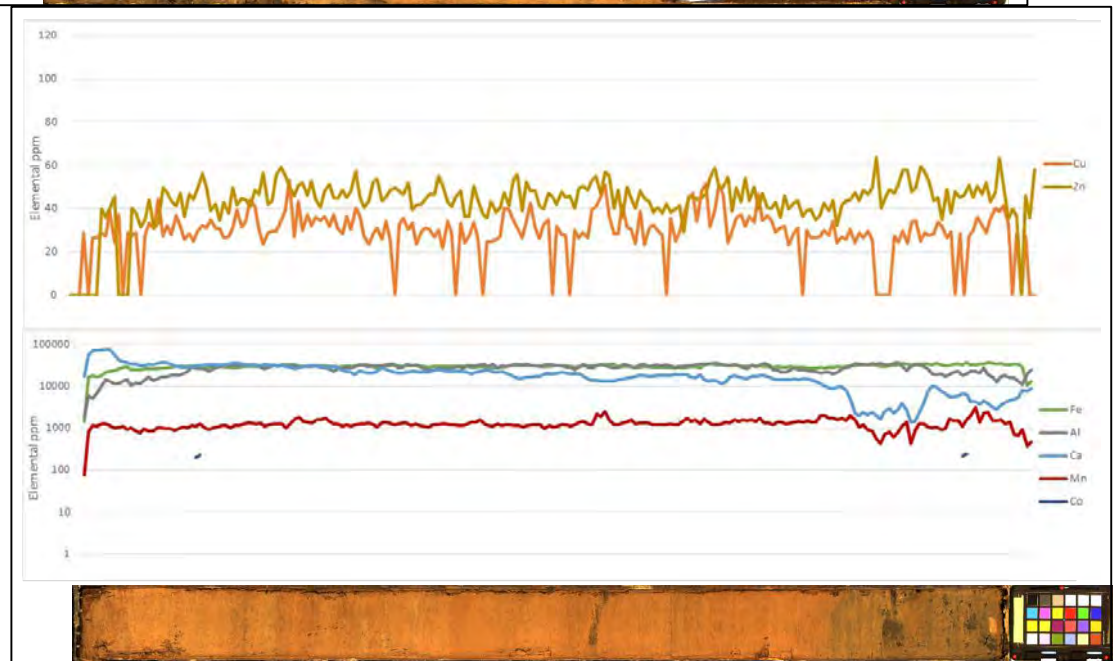
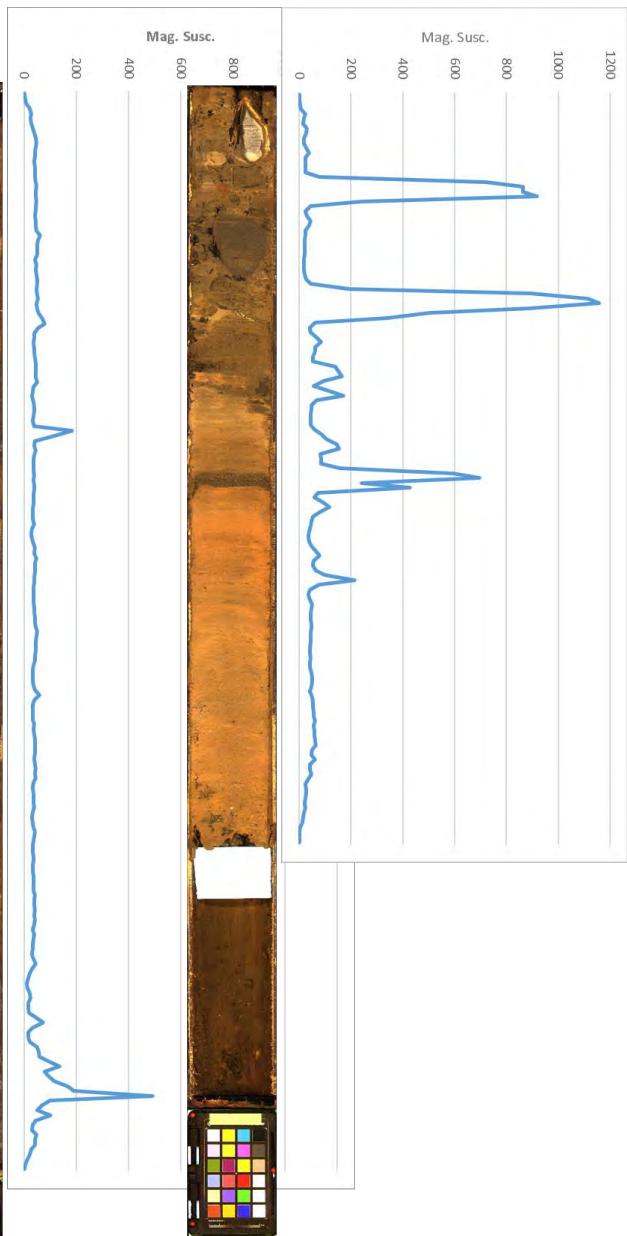
Snook et al., 2018



# Gravity cores

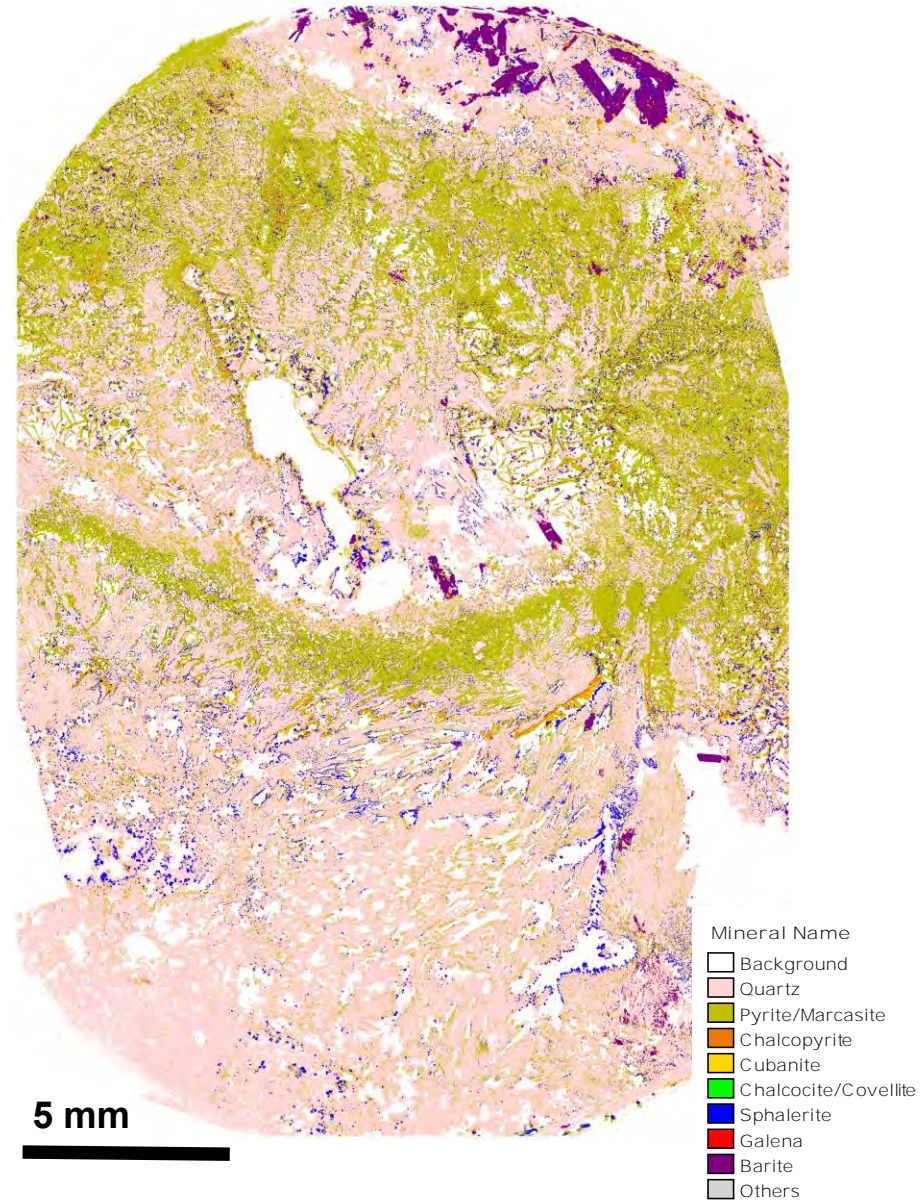






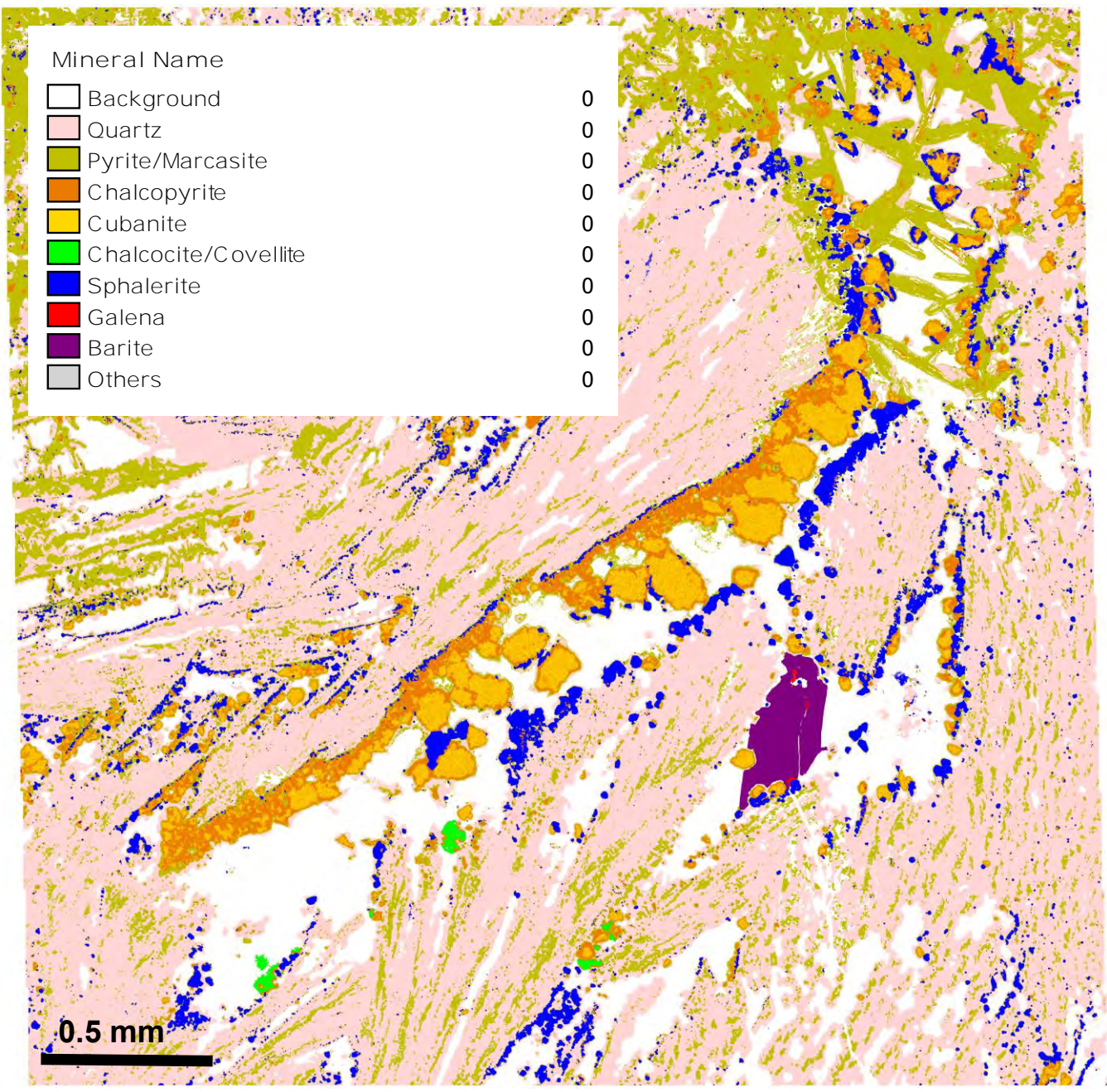
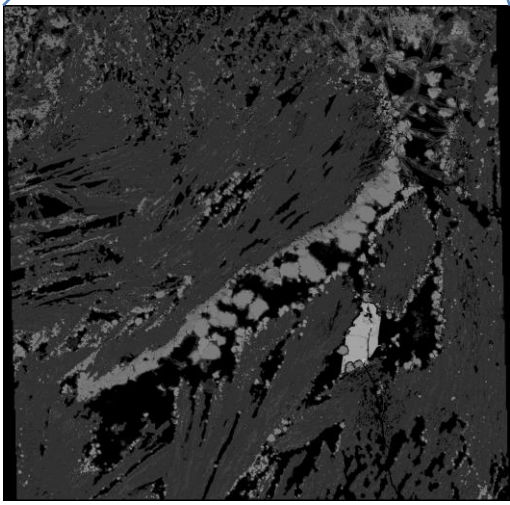
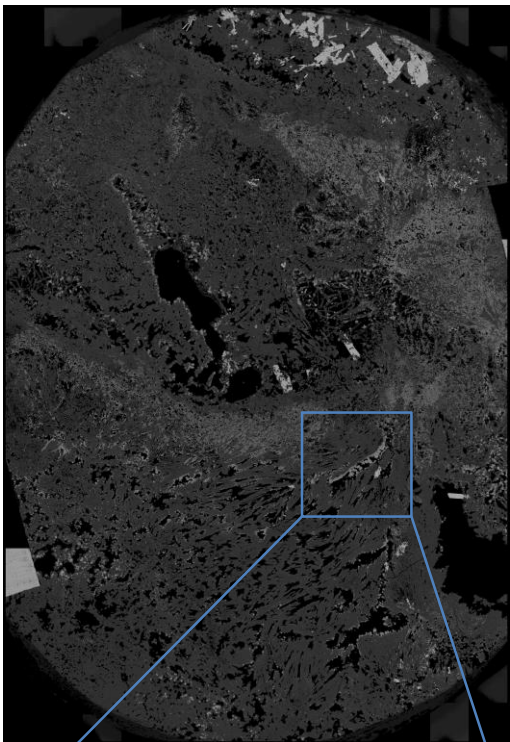
# Automated Mineralogy Systems (AMS) - QEMSCAN



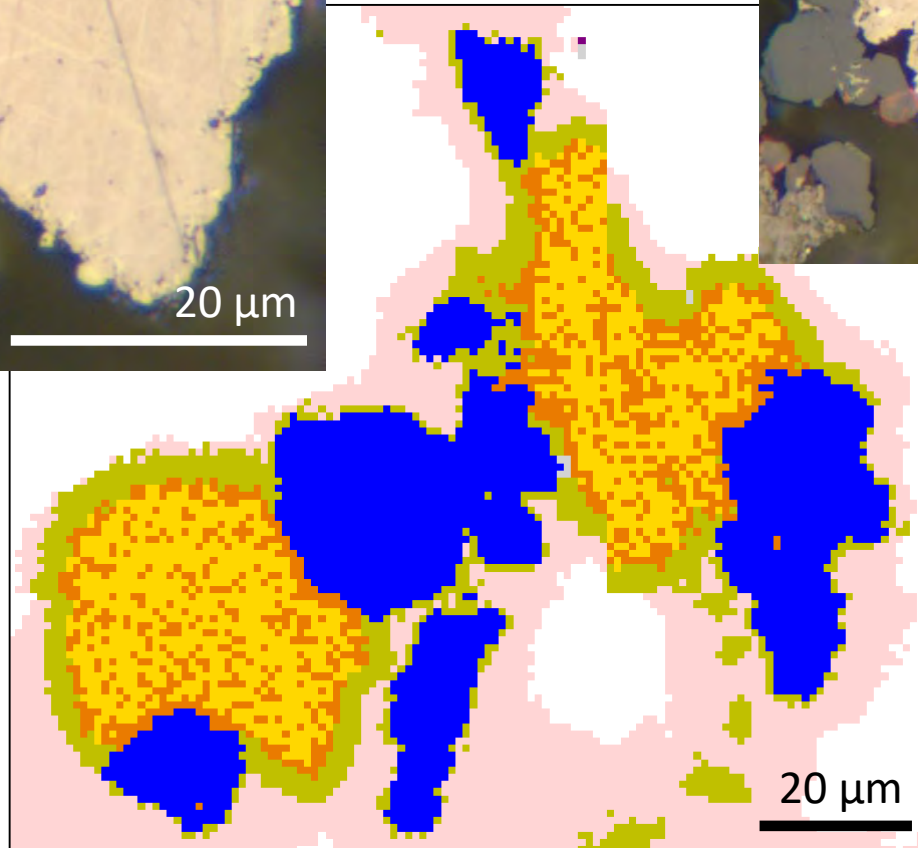
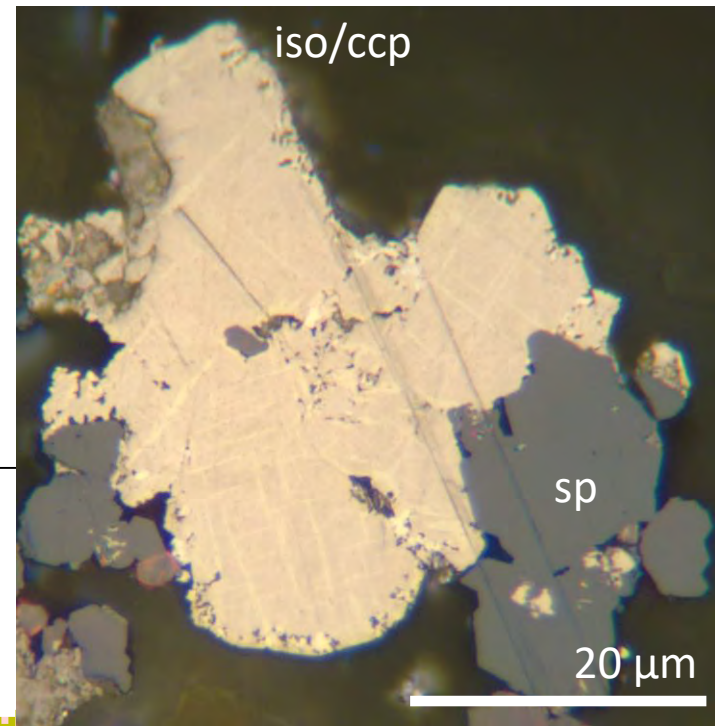
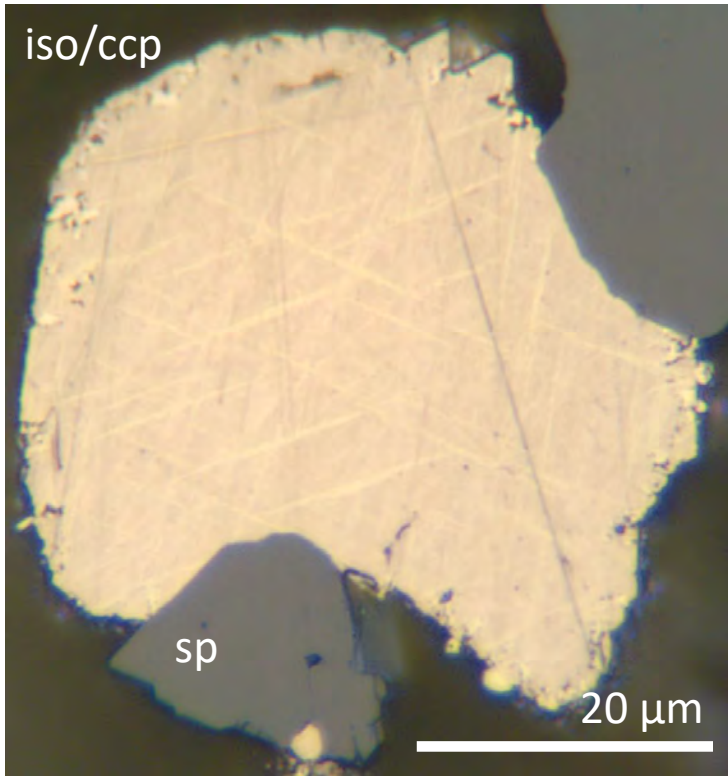


Snook et al., 2018









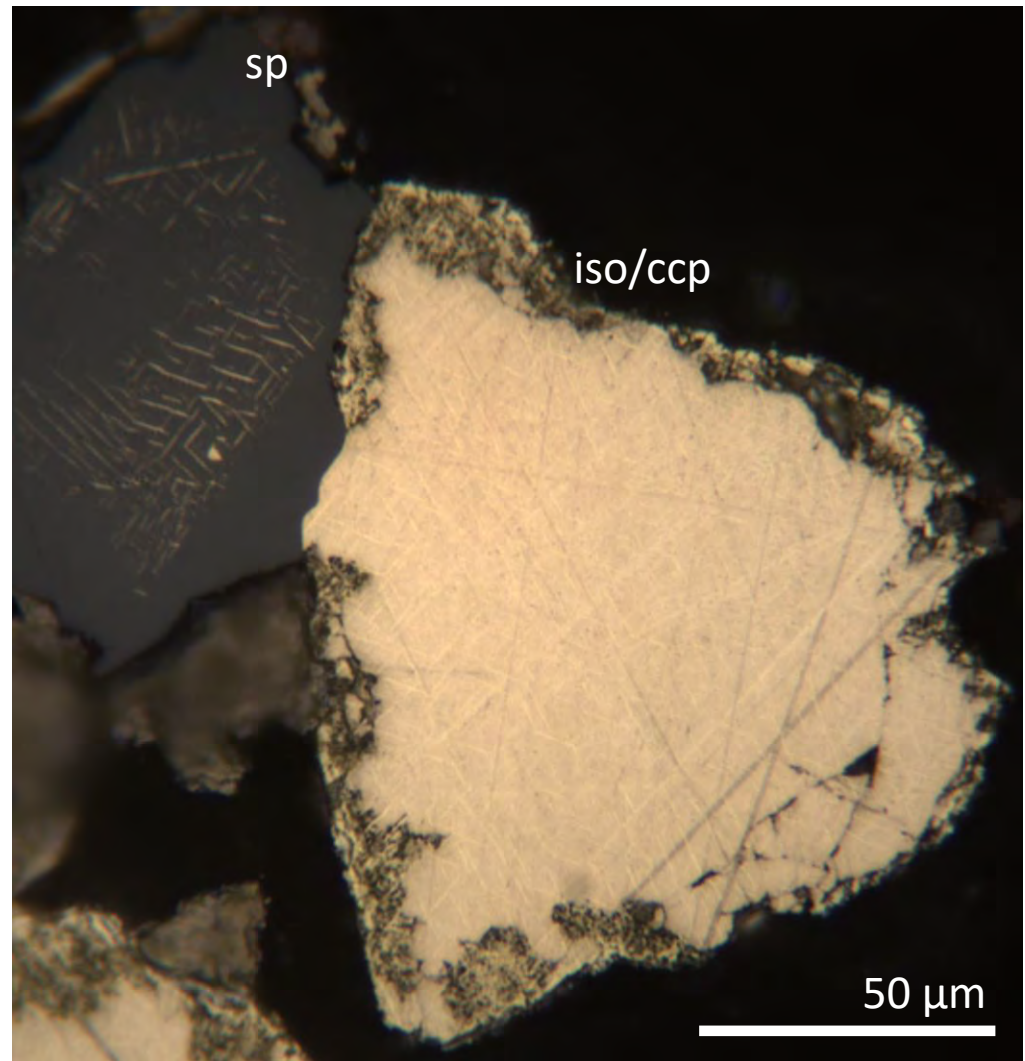
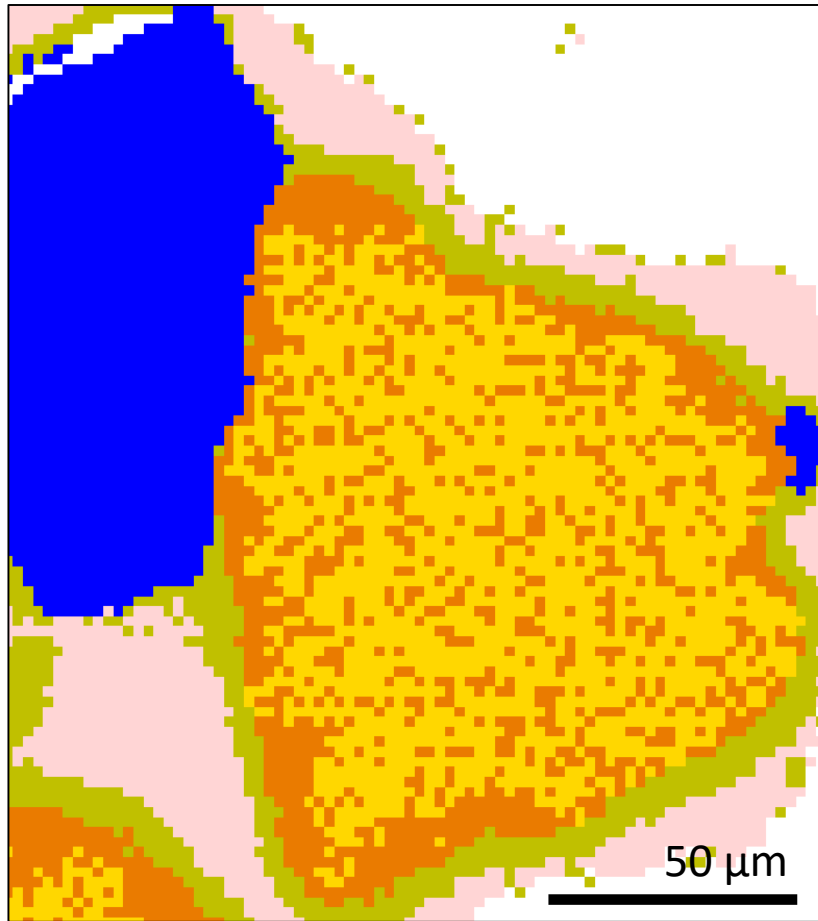


**Table 2.** Mineralogy of mineralised material after QEMSCAN analysis, performed at 10 and 1 µm pixel resolution, i.e., beam step size. Mineralogical data is normalised and is reported to the nearest 100 ppm. A minimum grain size of ≤15 or ≤1.5 µm is a product of scan resolution (fields are overlapped for stitching).

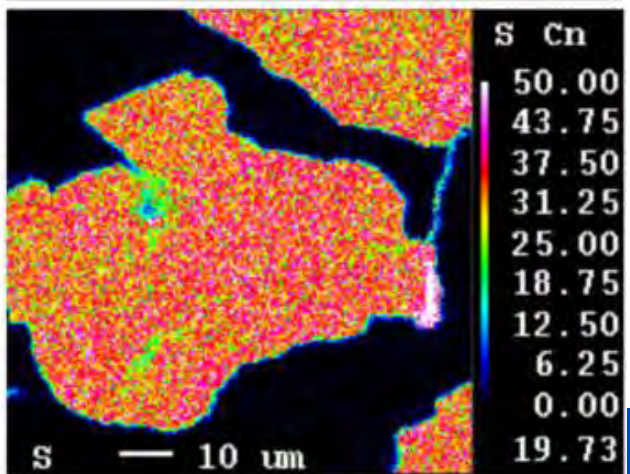
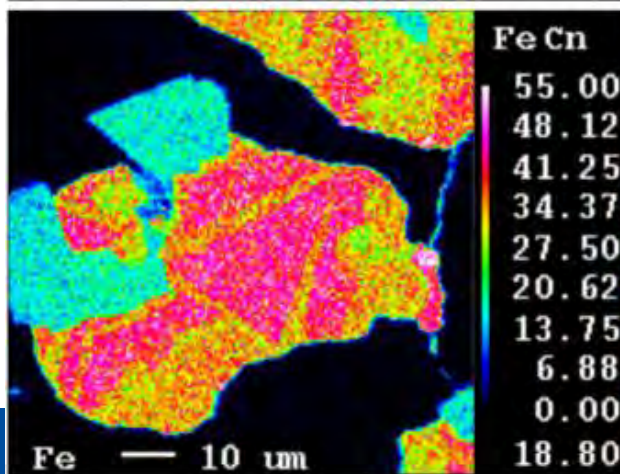
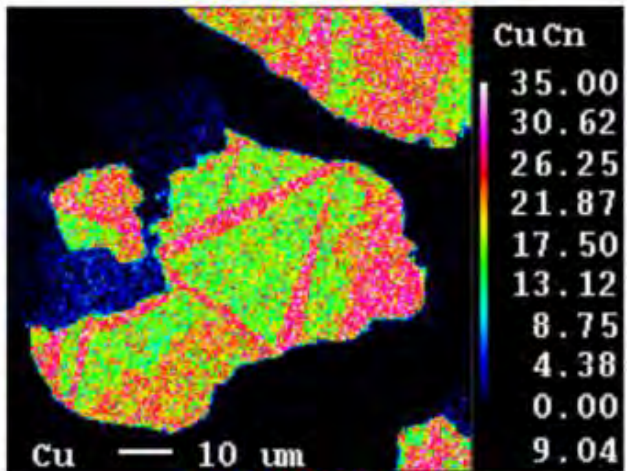
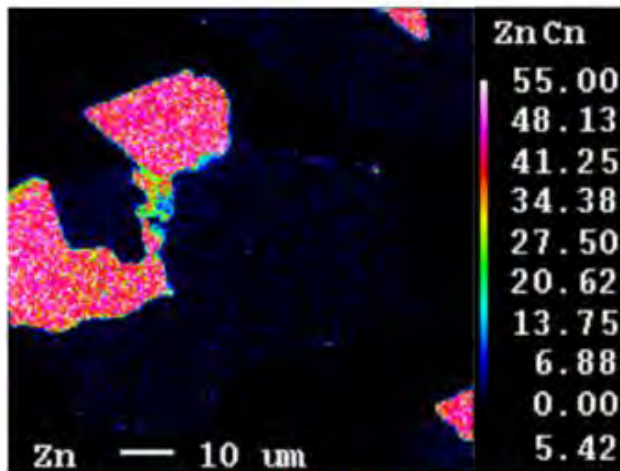
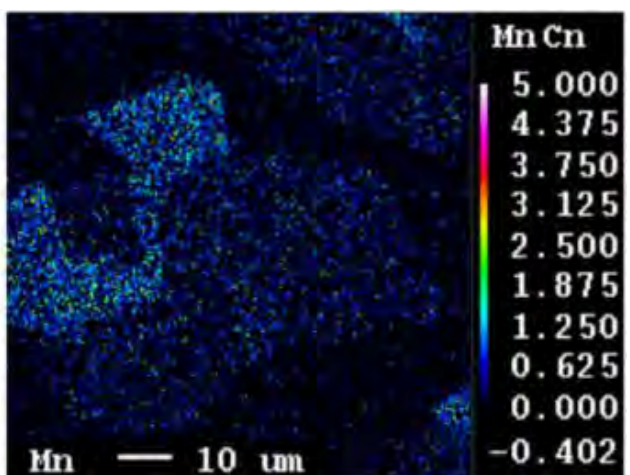
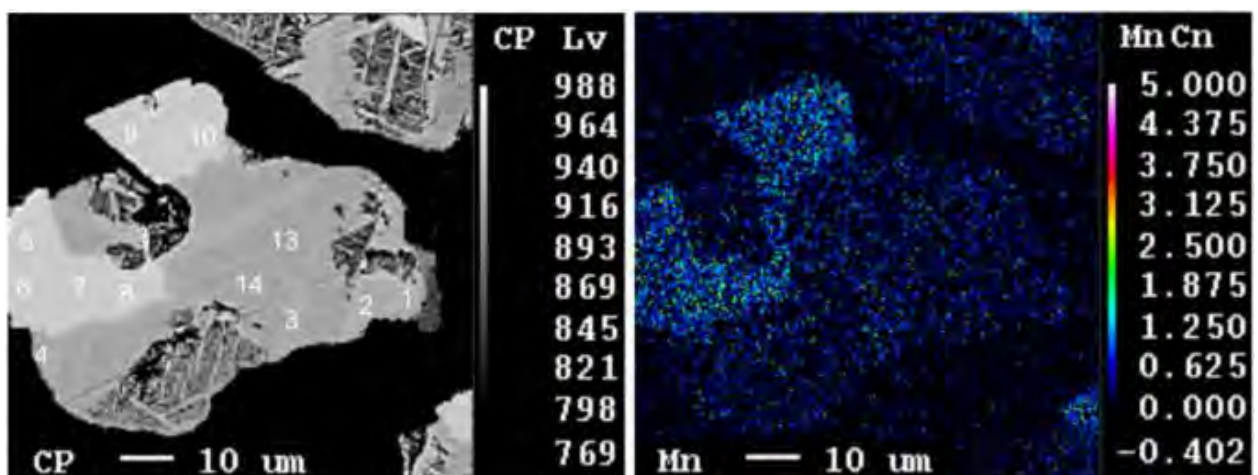
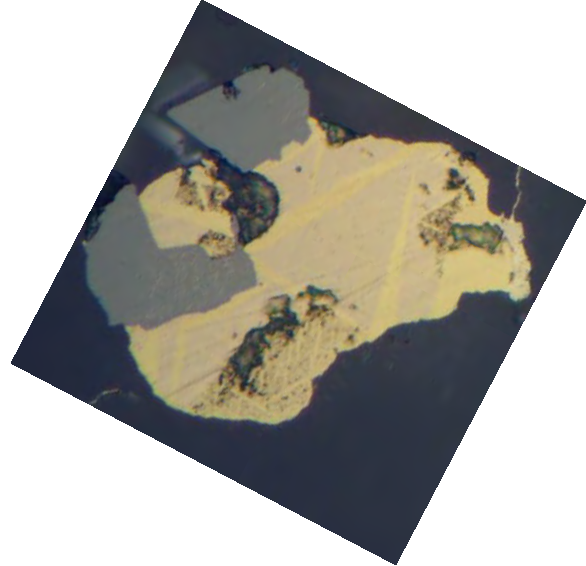
		10 µm	1 µm								
Measurement	Measurement Mode	Field Image	Field Image								
	Measurement Area (mm)	20 × 28	3 × 3								
	No. X-ray Analysis Points	3,831,192	8,598,413								
Mineral mass (wt %)	Quartz	48.08	51.32								
	Pyrite/Marcasite	43.69	35.23								
	Chalcopyrite	1.68	4.75								
	Isocubanite	0.68	3.73								
	Chalcocite/Covellite	0.01	0.19								
	Sphalerite	3.14	3.59								
	Galena	0.05	0.02								
	Barite	2.61	1.15								
	Others	0.08	0.04								
Mineral volume (area %)	Quartz	61.47	63.48								
	Pyrite/Marcasite	29.27	22.83								
	Chalcopyrite	1.92	4.95								
	Isocubanite	0.48	2.57								
	Chalcocite/Covellite	0.01	0.13								
	Sphalerite										
	Galena										
	Barite										
	Others										
Grain size min/avg/max (nearest µm)	Quartz										
	Pyrite/Marcasite										
	Chalcopyrite										
	Isocubanite										
	Chalcocite/Covellite										
	Sphalerite										
	Galena										
	Barite										
	Others										

**Table 3.** Summary (reading down, then left) of mineralogical associations of mineralised material identified by QEMSCAN (1 µm resolution). Mineral abbreviations after [43]. *iso* is isocubanite. *b/g* is background, i.e., epoxy resin (voids/cavities/pores).

		<i>b/g</i>	<i>qtz</i>	<i>py/mrc</i>	<i>ccp</i>	<i>iso</i>	<i>cc</i>	<i>spl</i>	<i>gn</i>	<i>brt</i>	<i>other</i>
wt %		n/a	51.32	35.23	4.75	3.73	0.19	3.59	0.02	1.15	0.04
		n/a	63.48	22.83	4.95	2.57	0.13	5.17	0.01	0.83	0.03
size µm		n/a	28	9	5	4	17	11	6	26	3
		0.00	20.99	10.52	1.08	0.47	28.17	7.10	2.74	18.57	22.06
		58.97	0.00	65.98	0.61	0.01	0.00	12.49	3.65	30.77	22.41
		33.86	75.55	0.00	27.67	2.78	0.56	66.50	47.03	39.33	24.70
		1.25	0.25	9.87	0.00	96.68	71.07	13.49	0.68	0.66	9.45
		0.35	0.00	0.65	62.89	0.00	0.15	0.08	0.00	0.01	0.00
		0.27	0.00	0.00	0.59	0.00	0.00	0.00	0.00	0.00	0.03
		4.24	2.66	12.35	7.02	0.06	0.00	0.00	5.48	2.79	5.78
		0.01	0.00	0.03	0.00	0.00	0.00	0.02	0.00	1.94	0.59
		0.72	0.43	0.48	0.02	0.00	0.00	0.18	36.07	0.00	14.98
		0.34	0.12	0.12	0.13	0.00	0.05	0.15	4.34	5.93	0.00



# EPMA



# SUMMARY

and...

What is the significance of these results for **future deep sea mining**?

- Hand specimens; reflected light microscopy; XRD; whole rock geochemistry (ICP-ES/MS and fire assay); QEMSCAN; EPMA.
- Cu and Zn present as chalcopyrite, isocubanite and sphalerite.
- Extremely intricate textures complicate characterization.
  
- Economically significant minerals (Cu, Zn, Au) are present;
- at potentially interesting concentrations;
- from a zone not typically considered the richest part of the deposit.
- *Feedback into mineral processing and extraction considerations.*
- *Potential extension of the deposit into the surrounding sediments.*

# Focus of remaining work

- Working with the new Zeiss system in conjunction with MarMine is an excellent opportunity apply automated mineralogy to SMS material;
- to efficiently find Au and Ag phases;
- to define Fe/Zn ratios in sphalerite to determine crystallization temperature (high temperature i.e. > 400°C may imply recrystallization and therefore mobilisation, meaning *reduced Zn* grades at depth due to increased Cu precipitation);
- to collaborate with EPMA to attempt to improve spatial resolution of AMS systems (where e.g. QEMSCAN failed to define Cu-Fe-S microtextures);
- to track pre and post Min Pro – grain size distribution, mineral association, effectivity of differing extraction methods;
- for sediment gravity core analyses (detailed geochemistry of mud and clast phases (with additional dating and shear strength testing)).




# Publications

Minerals	2019		Obtaining hyperspectral signatures for seafloor massive sulphide exploration
Minerals	2019		Simultaneous leaching of seafloor massive sulphides and polymetallic nodules
Marine Policy	2019		Strategic Environmental Goals and Objectives: Setting the basis for environmental regulation of deep seabed mining
Marine Policy	2018	90	Scientific rationale and international obligations for protection of active hydrothermal vent ecosystems from deep-sea mining
Natural Resources Research	2019	28	Multi-scale Quantitative Risk Analysis of Seabed Minerals: Principles and Application to Seafloor Massive Sulfide Prospects
Minerals	2018	8	Characterisation of mineralised material from the Loki's Castle hydrothermal vent on the Mohn's Ridge
Minerals	2018	8	Economic block model development for mining seafloor massive sulphides
Minerals	2018	8	Galvanic Leaching of Seafloor Massive Sulphides Using MnO <sub>2</sub> in H <sub>2</sub> SO <sub>4</sub> -NaCl Media
Minerals Engineering	2018	115	Efficient extraction of copper and zinc from seafloor massive sulphide rock samples from the Loki's Castle area at the Arctic Mid-Ocean Ridge
Sea Technology	aug.17		Low-cost drilling for deep-sea minerals exploration
<b>Conference papers</b>			
8th Sensor-Based Sorting & Control, Pretz T., Wotruba		18	Application of optical sensor-based sorting for preconcentration of seafloor massive sulphides
International Mineral Processing Congress, IMPC2018	sep.18		Application of X-ray transmission sensor-based sorting for preconcentration of seafloor massive sulphide rock samples from the Loki's Castle area at the Arctic Mid-Ocean Ridge
IEEE AUVs 2018	May 2018		Recognition of Cold-Water Corals in Synthetic Aperture Sonar Imagery
IEEE Oceans 2018	May 2018		The Subsea Quieter as a measure to reduce and control anthropogenic, industrial noise.
IEEE Oceans 2018	May 2018		Autonomous Optical Survey Based on Unsupervised Segmentation of Acoustic Backscatter
IEEE Oceans 2017	jun.17		Autonomous Underwater Vehicles as a Platform for Underwater Hyperspectral Imaging
IEEE Oceans 2017	jun.17		ROV based drilling for deep sea mining exploration.
The International Conference on Ocean, Offshore and Arctic Engineering (OMAЕ)	jun.17		Full cycle resource evaluation of SMS deposits along the Arctic Mid Ocean Ridge
8th Sensor-Based Sorting & Control			Application of optical sensor-based sorting for preconcentration of seafloor massive sulphides.


Ben Snook

Initial mineralogical description of MarMine rock samples




Ben Snook

Initial petrographic description of leached SMS material




Ben Snook

CT scanning of seafloor core material



Ben Snook

XRD analysis of SMS material





Ben Snook

Initial petrographic description of hydrothermal vent samples

Trondheim, 08 May 2017

MarMine 2017:06






Ben Snook

QEMSCAN analysis of SMS material

Trondheim, 04 September 2017

MarMine 2017:13

NTNU  
Norwegian University of  
Science and Technology  
Department of Geoscience and Petroleum  
The MarMine project

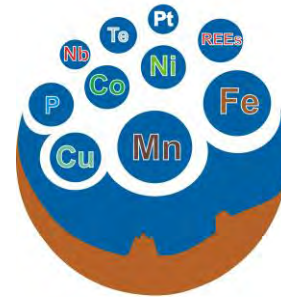
NTNU  
Norwegian University of  
Science and Technology  
Department of Geoscience and Petroleum  
The MarMine project

NTNU  
Norwegian University of  
Science and Technology  
Department of Geoscience and Petroleum  
The MarMine project

NTNU  
Norwegian University of  
Science and Technology  
Department of Geoscience and Petroleum  
The MarMine project

NTNU  
Norwegian University of  
Science and Technology  
Department of Geoscience and Petroleum  
The MarMine project

NTNU  
Norwegian University of  
Science and Technology  
Department of Geoscience and Petroleum  
The MarMine project



**MINDeSEA**  
Seabed Mineral Deposits in European Seas:  
Metallogeny and Geological Potential for  
Strategic and Critical Raw Materials

# Seabed Mineral Deposits in European Seas: Metallogeny and Geological Potential for Strategic and Critical Raw Materials **MINDeSEA**

Javier González and the MINDeSEA Scientific Party  
Marine Geology Div., Geological Survey of Spain (IGME)



Instituto Geológico  
y Minero de España



**Geological Survey**  
Suirbhéireacht Gheolaíochta  
Ireland | Éireann  
an t-Áiríne Comhábala, Gníomhaireacht na h-Éireann  
Department of Communications, Climate Action & Environment



Laboratório Nacional de Energia e Geologia, I. P.



**GEOLOGICAL  
SURVEY OF  
NORWAY**  
- NGU -



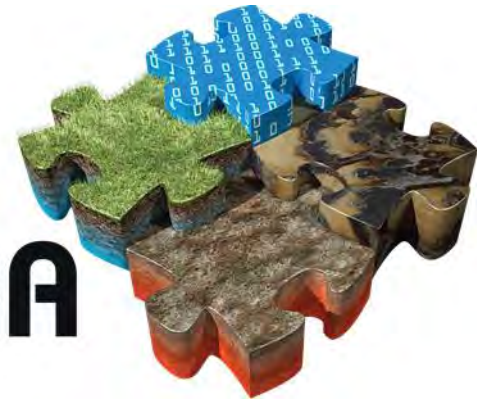
**NGU-Trondheim (Norway)**  
27 November 2019



This project has received funding from the European Union's Horizon 2020 research and innovation programme under grant agreement No 731166



# GeoERA



GeoERA is a 30M EUR research programme supported by both the European Commission and 48 European Geological Survey Organisations from 33 European countries that have joined forces to develop an ERA-NET Co-Fund Action:

***Establishing the European Geological Surveys Research Area to deliver a Geological Service for Europe (GeoERA)***



This project has received funding from the European Union's Horizon 2020 research and innovation programme under grant agreement No 731166



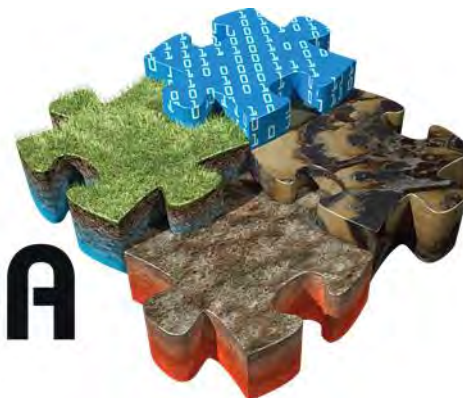


<http://geoera.eu/>

# 15 Projects

that will aim to support 1) a more integrated and efficient management and 2) more responsible and publicly accepted, exploitation and use of the subsurface.

# GeoERA



Secure, clean and efficient energy are at the heart of the H2020's Societal Challenge 3. As Europe progresses to make its transition to a reliable, sustainable and competitive energy...



The objective of the groundwater theme is to provide data, information and decision-support tools for the protection, sustainable management and improvement of groundwater resources...



Mineral Raw Materials underpin societal development and Europe's ambition for economic growth and well-being. The European Commission recognises the importance of Raw Materials...



The geo-energy, groundwater and raw materials themes share the common objective to provide and disseminate spatial information on their respective resources...



**GeoERA**  
is taking off...

Kick-off meeting for  
15 GeoERA projects,  
Brussels, 3 – 5 July 2018

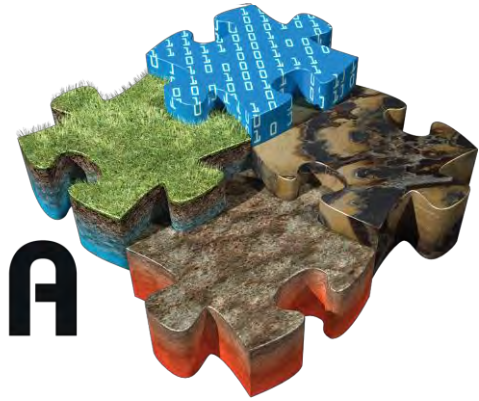


This project has received funding from the European Union's Horizon 2020 research and innovation programme under grant agreement No 731166



# Projects

# GeoERA



All results will be made public through the GeoERA Information Platform a web-based information system building up on the existing **European Geological Data Infrastructure (EGDI)**.

<http://www.europe-geology.eu/>



This project has received funding from the European Union's Horizon 2020 research and innovation programme under grant agreement No 731166



# Projects

**GeoERA**  
RAW MATERIALS



**Mineral Intelligence for Europe**

**EUROLITHOS** European Ornamental Stone Resources

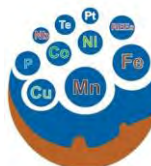


**Ornamental Stone Resources in Europe**



**FRAME**  
FORECASTING AND ASSESSING EUROPE'S  
STRATEGIC RAW MATERIALS NEEDS

**Forecasting and Assessing Europe's Strategic Raw Material Needs**

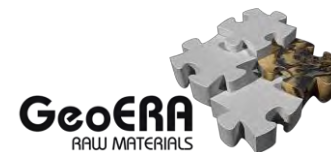


**MINDeSEA**  
Seabed Mineral Deposits in European Seas:  
Metallogeny and Geological Potential for  
Strategic and Critical Raw Materials

**Seabed Mineral Deposits in European Seas**

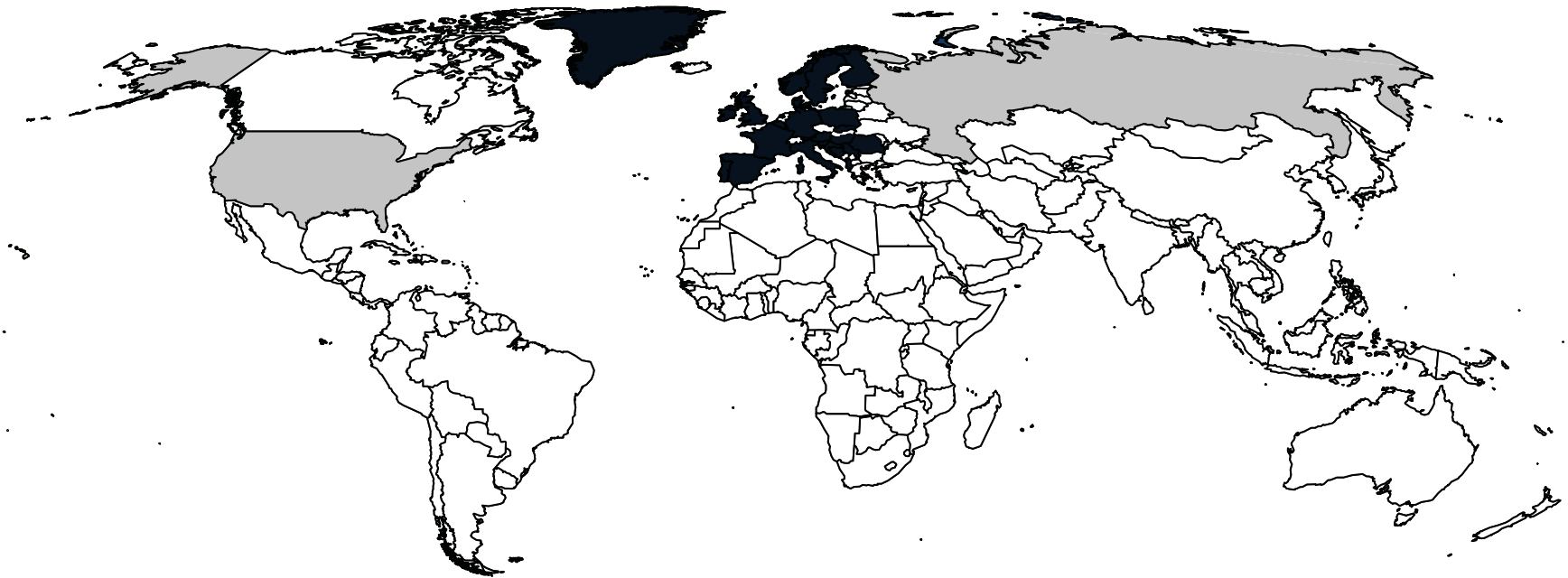


This project has received funding from the European Union's Horizon 2020 research and innovation programme under grant agreement No 731166





37 Regional and National Geological Survey Organizations and Marine Institutes  
 29 countries in Europe and beyond.

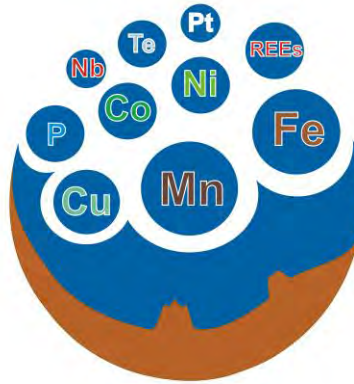


This project has received funding from the European Union's Horizon 2020 research and innovation programme under grant agreement No 731166





**GeoERA**  
RAW MATERIALS



**MINDeSEA**

Seabed Mineral Deposits in European Seas:  
Metallogeny and Geological Potential for  
Strategic and Critical Raw Materials



This project has received funding from the European Union's Horizon 2020 research and innovation programme under grant agreement No 731166



# Consortium

## Project Lead



Instituto Geológico y Minero de España

## WP Leads



Instituto Geológico y Minero de España



GEOLOGICAL SURVEY OF NORWAY  
- NGU -



Geological Survey  
Suirbhéireacht Gheolaíochta  
Ireland | Éireann

An Roinn Comairní, Gaileitheolaíochta agus na Meáin agus Comhaltóir  
Department of Communications, Climate Action & Environment

## Partners



SGU

Sveriges geologiska undersökning  
Geological Survey of Sweden

## (Non-Funded)



instituto português do mar e da atmosfera



science for a changing world



This project has received funding from the European Union's Horizon 2020 research and innovation programme under grant agreement No 731166



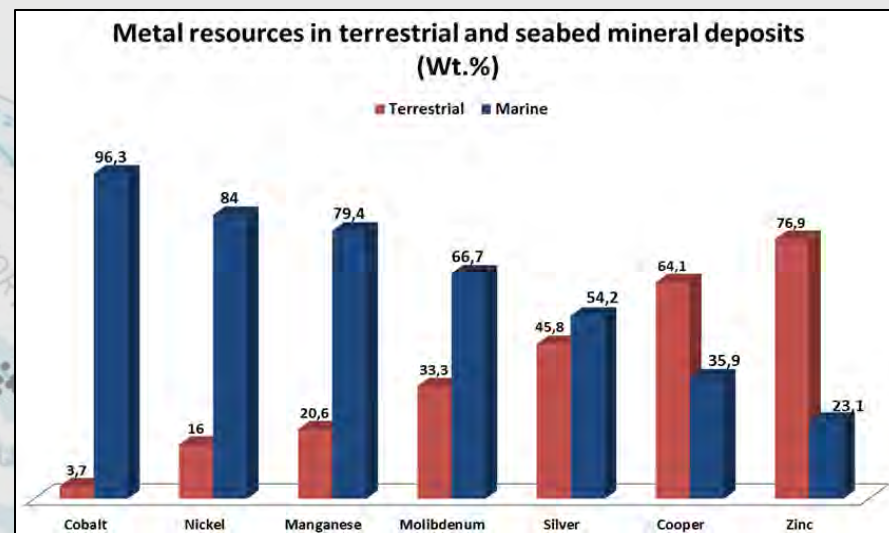
# Challenge

## Seafloor deposits:

the most important yet least explored resource of CRM

By 2030, 10% of the world's minerals, including cobalt, copper and zinc could come from the ocean floors.

Global annual turnover of marine mineral mining can be expected to grow from virtually nothing to **€10 billion by 2030**.



Source: USGS

### 2017 CRMs (27)

Antimony	Fluorspar	<b>LREEs</b>	<b>Phosphorus</b>
Baryte	<b>Gallium</b>	Magnesium	Scandium
Beryllium	<b>Germanium</b>	Natural graphite	Silicon metal
<b>Bismuth</b>	Hafnium	Natural rubber	Tantalum
Borate	Helium	<b>Niobium</b>	<b>Tungsten</b>
<b>Cobalt</b>	<b>HREEs</b>	<b>PGMs</b>	<b>Vanadium</b>
Coking coal	<b>Indium</b>	<b>Phosphate rock</b>	

Source: EC



This project has received funding from the European Union's Horizon 2020 research and innovation programme under grant agreement No 731166





# MINDeSEA Aim and Objectives

The **specific aim** of MINDeSEA is to establish the metallogenic context for different seabed mineral deposits with economic potential in the pan-European setting.

## Objectives

1. Characterise **deposit types**.
2. Characterise the **trace element** content of the deposit type including **CRM**.
3. Identify the principal **metallogenic provinces**.
4. Develop **harmonized mineral maps and datasets** of seabed deposits incorporating GSO datasets, along with mineral-potential and prospectivity maps.
5. Demonstrate how the **case study** results can be used in off-shore mineral exploration.
6. Analyse **present-day exploration and exploitation status** in terms of regulation, legislation, environmental impacts, exploitation and future directions.
7. Demonstrate **efficiency of a pan-European research approach** to understanding seabed minerals and modes of exploration.

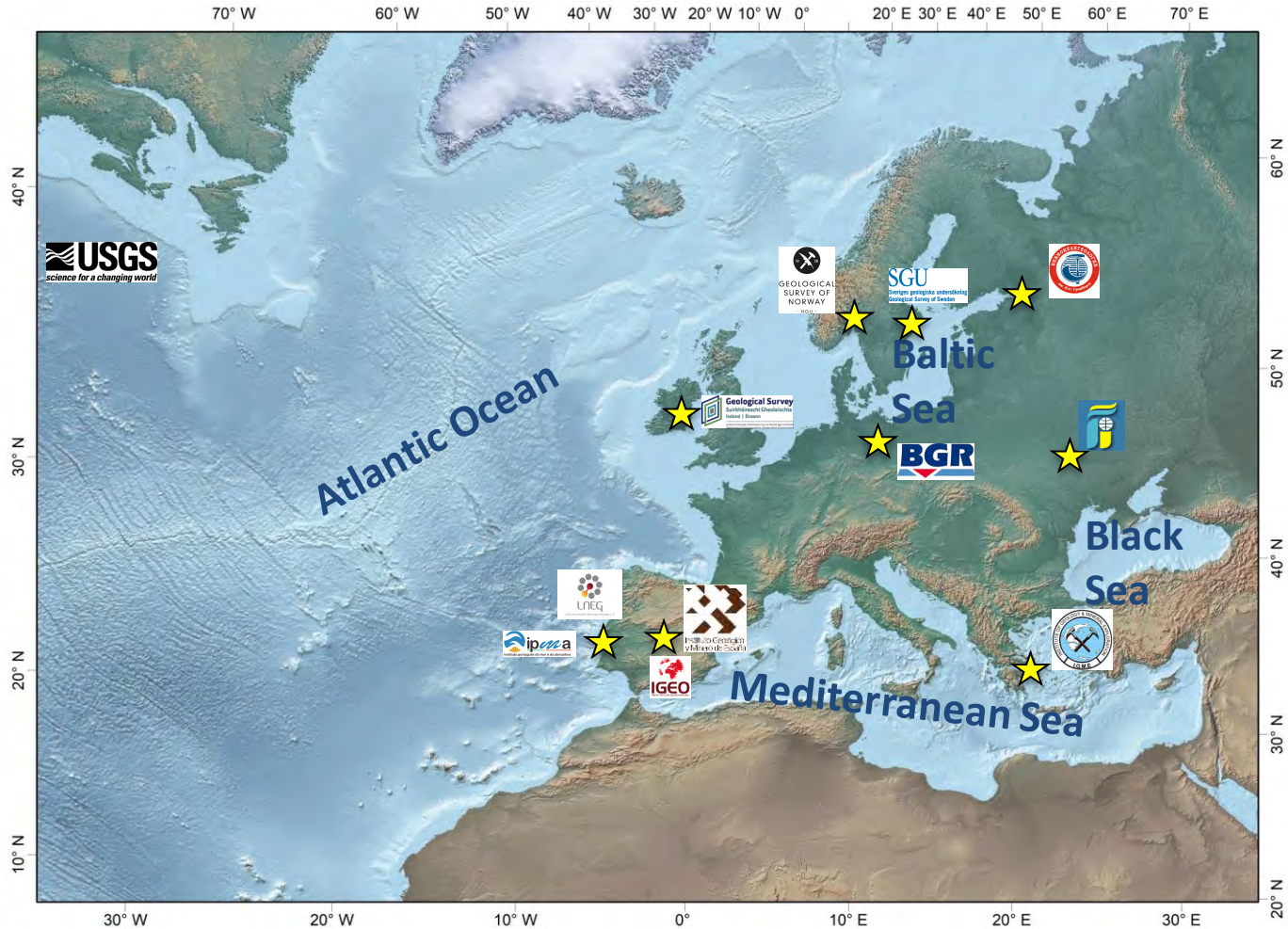


This project has received funding from the European Union's Horizon 2020 research and innovation programme under grant agreement No 731166





# MINDeSEA Geographical Scope



This project has received funding from the European Union's Horizon 2020 research and innovation programme under grant agreement No 731166



# MINDeSEA Outline

WP	Title / Lead	Contact
WP1	Project Management and Coordination. IGME-Spain	Javier González
WP2	Communication, Dissemination and Exploitation. IGME-Spain.	Teresa Medialdea
WP3	Seafloor Massive Sulphide Deposits. NGU-Norway	Henrik Schiellerup
WP4	Ferro-manganese crusts, phosphorites and Critical Raw Materials. IGME-Spain.	Javier González
WP5	Marine placer deposits. HSGME-Greece.	Irene Zananiri
WP6	Polymetallic nodules. LNEG-Portugal	Pedro Ferreira
WP7	Exploration in the Atlantic, Mediterranean, Baltic and Black Sea. IGME-Spain	Luis Somoza
WP8	Link to Information Platform. GSI-Ireland	Xavier Monteys



This project has received funding from the European Union's Horizon 2020 research and innovation programme under grant agreement No 731166





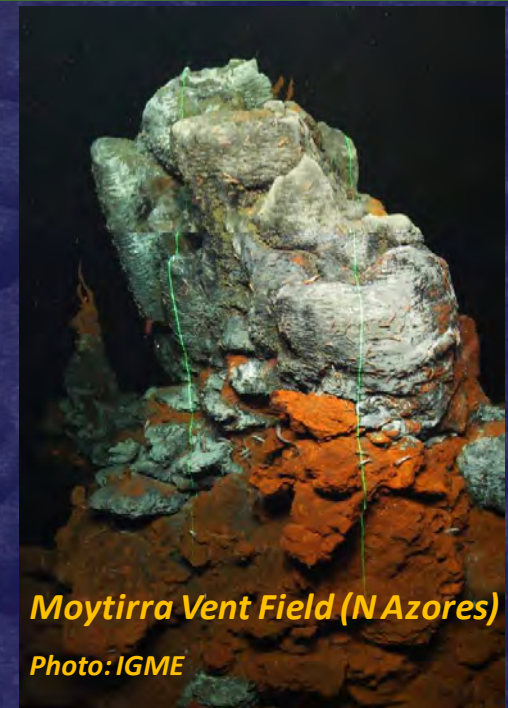
Low to high temperature precipitates (<100-400°C)

On Atlantic Ridge, seamounts, and islands

Chimneys and mounds

Hold Zn, Pb, Cu, Au...

Located sites and extremophiles associated



This project has received funding from the European Union's Horizon 2020 research and innovation programme under grant agreement No 731166





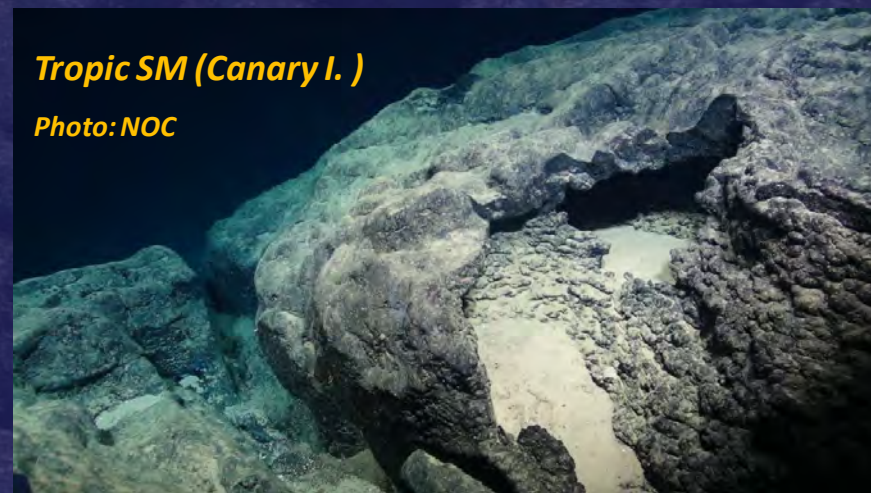
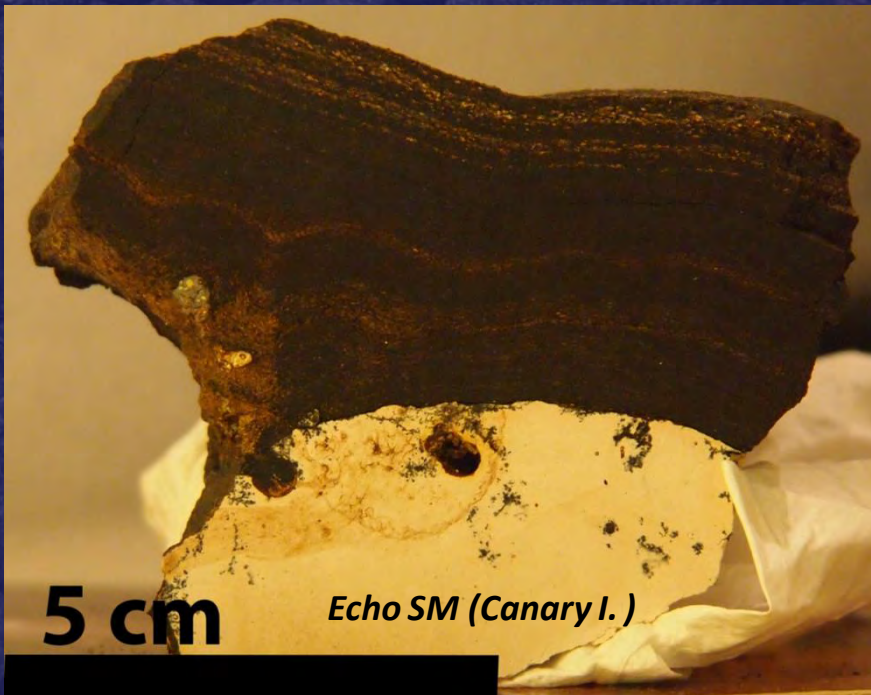
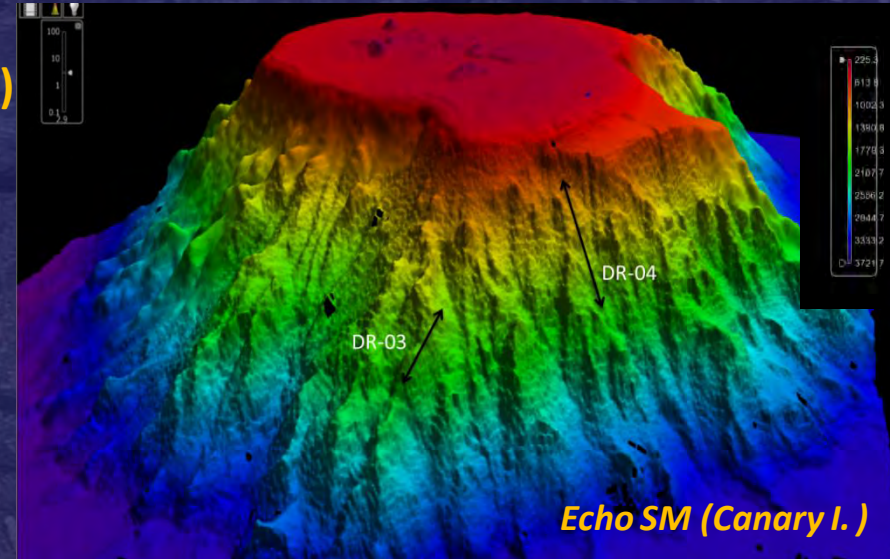
**Fe-Mn precipitates**

**On seamounts, ridges and plateaus (1000-4000 m)**

**Layers up to 25 cm**

**Hold Mn, Co, Ni, V, Mo, Te, Pt, REEs...**

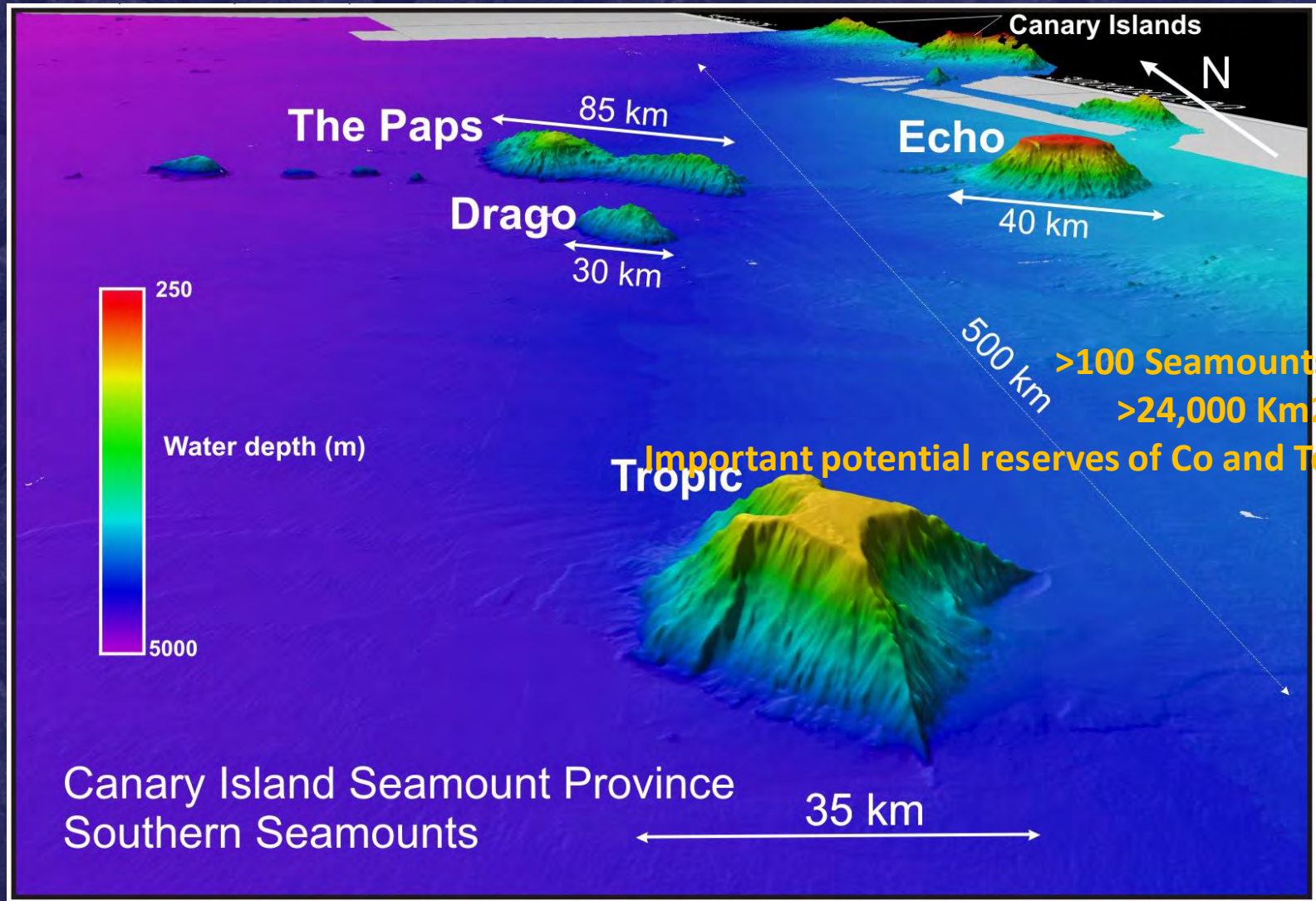
**The most important reserve of Co**



This project has received funding from the European Union's Horizon 2020 research and innovation programme under grant agreement No 731166







This project has received funding from the European Union's Horizon 2020 research and innovation programme under grant agreement No 731166





Non-detrital sedimentary rock which contains high amounts of phosphate minerals

On seamounts, ridges and banks

Cenozoic episodes of phosphatization (39-15 Ma)

Slabs and nodules

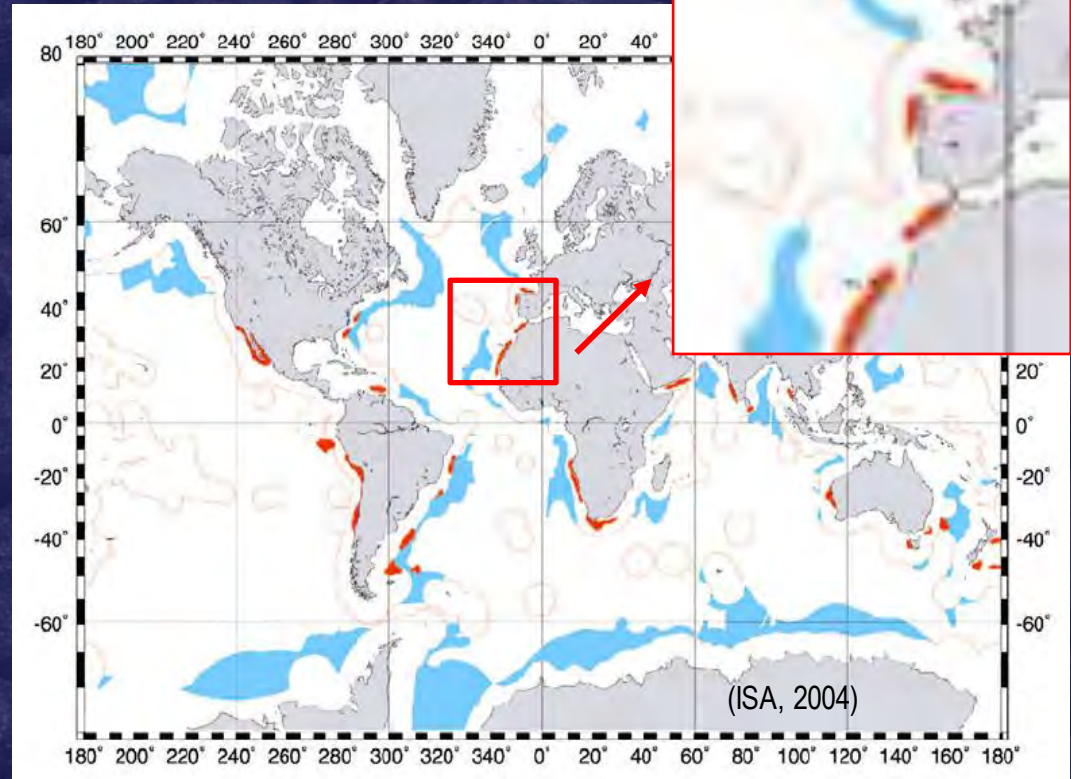
Hold P, Y and REEs...

Phosphorite nodule



E) **DRR38-2**  
2 cm

*Galicia Bank*

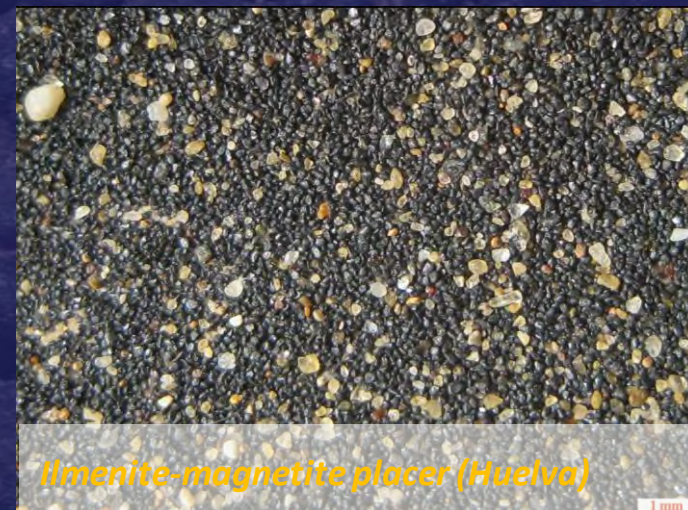


This project has received funding from the European Union's Horizon 2020 research and innovation programme under grant agreement No 731166





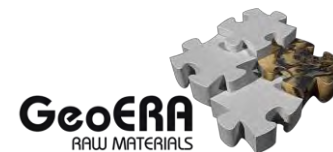
**Resistant and durable minerals**  
**shallow water favorable settings (<50 m water depth)**  
**concentrated by water motions (waves, tides, currents)**  
**On beaches, estuaries and deltas**  
**Hold Ti, Cr, Zr, Au, Sn and REEs...**



*Pérez et al. (2008)*



This project has received funding from the European Union's Horizon 2020 research and innovation programme under grant agreement No 731166





**Fe-Mn precipitates**

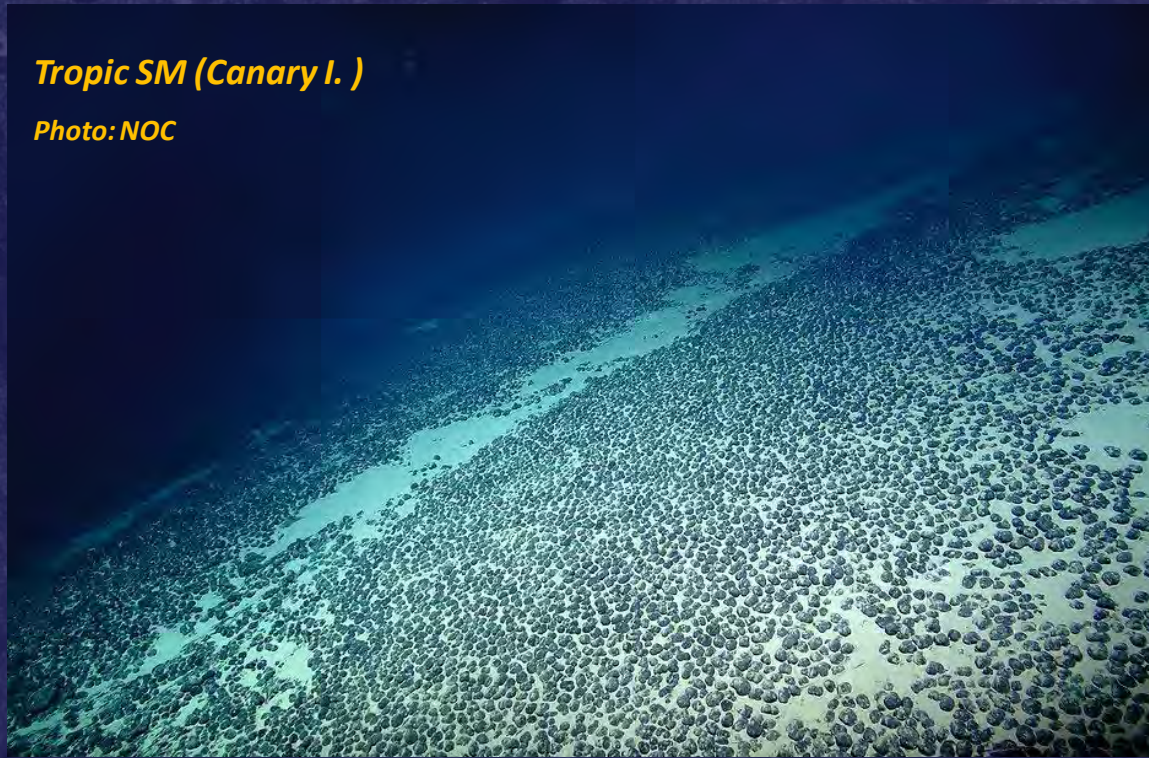
**On abyssal plains, seamounts, banks and plateaus**

**Potato-like concentric concretions up to 20 cm**

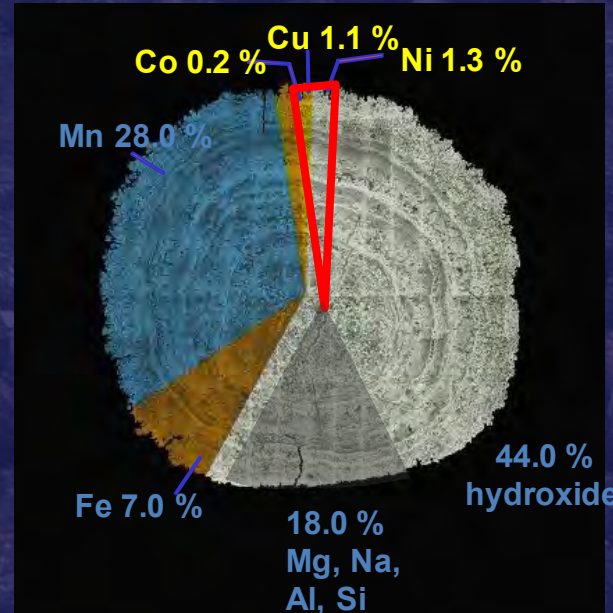
**Hold Mn, Cu, Ni, Co, V, Mo, Li, REEs...**

*Tropic SM (Canary I.)*

*Photo: NOC*



*Gulf of Cadiz (Portugal)*



This project has received funding from the European Union's Horizon 2020 research and innovation programme under grant agreement No 731166





# MINDeSEA: What and for whom?

Databases

Potential and Prospectivity Maps

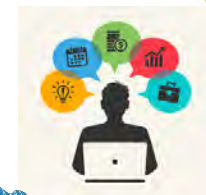
Case Study

Metallogenic Models

Status of regulation, legislation and exploitation

Dissemination Products and Workshops

Progress Reports



GeoERA



This project has received funding from the European Union's Horizon 2020 research and innovation programme under grant agreement No 731166



# MINDeSEA: Importance for policy makers?

## 1. Security

Marine Critical Raw Materials for European Industry  
Supply from EU domestic sources

## 2. Sustainability

Management of competing uses of the European Seas:  
environmental, health and societal impacts

## 3. Innovation

Contributing to the development of minerals intelligence:

- Improving European Seas geological and metallogenic knowledge;
- Improving existing genetic and exploration models; and
- Creating 3D/4D modelling and 3D predictive targeting systems



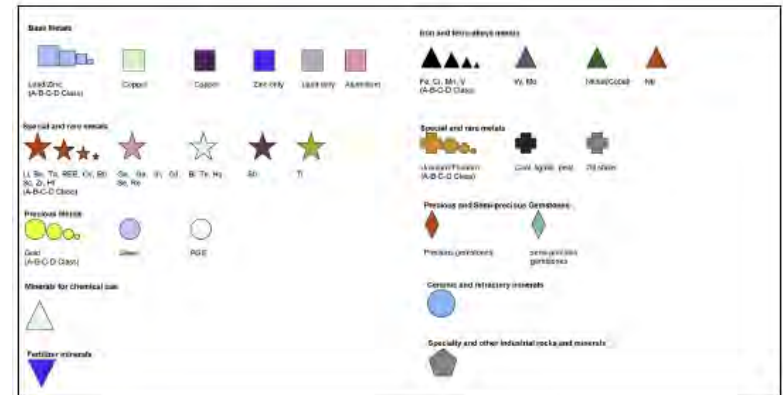
This project has received funding from the European Union's Horizon 2020 research and innovation programme under grant agreement No 731166



## INSPIRE-compliant harmonised datasets and maps

### DATA SPECIFICATIONS

- **Type:** shapefiles of points & polygons
- **Styles:** based on EMODnet-Geology III styles. Additional styles needed (e.g. deposit sub-type) will be based on INSPIRE Technical guides.
- **Attributes:** EMODnet-Geology III WP7 schema, complemented by additional fields to serve:
  - INSPIRE compliancy
  - Data interoperability with on-shore projects
  - Data interoperability with Geo-ERA Information Platform



<p><b>Co FeMn Crust:</b> Style colour based on INSPIRE mineral resources guide "Iron and ferro-alloys metals". As we could choose one style, the style for "Nickel/Cobalt" was chosen to represent all minerals associated with Co FeMn Crust.</p> <p>RGB: 0, 128, 0. Outline: Black.</p>		
<p><b>Phosphorites:</b> Style colour based on INSPIRE minerals guide, "Fertiliser minerals".</p> <p>RGB: 0, 0, 255 Outline: Solid Black</p>		



This project has received funding from the European Union's Horizon 2020 research and innovation programme under grant agreement No 731166

# Databases

	Field Alias	FIELDNAME	Format	Information
General Data	OBJECTID	FID	Number	Feature ID. An internally generated identification number for each
	Shape	SHAPE	Geometry	Polygon
	Country Code	CODE	Text (2)	Two letter country code, which corresponds to ISO3166- code ht
	Administration	ADM	Text (40)	Legal status following the division of the Law of the Sea Conventi
	Geographical Area	GEO_AREA	Text (40)	Atlantic Ocean, Mediterranean Sea, etc
Metallogeny	Sector	SECTOR	Text (40)	Canary Island Seamount Province, Eolian Islands, Gulf of Bothnia, .
	Deposit Group	DEPOSIT_G	Text (100)	Sediment-related deposits, hydrothermal deposits, volcanogenic d
	Deposit Type	DEPOSIT_TY	Text (40)	<b>Co-rich ferromanganese crust</b> -this exact wording must be ent
	Setting	SETTING	Text (250)	Description of geological setting
	Geomorphic features	GEOMORPH	Text (250)	Geomorphology of area of FeMn crust occurrence
	Age	AGE	Text (250)	Age of the mineral deposit and host rock
	Host rock	HOST_ROCK	Text (250)	Substrate rock or sediment surrounding the ore deposit
	Metallic Commodity	METAL_COMM	Text (40)	Including precious and non-precious metals
	Commodity Group	COMM_G	Text (40)	Base metals, precious metals, energy metals, technological metals
	Ore Minerals	ORE_MIN	Text (250)	Principal minerals/commodities
	Gangue Minerals	GANGUE	Text (250)	Accessory minerals/commodities (gangue minerals)
	Alteration	ALTER	Text (250)	Alteration minerals formed during/after the process of mineralizati
	Morphology	MORPH	Text (250)	Shape and internal structure (thickness and texture) of the miner
	Geochemistry	GEOCHEM	Text (250)	Link to Geochemistry table
Economic Data	Size	SIZE	Text (250)	Magnitude of the mineral deposit (unknown, occurrence, small, m
	Economic feasibility	ECON_FEAS	Text (250)	Specify assessments of reserve (tonnage Mt), grade (Mean conte
	Data Scale	SCALE	Text (100)	Specify the scale in which the deposit has been mapped and deliv
	Measured Units	UNITS	Text (50)	Quantitative measurement of deposit if available.
	Status	STATUS	Text (250)	e.g. under exploration, research, identified deposits, hypothetical
	Operator	OPERATOR	Text (250)	Research, exploration or operating agency/company
	Exploration Type	EXPLOR_TY	Text (250)	Exploration techniques employed to describe the mineral deposit h
	Cruises	CRUISES	Text (250)	Cruises identification
	Sampling Methods	SAMPLING_M	Text (250)	Type of method to recover samples (dredge, ROV...)
	Sites Number	SITES_NO	Text (250)	Sampling sites identification
	Deposit Name	DEPOSIT_NAME	Text (250)	Name of the area of the deposit, concession or resource area
	Deposit Number	DEPOSIT_NO	Text (50)	Number of the area of the deposit, concession or resource area
	Data Provider	DATA_PROVI	Text (150)	Name of organisation providing data
	Data Provider Contact	DATA_CONT	Text (150)	The data providing <b>organisation/institute</b> contact details - ema
Environment	Deposit Extent	DEPOSIT_KM2	No. Double (11,4)	Area of deposit ( <b>Sq. Km</b> )
	Depth to Deposit (m)	DEPTH_TO_D	No. Double (11,4)	Depth to deposit from sea surface
Other Data	Fauna	FAUNA	Text (100)	Type of fauna (e.g. corals,...)
	Description	DESCRIPTION	Text (500)	Deposit summary and metallogenic model
	Gallery	GALLERY	Image	Images on the mineralization (geophysical, sampling, textural feat
	References	REFERENCES	Text (250)	Link to bibliographic references (DOI and/or Author, Year & Title if
	Comments	COMMENTS	Text (250)	Any additional comments or observations

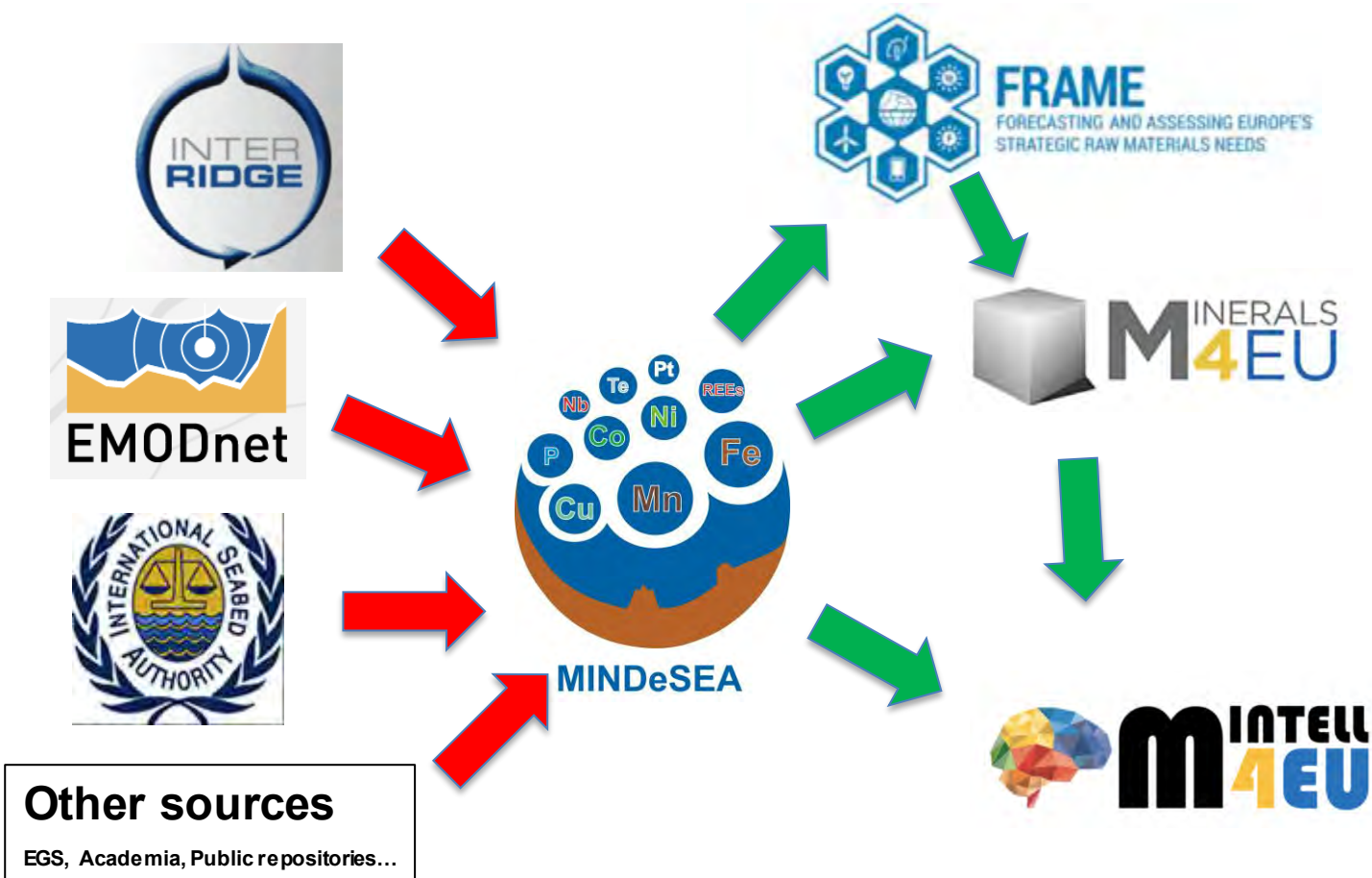


This project has received funding from the European Union's Horizon 2020 research and innovation programme under grant agreement No 731166





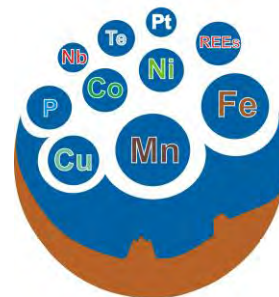
# MINDeSEA: Data flow



This project has received funding from the European Union's Horizon 2020 research and innovation programme under grant agreement No 731166



# Pan-European Map of Submarine Energy-critical Elements



**MINDeSEA**  
Seabed Mineral Deposits in European Seas: Metallogeny and Geological Potential for Strategic and Critical Raw Materials

## Polymetallic nodules



Average abundances of elements

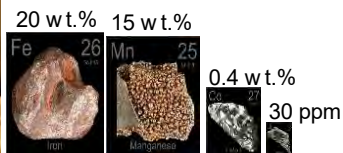
215 Occurrences

Distribution: Abyssal plains, shallow waters

Potential deposits: Arctic Ocean and Baltic Sea

Occurrences ( $\text{Li}_2\text{O}$  average content <660 g/t; potential resources <5,000Mt)

## Co-rich ferromanganese crusts



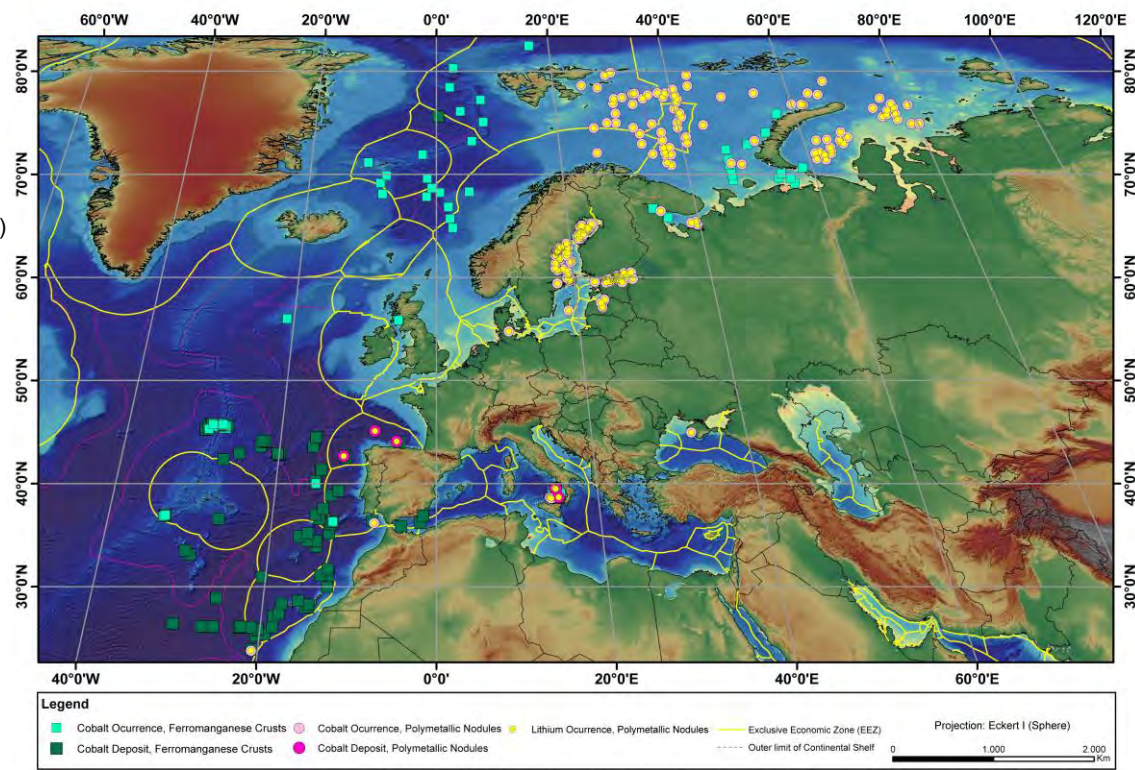
Average abundances of elements

164 Occurrences

Distribution: Seamounts, plateaus and ridges

Potential deposits: Macaronesia Region

Deposits (Co average content >500 g/t; potential resources >200Mt)



Copyright © 2018 GeoERA. This project has received funding from the European Union's Horizon 2020 research and innovation programme under grant agreement No 731166.



This project has received funding from the European Union's Horizon 2020 research and innovation programme under grant agreement No 731166

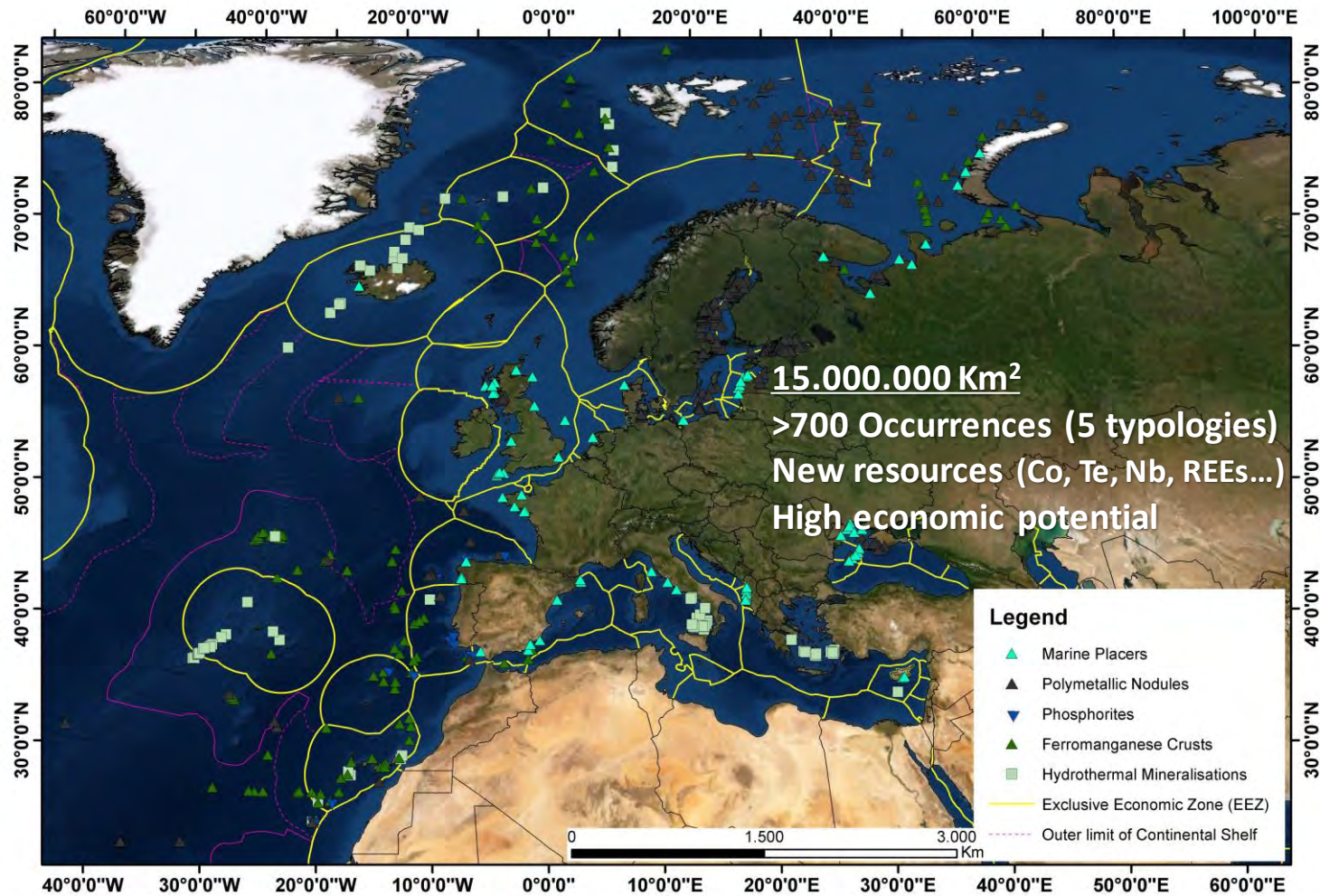


This project has received funding from the European Union's Horizon 2020 research and innovation programme under grant agreement No 731166





# Database and Maps Progresses



Copyright © 2018 GeoERA. This project has received funding from the European Union's Horizon 2020 research and innovation programme under grant agreement No 731166.



This project has received funding from the European Union's Horizon 2020 research and innovation programme under grant agreement No 731166



# MINDeSEA: Social Media

Establishing the European Geological Surveys Research Area to deliver a Geological Service for Europe



Home Projects Themes Call FAQ GeoERA material About GeoERA Contact Search

## Seabed Mineral Deposits in European Seas: Metallogeny and Geological Potential for Strategic and Critical Raw Materials (MINDeSEA)

### Abstract

The project MINDeSEA results of the collaboration between eight GeoERA Partners and four Non-funded Organizations at various points of common interest for exploration and investigation on seafloor mineral deposits. This project addresses an integrative metallogenetic study of principal types of seabed mineral resources (hydrothermal sulfides, ferromanganese crusts, phosphonites, marine placers and polymetallic nodules) in the European Seas. The MINDeSEA working group has both knowledge of and expertise in such types of mineralisation, providing exploration results, sample repositories and databases to produce innovative contributions. The importance of submarine mineralisation systems is related to the abundance and exploitation-potential of many strategic metals and Critical Raw Materials (CRM), necessary for the modern society development.



The objectives of this project are the following: 1) Characterise deposit types; 2) Characterise the trace element content of the deposit type including CRM; 3) Identify the principal metallogenic provinces; 4) Develop harmonised mineral maps and datasets of seabed deposits incorporating GSD datasets, along with mineral-potential and prospectivity maps; 5) Demonstrate how the cases study results can be used in off-shore mineral exploration; 6) Analyse present-day exploration and exploitation status in terms of regulation, legislation, environmental impacts, exploitation and future directions. 7) Demonstrate efficiency of a pan-European research approach to understanding seabed minerals and modes of exploration. The methodology will include: procedures for submarine minerals exploration; mineral evaluation and seafloor minerals mapping; a web service that will disseminate procedures, maps and information to the general public, downstream users and decision makers.

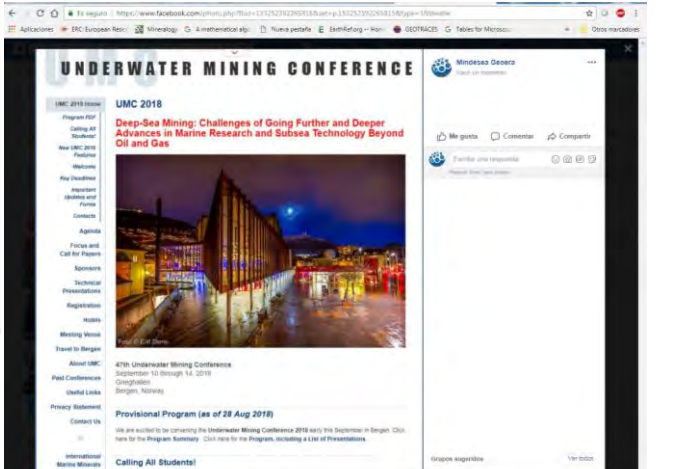
Project website <http://geoera.eu/projects/mindesea/>

Further details about the project will be available later.

<https://www.facebook.com/mindesea.mindesea.9>



<https://twitter.com/MINDeSEA>



<https://www.facebook.com/mindesea.mindesea.9>



This project has received funding from the European Union's Horizon 2020 research and innovation programme under grant agreement No 731166

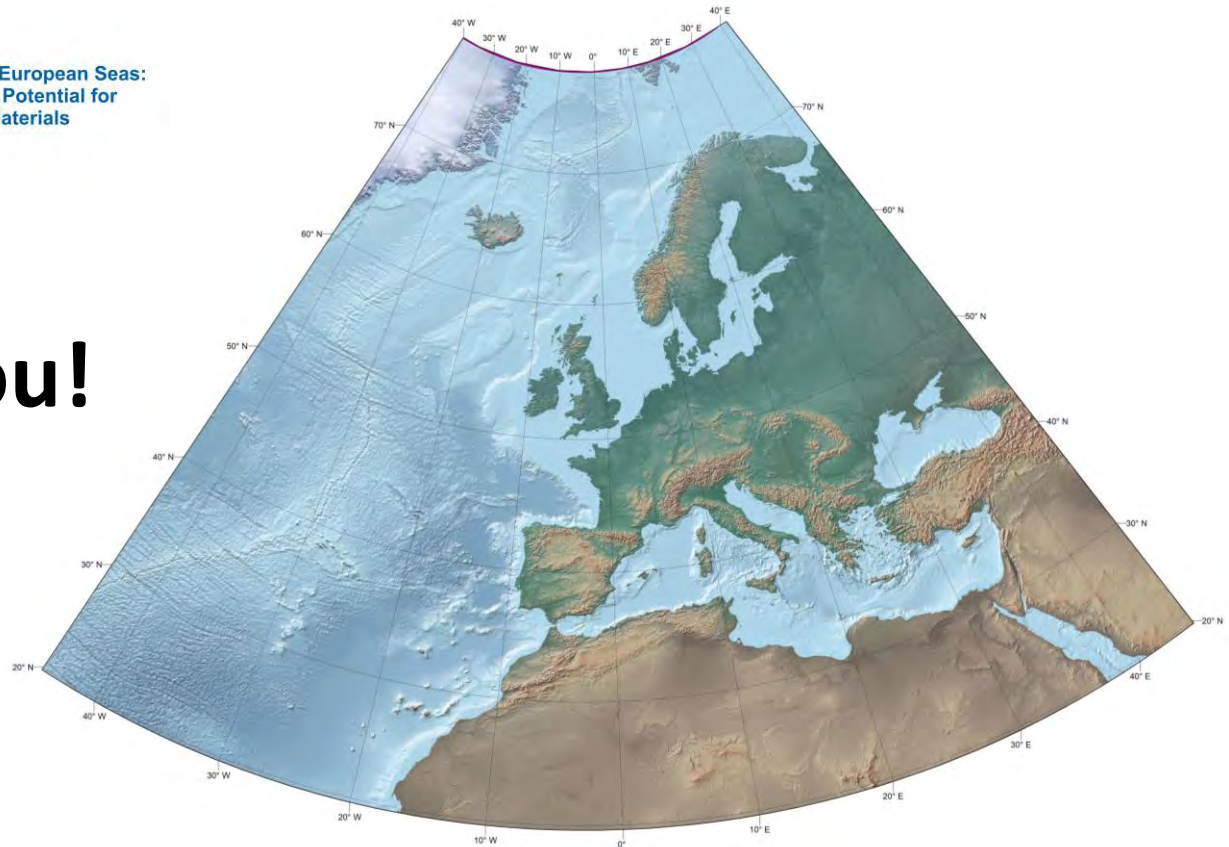






**MINDeSEA**  
Seabed Mineral Deposits in European Seas:  
Metallogeny and Geological Potential for  
Strategic and Critical Raw Materials

# Thank you!



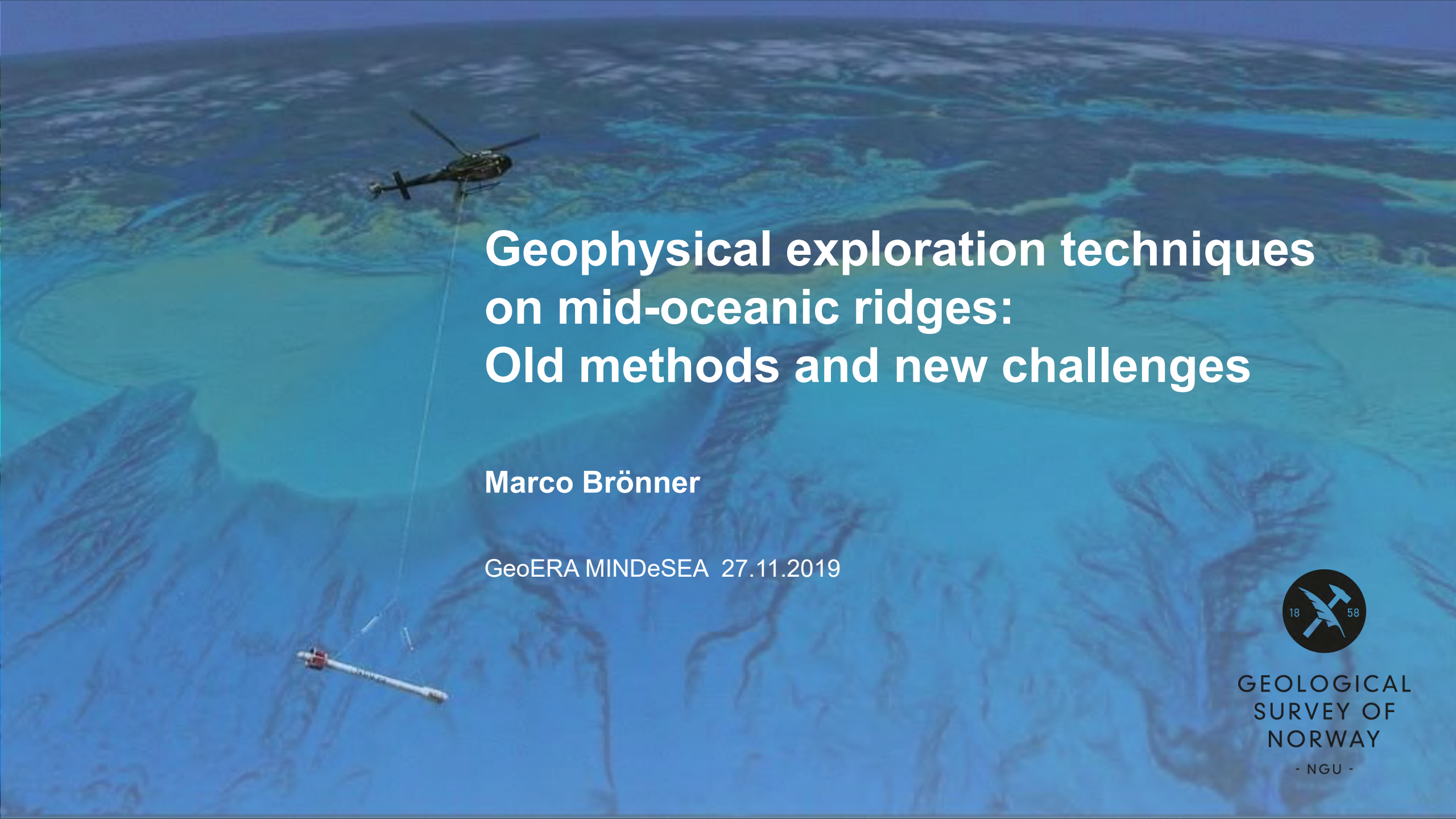
Learn more about the GeoERA-MINDeSEA project at: <http://geoera.eu/projects/mindesea/>

Follow us on Twitter [@MINDeSEA](https://twitter.com/MINDeSEA)



This project has received funding from the European Union's Horizon 2020 research and innovation programme under grant agreement No 731166





# Geophysical exploration techniques on mid-oceanic ridges: Old methods and new challenges

Marco Brønner

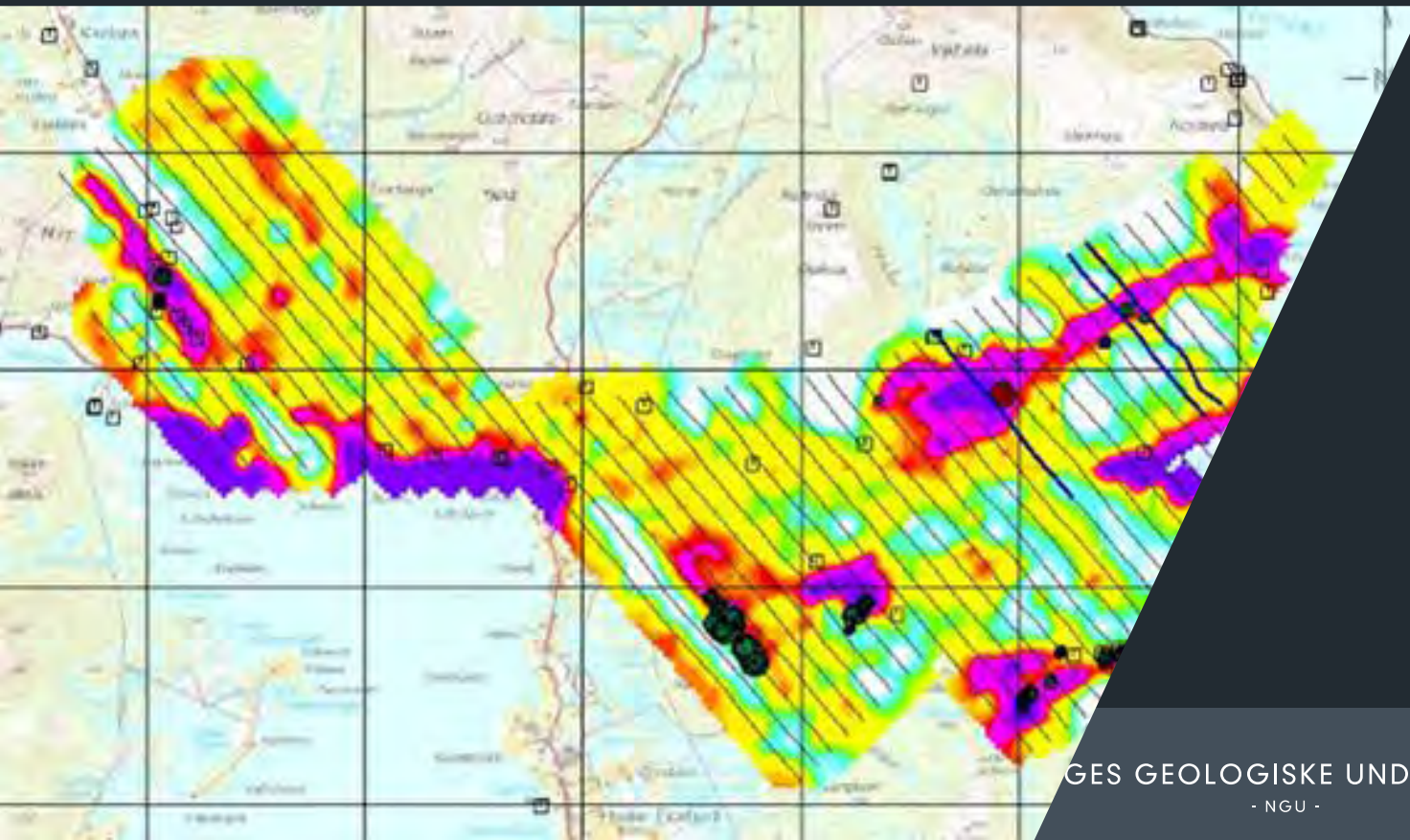
GeoERA MINDeSEA 27.11.2019



GEOLOGICAL  
SURVEY OF  
NORWAY

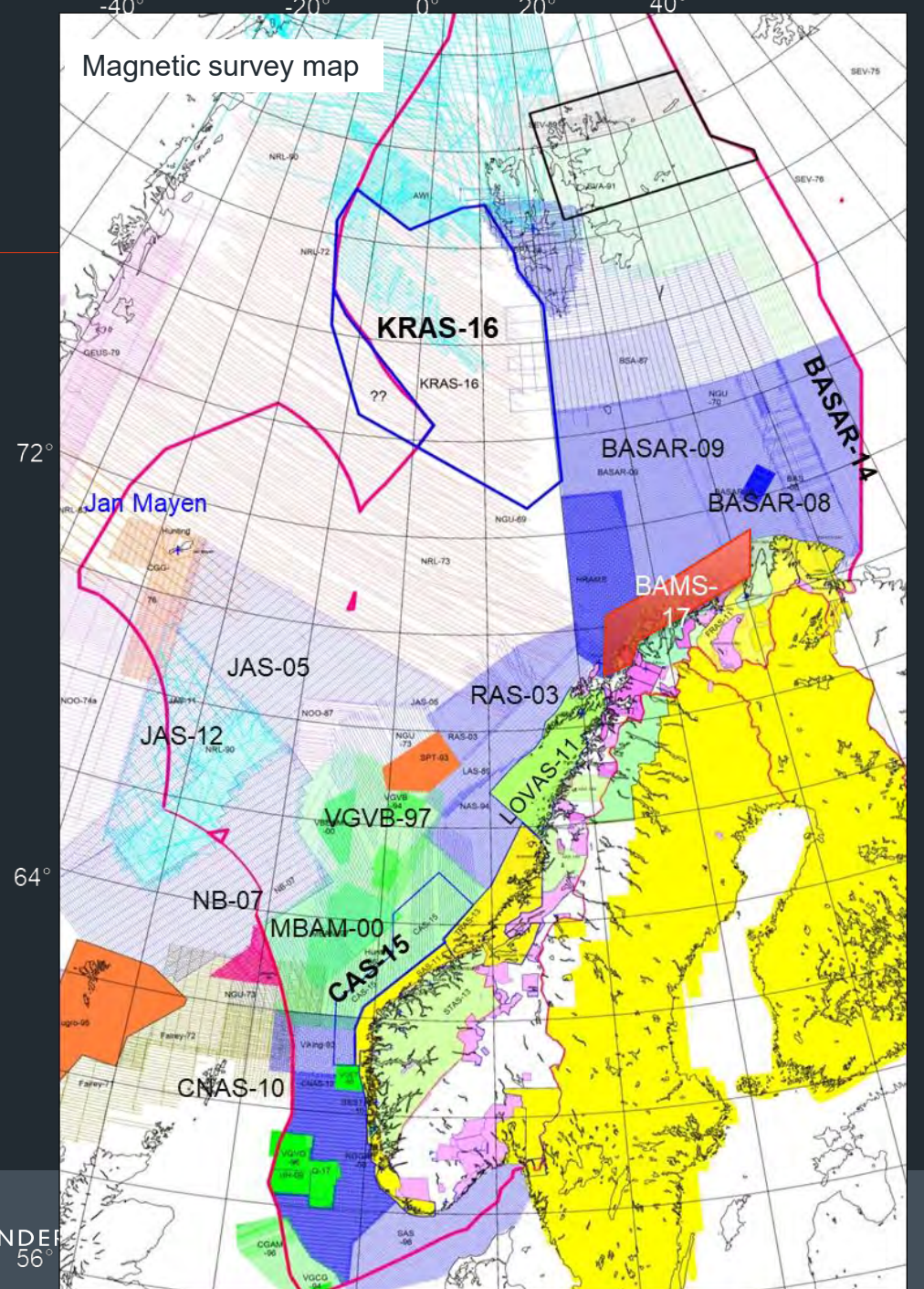
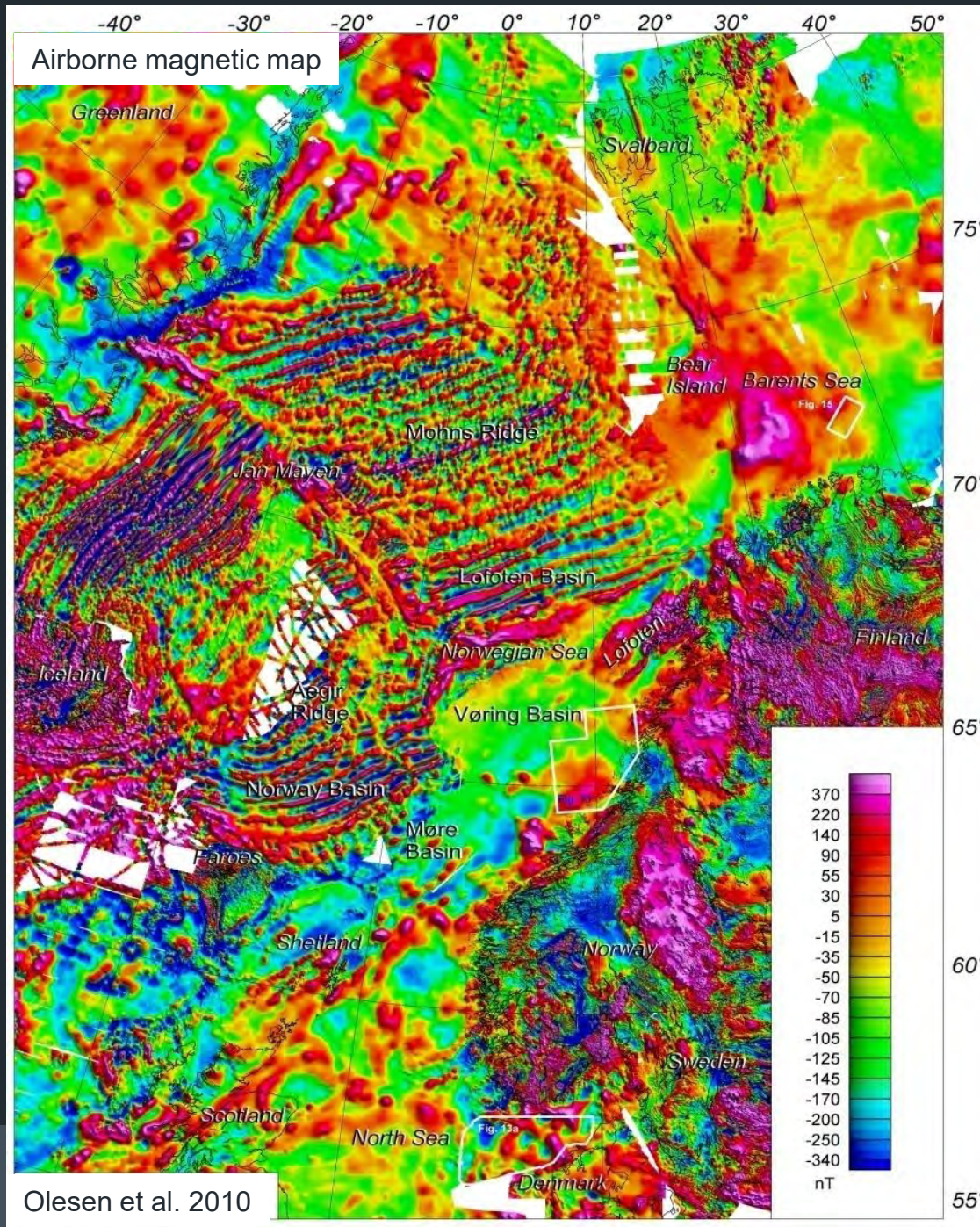
- NGU -



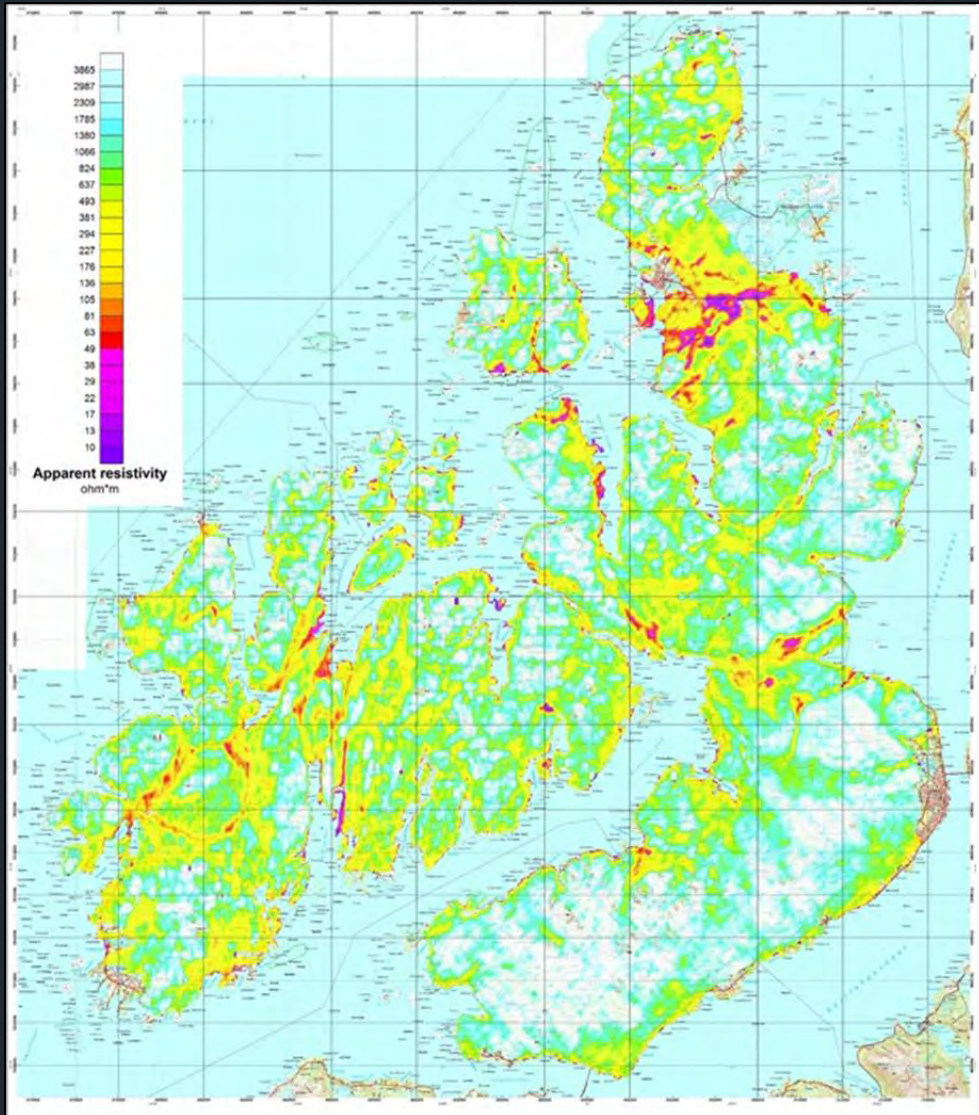


# Geophysical data acquisition to map geology

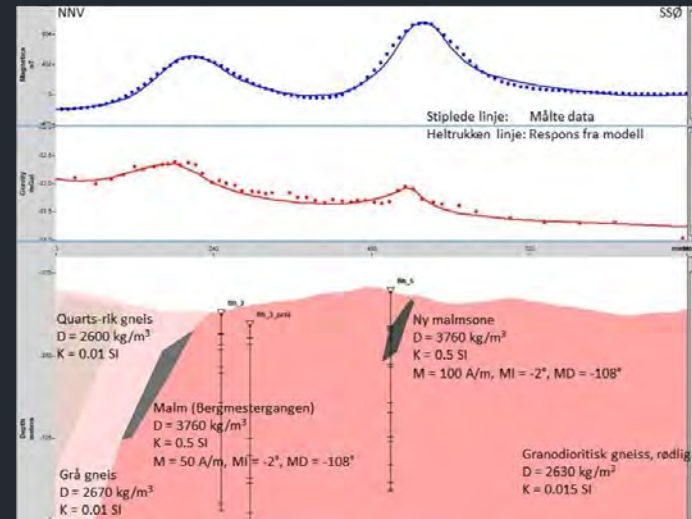




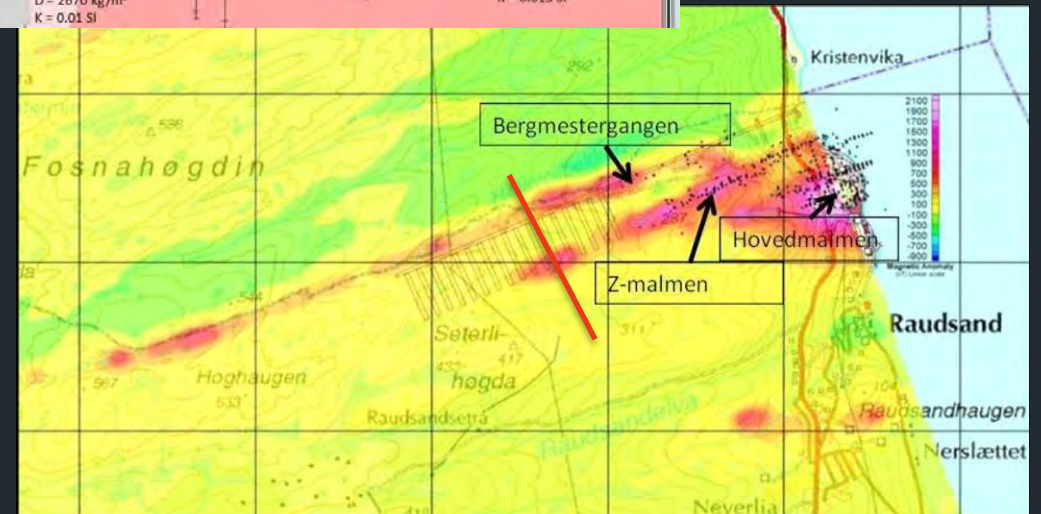




Airborne frequency EM data identify graphite deposit



Grav-mag modelling to estimate volume and depth of the deposit



Airborne magnetic and ground-borne gravity data identify iron ore deposit

# Bedrock characterisation onshore and on the Norwegian shelf

Table 1. Applicability of different geophysical methods in the exploration of various mineral systems (modified from Ford et al. 2007).

● Highly effective    ● Moderately effective    ● Generally ineffective

Geo-physical method	Air or ground	Application	Ni-Cu-PGE	Fe-Ti-BIF	Gold	VMS	Olympic Dam-type	SEDEX	Porphyry Cu	Pb-Zn	Diamonds
Magnetic	Air	Geological framework	●	●	●	●	●	●	●	●	●
		Direct targeting	●	●	●	●	●	●	●	●	●
	Ground	Geological framework	●	●	●	●	●	●	●	●	●
Direct targeting		●	●	●	●	●	●	●	●	●	
Electro-magnetic	Air	Geological framework	●	●	●	●	●	●	●	●	●
		Direct targeting	●	●	●	●	●	●	●	●	●
	Ground	Geological framework	●	●	●	●	●	●	●	●	●
		Direct targeting	●	●	●	●	●	●	●	●	●
Electric	Ground	Geological framework	●	●	●	●	●	●	●	●	●
		Direct targeting	●	●	●	●	●	●	●	●	●
Gravity	Air	Geological framework	●	●	●	●	●	●	●	●	●
		Direct targeting	●	●	●	●	●	●	●	●	●
	Ground	Geological framework	●	●	●	●	●	●	●	●	●
Direct targeting		●	●	●	●	●	●	●	●	●	
Radio-metric	Air	Geological framework	●	●	●	●	●	●	●	●	●
		Direct targeting	●	●	●	●	●	●	●	●	●
	Ground	Geological framework	●	●	●	●	●	●	●	●	●
Direct targeting		●	●	●	●	●	●	●	●	●	
Seismic	Ground	Geological framework	●	●	●	●	●	●	●	●	●
		Direct targeting	●	●	●	●	●	●	●	●	●



# Mineral exploration onshore

Table 1. Applicability of different geophysical methods in the exploration of various mineral systems (modified from Ford et al. 2007).

● Highly effective    ● Moderately effective    ● Generally ineffective

Geo-physical method	Air or ground	Application	Ni-Cu-PGE	Fe-Ti-BIF	Gold	VMS	Olympic Dam-type	SEDEX	Porphyry Cu	Pb-Zn	Diamonds
Magnetic	Air	Geological framework	●	●	●	●	●	●	●	●	●
		Direct targeting	●	●	●	●	●	●	●	●	●
	Ground	Geological framework	●	●	●	●	●	●	●	●	●
		Direct targeting	●	●	●	●	●	●	●	●	●
Electromagnetic	Air	Geological framework	●	●	●	●	●	●	●	●	●
		Direct targeting	●	●	●	●	●	●	●	●	●
	Ground	Geological framework	●	●	●	●	●	●	●	●	●
		Direct targeting	●	●	●	●	●	●	●	●	●
Electric	Ground	Geological framework	●	●	●	●	●	●	●	●	●
		Direct targeting	●	●	●	●	●	●	●	●	●
Gravity	Air	Geological framework	●	●	●	●	●	●	●	●	●
		Direct targeting	●	●	●	●	●	●	●	●	●
	Ground	Geological framework	●	●	●	●	●	●	●	●	●
		Direct targeting	●	●	●	●	●	●	●	●	●
Radio-metric	Air	Geological framework	●	●	●	●	●	●	●	●	●
	Ground	Direct targeting	●	●	●	●	●	●	●	●	●
		Ground	Geological framework	●	●	●	●	●	●	●	●
	Direct targeting		●	●	●	●	●	●	●	●	
Seismic	Ground	Geological framework	●	●	●	●	●	●	●	●	●
		Direct targeting	●	●	●	●	●	●	●	●	●



# Deep sea mineral exploration in Norway

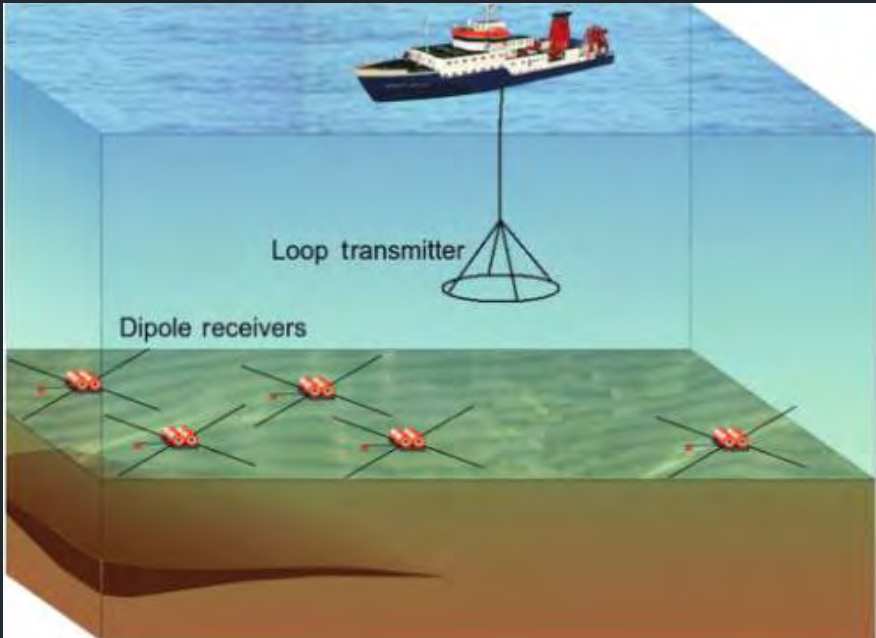
Table 1. Applicability of different geophysical methods in the exploration of various mineral systems (modified from Ford et al. 2007).

● Highly effective    ● Moderately effective    ● Generally ineffective

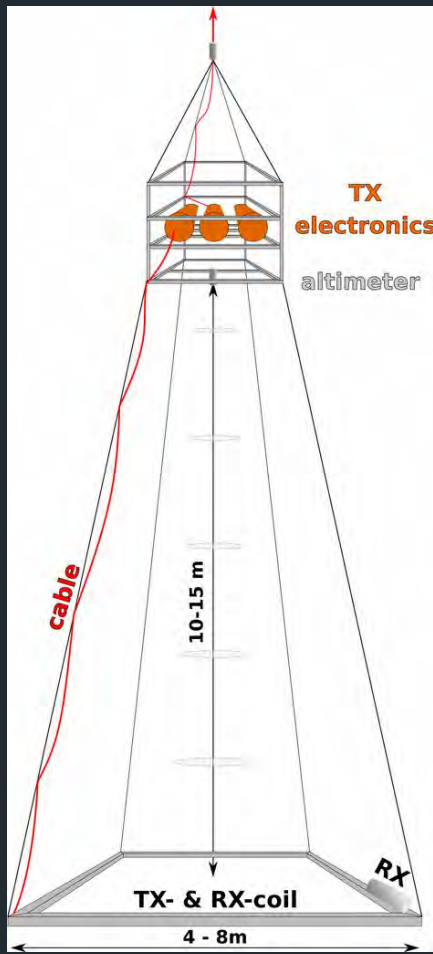
Geo-physical method	Air or ground	Application	Ni-Cu-PGE	Fe-Ti-BIF	Gold	VMS	Olympic Dam-type	SEDEX	Porphyry Cu	Pb-Zn	Diamonds
Magnetic	Air	Geological framework	●	●	●	●	●	●	●	●	●
		Direct targeting	●	●	●	●	●	●	●	●	●
	Ground	Geological framework	●	●	●	●	●	●	●	●	●
		Direct targeting	●	●	●	●	●	●	●	●	●
Electromagnetic	Air	Geological framework	●	●	●	●	●	●	●	●	●
		Direct targeting	●	●	●	●	●	●	●	●	●
	Ground	Geological framework	●	●	●	●	●	●	●	●	●
Electric	Ground	Geological framework	●	●	●	●	●	●	●	●	●
		Direct targeting	●	●	●	●	●	●	●	●	●
Gravity	Air	Geological framework	●	●	●	●	●	●	●	●	●
		Direct targeting	●	●	●	●	●	●	●	●	●
	Ground	Geological framework	●	●	●	●	●	●	●	●	●
		Direct targeting	●	●	●	●	●	●	●	●	●
Radiometric	Air	Geological framework	●	●	●	●	●	●	●	●	●
		Direct targeting	●	●	●	●	●	●	●	●	●
	Ground	Geological framework	●	●	●	●	●	●	●	●	●
		Direct targeting	●	●	●	●	●	●	●	●	●
Seismic	Ground	Geological framework	●	●	●	●	●	●	●	●	●
		Direct targeting	●	●	●	●	●	●	●	●	●

**Challenge!**

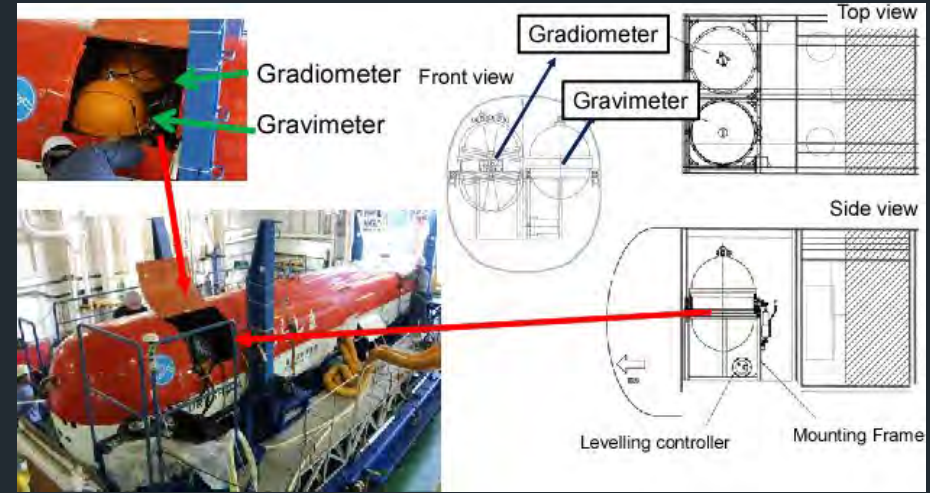
SP



Concept marine CSEM



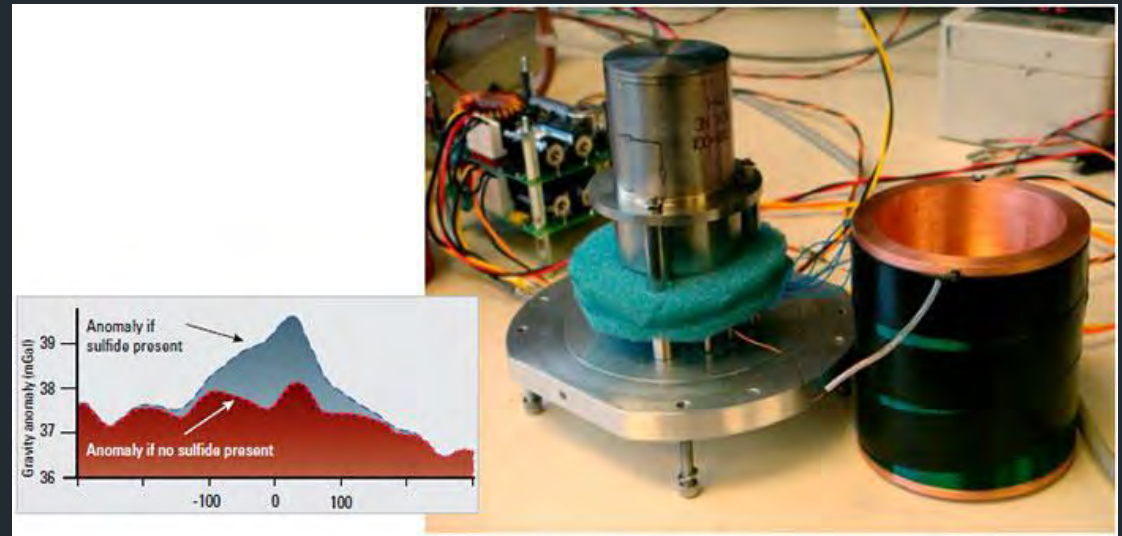
MARTEMIS coil system



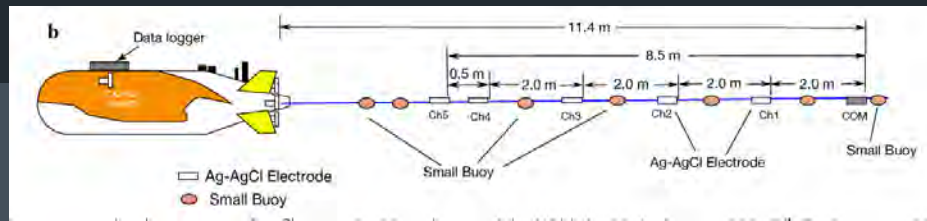
AUV mounted gravimeter on Urashima, Jamtec



Photo A. Lim



AUV mounted gravimeter by Woods Hole Oceanographic Inst.

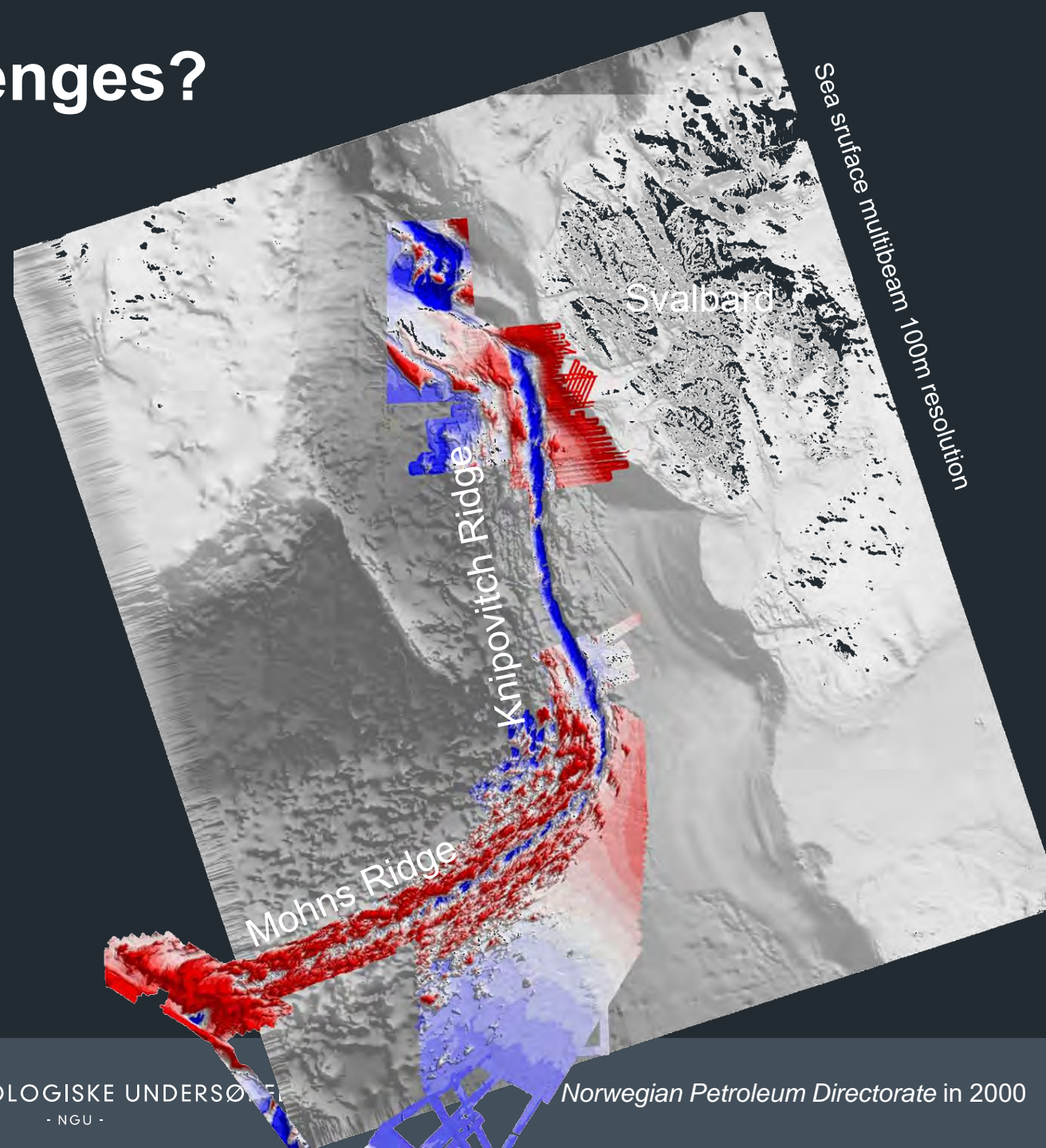
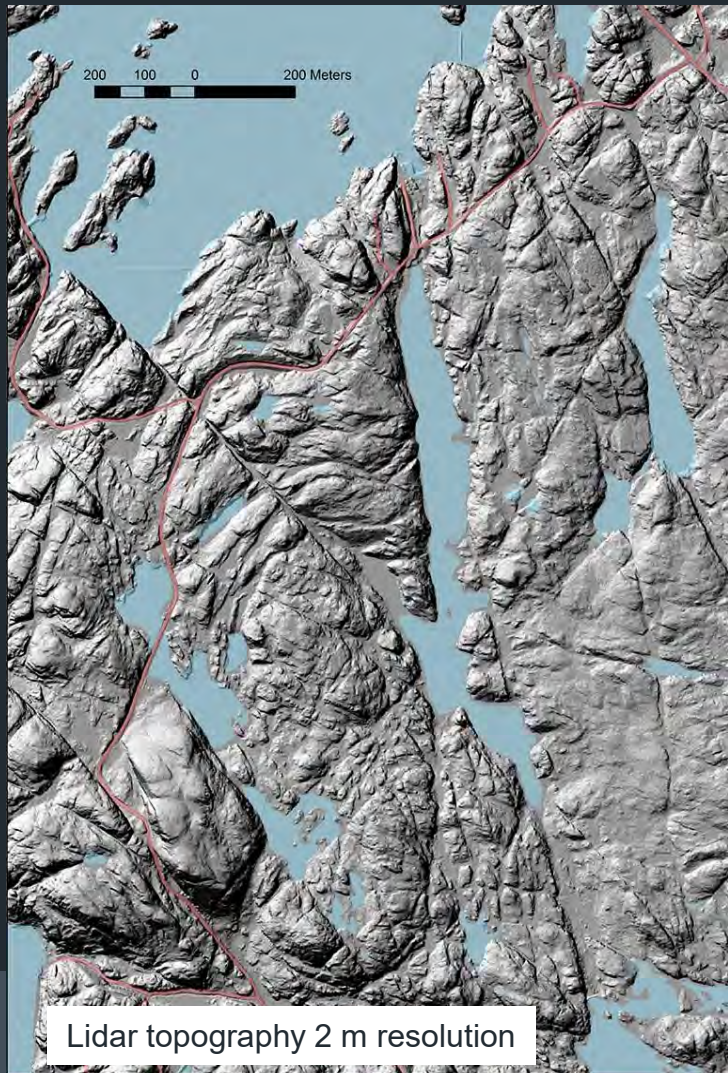


Self Potential, Jamtec



# Old methods and new challenges?

High resolution - high precision underlying data



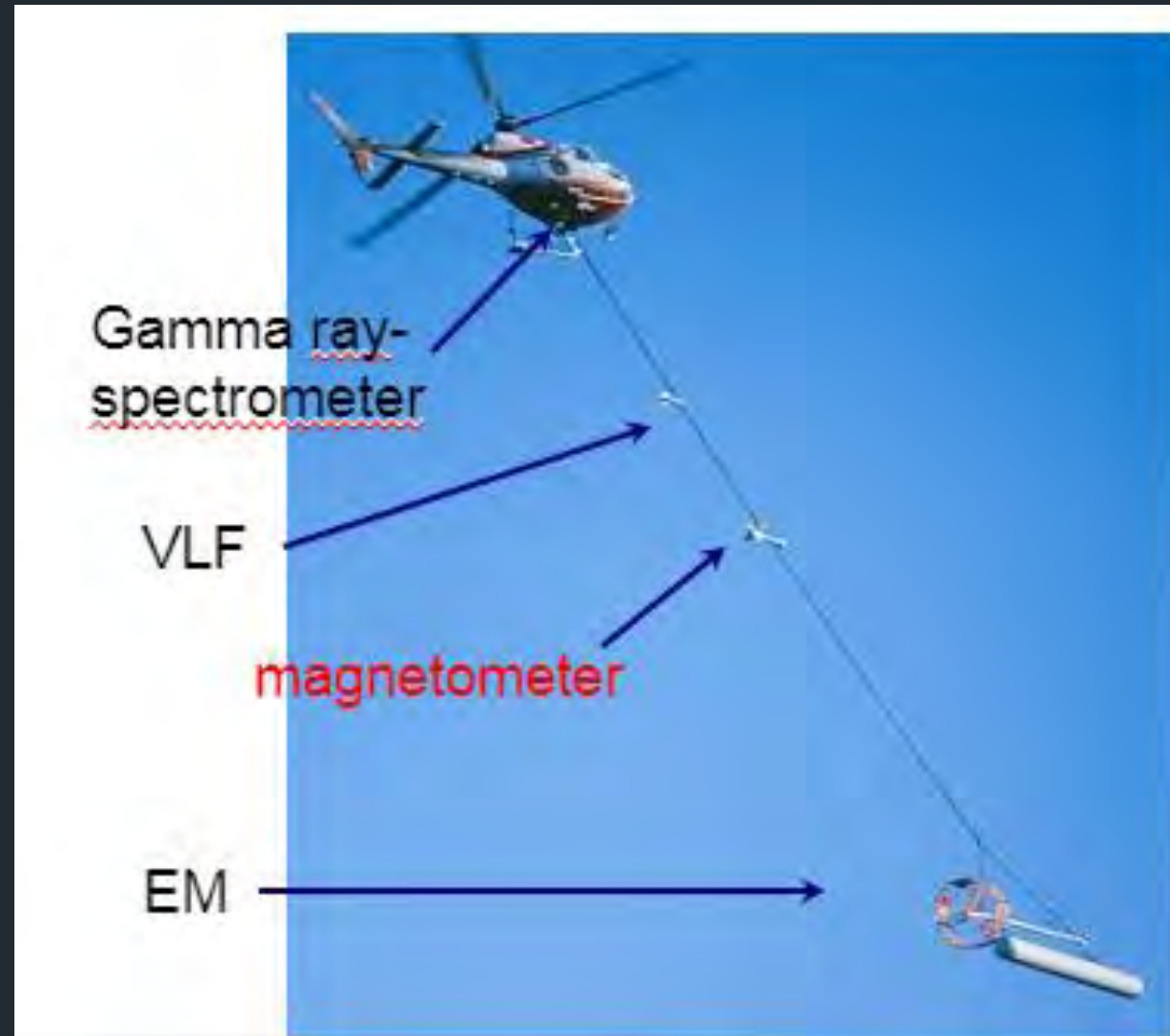


# Old methods and new challenges?

Time and economical efficient data acquisition

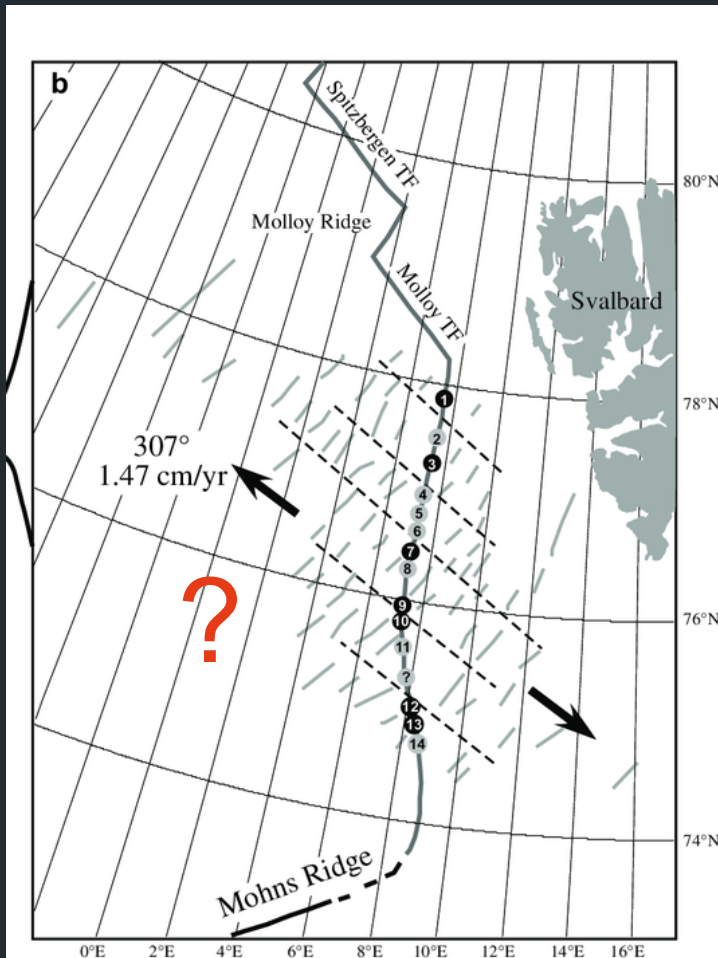


Hugin AUV, Ocean Infinity

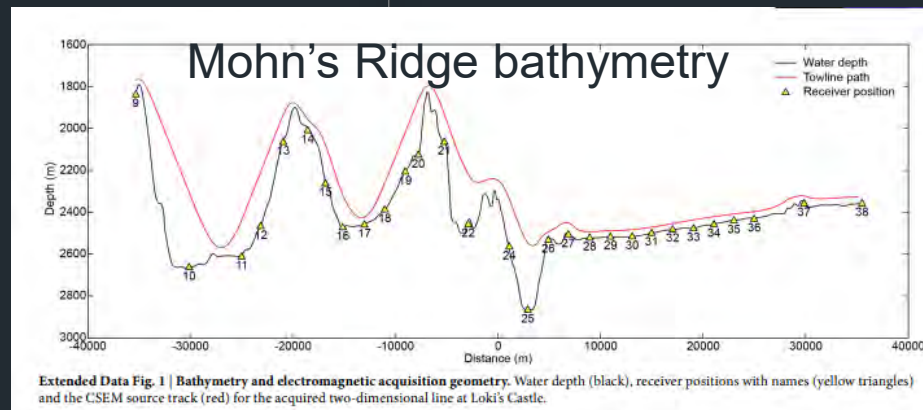


# Old methods and new challenges?

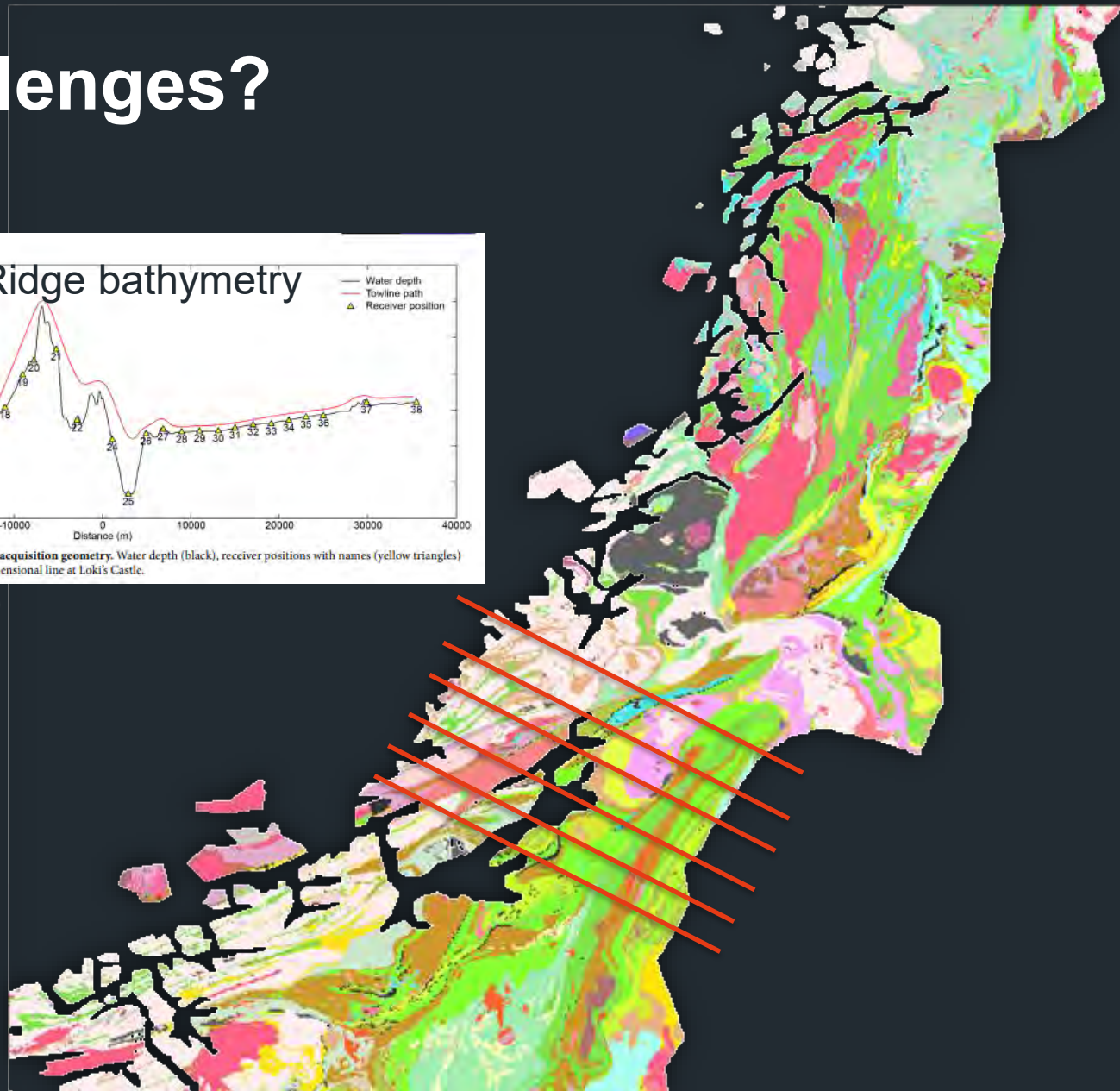
Regional geological-tectonic understanding



From Curewitz et al. 2010



From Johansen et al. 2019



Data acquisition onshore Norway





## New old challenges:

- Generate accurate underlying data
- Optimizing data acquisition techniques
- Regional geological-tectonic understanding
- Navigation accuracy? **We can ask Martin!**





*Thank you !*





# Exploration methodology from petroleum to mineral resources

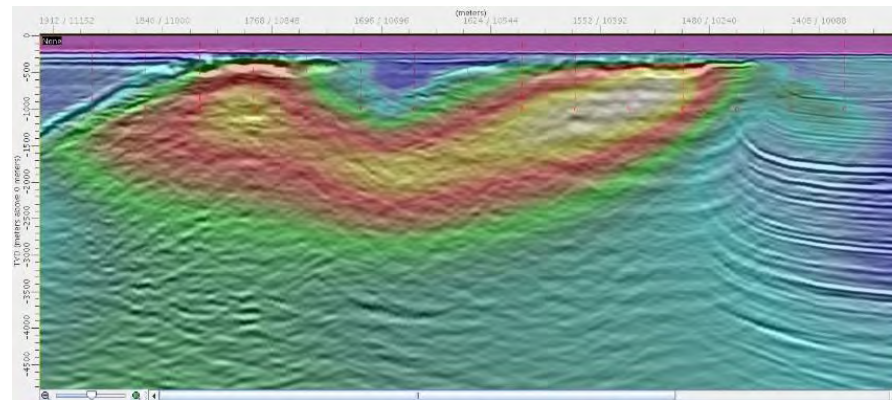
Ketil Hokstad  
MINDeSEA Workshop, 27. November 2019



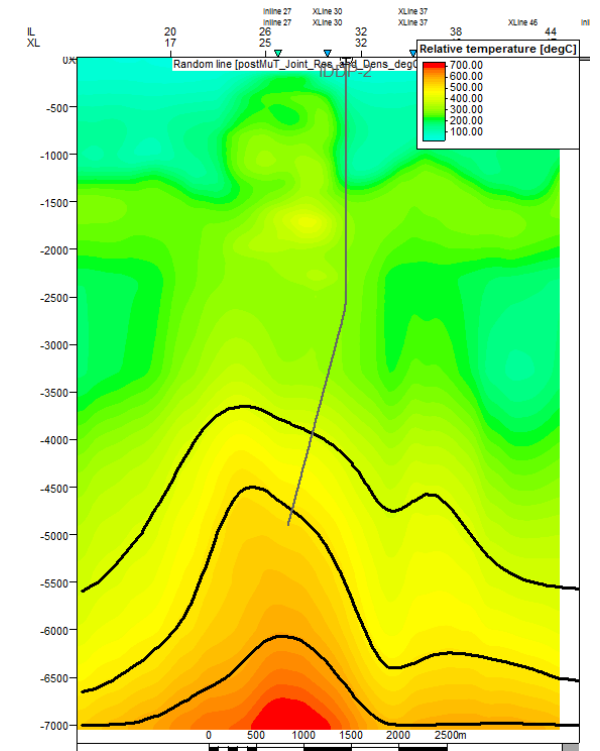
# Integration of geoscience

Complex exploration problems require a multidisciplinary approach:

- Petroleum exploration
  - Subsalt imaging
  - Lithology and fluid prediction
  - Heat flow (basin modeling)
- Geothermal exploration
- Seabed mineral exploration
  
- Multigeophysics
- Quantifying geology



Salt imaging: 3D seismic and MT



Geothermal: MT and gravity



# Play concepts

## Petroleum

«Petroleum system analysis»

- Source
- Reservoir
- Seal

## Geothermal

«Play fairway analysis»

- Heat source
- Recharge
- Producibility (container)

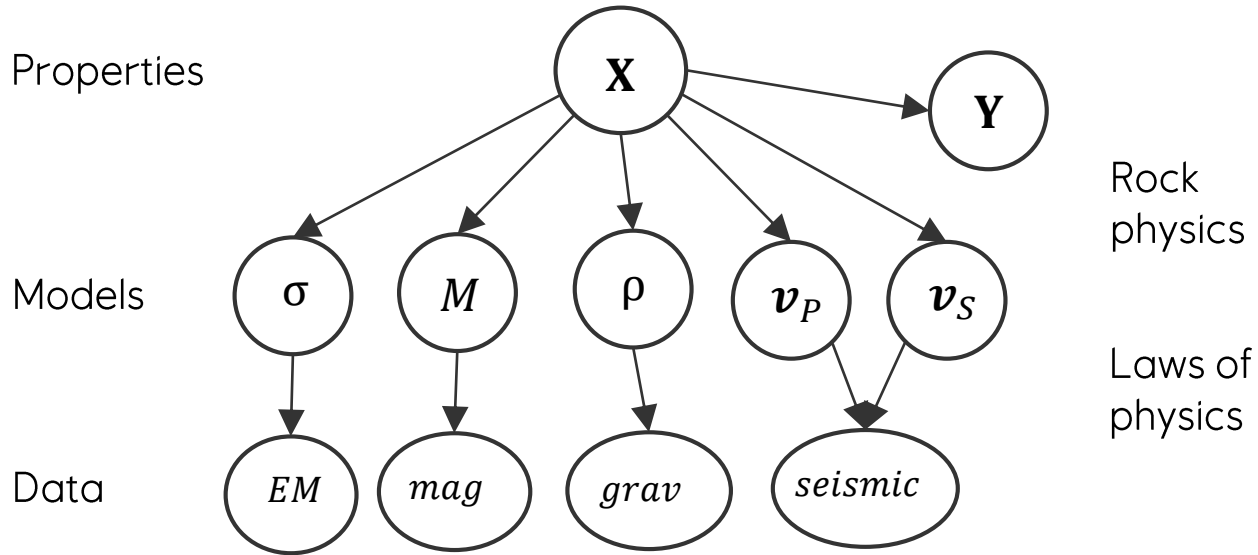
## Deep-sea minerals

«Mineral systems approach»

- Metal source
- Fluid pathway
- Accumulation and preservation

- ✓ Every exploration activity should contribute to the derisking of at least one play element
- ✓ Focus on what is mappable

# Multigeophysical inversion (MGI)



**Applications:**

1. Petroleum exploration
2. Geothermal exploration
3. Seabed mineral exploration (on-going research)
4. Dual play (or multiplay) exploration

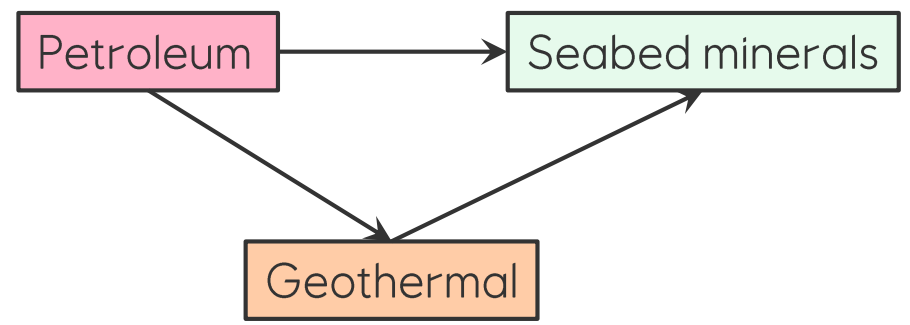
- Exploit the similarities
- Be aware of the differences



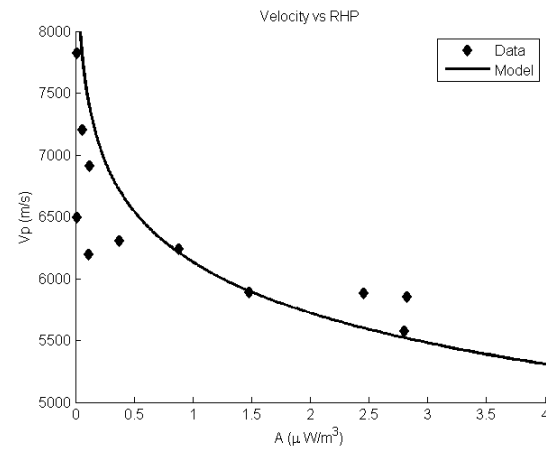
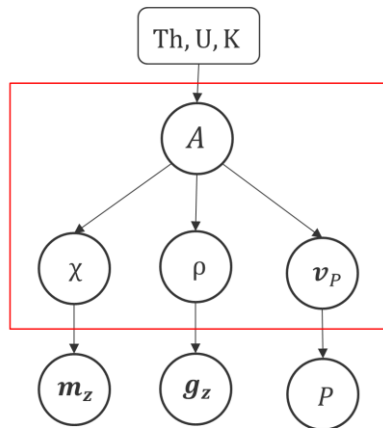
Thomas Bayes (1701 - 1761)

Bayesian network for MGI

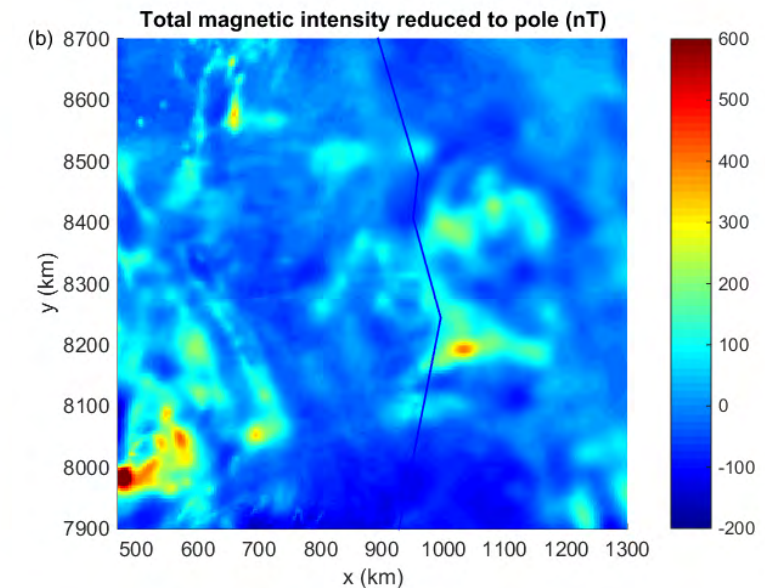
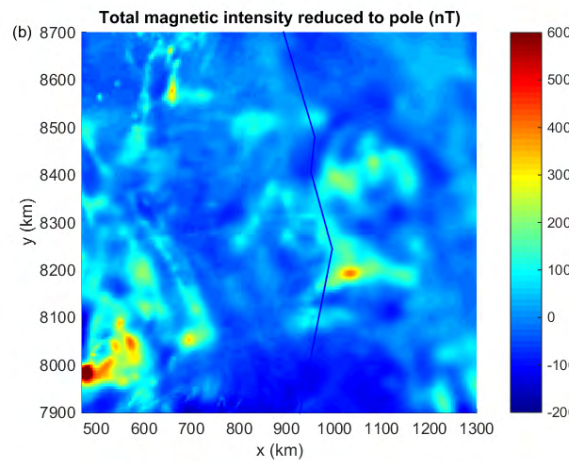
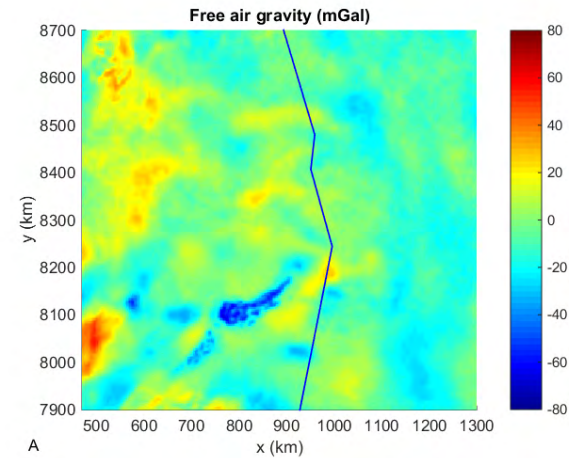
$$p(\mathbf{X}|m_1, \dots, m_n) = C \prod_{i=1}^n p(m_i|\mathbf{X})p(\mathbf{X}; \lambda)$$



# Barents Sea: Inversion for radiogenic heat production (RHP) in the crust



- P-wave velocity vs RHP: Published by Rybach (1978)
- Corresponding models for density and susceptibility
- Incompatible elements: Th and U tend to follow the quartz



Radiogenic heat production in the crust [ $\mu W/m^3$ ]

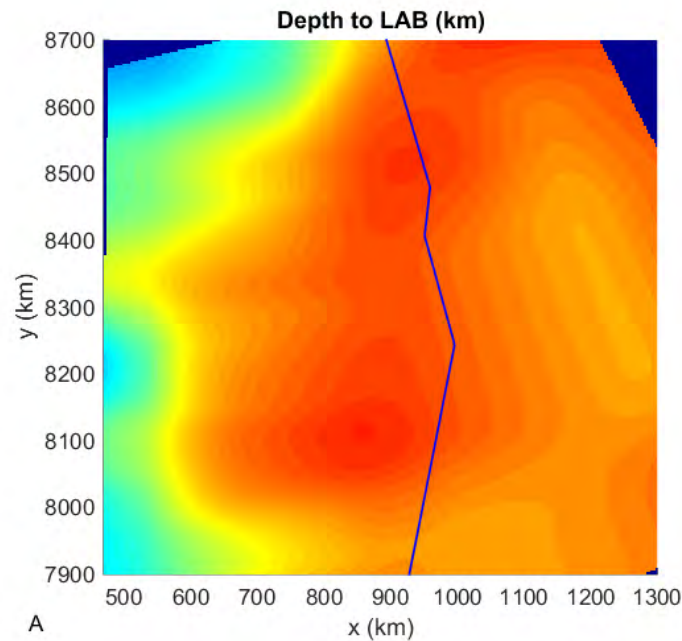
Gravity and magnetic data

Hokstad, K., Alasonati Tašárová, Z., Clark, S. A., Kyrkjebø, R., Duffaut, K., Fichler, C., Wiik, T. (2017), **Radiogenic heat production in the crust from inversion of gravity and magnetic data. NJG Vol 97, Nr. 3**

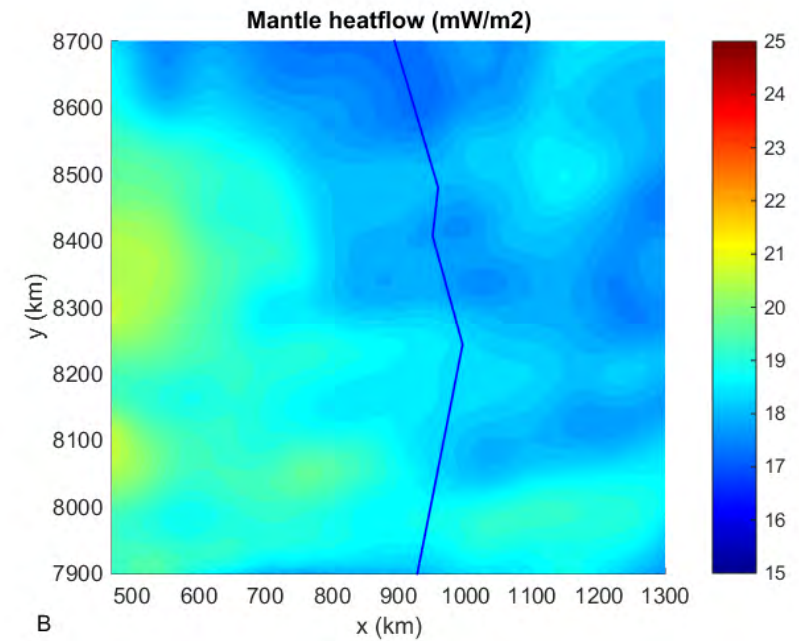


# Mantle heatflow – the contribution from LAB

- Start from mantle composition
  - Rock types depend on pressure and temperature
- Adjust LAB constrained on
  - Topography (sea bed)
  - Long-wavelength gravity
  - Geoid anomaly
- LitMod3D: Fullea et al (2009)
  
- Barents Sea: LAB at ~200 km
- MOR: LAB at ~10 km



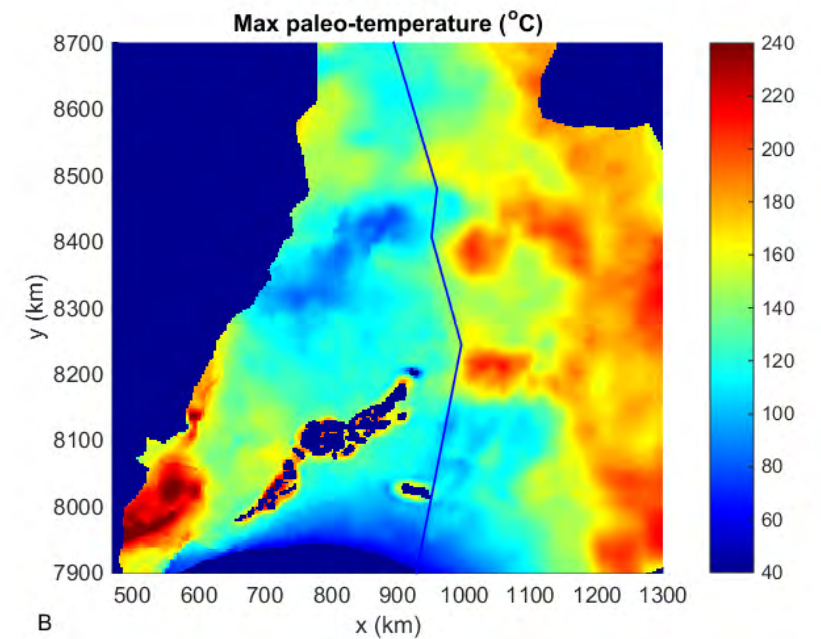
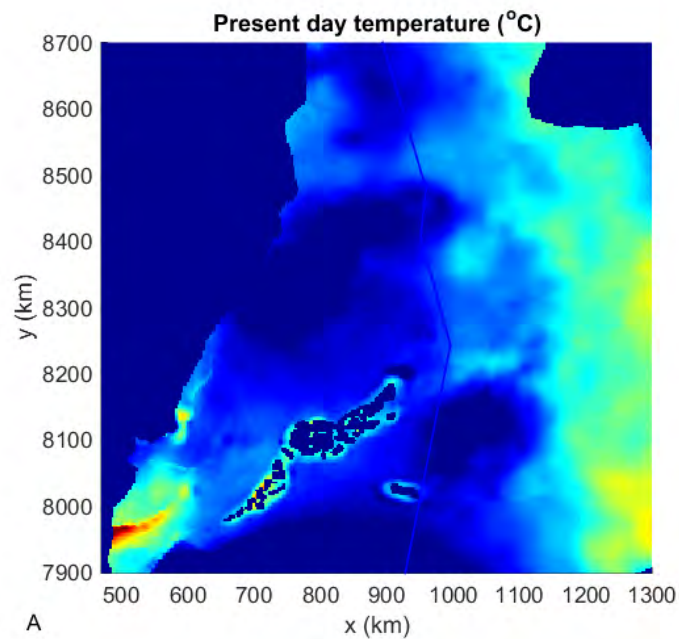
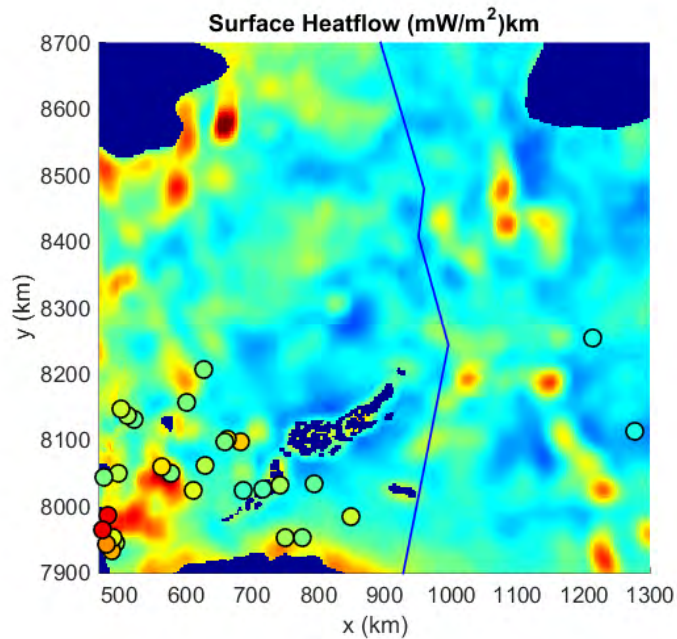
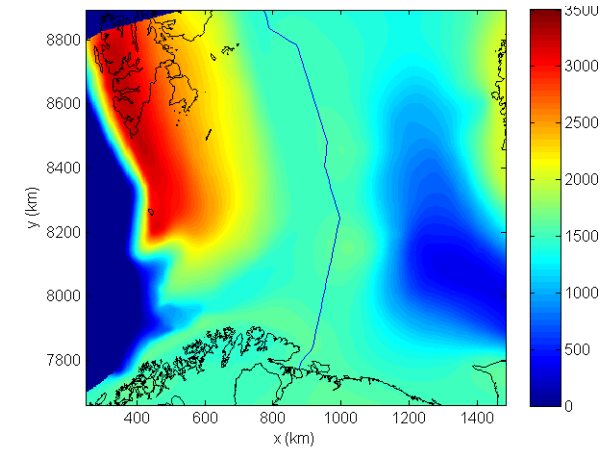
Depth to LAB



Mantle Heatflow

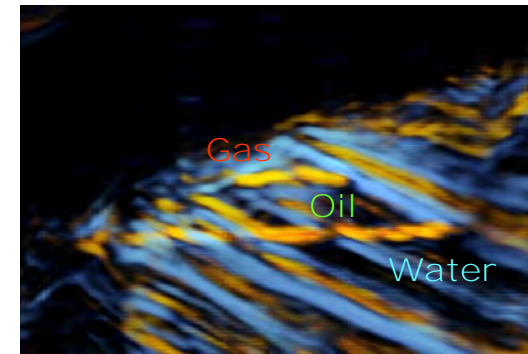
LAB = Lithosphere-Astenosphere Boundary; ~1300 °C isotherm

# Heatflow and temperature

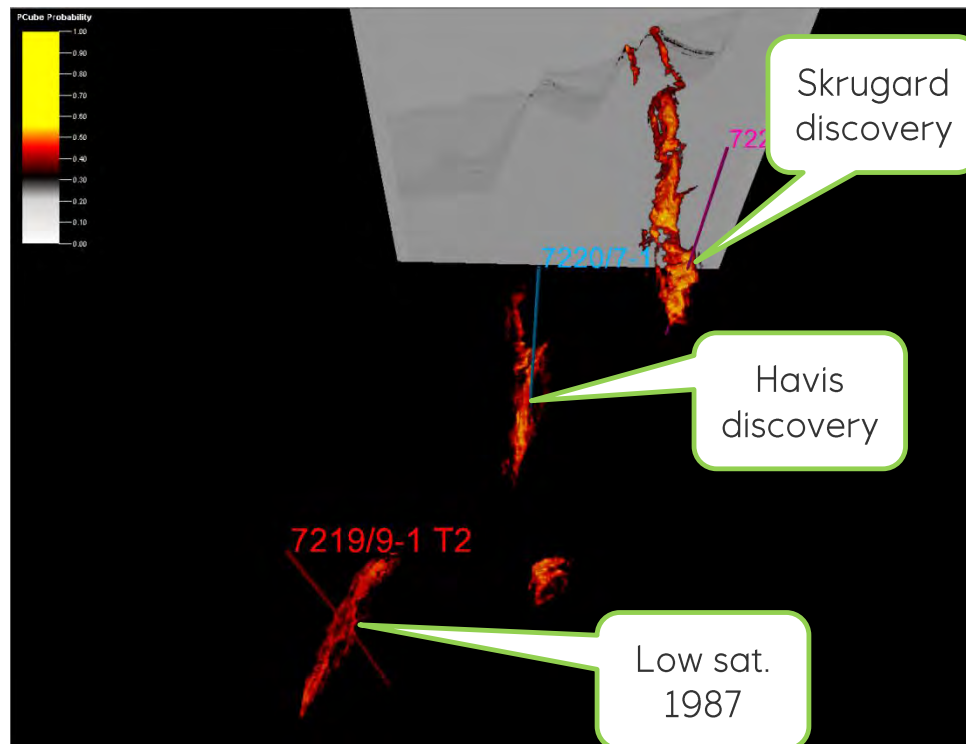


- Input to basin modeling and source rock maturation modeling

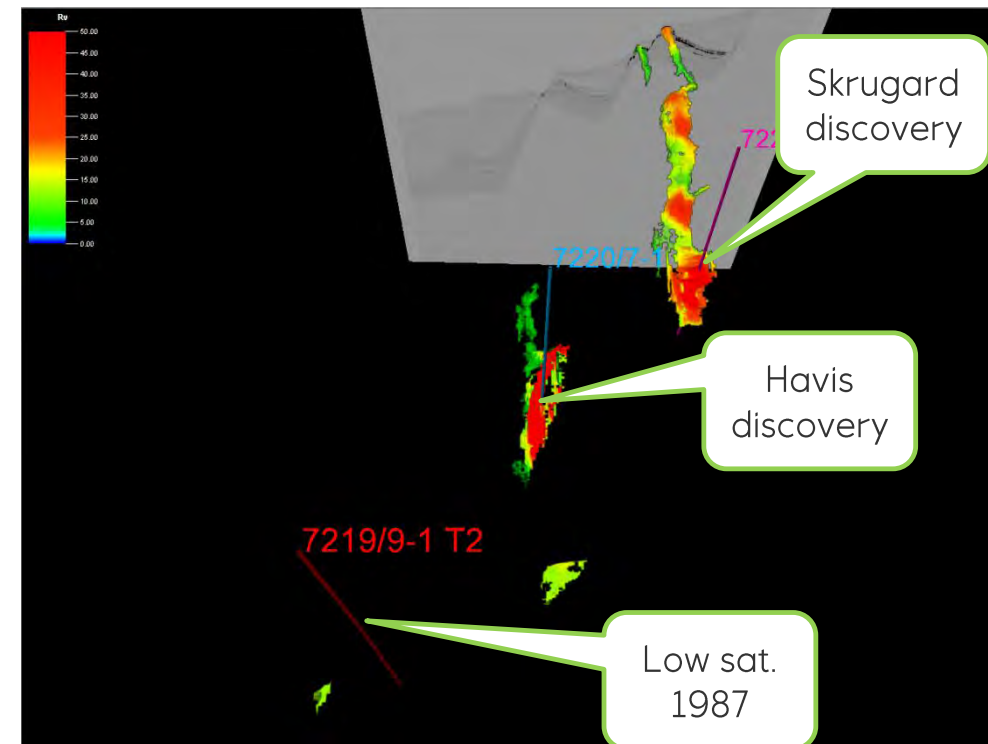
# Barents Sea: Fluid prediction using seismic AVO and EM



Lithology and fluids predicted by seismic AVO inversion



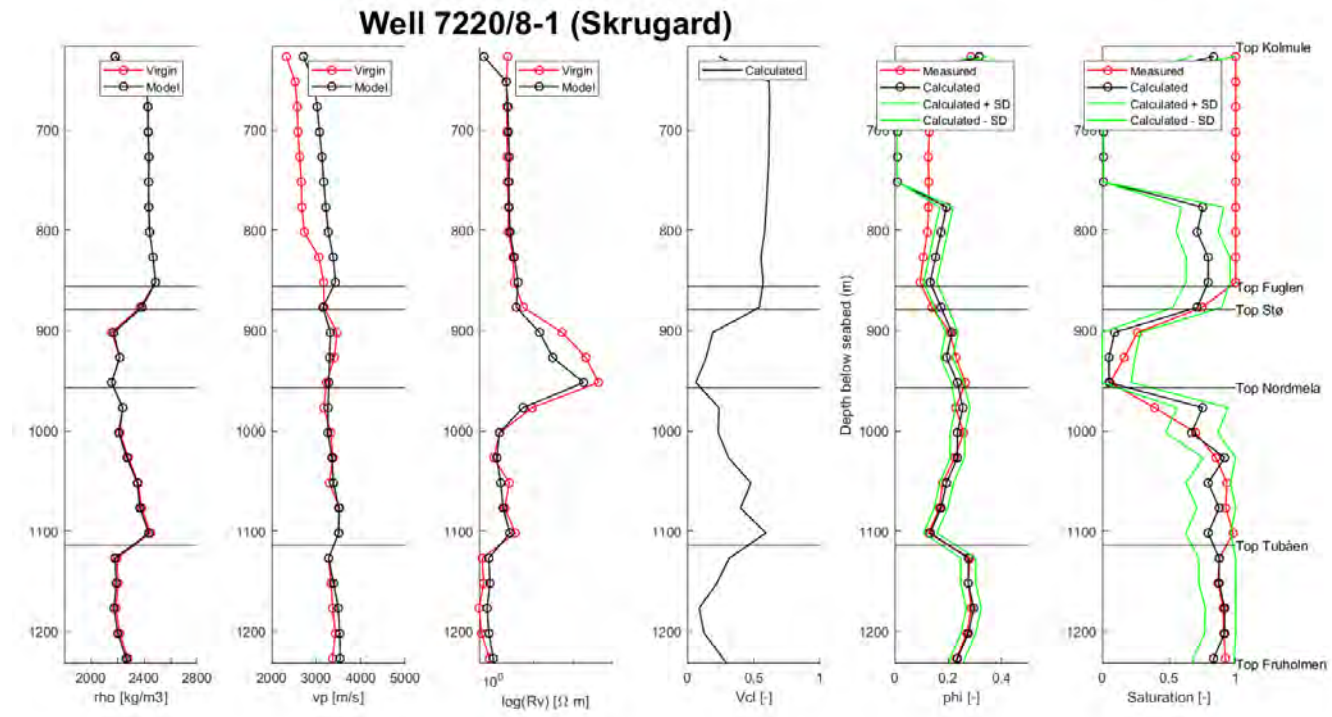
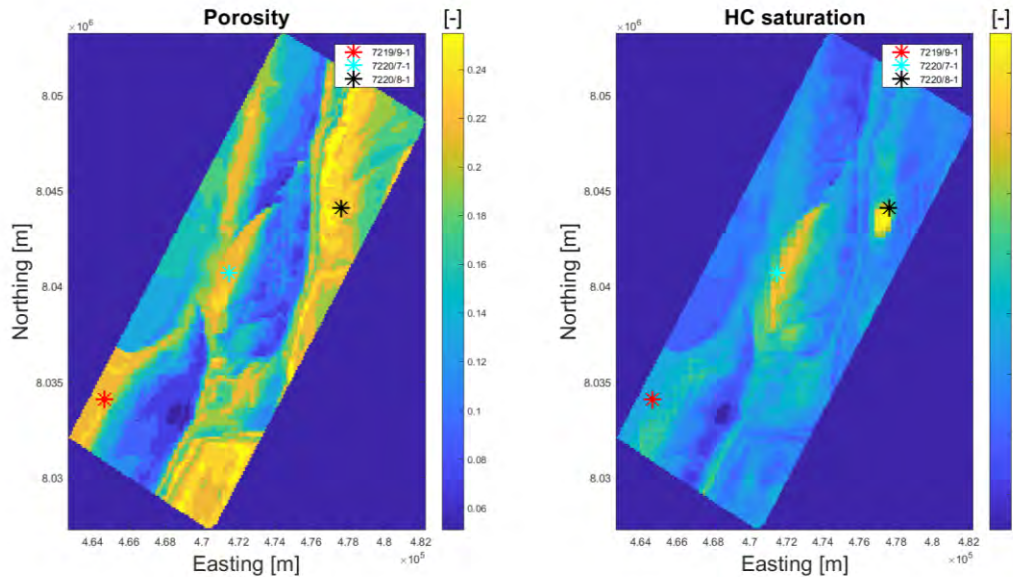
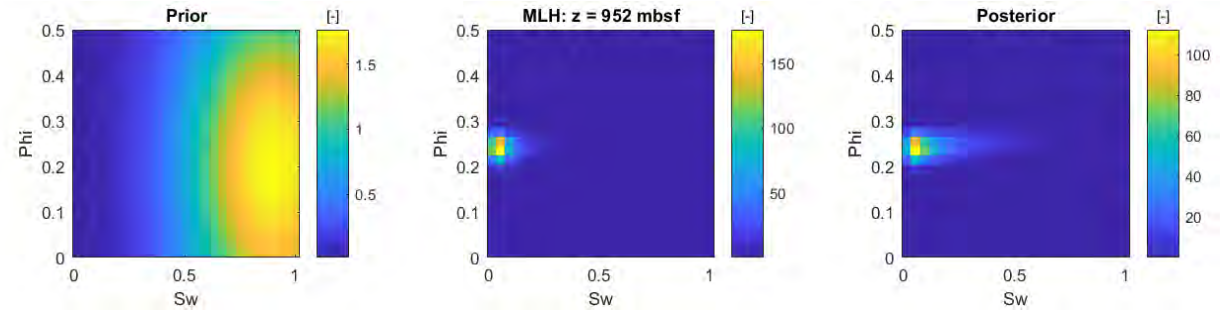
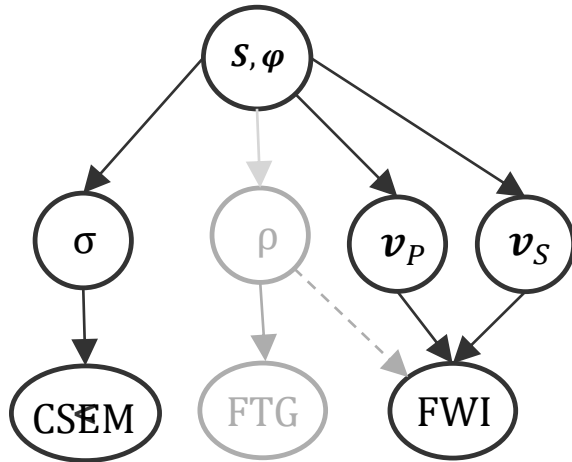
Lithology and fluids predicted by seismic and CSEM



Nordskog J.I, Kjøsnes, Ø., Nguyen, A.K., and Hokstad, K., SEG 2013: CSEM exploration in the Barents Sea: Joint CSEM & Seismic interpretation



# Fluid saturation and porosity from resistivity and velocity



From MSc project of Sondre Olsson

# Geothermal exploration: Reykjanes, Iceland

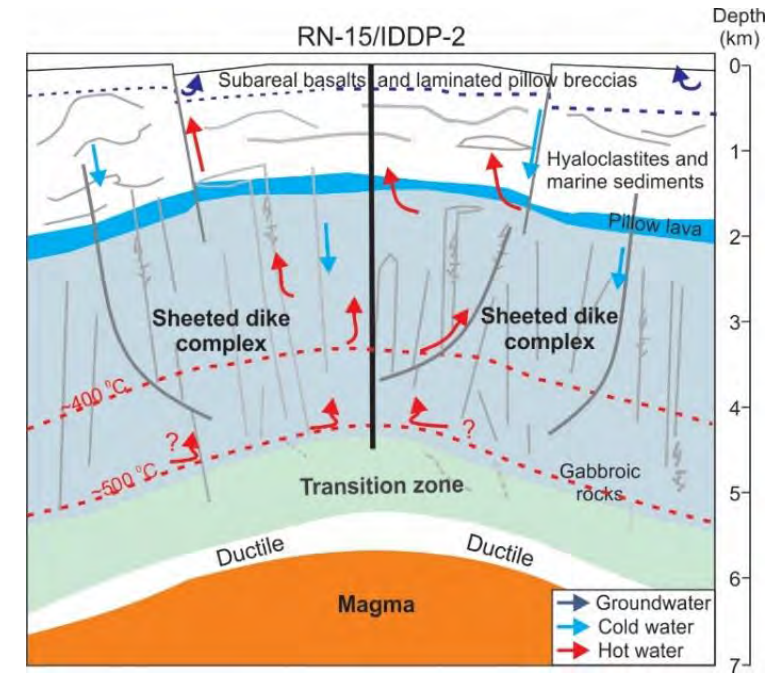
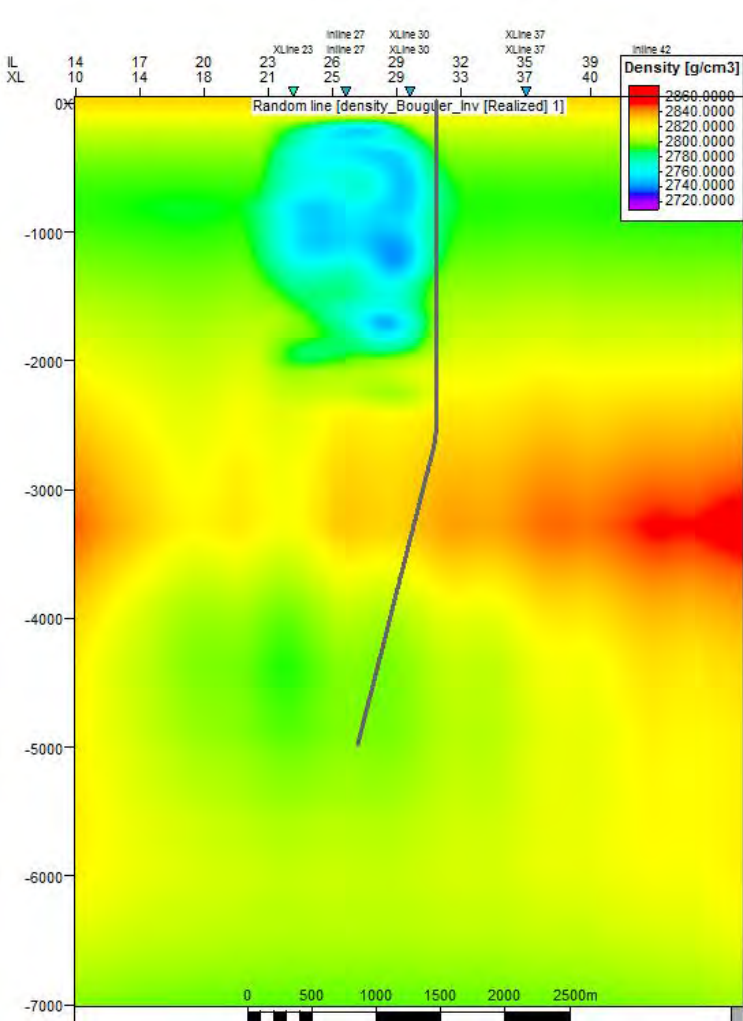
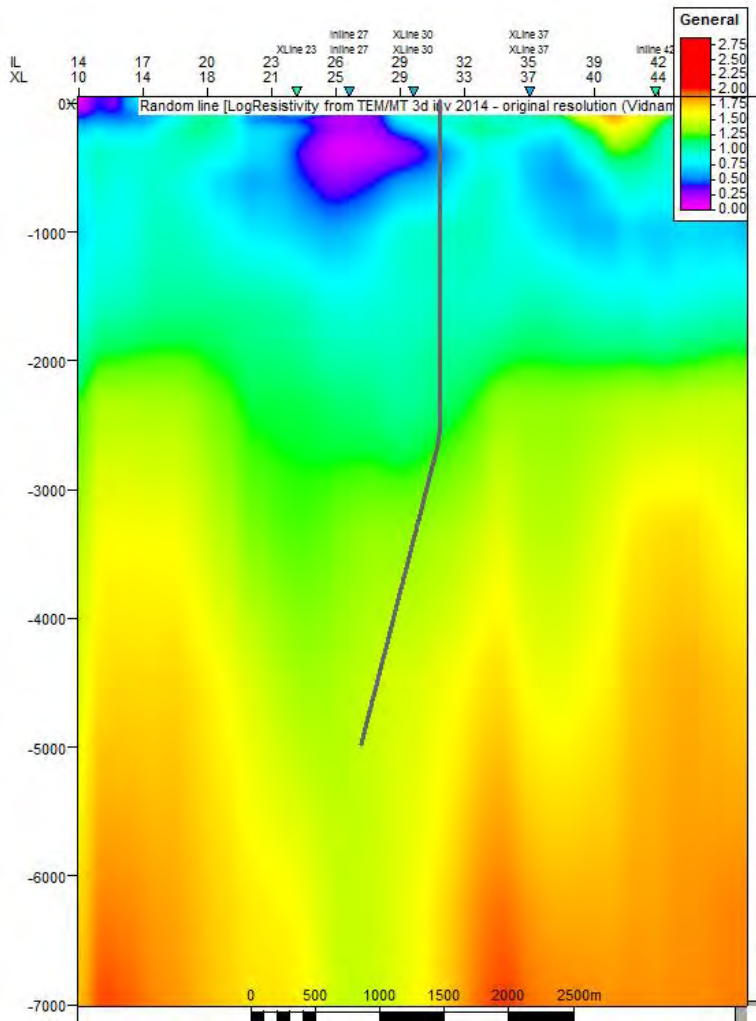
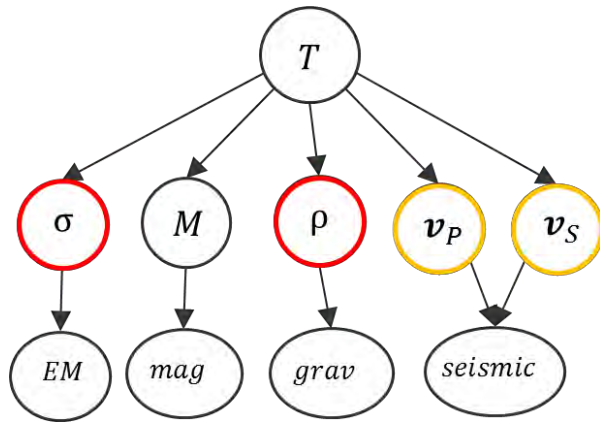


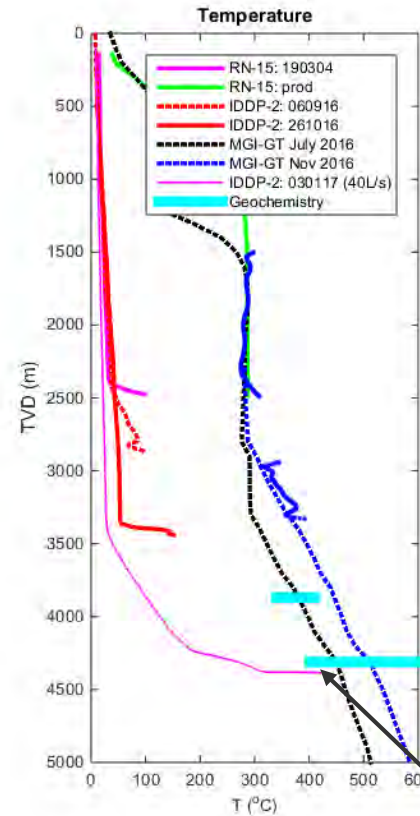
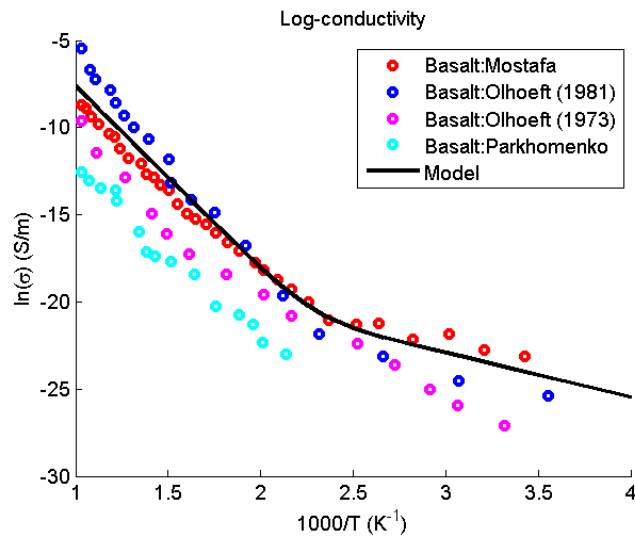
Photo: Carsten F. Sørli, Statoil



# Geothermal exploration: Reykjanes, Iceland



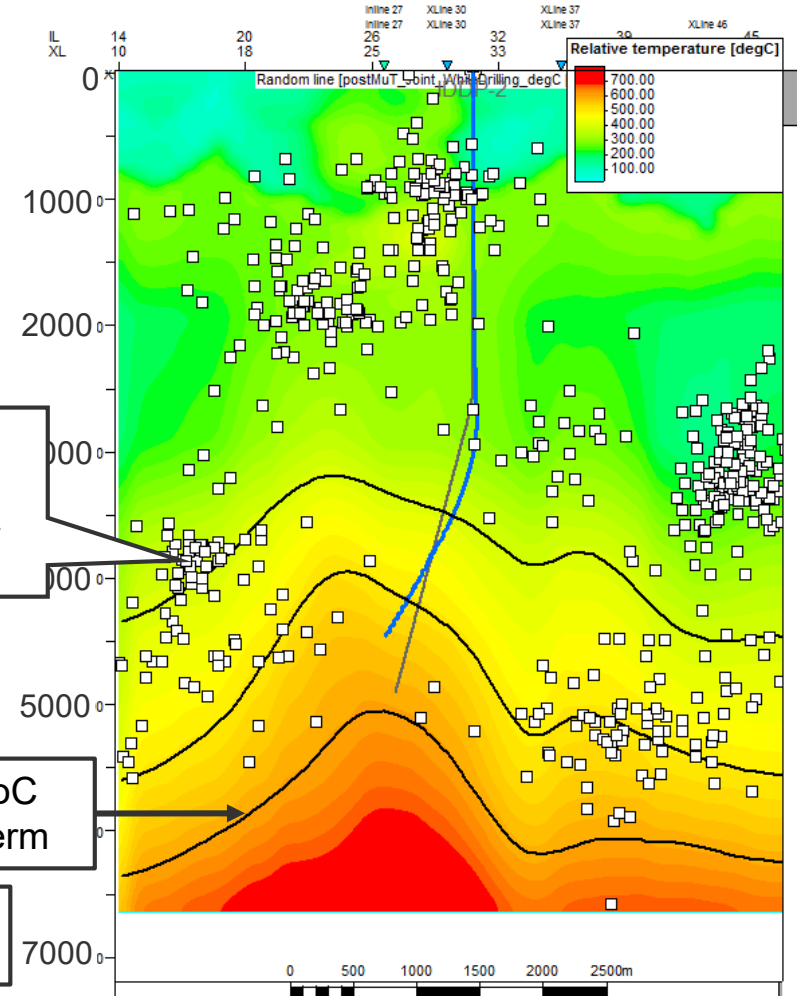
- TD (4659 mMD):
- Inversion:  $535 \pm 50 \text{ } ^\circ\text{C}$
  - Horner plot:  $\sim 530 \text{ } ^\circ\text{C}$



□ Earthquake locations  
No earthquakes in ductile zone

600 °C isotherm

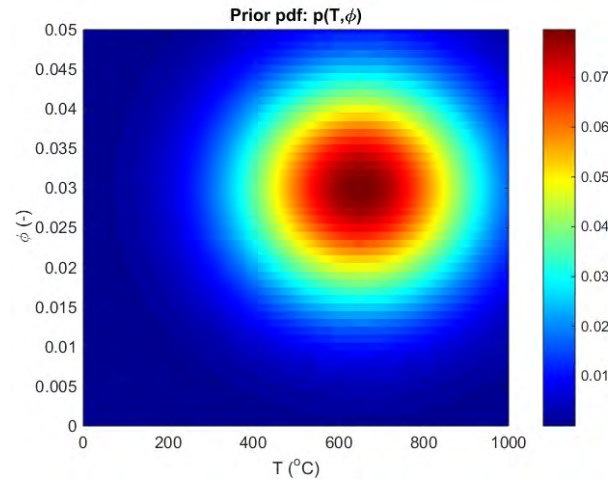
3. January 2017:  
Measured 426 °C



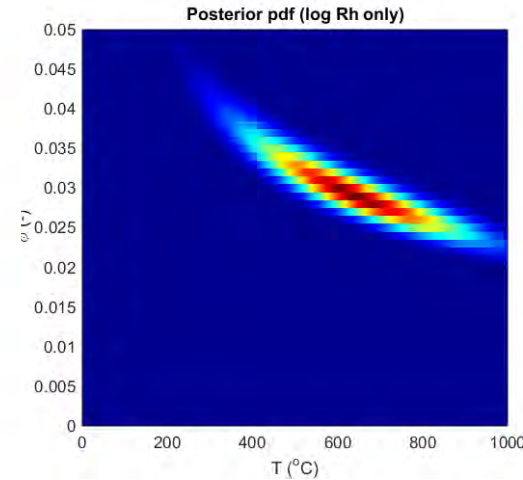
Hokstad, K. and K. Tānavsuu-Milkeviciene, 2017. Temperature Prediction by Multigeophysical Inversion: Application to the IDDP-2 Well at Reykjanes, Iceland, Geothermal Resource Council, Transactions, 42, 1141-1152.



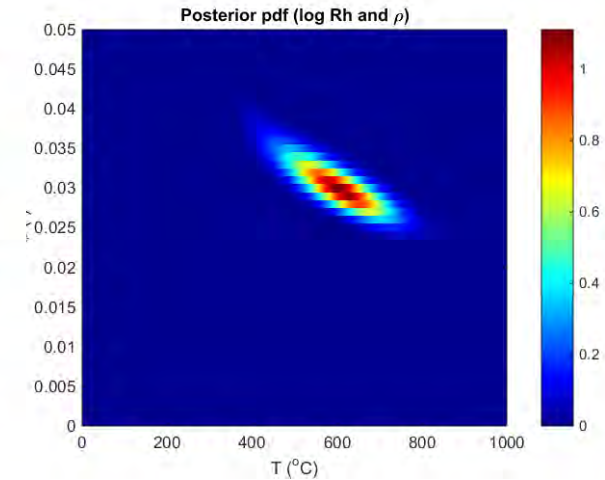
# Illposedness: Inversion for temperature and porosity



Prior pdf



Posterior pdf:  
Inversion of resistivity

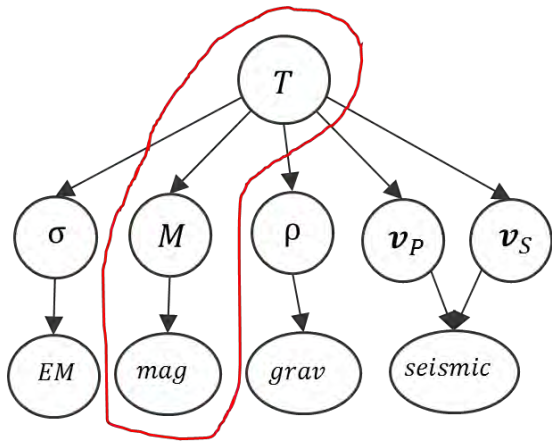


Posterior pdf:  
Joint inversion of  
resistivity and density

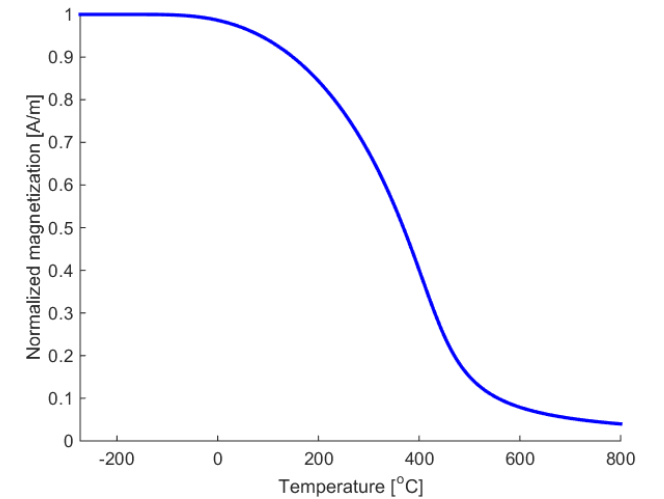
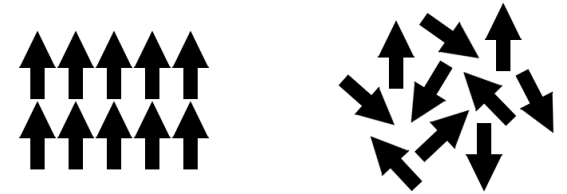
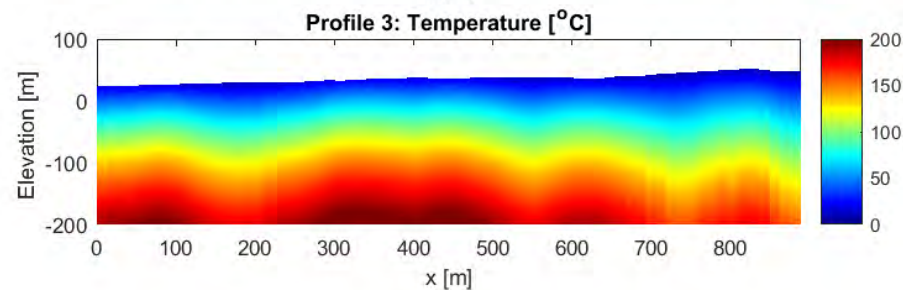
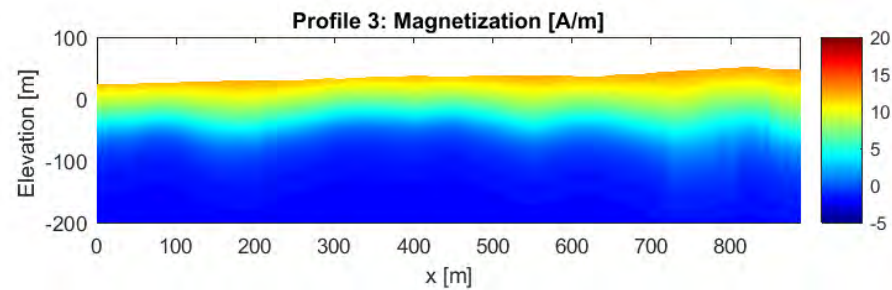
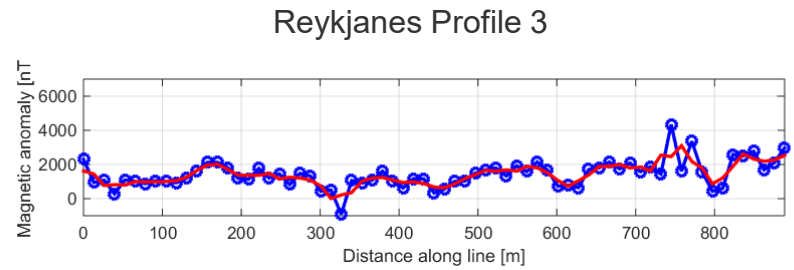
$$p(T, \phi | m_1, \dots, m_n) = C \prod_{i=1}^n p(m_i | T, \phi) p(T, \phi)$$

- In results shown here, we have treated the porosity as a deterministic parameter
- Sensitivity tests varying the porosity profile

# Including magnetization – first test



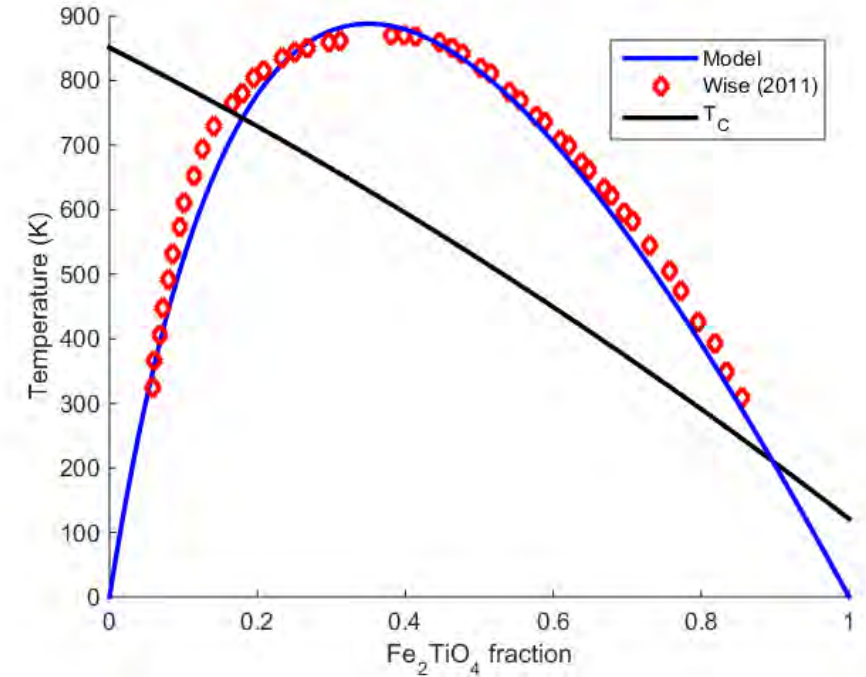
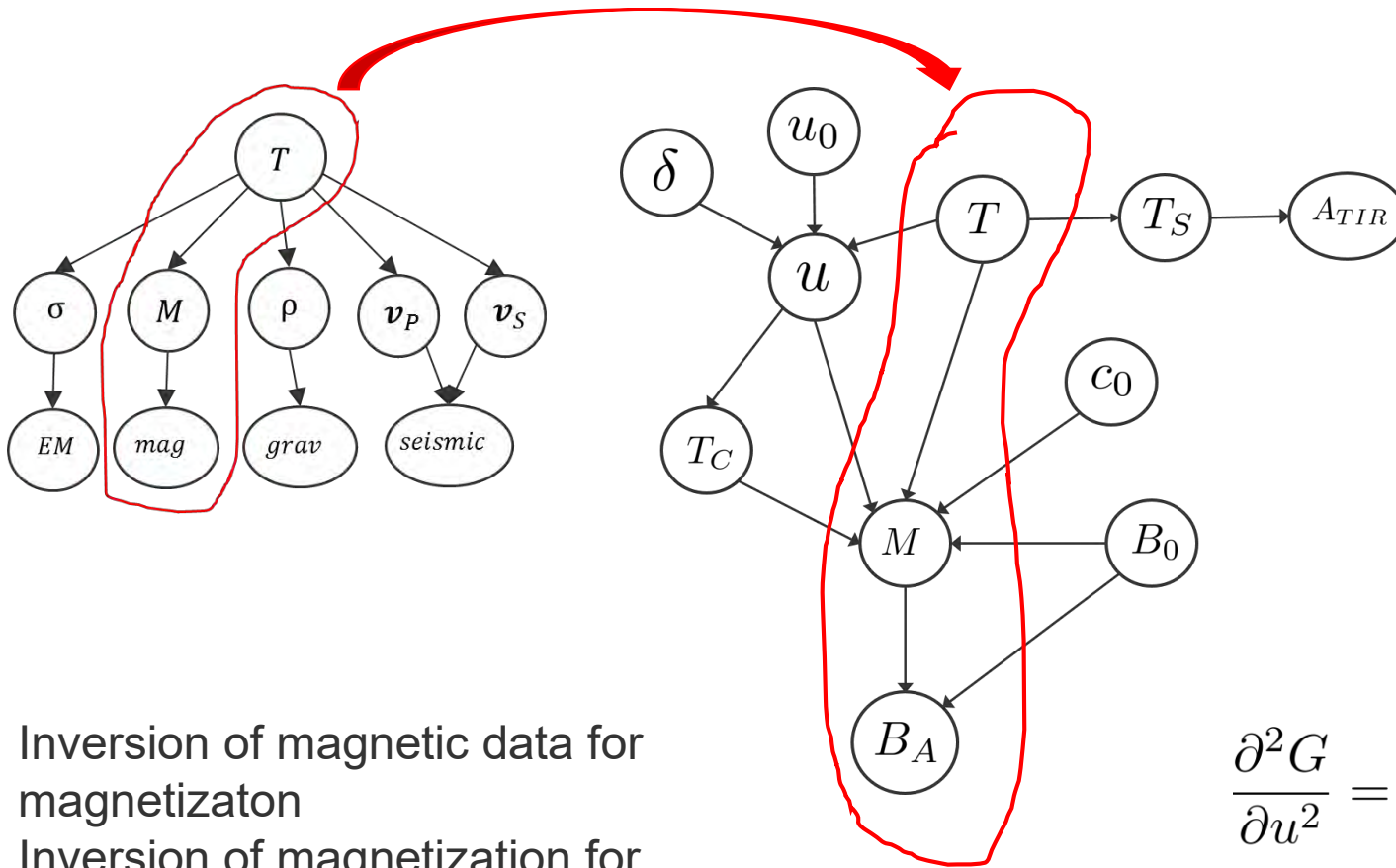
Magnetic test acquisition on Iceland 2017  
Photo: Bjørn M. Sæther, Equinor



Ising (1925) model

Hokstad, K., Tănăvsuu-Milkeviciene, K.-, Sæther, B.M., Tašárová, Z., 2018. **Subsurface temperature from inversion of magnetic data.** UK Patent Application No. 1812189.7

# Inversion for magnetic properties



1. Inversion of magnetic data for magnetization
2. Inversion of magnetization for temperature and Curie temperature

$$\frac{\partial^2 G}{\partial u^2} = -2W + k_b T \left[ \frac{(1+h)}{u} + \frac{(1-h)}{v} \right] = 0$$

$$T_C(u) = -150u^2 - 580u + 851 \quad (\text{Lattard et al., 2006})$$

Hokstad, K., Tănăvsuu-Milkeviciene, K.-, Sæther, B.M., Tašárová, Z., 2018. **Subsurface temperature from inversion of magnetic data.** UK Patent Application No. 1812189.7



# Measured magnetization: Mohns Ridge vs Reykjanes

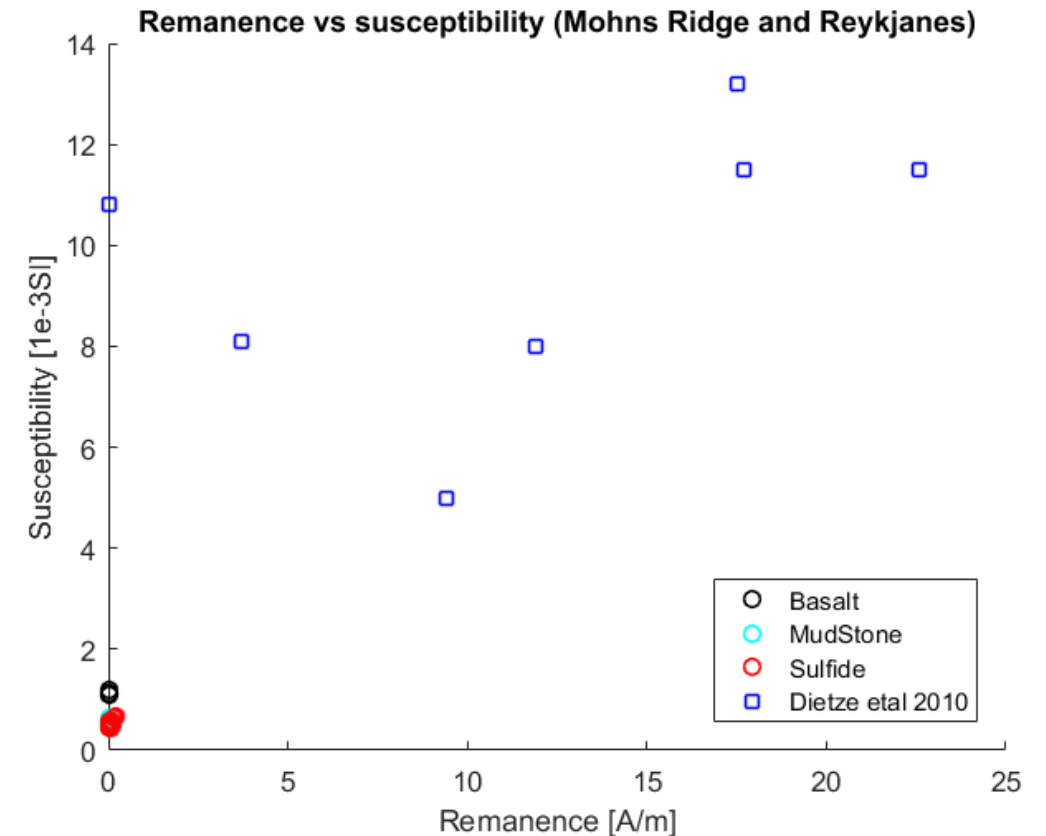


## The Iceland Deep Drilling Project at Reykjanes: Drilling into the root zone of a black smoker analog

Guðmundur Ó. Friðleifsson<sup>a,\*</sup>, Wilfred A. Elders<sup>b</sup>, Robert A. Zierenberg<sup>c</sup>, Andrew P.G. Fowler<sup>d</sup>, Tobias B. Weisenberger<sup>e</sup>, Kiflom G. Mesfin<sup>a</sup>, Ómar Sigurðsson<sup>a</sup>, Steinþór Níelsson<sup>e</sup>, Gunnlaugur Einarsson<sup>e</sup>, Finnþogi Óskarsson<sup>e</sup>, Egill Á. Guðnason<sup>e</sup>, Helga Tulinius<sup>e</sup>, Ketil Hokstad<sup>f</sup>, Gibert Benoit<sup>g</sup>, Frank Nono<sup>g,h</sup>, Didier Loggia<sup>g</sup>, Fleurice Parat<sup>g</sup>, Sarah B. Cichy<sup>g,i</sup>, David Escobedo<sup>g</sup>, David Mainprice<sup>g</sup>



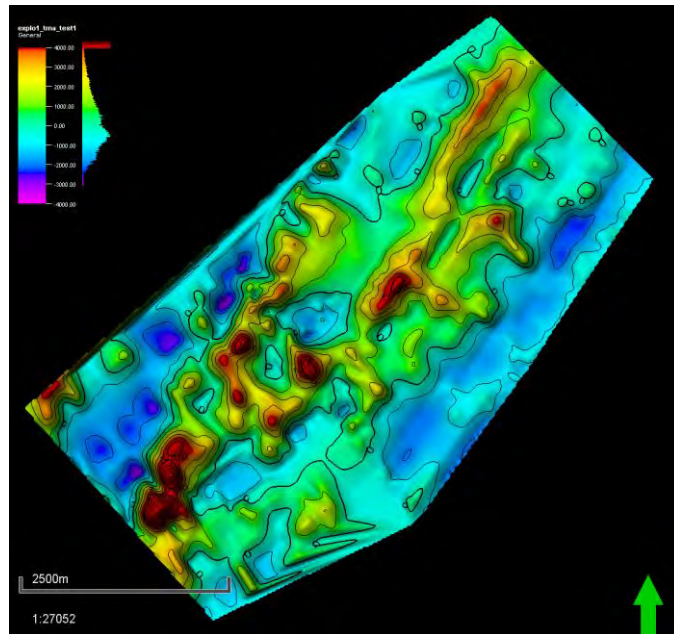
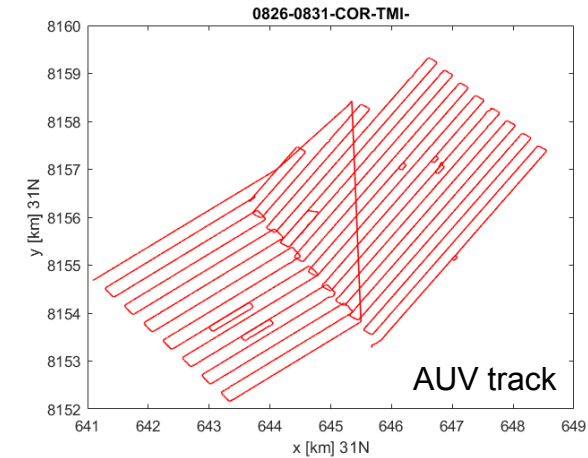
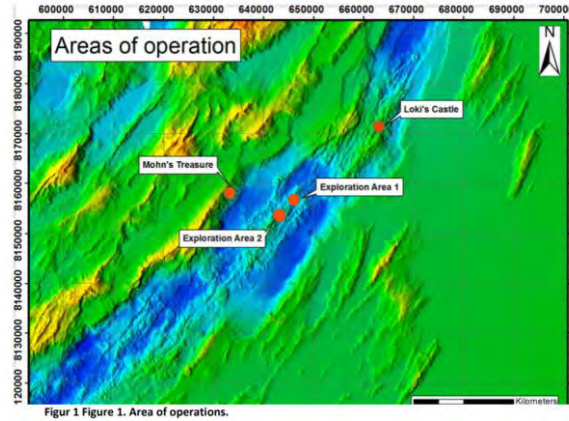
Gunnuhver hot spring, Reykjanes



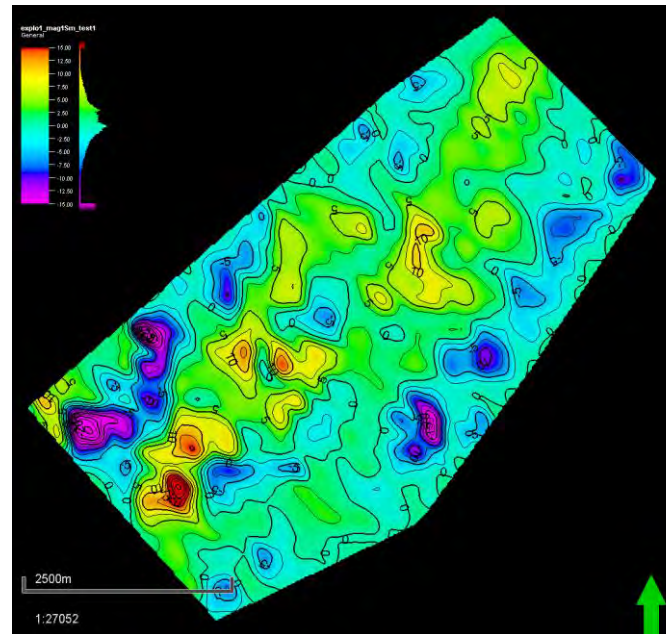
Data from Mohn's Ridge (Lim et al., 2019) and from Reykjanes (Dietze et al., 2010)

# Seabed mining exploration

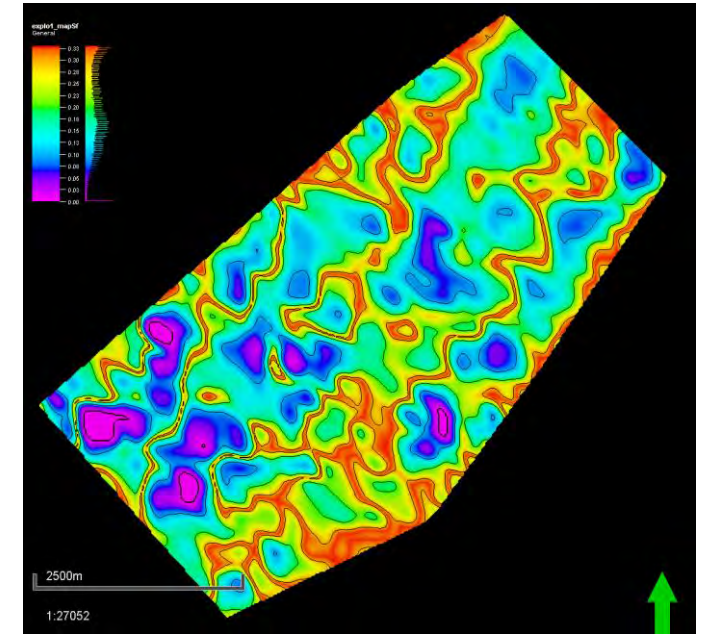
- Data from NTNU MarMine 2016 cruise to Mohn's Ridge (Lim et al., 2019)
- Inversion with our new magnetic inversion codes (WIP)
- Remanent and induced magnetization



Total magnetic anomaly (TMA)



Magnetization from inversion



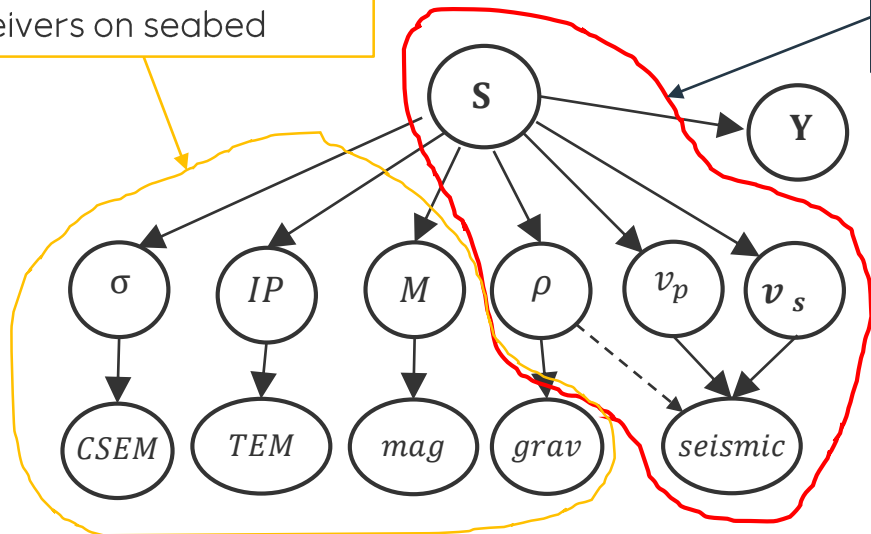
Demagnetized areas; sulfides?



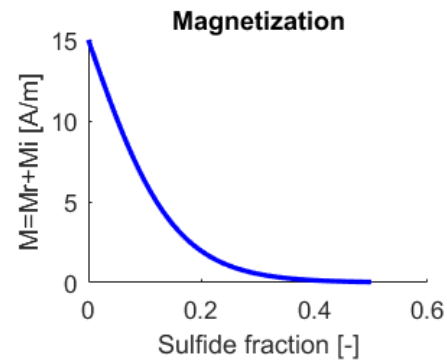
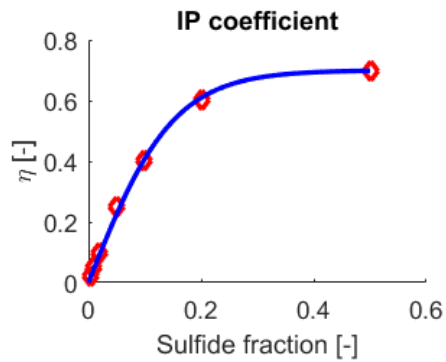
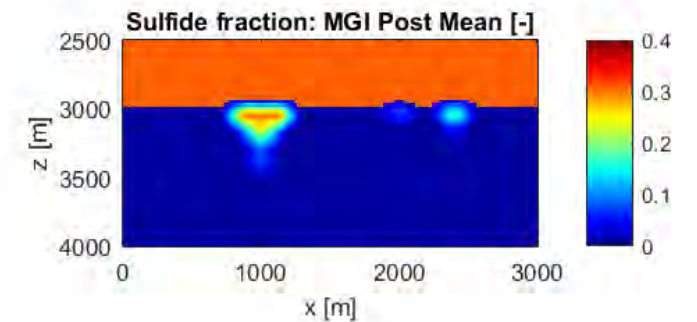
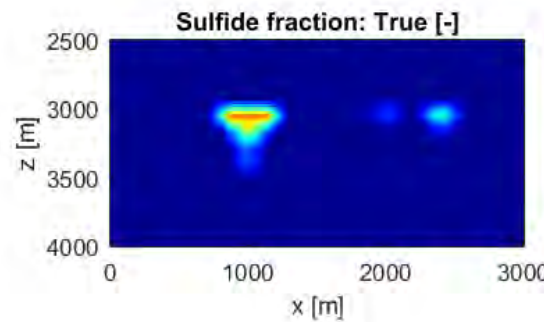
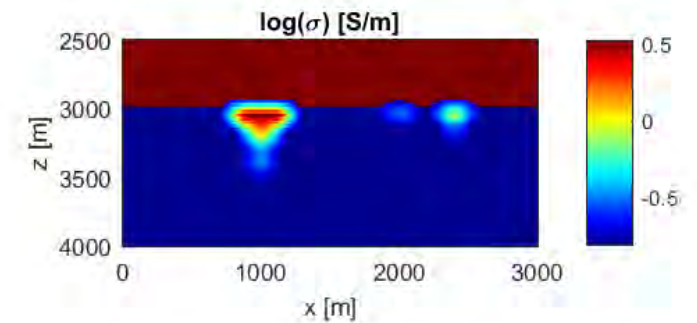
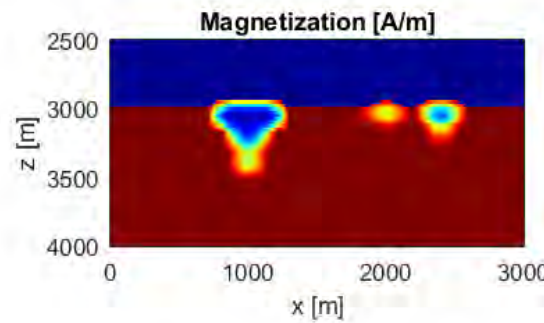
# Multigeophysical inversion (MGI) synthetic test model

This part requires AUV or receivers on seabed

This part can be done with surface seismic



Multigeophysical inversion for metal sulfides



Rock physics models (on-going research)



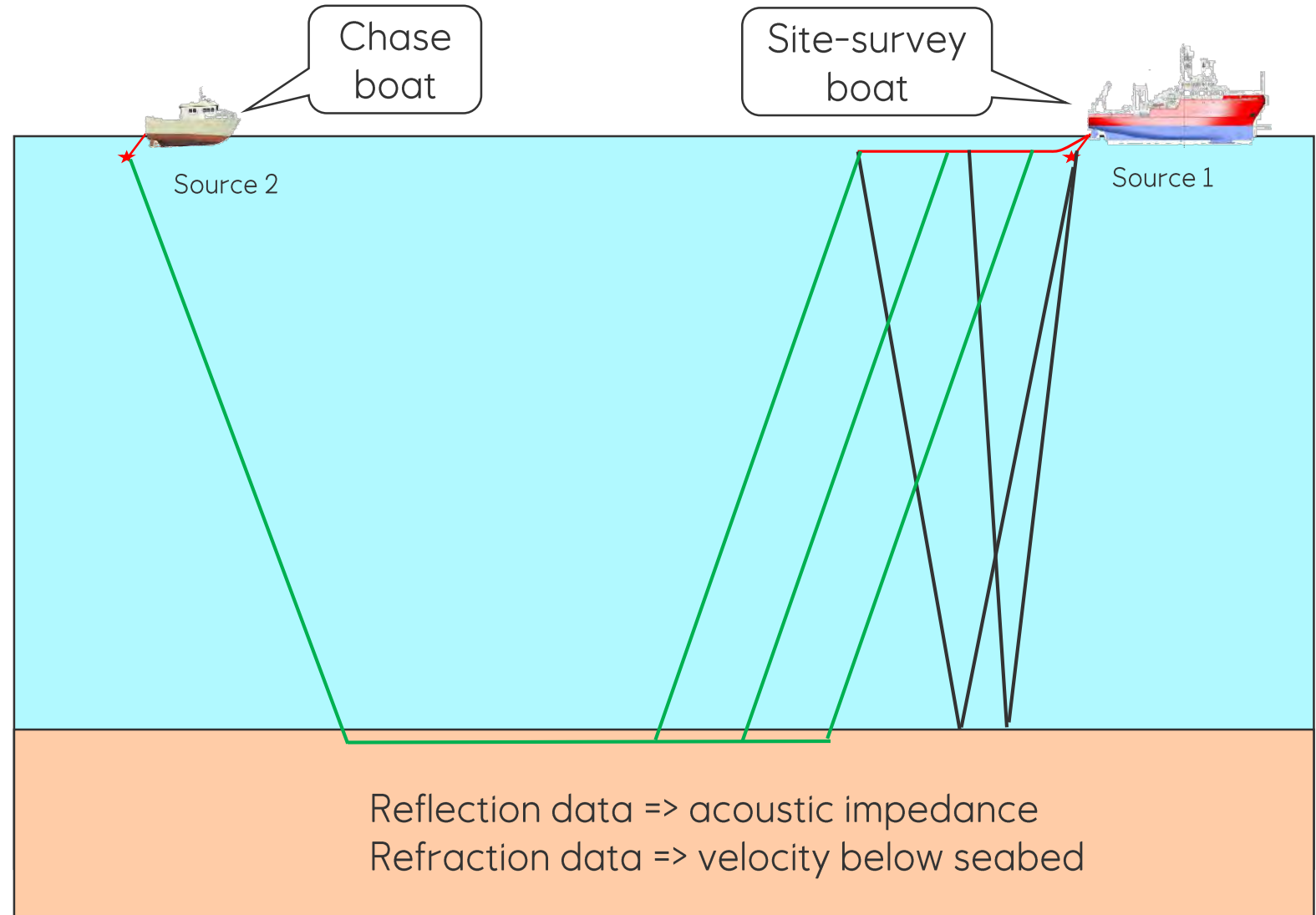
# Reflection and refraction imaging with site survey vessel

Source 1:

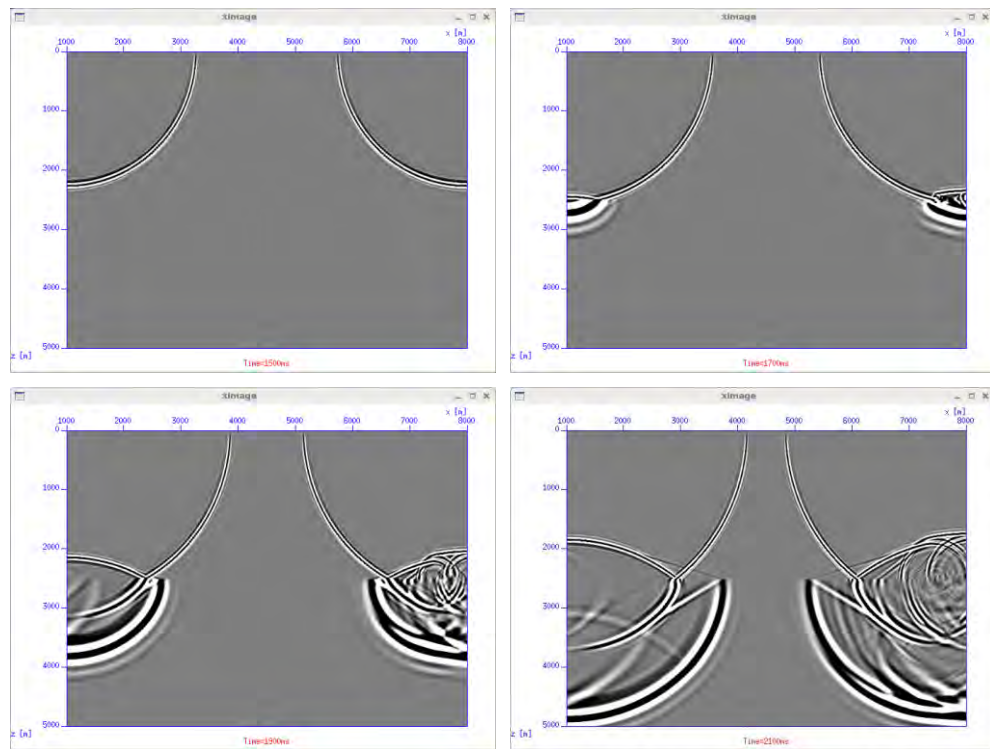
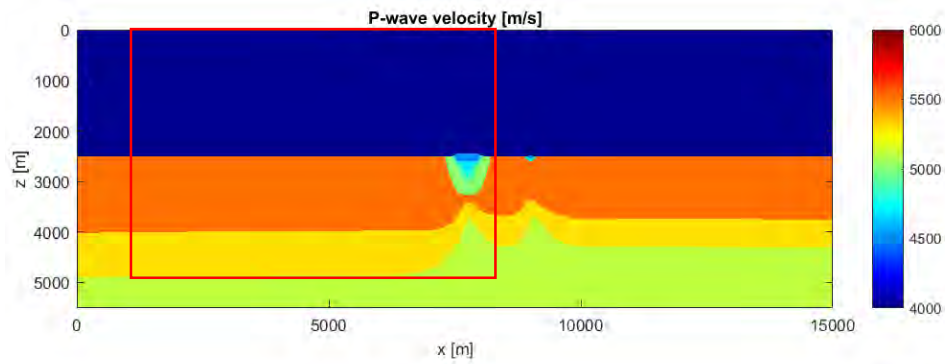
- Short-spread receiver tow
- Acoustic impedance

Source2:

- Needed for refraction data
- Velocity below seabed



# Finite-difference feasibility modeling



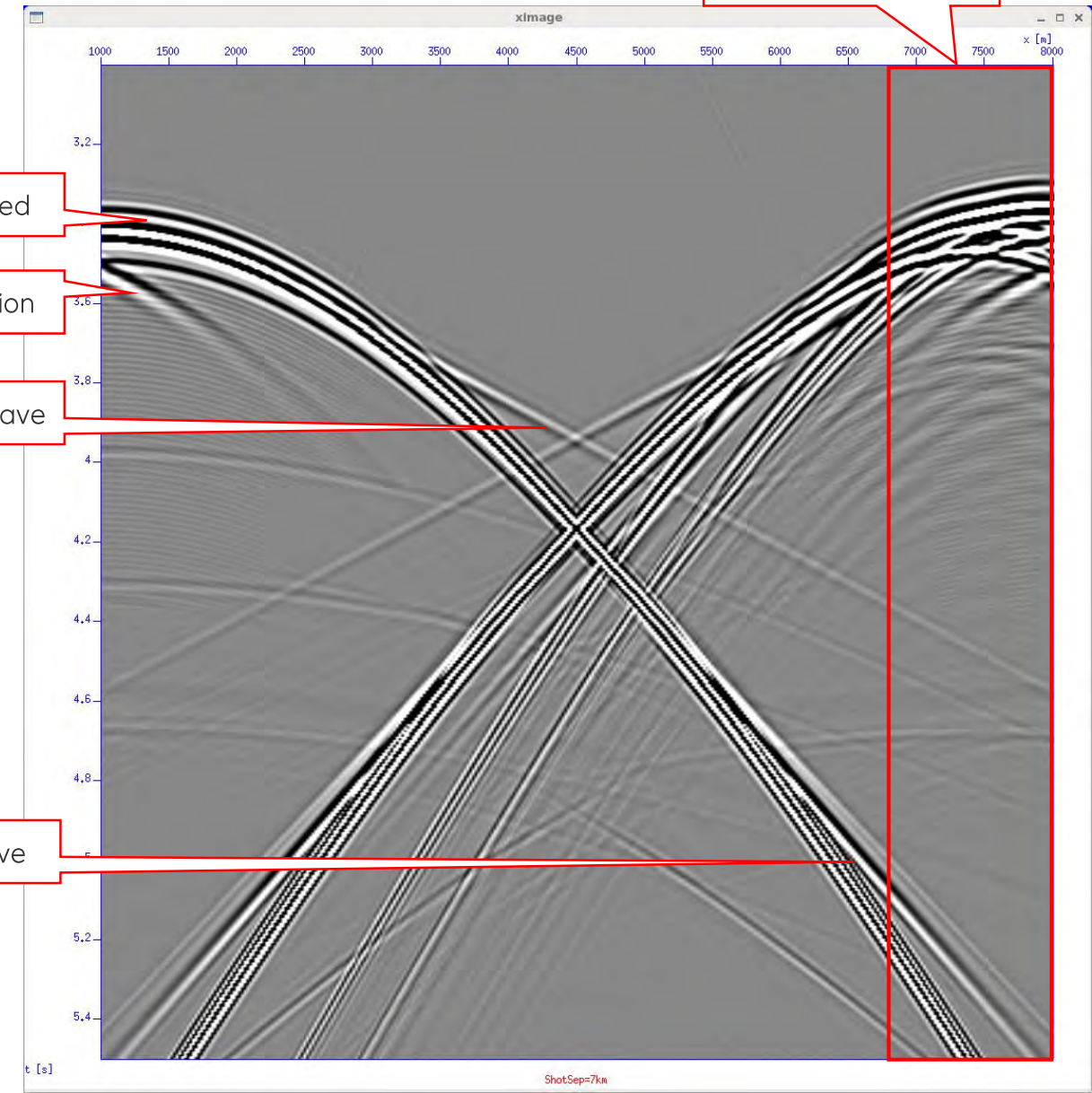
Seabed

Boundary reflection

1st head wave

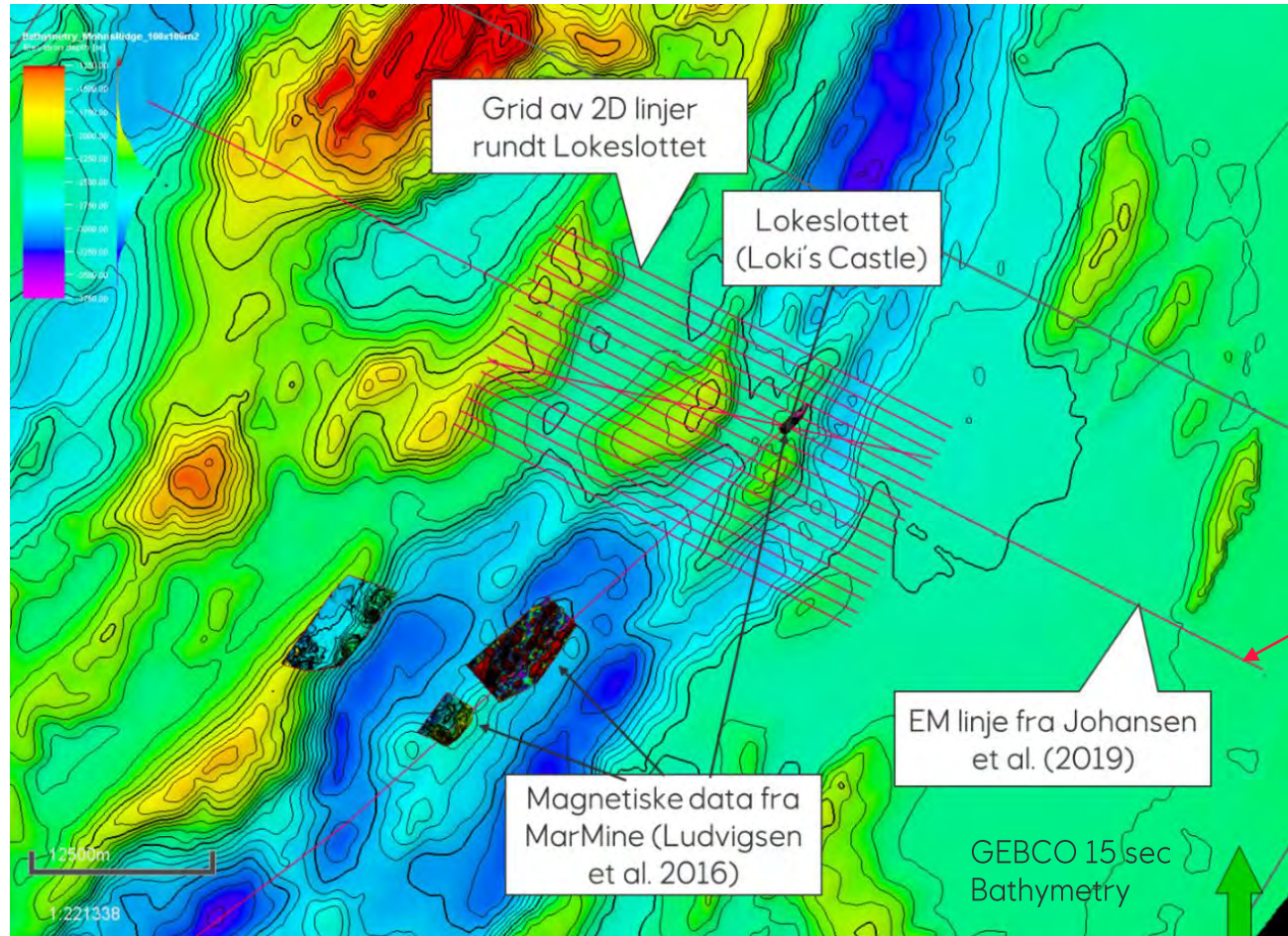
2nd head wave

Shot record with 1200m streamer





# Loki's Castle seismic test design



Figur 4. Havbunnskart i området rundt Lokeslottet på Mohnsryggen. Røde linjer viser planlagte seismiske linjer. De innfelte små polygonene viser magnetiske data samlet inn med AUV av Marmine, NTNU.

From Equinor's application to NPD and MPE

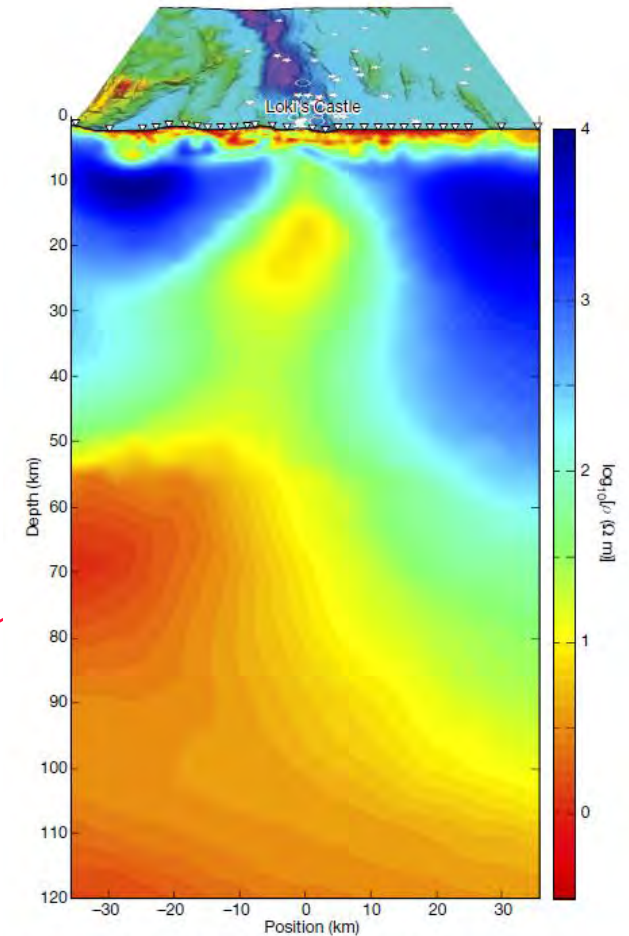


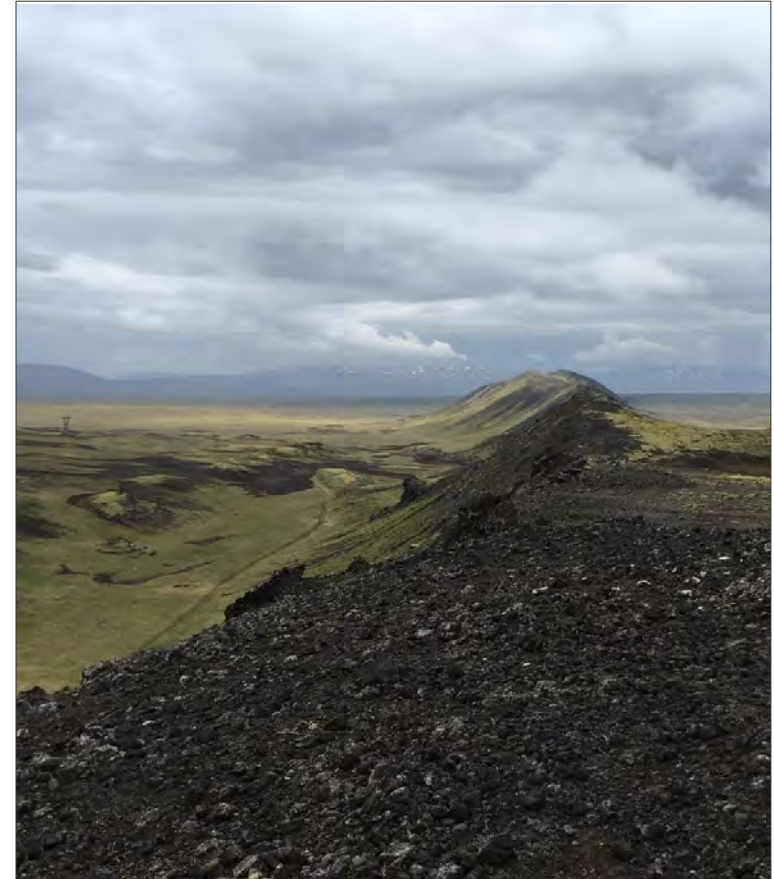
Fig. 2 | Joint MT and CSEM resistivity image of mantle upwelling beneath the ultraslow-spreading Mohns Ridge. Top panel, surface view of seafloor topography, seabed volcanoes and earthquake epicenters from Fig. 1b. In the main panel, colours show resistivity  $\rho_T$  in the horizontal inline direction obtained from joint nonlinear inversion of MT and CSEM data from receivers at the seafloor (inverted triangles). Full anisotropic resistivity results are shown in Extended Data Fig. 5.

Johansen et al, Nature, 2019



# Conclusions

- Multigeophysics is a general concept, applicable to many exploration problems
- Better posterior means and smaller variance
- Main uplift comes from combination of at least **one mechanical** parameter and **one electromagnetic** parameter



# Acknowledgements

## **Barents Sea cases:**

- Rune Kyrkjebø, Zuzana Alasonati Tašárová, Torgeir Wiik, Christine Fichler, Kenneth Duffaut, Janniche I. Nordskog, and Øyvind Kjøsnes
- Ketil Kåsli for initiating our research on thermal modeling
- Ketil Kåsli, Jan Ove Hansen, Kristin Rønning, Torbjørn Dahlgren, Stoney Clark, Olav K. Leirfall for discussions
- Statoil Harstad for providing interpreted regional horizons

## **Iceland case:**

- Kati Tänävsuu-Milkeviciene, Sturla Sæther, Carsten F. Sørli, Keshvad Goodarzi, Jostein Alvestad for discussions
- ISOR for providing the 3D MT inversion cube and gravity data
- EU H2020 DEEPEGS Grant Agreement No 690771

## **Mohn's Ridge case:**

- Anna Lim, NTNU, for providing the magnetic data and sample data
- MarMine project for permission to show the magnetic inversion example

Thanks to Equinor for permission to present this work

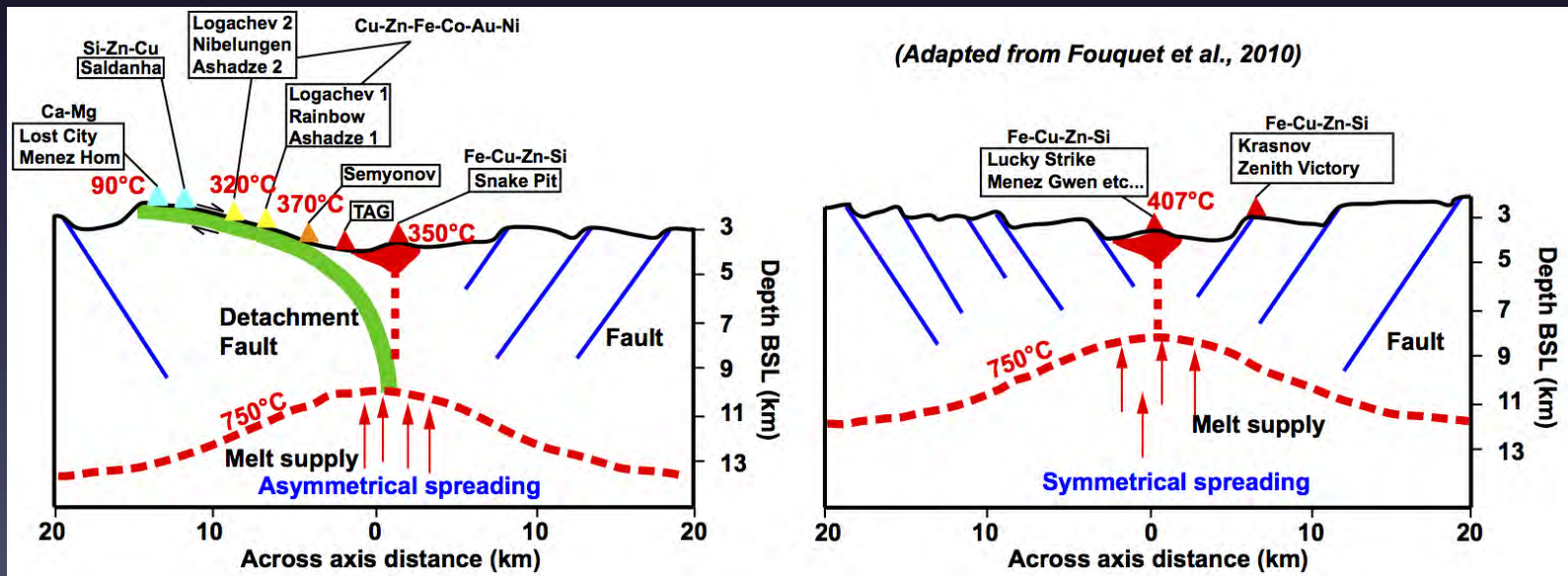
# The magnetic response of hydrothermal systems

Dr. Florent Szitkar  
Trondheim, 27<sup>th</sup> November 2019



The increasing demand for raw materials underlines the need to find new prospects areas.

Deep-sea hydrothermal sites located on Mid-Ocean Ridges have a strong mining potential that may become economically viable.

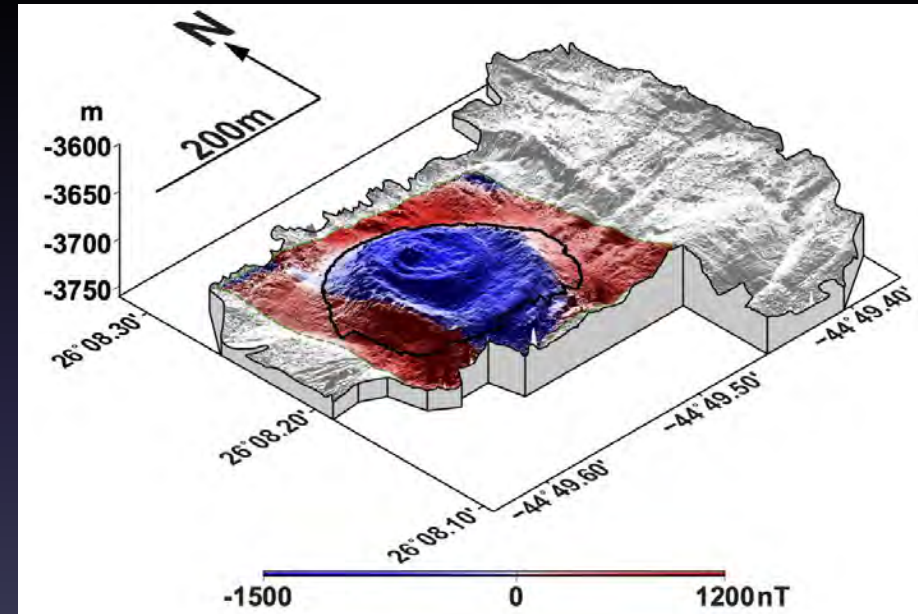
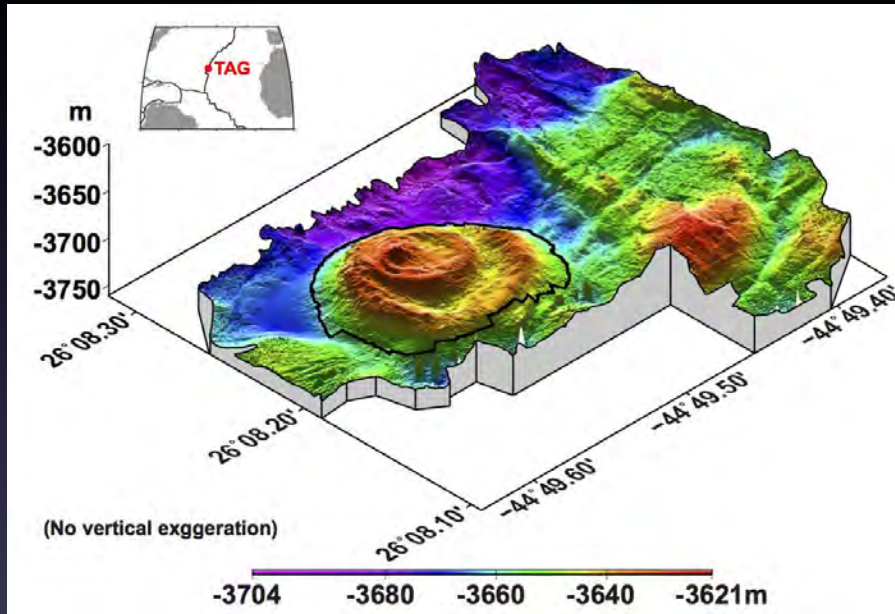


Can we use magnetics to locate and characterize hydrothermal sites???



## What do we know?

(After Tivey et al., EPSL, 1993; Szitkar and Dyment, Geology, 2015a)



Active basalt-hosted hydrothermal site TAG is associated with a negative magnetic anomaly, i.e., a lack of magnetization.



Basalt-hosted hydrothermal sites are associated with **a lack of magnetization.**

This specific signature results from:

- 1) The alteration of magnetic minerals in the basalt by contact with reducing hydrothermal fluids.
- 2) The progressive accumulation of a thick, non-magnetic hydrothermal deposit covering the underlying magnetized basement and increasing the distance between the magnetized source and the magnetometer.
- 3) At active sites, a thermal demagnetization if the temperature exceeds the Curie temperature of titanomagnetite.

However...

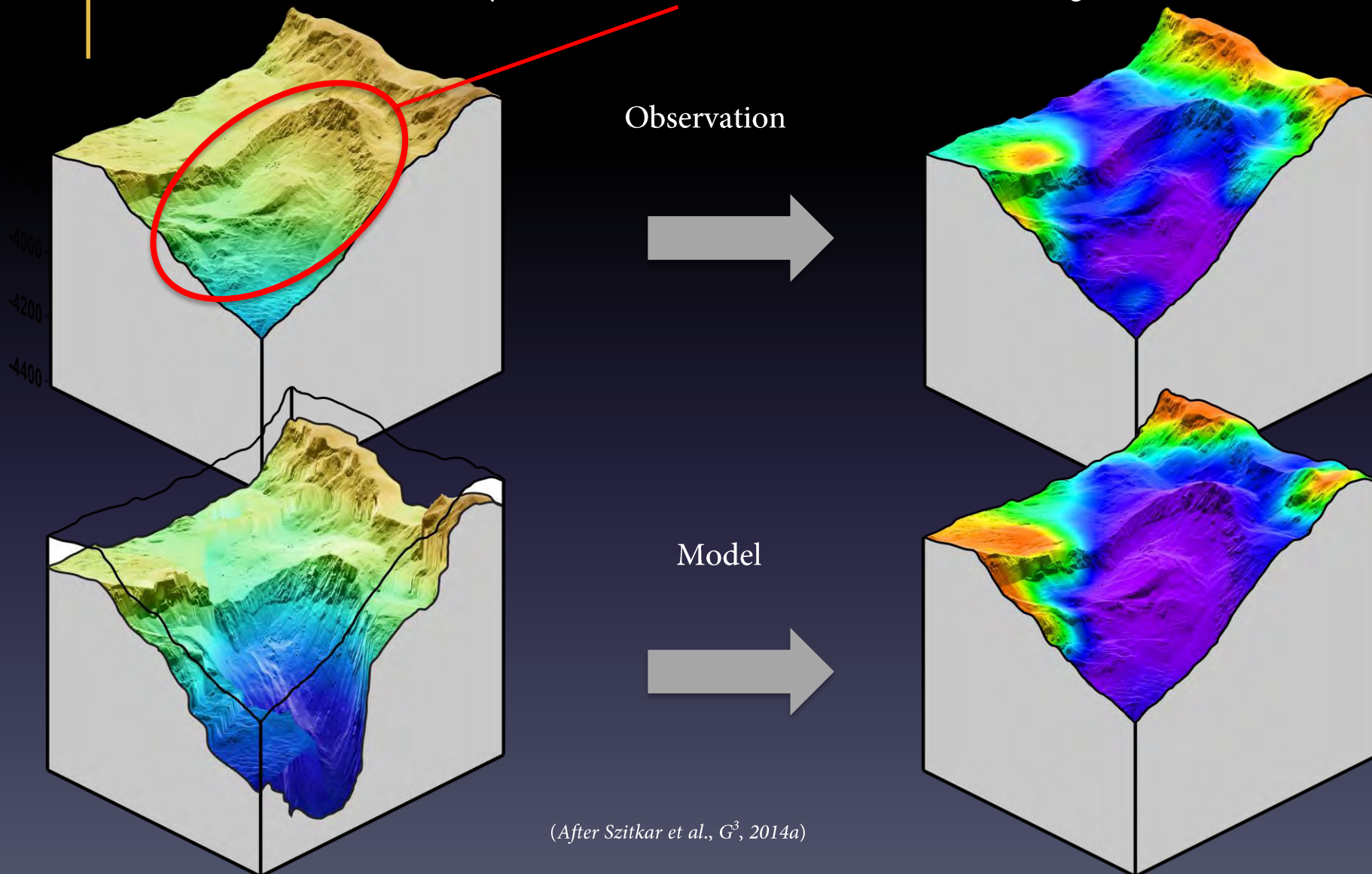
Active sites are also characterized by:

- 1) A specific fauna that needs to be protected.
- 2) Hot temperatures that may damage mining tools.
- 3) Growing deposits (=> Not yet at their maximal size).

None of these problems remain at inactive sites. Unfortunately, such sites can no longer be detected through their plume in the water column.

**Do inactive basalt-hosted hydrothermal sites retain their specific magnetic signature after the end of activity?**

## Inactive basalt-hosted hydrothermal site Krasnov (Mid-Atlantic Ridge)





Let's conclude

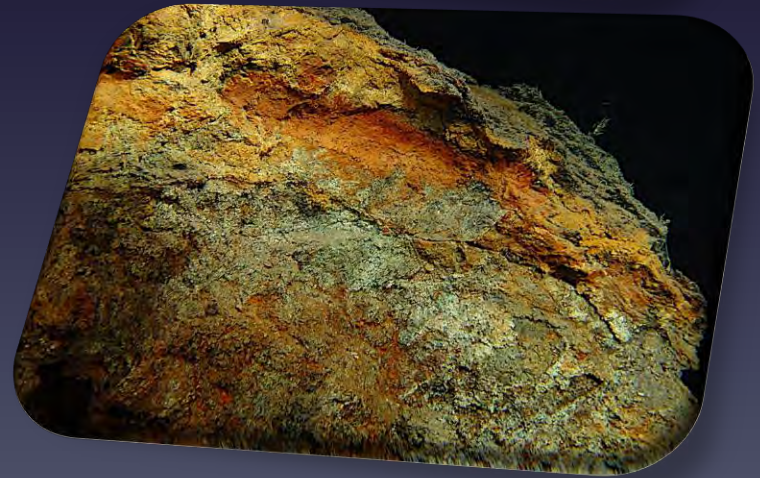
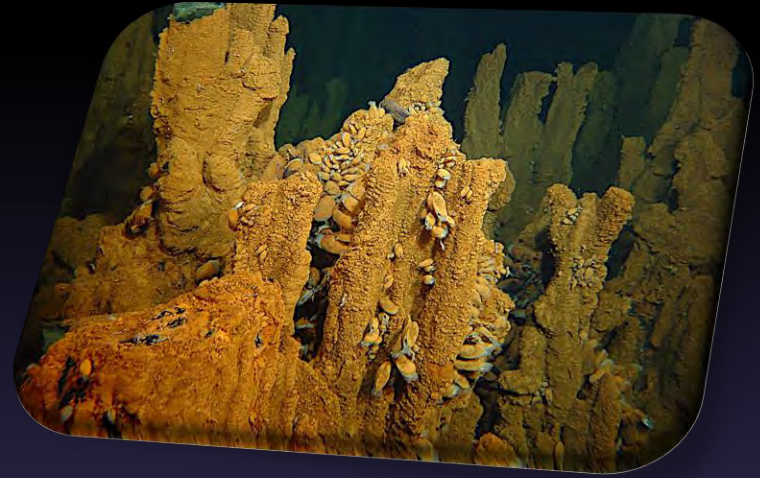
At basalt-hosted hydrothermal sites, the specific signature is mainly a consequence of magnetic minerals alteration and the progressive accumulation of a non-magnetic hydrothermal deposit.

Both are non-reversible processes, i.e., remain after the end of hydrothermal activity.

**Inactive basalt-hosted hydrothermal sites retain their specific magnetic signature.**

**=> Magnetics can be used as a tool to locate and characterize the deep parts of active and inactive basalt-hosted hydrothermal systems.**

Do all types of hydrothermal sites share a similar magnetic signature...?



Along slow-spreading centers...

The magma supply is weak.

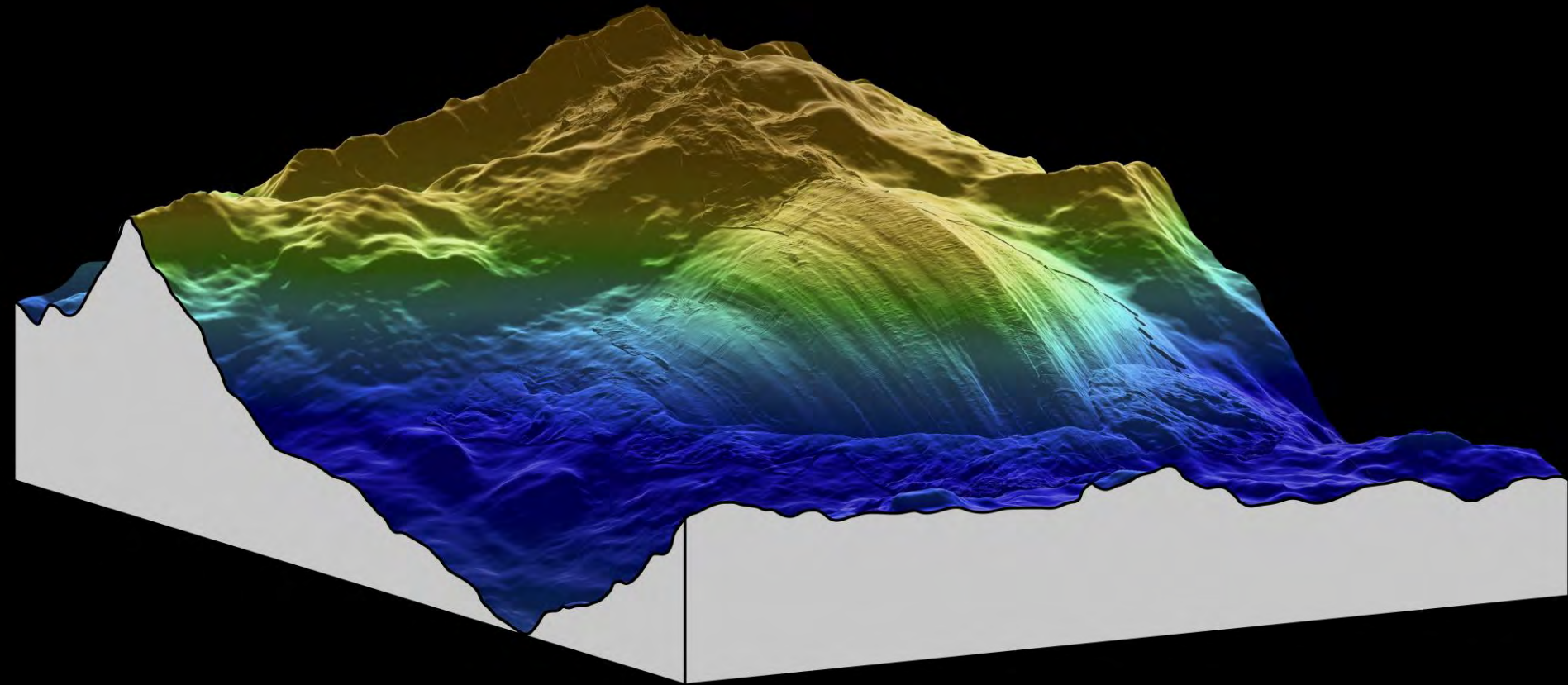
The geology is tectonically driven.

Detachment faults contribute to accommodate the spreading.

=> Existence of Oceanic Core Complex with lower crust/upper mantle rocks outcrops.



## Oceanic Core Complex

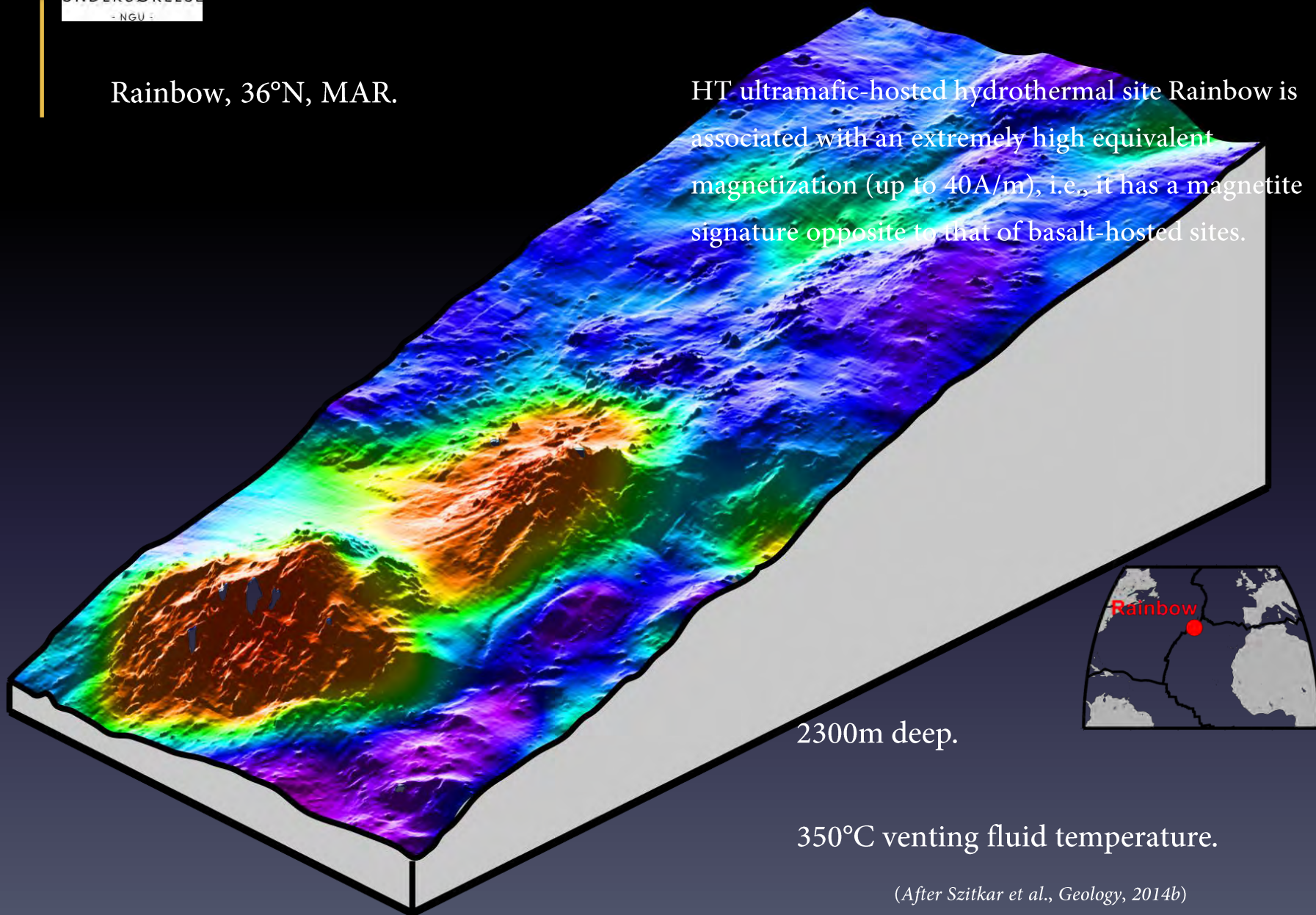


Hydrothermal sites in such ultramafic environment have been discovered.

**Do basalt-hosted and ultramafic-hosted hydrothermal sites have a comparable magnetic signature?**

Rainbow, 36°N, MAR.

HT ultramafic-hosted hydrothermal site Rainbow is associated with an extremely high equivalent magnetization (up to 40A/m), i.e., it has a magnetite signature opposite to that of basalt-hosted sites.



(After Szitkar et al., *Geology*, 2014b)



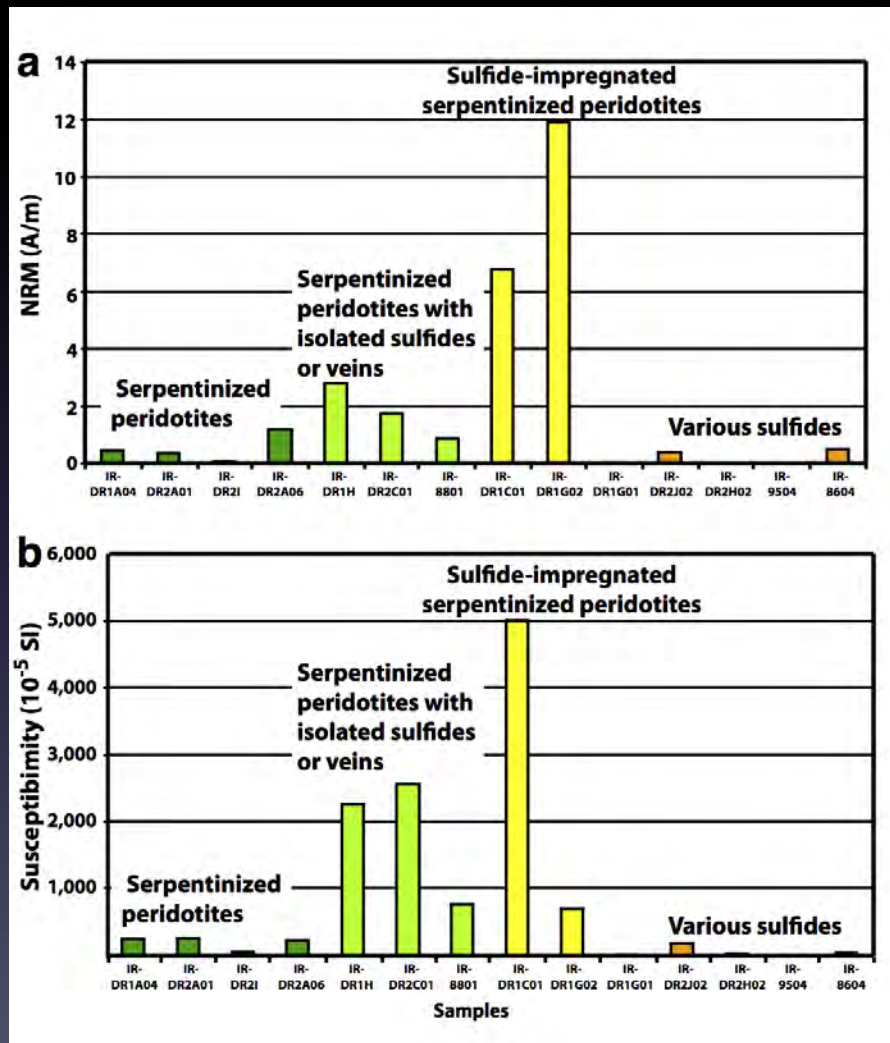
Is Rainbow unique...?

**No!**

**Ashadze 1 (13°N, MAR) is another example of a HT ultramafic-hosted hydrothermal site with the same kind of magnetic response.**

However, neither Ashadze 2 (13°N, MAR), nor Logachev (14°45'N, MAR) exhibit any specific signature (=> they are magnetically neutral) as a result of an unstable and episodic explosive activity.

Where does this magnetic response come from (**Large sites**)?



NRM and susceptibility measured on rock samples, including massive sulfides, stockwork mineralization and ultramafic basement rocks reveal that neither the pure sulfide nor the pure serpentinized peridotite bear a significant magnetization.

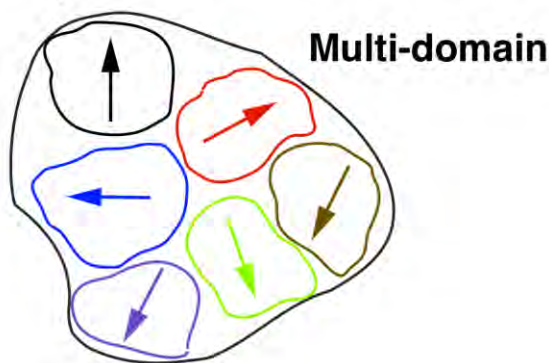
Conversely, sulfide-impregnated serpentinites exhibit both strong NRM and susceptibility, which combined explain the observed anomalies.

Where does this magnetic response come from (**Large sites**)?

# Magnetite

**Big grains**

$$\sum_i \vec{M}_i \approx \vec{0}$$



**Small grains**

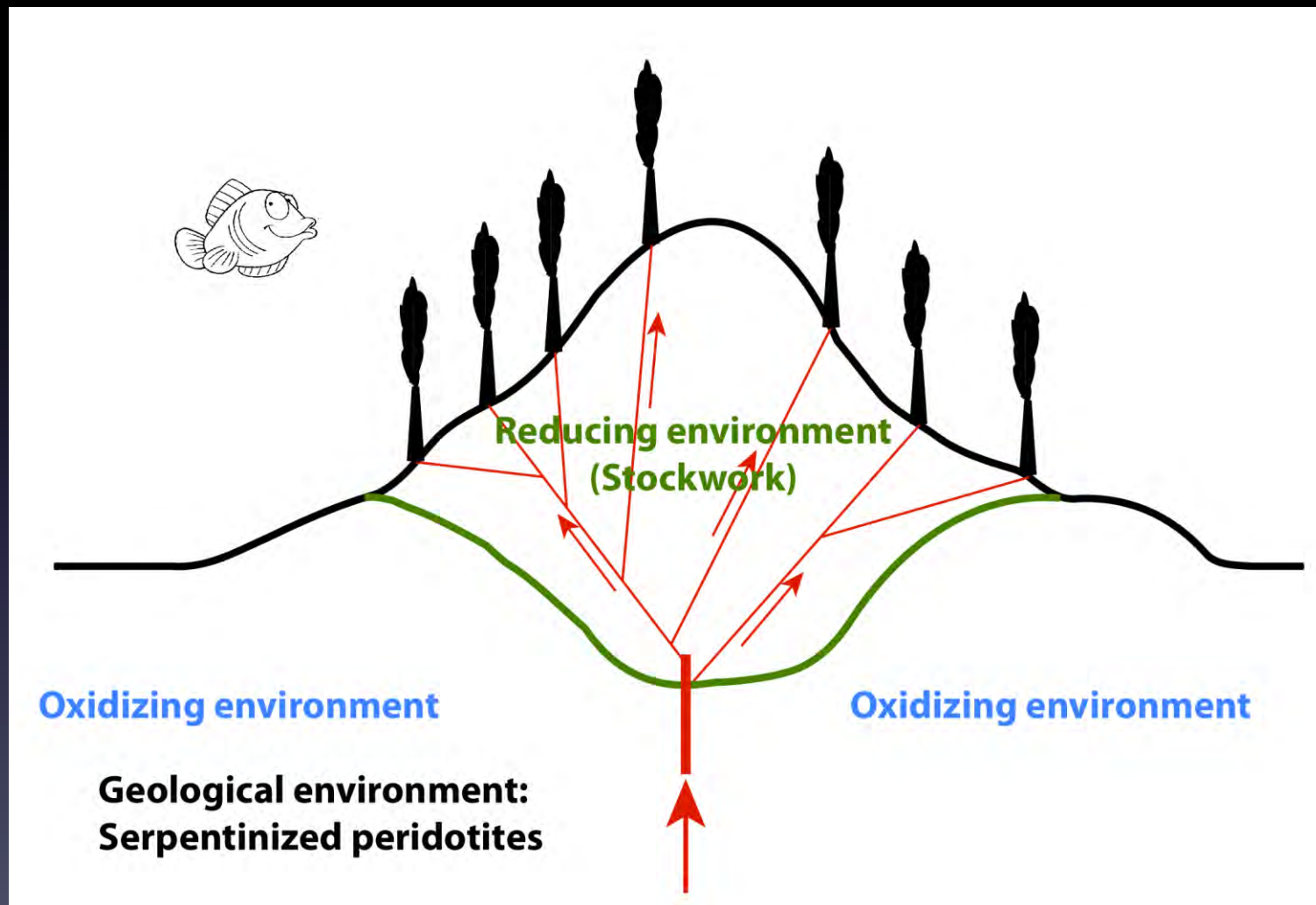
$$\sum_i \vec{M}_i \approx \vec{Max}$$



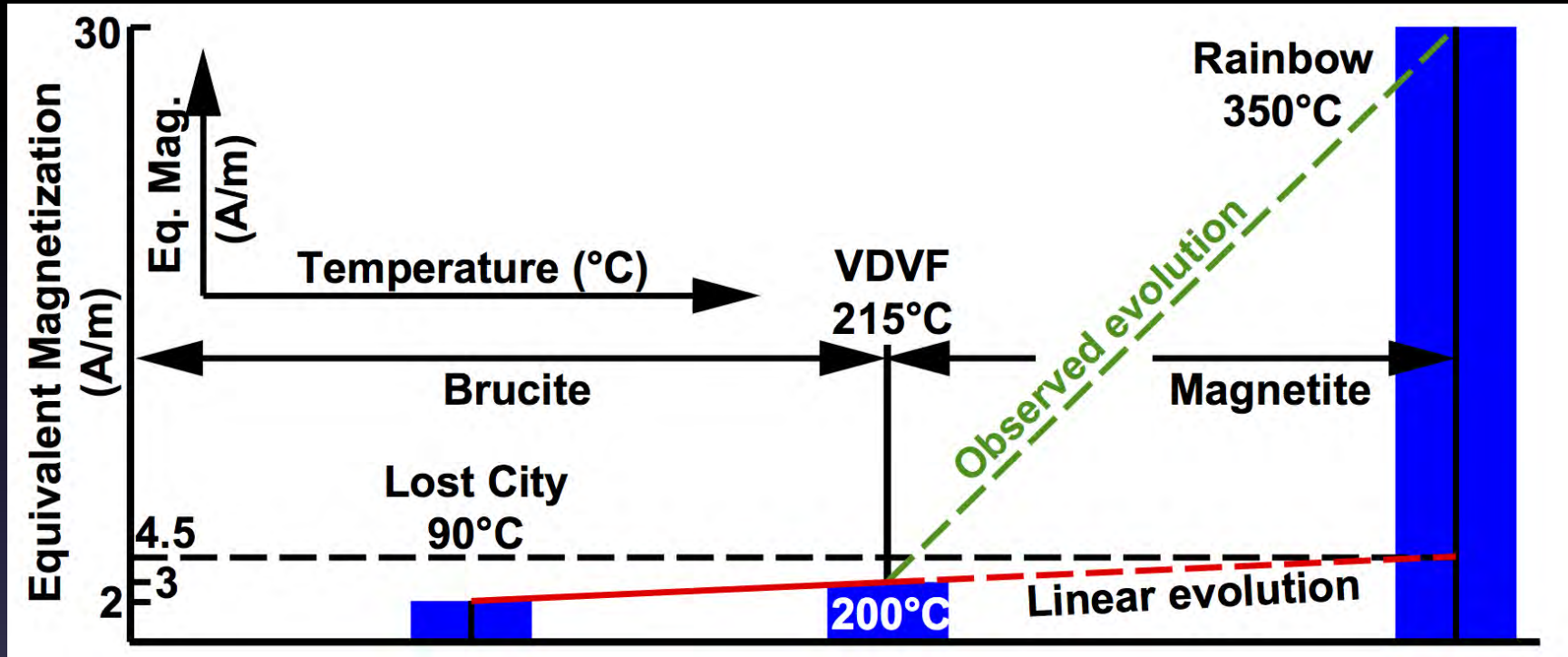
High-temperature serpentinization may generate small grain magnetite.



Where does this magnetic response come from (**Large sites**)?



What about temperature?



Under 200°C, serpentinization reaction mostly triggers iron partition into weakly magnetic brucite. Above this critical temperature, the dynamics of the reaction changes, resulting in the formation of magnetite and a dramatic increase of the site's magnetic signature.

## Conclusions

Can we use magnetics to locate and characterize hydrothermal systems?

**Yes!**

Depending on the nature of the geological basement, magnetism contributes to detect both active and inactive hydrothermal sites and their associated deposits.

Moreover, the characteristics of the anomaly allow estimating the size and shape of the deposits, underlining the importance of geophysics for any hydrothermal mining project.



The future of hydrothermal research...?

Magnetic data have two **BIG** advantages:

On land or at sea, they are **CHEAP AND EASY** to collect.

Surface magnetometers are **SMALL** and cost between **5000 and 10 000\$**. Once purchased, they can be used on almost any ship by simply towing them at the end of a long cable.

## The future of hydrothermal research...?

High-resolution, near-seafloor magnetic data are of course more expensive to collect, as they require both a 3-component magnetometer and an underwater vehicle but they still remain considerably more affordable than other kinds of datasets.

Moreover, **the current development of basic and efficient AUVs** is going to further drop their acquisition cost.

**A small fleet of cost-efficient AUVs equipped with magnetometers is therefore the perfect way to quickly explore large parts of the seafloor at a reasonable price and discover / characterize unsuspected amounts of hidden resources.**

Contact: [florent.szitkar@ngu.no](mailto:florent.szitkar@ngu.no)

**Thank you!**





Tools



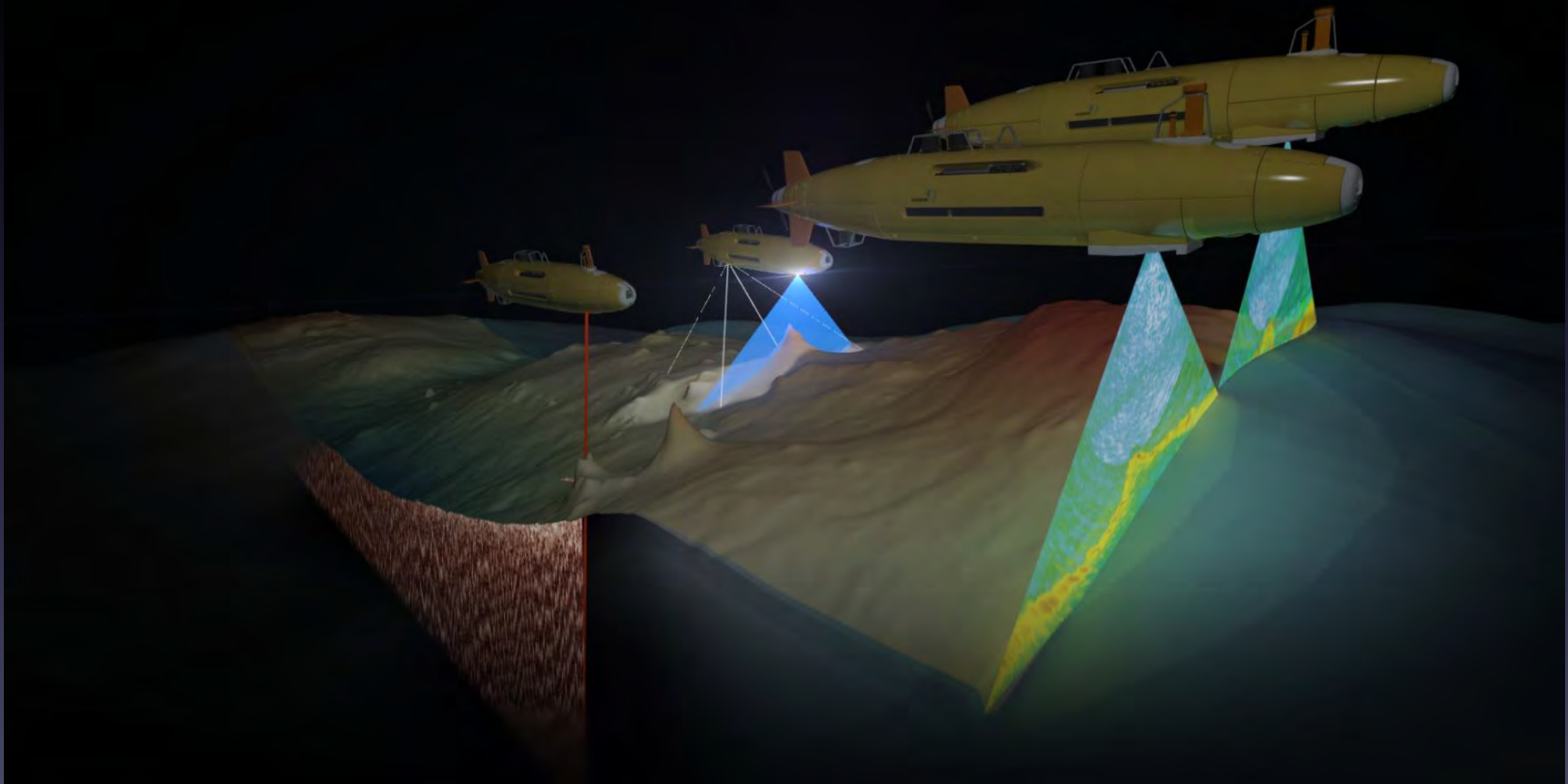
Remote-Operated Vehicles

Vector magnetometer



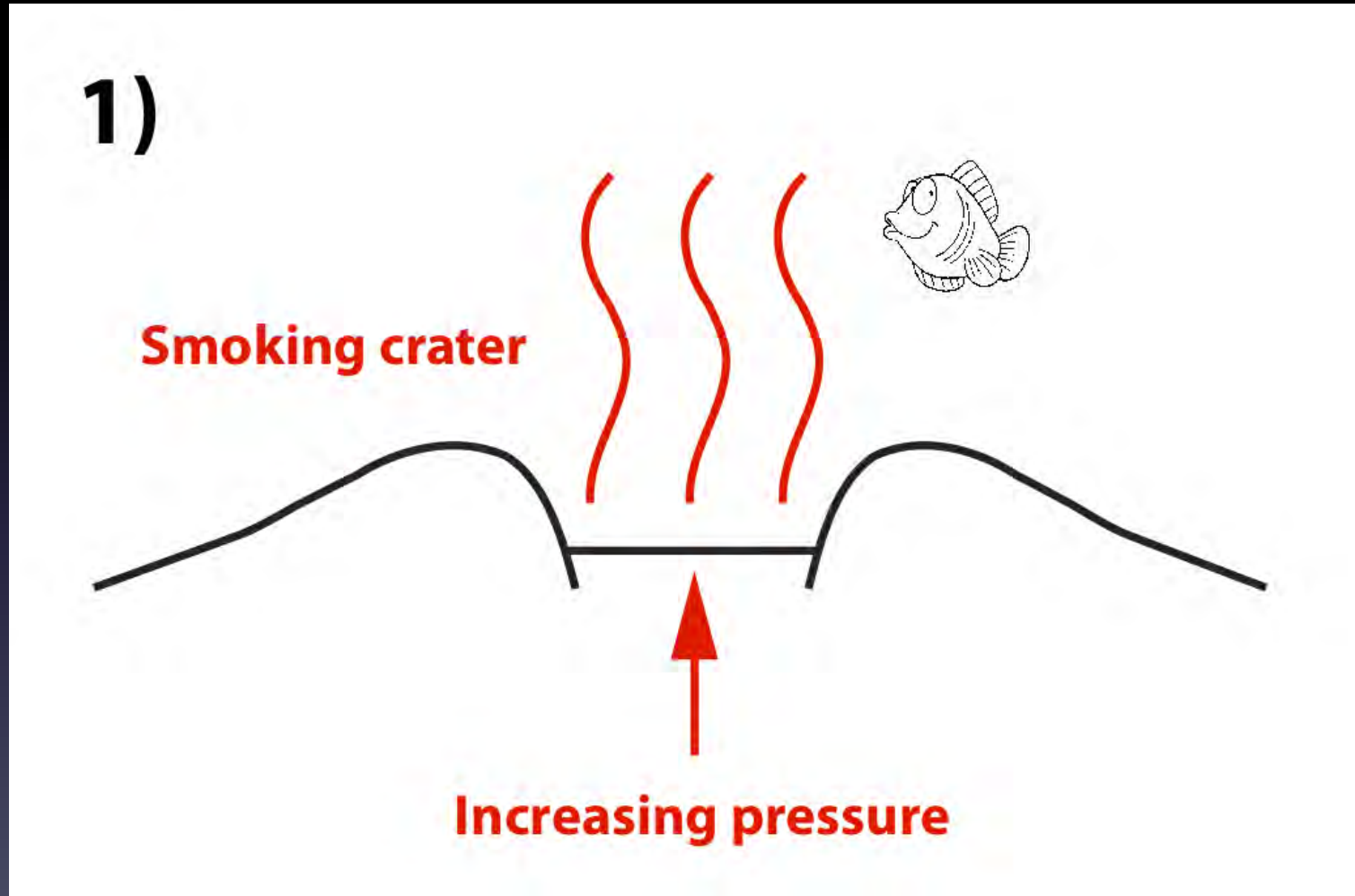


Tools



Automatic Underwater Vehicles

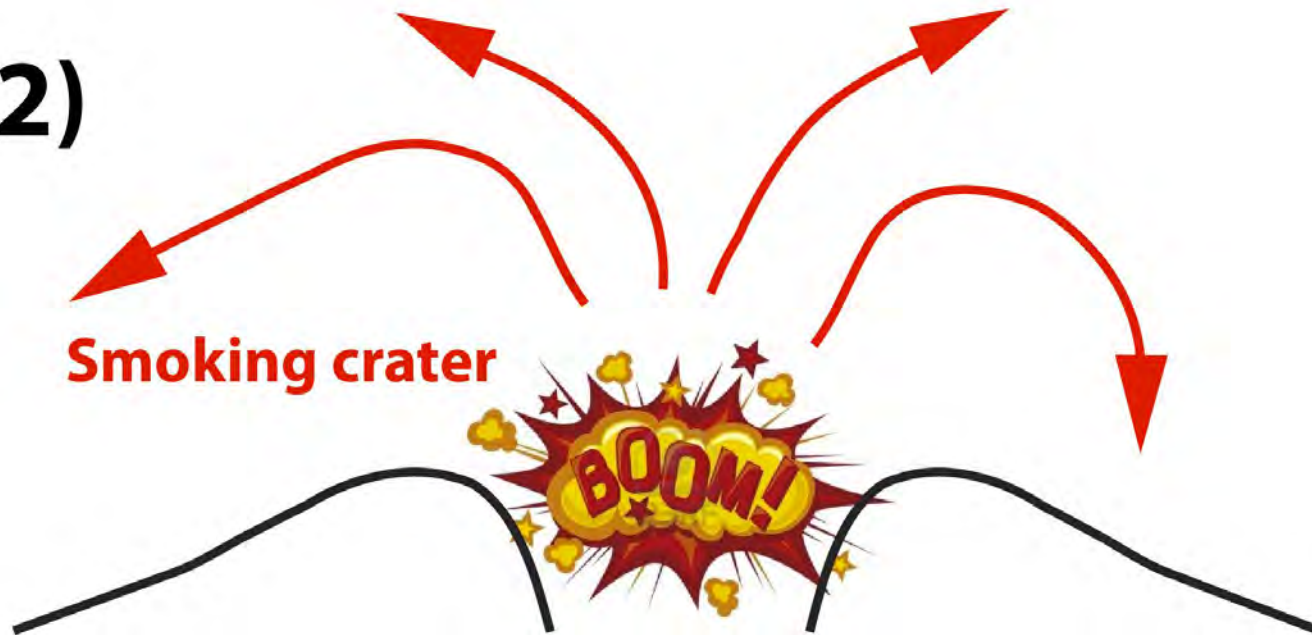
Where does this magnetic response come from (**Small sites**)?





Where does this magnetic response come from (**Small sites**)?

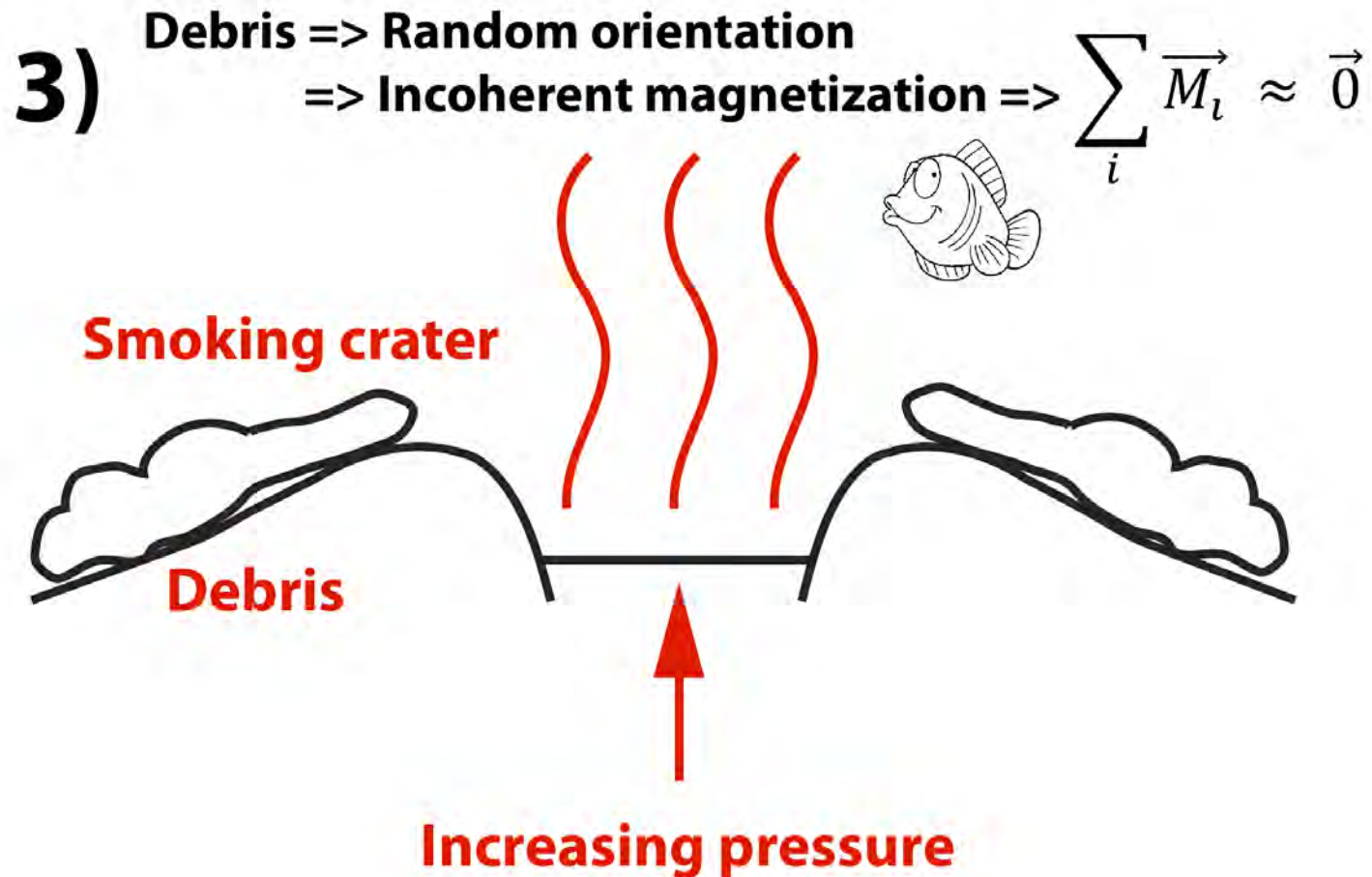
**2)**



**Smoking crater**

**Episodic explosive activity**

Where does this magnetic response come from (**Small sites**)?





## RESEARCH ARTICLE

10.1029/2019GC008439

## Hydrothermal Activity at the Ultraslow-Spreading Mohns Ridge: New Insights From Near-Seafloor Magnetics

Anna Lim<sup>1</sup> , Marco Brønner<sup>1,2</sup>, Ståle Emil Johansen<sup>1</sup>, and Marie-Andrée Dumais<sup>1,2</sup>

<sup>1</sup>Department of Geoscience and Petroleum, Norwegian University of Science and Technology, Trondheim, Norway, <sup>2</sup>Geological Survey of Norway, Trondheim, Norway

**Key Points:**

- We present first geophysical observations from the basalt-hosted active hydrothermal site Loki's Castle, situated at the axial volcanic ridge
- Sediment-hosted extinct hydrothermal site Mohn's Treasure, located at the ridge flank, is associated with magnetization high
- Magnetic data analysis reveals two new fossil hydrothermal sites in the vicinity of the Mohn's Treasure

**Correspondence to:**

A. Lim,  
anna.lim@ntnu.no

**Citation:**

Lim, A., Brønner, M., Johansen, S. E., & Dumais, M.-A. (2019). Hydrothermal activity at the ultraslow-spreading Mohns Ridge: New insights from near-seafloor magnetics. *Geochemistry, Geophysics, Geosystems*, 20. <https://doi.org/10.1029/2019GC008439>

Received 15 MAY 2019

Accepted 24 OCT 2019

Accepted article online 19 NOV 2019

**Abstract** Hydrothermal circulation is a process fundamental to all types of mid-ocean ridges that largely impacts the chemical and physical balance of the World Ocean. However, diversity of geological settings hosting hydrothermal fields complicates the exploration and requires thorough investigation of each individual case study before effective criteria can be established. Analysis of high-resolution bathymetric and magnetic data, coupled with video and rock samples material, furthers our knowledge about mid-ocean-ridge-hosted venting sites and aid in the interpretation of the interplay between magmatic and tectonic processes along the axial volcanic ridges. The rock-magnetic data provide constraints on the interpretation of the observed contrasts in crustal magnetization. We map the areal extent of the previously discovered active basalt-hosted Loki's Castle and inactive sediment-hosted Mohn's Treasure massive sulfide deposits and infer their subsurface extent. Remarkably, extinct hydrothermal sites have enhanced magnetizations and display clear magnetic signatures allowing their confident identification and delineation. Identified magnetic signatures exert two new fossil hydrothermal deposits, MT-2 and MT-3. The Loki's Castle site coincides with negative magnetic anomaly observed in the 2-D magnetic profile data crossing the deposit. First geophysical investigations in this area reveal the complexity of the geological setting and the variation of the physical properties in the subsurface.

### 1. Introduction

Marine magnetic data provided one of the most powerful tools in the development of plate tectonic theory (Vine & Wilson, 1965) and have largely contributed to mid-ocean ridge (MOR) research ever since. Discoveries of hydrothermal activity along the MORs and the resource potential associated with these processes have brought more extensive and detailed exploration to these deep and remote environments. Early studies only attributed hydrothermal activities to fast spreading ridges. Reports of hydrothermal venting at the slow and ultra-slow spreading ridges (less than 20 mm/year; Baker et al., 2004; Dick et al., 2003; Edmonds et al., 2003; German et al., 1998; Pedersen et al., 2010) have opened new areas, like the Arctic Mid-Ocean Ridge (AMOR), to more rigorous research and exploration. At the ultra-slow MOR system north of Iceland, 37 hydrothermal vent sites have been reported since the first discovery in 1980 in the area (Varentsov et al., 1980), followed by more systematic exploration at the end of the 1990s (Beaulieu & Szafranski, 2018). The Mohns ultra-slow-spreading ridge hosts five vent sites (Figure 1a), two of these sites are discussed in this paper. Loki's Castle is an active basalt-hosted vent field investigated by several research cruises (Baumberger et al., 2016; Johansen et al., 2019; Ludvigsen et al., 2016; Pedersen, Thorseth, et al., 2010). High-resolution magnetic data, however, are presented in this paper for the first time. Mohn's Treasure is an extinct vent field approximately 30 km southwest of Loki's Castle (Figure 1b) that was discovered by dredging of sulfide material from the seafloor (Pedersen et al., 2010) but has not yet been studied in detail.

Earlier studies have employed video surveying and water column measurements (Beaulieu & Szafranski, 2018) that have very localized relevance and are only applicable to active venting sites. Thus, geophysical remote sensing becomes critical for locating extinct hydrothermal areas, especially when buried by sediments or lava flows. Several studies (Zierenberg et al., 1998, and references therein) have stated the higher economic potential of such sites that are usually mature and well-developed deposits (Houghton et al., 2004). In this study, we report two new potential fossil hydrothermal deposits in the vicinity of the previously discovered Mohn's Treasure. Even though active sites are easier to identify in this respect, the factual subsurface database from these areas is largely incomplete due to ethical concerns of direct drilling, and technical

©2019. The Authors.

This is an open access article under the terms of the Creative Commons Attribution License, which permits use, distribution and reproduction in any medium, provided the original work is properly cited.



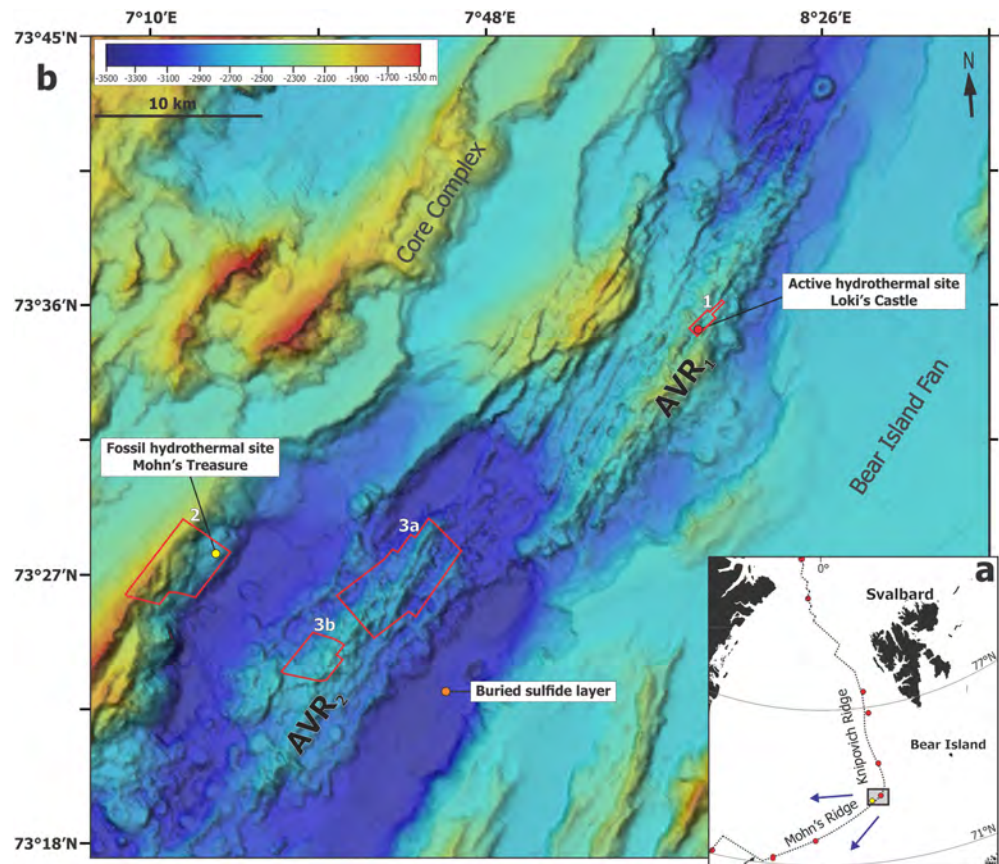


**Figure 1.** Location of the near-seafloor surveys. (a) Regional bathymetric map of the Mohns Ridge northernmost segment resolved at 100 m (Norwegian Mapping Authority, 2015). Red lines mark survey outlines. Active hydrothermal venting site, Loki's Castle, is denoted by red filled circle, extinct venting site, Mohn's Treasure, by yellow filled circle, an orange circle denotes the location of sediment core sample where sulfide layer was found around 1.5-m subsurface (Pedersen, Rapp, et al., 2010). Both flanks of the rift and the valley itself are covered by distal parts of Bear Island Fan sediments (Bruvold et al., 2009). AVR stands for axial volcanic ridge. (b) Regional overview map of the Mohns and Knipovich ridges. The black rectangle marks the location of panel a. Red circles denote active hydrothermal venting sites, yellow circle—extinct hydrothermalism sites (Beaulieu & Szafranski, 2018). The black dotted line marks the spreading axis. Blue arrows denote the North American and Eurasian plate-movement directions relative to a fixed hotspot reference frame (Gripp & Gordon, 2002).

challenges associated with it. Detailed magnetic data helps us in constraining both areal and depth extent of the identified deposits.

Regional, publicly available bathymetry (Norwegian Mapping Authority, 2015), electromagnetic and magnetotelluric data (Johansen et al., 2019), reflection seismic data (Bruvold et al., 2009) proved to be highly instrumental in understanding and describing large-scale processes driving hydrothermal circulation. However, the localization of the associated deposits within the permissive tracts, favorable for exploration, is still not well understood and mainly based on probabilistic assessment rather than on geological and physical characteristics (Juliani & Ellefmo, 2018). Here, we use the interpretation of high-resolution bathymetry and near-seafloor magnetics from the confirmed active and inactive hydrothermal sites and adjacent axial volcanic ridges to further our understanding about the factors controlling the occurrence of such deposits. By doing so, we contribute to the current knowledge base in a local context of the Mohns Ridge geology, and the global context of mid-ocean-ridge venting. The data examination provides a few insights on subsurface processes of hydrothermal circulation and its interplay with tectonic and magmatic processes at the slow-spreading ridges.

## 2. Geological Setting

The study area is located at the northern part of the Mohns Ridge where the MOR transitions into the Knipovich Ridge after bending  $\sim 80^\circ$  along axis strike (Figure 1a). The Mohn-Knipovich Bend was formed as a result of the major plate boundaries reorganization, involving a  $30^\circ$  shift in the plate motion, followed by the initiation of oblique spreading of the previously orthogonal spreading Mohns Ridge and the inception of the Knipovich Ridge at about chron 13 (38 Ma; Talwani & Eldholm, 1977; Vogt, 1986). The Mohns Ridge is an ultraslow and obliquely spreading ridge with a full rate estimated at  $\sim 15.6$  mm/year for the last 10 Ma (Mosar et al., 2002; Vogt, 1986). Topography is rough and has a pronounced difference between the ridge flanks, reflecting the complexity of the spreading history of the Norwegian-Greenland basins. The asymmetry is expressed at multiple levels and is attributed to the oblique and asymmetric motion of the European and North American plates rather than asymmetric sediment loading, which barely follows the basement topography (Johansen et al., 2019; Talwani & Eldholm, 1977; P Vogt et al., 1982). Both flanks of the rift valley and the valley floor are covered by sediments from the Bear Island Fan with thickness reaching up to  $\sim 800$  m with larger volumes deposited on the eastern side (Bruvoll et al., 2009).

Transform faults do not dissect the ridge, yet the MOR is characterized by linked magmatic (volcanic) and amagmatic (tectonic) segments (Dick et al., 2003). Topographic highs present in the axial valley of the study area are interpreted as being volcanic in origin (Crane et al., 1999; Géli et al., 1994). Abundant volcanic features such as prominent cones, flat-topped volcanoes, and volcanic ridges, are observed in the bathymetric data and have corresponding short-wavelength anomalies in regional magnetic data (Géli et al., 1994; Pedersen, Rapp, et al., 2010) that support the hypothesis that the two domed elongated edifices discussed in this paper are neovolcanic axial volcanic ridges (AVR<sub>1</sub> and AVR<sub>2</sub>). The life cycle of an AVR alternates between magmatic and tectonic phases, following the intermittent magmatic and tectonic focusing and defocusing along the axis due to restricted magma supply (Parson et al., 1993). The area is seismically active—earthquake epicenters located within the ridge valley closely correlates with the major faults and volcanoes at the graben floor, suggesting a tight link between melt placement and faulting processes (Hopper et al., 2014; International Seismological Centre, 2018; Johansen et al., 2019). The interplay between these processes is of major importance for hydrothermal circulation along the ridges (McCaig et al., 2007).

Loki's Castle is an active high-temperature hydrothermal venting field discovered in 2008 (Pedersen, Thorseth, et al., 2010). It occurs at the northernmost AVR of the Mohns Ridge that rises approximately 1,300 m above the rift valley floor at 2,000-m depth. This AVR is locally perpendicular to the spreading direction and reaches around 30-km length. Topographically the ridge is composed of hummocky terrain with notable tectonic disruption. En echelon faults can be traced along the entire ridge, which is locally covered by fresh lava flows. Volcanic cones, smaller ridges, flat-topped volcanoes are common features. Sediment thickness varies across the area providing information on the relative age of the underlying volcanic features (Mitchell et al., 1998). Geochemical analysis of the hydrothermal fluid collected from the black smokers, that is, end-member volatile concentrations, supports magmatic influence in the area (Pedersen, Thorseth, et al., 2010), confirming that Loki's Castle is a basalt-hosted site. There are also indications of fluid interaction with ultramafic rocks and a significant footprint of sediment influence (Baumberger et al., 2016), which likely results from the deep fault and across-axis circulation as shown in a recent deep electromagnetic imaging study across the ridge by Johansen et al. (2019).

Unlike the AVR hosting Loki's Castle, the southern neo-volcanic ridge (AVR<sub>2</sub>) is less pronounced and exhibits terrain strongly dominated by young pillow flows. The tectonic disruption here is less prominent than at the northern AVR and is primarily attributed to syn-magmatic tectonism. Vertical disruption is not significant, whereas crustal fissures are a common observation. The AVR extends for approximately 25 km in a northeasterly direction and is locally orthogonal to the spreading direction and rises on average 500 m above the valley floor. The summit is located at the center of the neo-volcanic zone, at 2,500-m water depth reaching around 800 m above the valley floor.

Mohn's Treasure area is the most geologically distinctive among three study areas as it is situated at the flank of a rift valley, west of the AVR<sub>2</sub>. The general trend of the major extensional fault creating the inner wall of the axial rift is about  $039^\circ\text{N}$ . The area is predominantly composed of lithified and partly lithified sediments that represent distal parts of Bear Island fan deposited in the rift valley, subsequently uplifted by the marginal faults, and then mass wasted (Pedersen, Rapp, et al., 2010).

### 3. Data Collection and Processing

Near-bottom high-resolution magnetic data, bathymetry, and rock samples were collected during the MarMine cruise onboard *Polar King* multipurpose vessel in 2016 (Ludvigsen et al., 2016). Data acquisition was carried out using an autonomous underwater vehicle (AUV) *Hugin* by *Kongsberg Maritime*. Two heavy-duty remotely operated vehicles (ROVs), *Triton XLX* and *XLR*, were used for sampling and video surveying.

A total of five different AUV dives are presented in this paper and are grouped according to their location into three survey areas: Loki's Castle active venting site: Survey Area 1 (AVR<sub>1</sub>); Mohn's Treasure extinct venting site: Survey Area 2; axial volcanic ridge (AVR<sub>2</sub>) exploration areas: Survey Areas 3a and 3b (Figure 1). The AUV surveyed along parallel profiles spaced by 150 m apart (250 m for Surveys 3a and b) at the nominal altitude of 100 m above the valley floor, ranging from 40 to 270 m. The bathymetric data were provided by a combination of *EM 2040* multibeam echosounder and interferometric side-scan sonar *HiSAS 1030* (both provided by *Kongsberg Maritime*). Resulting bathymetric maps were gridded at 1 m each, except for the Mohn's Treasure site where the grid resolution is 4 m due to the difficulties experienced by the AUV while surveying a steep slope. The regional overview bathymetric map is a ship-based grid resolved at 100 m collected for the *Norwegian Petroleum Directorate* in 2000 (Norwegian Mapping Authority, 2015).

#### 3.1. Magnetic Data

The high-resolution vector magnetic field data were collected using a self-compensating three-axis fluxgate magnetometer system developed by *Ocean Floor Geophysics* that was rigidly mounted inside the AUV. The dynamic range of the magnetometer covers  $\pm 65,000$  nT with a resolution of 0.01 nT, and  $\pm 0.5$ -nT peak-to-peak noise level. Raw data consisted of magnetic intensity for three components, and vehicle attitude data (heading, roll, and pitch) that were logged simultaneously and interpolated to the magnetic data sampling rate of 19 Hz. The topography of the seafloor acquired by the multibeam echosounder was sampled to 1-m cell size grid (and 4 m for Survey 2).

Even though the AUV body is made from nonmagnetic carbon fiber laminate and synthetic foam, the propulsion motor and other payload sensors still affect the magnetic measurements. At the beginning of each survey, calibration maneuvers were performed to estimate the best correction for the vehicle-induced field and its interaction with the Earth's magnetic field. It involved flying a square pattern with the change of both the heading and altitude, creating a set of reciprocal lines. Recorded data were then used to calculate correction terms to remove the influence of the vehicle movements and the heading effects on the measured magnetic data as described by Honsho et al. (2013) and Bloomer et al. (2014). The maneuver and correction were performed for each dive separately. The level of noise related to the platform in the recorded data was estimated to be  $\pm 10$  nT. The correction removed most of the false maneuver-related short-wavelength apparent anomalies and improved the noise level marginally.

No crossing tie-lines were performed during the survey to correct for variations of the Earth's magnetic field due to ionospheric influences and/or ocean current induced magnetic fields; neither there was a base station on the seafloor. Geomagnetic observatory recordings of the magnetic field at Bjørnøya and Tromsø, and calibrated variometers at Longyearbyen and Jan Mayen showed moderate magnetic activity during the surveys with a peak magnitude of around 100–150 nT (Tromsø Geophysical Observatory, 2018). However, no correlation was found upon visual inspection when comparing the diurnal data with recorded magnetic field data, and consequently, no such correction was performed on the data. The compensated magnetic field data for all datasets were low-pass filtered to remove residual uncompensated vehicle motion noise at wavelengths shorter than 50 m using a Butterworth filter.

Due to autonomous character of the data acquisition in a relatively poorly known and very rugged topography—the NMA 2015 bathymetric map of 100-m grid resolution was used for survey planning and navigational purposes—recorded survey altitudes were not consistent with the nominal constant drape values. While direct effects of vehicle behavior like heading change, pitching, rolling, and vehicle-induced field noise was taken care of in the first steps of the processing sequence, nonconsistent terrain clearance caused a loss of signal resolution and distortion of some anomalies. To account for these issues, we used the *CompuDrape* extension integrated into *Oasis Montaj* software suite (Paterson et al., 1990). It computes the continued field at a set of different levels then interpolating the values on a specified draped surface. As



pointed out by several studies (Cordell, 1985; Pilkington & Roest, 1992; Pilkington & Thurston, 2001), even though this method is not very rigorous mathematically it proved to work well in practice. It maintains the data resolution compared to other upward continuation approaches. An example of the drape correction applicability test is illustrated in Figure 2. Having measurements at two different altitudes at the Loki's Castle survey allowed us to test this method. We compared the continued field intensity profiles using low- and high-flight modes data. Assuming the drape-fixed TMI profile from high-flight data is close to ideal, as the terrain clearance is highly consistent for the most part, and thus the corrections were minor (Figures 2b and 2c), the comparison of this profile and the TMI profile computed from the low-flight data, acquired 40 m lower on average, demonstrates satisfactory results and the utility of the approach. A standard deviation lies within 150 nT for all profiles with two flight-modes tested. However, the decline in the resolution for larger altitude difference is considerable. As this method involves both a downward field continuation and a more stable upward field continuation, careful attention was given to the choice of the new observation height. This choice was based on the dominant altitude value, and the magnetic frequency content to minimize downward continuation noise amplification and upward continuation signal loss. Thus, the drape recomputed nominal altitude was set to 100 m for surveys 1, 2, and 3a, 150 m for the Survey 3b, and 60 m for Loki's Castle low-altitude dataset. Given the average variation in the flight altitude for all surveys and the frequency content of the signal of interest, the results of this method are satisfactory. We also tested both line- and grid-based approaches on the data, displaying better results in the former approach since grid-based draping tends to amplify interpolation errors, especially in case of bigger difference in altitude between the adjacent lines, producing errors in the computed gradients orthogonal to the lines.

Subsequently, a microleveling correction was applied to the profile data to reduce the long-wavelength noise caused by the discrepancy between adjacent survey lines (Ferraccioli et al., 1998; Minty, 1991). The TMI data was then transformed into magnetic anomaly data by removing the mathematically approximated geomagnetic field—International Geomagnetic Reference Field (IGRF; Thébault et al., 2015). In the end, a reduction to the pole (RTP) transformation (Baranov, 1957) was applied by placing magnetic anomalies over their sources. The magnetic field direction in the survey area was assumed to have a declination of  $2^\circ$  and inclination of  $80^\circ$ . Finally, the resultant magnetic anomaly data were interpolated onto 30 m spaced grid (40 m for Survey 3b) by a minimum curvature algorithm.

Other techniques used in this paper have qualitative or semi-quantitative character, utilize total magnetic field derivatives for the interpretation and include tilt derivative (Miller & Singh, 1994), analytical signal (Nabighian et al., 2005; Roest et al., 1992) and Euler deconvolution (Reid et al., 1990; Thompson, 1982). The analytic signal is independent of the inclination of the magnetic field and of the source magnetization. Following the assumption that the isolated anomalies are caused by vertical contacts, the analytic signal can be used to estimate depth using a simple amplitude half-width rule (Roest et al., 1992). Euler deconvolution is an automated technique for depth estimation that is based on Euler's homogeneity relationship and does not require any a priori knowledge of the geology (Thompson, 1982). However, the depth resolution is limited by the grid spatial resolution. The data were analyzed using the standard Euler deconvolution for contacts and step-like structures (Reid et al., 1990) to aid interpretation of the gross structural trends. The Located Euler deconvolution, which locates confined peak-like structures in the data, was performed to examine cylinder-like structures that are assumed to represent the geometry of the studied deposits. In the case of Loki's Castle, we used the measured vertical gradient obtained by calculating the difference between the two datasets of low- and high-flight modes and dividing it by the difference in their nominal altitudes instead of using the calculated vertical derivative.

The magnetic tilt derivative enhances the magnetic fabric. Originally introduced by Miller and Singh (1994), it has the useful property of being positive over the source, and negative outside the source region, crossing through zero at, or near, the edge of a vertical-sided polygon. TDR aids in mapping subtle basement fabric through enhancing small-amplitude signals so weak magnetic bodies such as hydrothermal deposits are treated with the same weight as strongly magnetic bodies (Verduzco et al., 2004). The combination of these attributes provides a useful tool for data enhancement and further interpretation and mapping of geologic features.

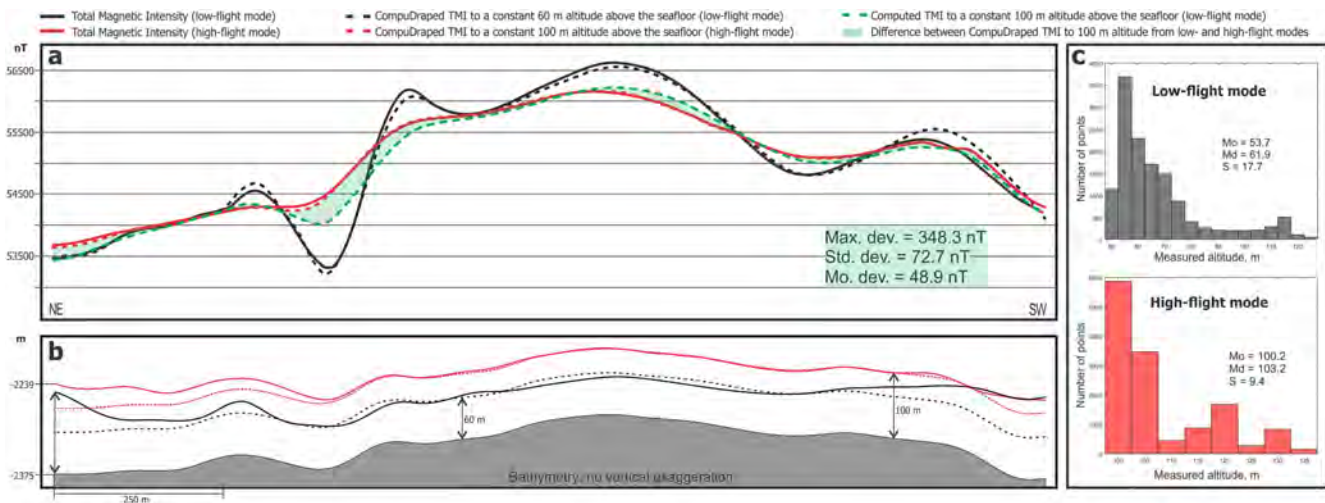


**Figure 2.** Comparison between the measured- and constructed-drape TMI profiles in the rough terrain of Loki’s Castle: Line 5 in Figure 5. (a) Original TMI profiles are denoted by solid lines: low-flight mode is black, high-flight mode is red. Both modes were acquired with inconsistencies in altitude displayed in (b) and (c) panels. Dashed lines are obtained using a CompuDrape algorithm and correspond to the new constant altitudes above the seafloor: 60 and 100 m. (b) Bathymetric profile with original loose drapes for low- and high-flight mode surveys, in black and red solid lines respectively. Dashed lines mark fixed-drape profiles. (c) Original altitude distributions for low- and high-mode surveys for the displayed survey line with modal, median, and standard deviation values.

The 2-D magnetic forward modeling has been carried out using the GM-SYS Profile Modeling module integrated in *Oasis Montaj* software package. This type of analysis is used to calculate the magnetic response from a geological model and compare to the observed data. The method is based on calculation algorithm developed by Talwani and Heirtzler (1964) and refined according to Rasmussen and Pedersen (1979). The geologic model whose upper boundary is constrained by the observed topography was adjusted by a semi-automatic trial and error approach to ensure the best fit.

### 3.2. Rock Samples

All rock samples collected from the Loki’s Castle hydrothermal venting site are non-in-situ grab-samples. A total of 25 samples were measured for their petrophysical properties and represented mudstone, hydrothermally altered basalt, and highly heterogeneous loose probable-chimney fragments from the mound flanks (Snook et al., 2018).

One sample from the Mohn’s Treasure site is a drill-core that was first video recognized as a basalt (Figure 3d shows the drilling site): black hard rock that did not break or crumble in ROV-manipulator as immediately happened to sedimentary or hydrothermal rocks in the area (Ludvigsen et al., 2016). Upon closer examination, including petrophysical measurements at the Norwegian Geological Survey (NGU), this sample was recognized as a claystone. This fact changed our understanding of the lithology presented in the Mohn’s Treasure area and largely contributed to the interpretation of hydrothermal deposits and their magnetic signatures.

All petrophysical measurements were performed at the NGU petrophysical laboratory using commercial and proprietary instruments. Rock density, volume and porosity were determined according to the methodology of EN 1936:2006 (CEN, 2006) using *Sartorius AX 4202* instrument. The rock-magnetic properties measurements included magnetic susceptibility (performed using *NGU* proprietary system) and magnetic remanence intensity (performed using a  $3 \times 3$  component *Sensys FGM3D* fluxgate magnetometer system installed in a nullspace). The direction of the NRM could not be measured because the in-situ orientation of the samples was not known. The Königsberger ratio was calculated based on the average IGRF magnetic field intensity value for the area equal to 53,800 nT. Measurement uncertainties are presented in Table 1.

## 4. Results and Discussion

The surface geology at the Loki’s Castle, Mohn’s Treasure, and exploration site was video examined by the ROV mounted cameras. The observed geologic features can be grouped into five categories: (1) different

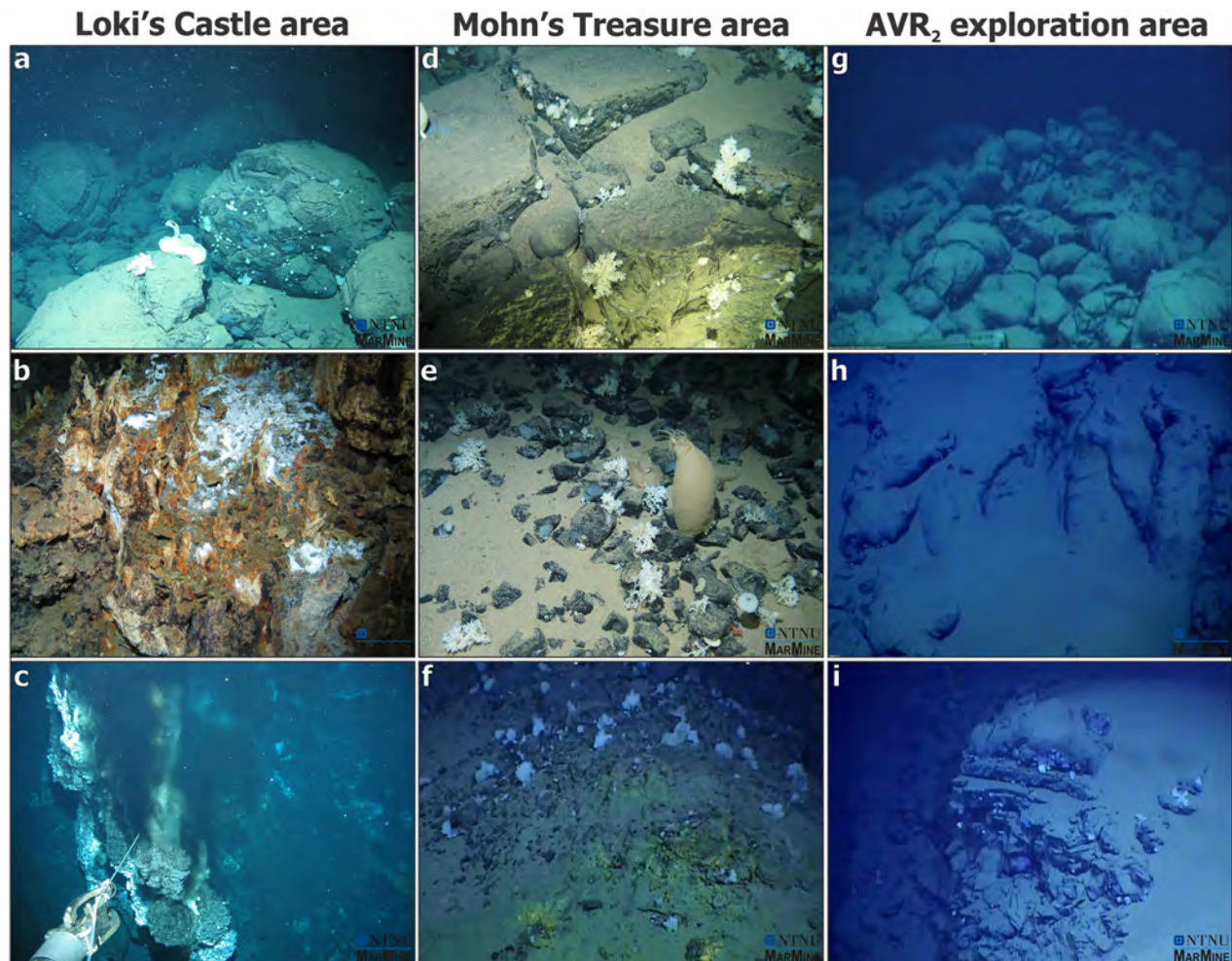


**Figure 3.** Photo observations from ROV-mounted photo and video cameras. AVR<sub>1</sub> Loki's Castle hydrothermal field: (a) Pillow basalt talus at the base of the border fault cliff near Loki's Castle. (b) Hydrothermal vent material commonly observed at the mound. (c) Black smoker at the eastern mound. Mohn's Treasure survey area: (d) Fractured lithified sediments outcrop. (e) Lithified sediment debris on top of loose sediments. (f) An outcrop of yellow hydrothermally altered material at the Mohn's Treasure deposit. AVR<sub>2</sub> exploration area: (g) Pillow lava mound. (h) Elongated lava flow tubes. (i) Lava flow beds exposed in a near-vertical cliff (ROV was at an altitude of more than 20 m above the valley floor giving a lower border estimate of the cliff height).

types of lava flows: low-relief sheet flows, lobate pillow flows, and interconnected lava tubes; (2) extensively fractured pillow-lava talus, truncated pillows, and basaltic breccia; (3) loose and partly lithified sediment cover; (4) lithified sediment; and (5) hydrothermal material including black and white smokers, broken chimney material, and sulfide deposits. Figure 3 shows typical photo-observations from each site.

Aside from geological expressions, all three study areas exhibit different biodiversity backgrounds. Since hydrothermal venting sites are also known as deep-sea “oases”—an abundant source of chemoautotrophic bacteria that attract underwater animals have developed to tolerate this extreme habitat and thrive (Fisher et al., 2013, and references therein), the presence of certain biospecies endemic to vent environments and their abundance become important direct characteristics of the present and or past hydrothermal activity. The video footage indicates that both Loki's Castle and Mohn's Treasure hydrothermal sites display notably greater abundance and diversity of species than the exploration AVR<sub>2</sub> site where no hydrothermal activity was reported. At the same time, Mohn's Treasure (a comprehensive study on biodiversity and community structure is reported in Paulsen, 2017) and Loki's Castle are distinctive from each other, which can indicate different stages of hydrothermal activity, in addition to the difference in host rock and overall setting.



**Table 1**  
*Petrophysical Properties of Loki's Castle Hydrothermal Field Grab Samples and Mohn's Treasure Area Drill Core*

Description	IGSN	Volume (cm <sup>3</sup> )	Density (g/cm <sup>3</sup> )	Porosity (%)	Magnetic susceptibility (10 <sup>-6</sup> SI)	Magnetic remanence (mA/m)	Königsberger ratio
Measurement uncertainty		0.01 g			<1,000–6% >1,000–0.6%	<50–5% >50–1%	
Mohn's Treasure: Claystone	MT01	194.3	2.31	0.15	549	3	0.10
Loki's Castle: Mudstone	01	80.16	1.1	0.52	611	14	0.43
	02	130.31	1.05	0.52	630	6	0.18
Loki's Castle: Hydrothermally altered Basalt	03	74.32	2.84	0.02	1,194	2	0.03
	04	116.6	2.84	0.02	1,112	10	0.17
	05	104.65	2.86	0.02	1,126	7	0.12
Loki's Castle: Heterogeneous hydrothermal material	06	115.15	1.62	0.14	451	4	0.16
	07	112.22	1.58	0.16	538	5	0.17
	08	122.53	2.07	0.24	583	57	1.82
	09	115.6	1.84	0.21	559	102	3.39
	10	98.15	1.65	0.1	557	46	1.54
	11	101.09	1.95	0.22	543	88	3.01
	12	129.58	1.54	0.13	503	6	0.22
	13	191.7	2	0.14	518	60	2.15
	14	182.08	1.51	0.16	465	9	0.36
	15	119.85	1.49	0.21	460	5	0.20
	16	69.12	1.62	0.19	474	6	0.24
	17	93.29	2.08	0.1	497	106	3.96
	18	125.62	2.12	0.16	641	149	4.32
	19	137.57	2.22	0.1	624	159	4.74
	20	113.59	2.25	0.14	676	223	6.13
	21	141.03	1.67	0.19	527	12	0.42
	22	128.37	1.85	0.15	490	26	0.99
	23	140.57	1.9	0.11	447	66	2.74
	24	125.46	1.5	0.24	500	21	0.78
	25	117.35	1.42	0.27	513	23	0.83

*Note.* Volume gives the bulk volume of the measured sample material. All samples are assigned International GeoSample Numbers (IGSN) with a prefix IELIM00.

*Loki's Castle active hydrothermal venting site.* Detailed bathymetry and direct ROV observations reveal hummocky volcanic terrain composed of pillowed flows of varying ages, locally covered by sediments. Extensional tectonics influence is pronounced in the normally faulted terrain (Figure 4) that alternate with recent magmatic activity centers. Observed lithologies include fresh and fractured pillow-basalts and breccia (Figure 3a), patches of loose and partly lithified sediment, and diverse hydrothermal material (Figures 3b and 3c). Loki's Castle deposit consists of two mounds that are situated in the middle of the AVR on a flat-topped seamount, just west of the rift. Each mound is approximately 150 m in diameter, overlapping by roughly 30 m as their centers are approximately 120 m apart.

The detailed 1-m resolution bathymetry data provides a solid basis for the deposit detailed mapping. Bathymetry analysis shows that the mounds are situated on an en echelon normal faults structure complicated by connecting faults and a horse-tailing fault termination (Granier, 1985). They appear to be formed on relay structures—in between overlapping normal fault segments where multiple minor faults provide hard linkage to the major faults (Figure 4). The increased structural complexity associated with the increased number of faults and diversely oriented fractures enhances the vertical permeability, thus creates potential pathways for vertical migration of fluids. Hence, relay structures represent a very important control on fluid transport in the crust, for all types of fluids (Fossen & Rotevatn, 2016, and references therein) yielding important implications for hydrothermal systems—that is, creating favorable conditions for magma emplacement, and even more importantly, focusing of hydrothermal discharge. In the case of Loki's Castle, it is clear that the occurrence of the deposit can be attributed to fault relays and intersections as both mounds are formed on top of them with black smokers predominantly concentrated along the faults. Given that plumbing system is well established on a large scale—the heat source, deep faults and fractures facilitating vertical transport of melt and hydrothermal fluid, and long-lived nature of such systems (Johansen et al., 2019; Pedersen,

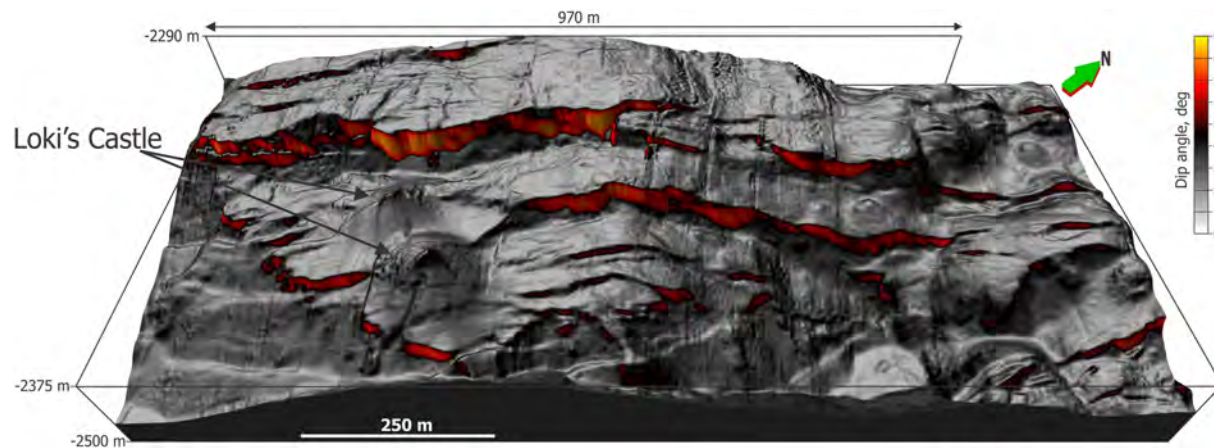


**Figure 4.** Loki's Castle hydrothermal venting field bathymetry in 3-D view. Color scheme corresponds to the change in dip angle. The sulfide deposit mounds are marked by the arrows.

Rapp, et al., 2010)—all these factors make a strong case for the formation of hydrothermal deposits in the studied area. We suggest that structural complexity associated with intensive faulting of diverse orientation, and transfer zones in particular, is the major factor in the localization of hydrothermal discharge on the seafloor and subsequent deposit formation.

Basalt-hosted hydrothermal sites are typically associated with a negative magnetic anomaly in normal polarity areas (Szitkar et al., 2014; Tivey et al., 1993; Tivey & Johnson, 2002; Zhu et al., 2010). The reduction in magnetic intensity observed over such sites can be caused by several reasons and often results from a combination of them: hydrothermal alteration of titanomagnetite to less magnetic minerals (Ade-Hall, 1964; Pariso & Johnson, 1991); and formation of thick nonmagnetic hydrothermal deposits above deep-seated magnetic layers (Szitkar et al., 2014); or the transient effect of thermal demagnetization of titanomagnetite in basalt as temperature of the circulating fluid in active sites—300+ °C—exceeds Curie temperature of titanomagnetite—120–200 °C (Kent & Gee, 1996).

Black smokers at Loki's Castle release 310–320 °C vent fluid that makes it a high-temperature vent field and the thermal demagnetization effect viable. A semi-quantitative XRD analysis of a basalt sample collected from the flank of the hydrothermal mound (a parent sample for samples no. 03–05 in Table 1) shows following composition: albite (52.06%: interior; 48.08%: outer rim) and augite (34.31%: interior, 28.61%: outer rim), chlorite (10.2%: interior, 18.16% outer rim), quartz (3.43%, 5.15%: outer rim; *B. Snook*, personal communication, 2017). A significant amount of alteration products such as chlorite and albite in the studied basalt sample suggests that it was subjected to hydrothermal alteration (Humphris & Thompson, 1978). Basalt samples previously collected in the vicinity of the Loki's Castle area were classified as typical tholeiitic basalt (Cruz et al., 2011). Magnetic properties of the same basalt sample split into three smaller samples (samples no. 03–05 in Table 1) coincide with the observation that chloritization and spilitization is associated with decreasing intensity of magnetization and Königsberger ratio (Opdyke & Hekinian, 1967). At the same time, the magnetic susceptibilities of the hydrothermal material and the mudstones, collected from the mounds, exhibit even lower values, on average twice as low as the altered basalt, and much lower than fresh mid-ocean ridge basalt (Ade-Hall, 1964). Each of these observations would indicate a magnetic low over Loki's Castle. However, the magnetic signature of this particular area is quite complex—we do not observe a confined magnetic anomaly directly above the mounds (Figure 5), even though the reduction to pole procedure was performed and the geological area was formed during the normal polarity Brunhes epoch (Heirtzler et al., 1968; Ogg, 2012). Instead, we observe a long-wavelength magnetic anomaly low skewed in the southeastern direction perpendicular to the major fault and a much steeper southeastern side of the anomaly. The emerged indentation in the TDR map coincides with the eastern mound of the Loki's Castle and could be explained by the presence of demagnetized sulfide mounds in the shallow part and potentially a hydrothermal fluid upflow zone shifted toward the eastern mound. Yet, the resolution and configuration of the magnetic survey requires close attention to the interpretation: the distance between the survey lines

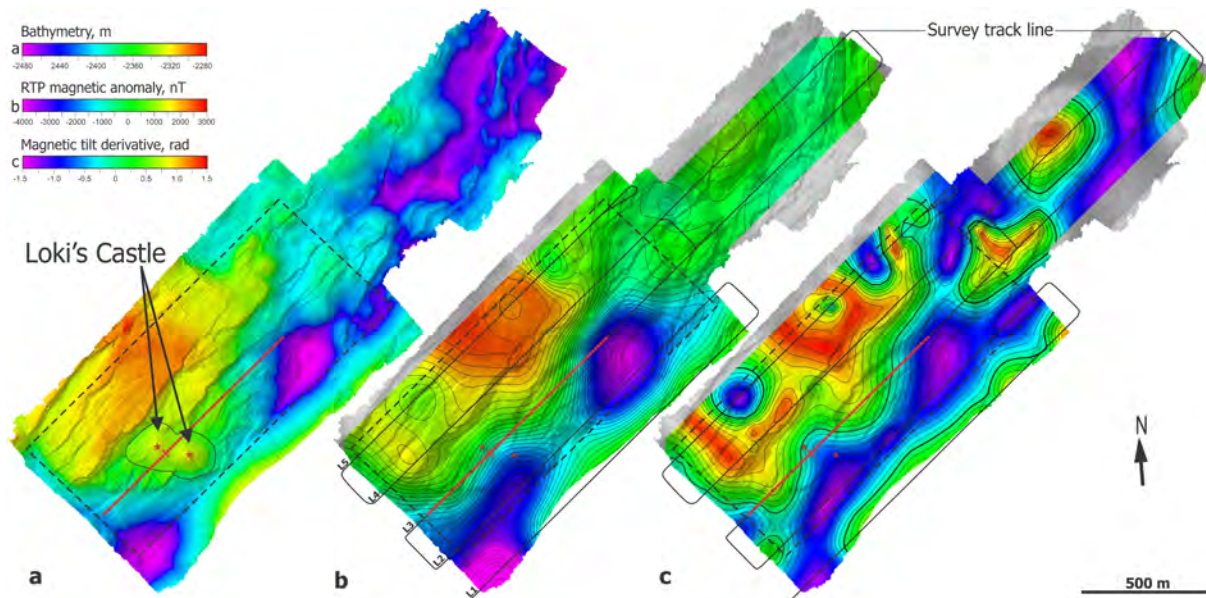


**Figure 5.** Loki's Castle survey area in color shaded-relief representation, all illuminated from northwest. Striped black line marks extent of the Figure 4. The bold solid red line marks the extent of the profile depicted in Figure 6. (a) Bathymetry resolved at 1-m scale. (b) Reduced-to-pole (RTP) total-field magnetic anomaly map generated from a low-flight mode dataset gridded at 30 m and draped over bathymetry grid. The spacing between isolines is 250 nT. Solid black line denotes survey track line with 150-m line spacing. (c) Magnetic Tilt Derivative (TDR) map with isolines at 0.2 and zero-crossing line in bold draped over bathymetry.

equal to 150 m is comparable with the mounds size; the survey track lines are aligned with the main faulting direction  $044^\circ$ . In fact, only one survey line runs over the deposit; however, it does not cross either mound but goes between them, while the two adjacent lines run over the very edges of the mounds parallel to the major faults defining the hosting structure (Figure 5). Such configuration of the survey does not allow a 3-D reconstruction of the deposit.

The profile crossing the deposit (L3 in Figures 5 and 6) indicates a negative magnetic anomaly that coincides with the Loki's Castle deposit. Magnetization low is present and detectable in the profiles collected at different altitudes of 60 and 100 m above the seafloor. The observed difference between the two profiles in this pseudo-measured gradient along the line 3 proposes that the anomaly derives from the shallow subsurface source. Forward modeling was used to assess the hypothesis. While small variations in thickness of a layer with constant crustal magnetization value (Zhang et al., 2018, and references therein) were enough to explain the long-wavelength trends in the observed magnetic data, a short-wavelength anomaly over the deposit and the pseudo-measured vertical gradient required a reduced magnetization body to generate sufficient contrast in the data. Figure 6 shows the magnetic signal calculated from such model. The uniformly magnetized layer with a varying thickness represents recent extrusive basalts; a reduced magnetization body represents a narrow alteration pipe associated with hydrothermal upflow zone feeding the broader shallow mounds as in concept described by Tivey et al. (1993). Considering the small size of the mounds ( $\sim 150$  m each) and short distance between them (120 m between the mound peaks), an alteration pipe is shared by the mounds rather than they have two separate feeder zones. This conceptual model of the 137 data cross-over fits the data with the root-mean-square misfit of less than 100 nT after constant offset correction. Magnetic susceptibilities required to match the observed anomaly amplitudes, however, greatly exceed the range of susceptibility measurements indicating high remanent magnetization. The model is only able to identify the bulk contrasts in the subsurface and reveal the complexity in the magnetization structure, but it cannot uniquely resolve internal compositional and structural detail. Variations in both remanent and induced magnetization corresponding to the changes in lithology could explain the observed signal along with the variation in thickness. Closer line spacing and additional constraints are required to distinguish between different models and resolve the deposit in 3-D.

*Mohn's Treasure extinct hydrothermal venting site.* Figure 7 shows an off-axis area of the mid-ocean ridge, focused on the middle valley rift flank. The survey extends for 5,000 m along the rift valley wall fault and



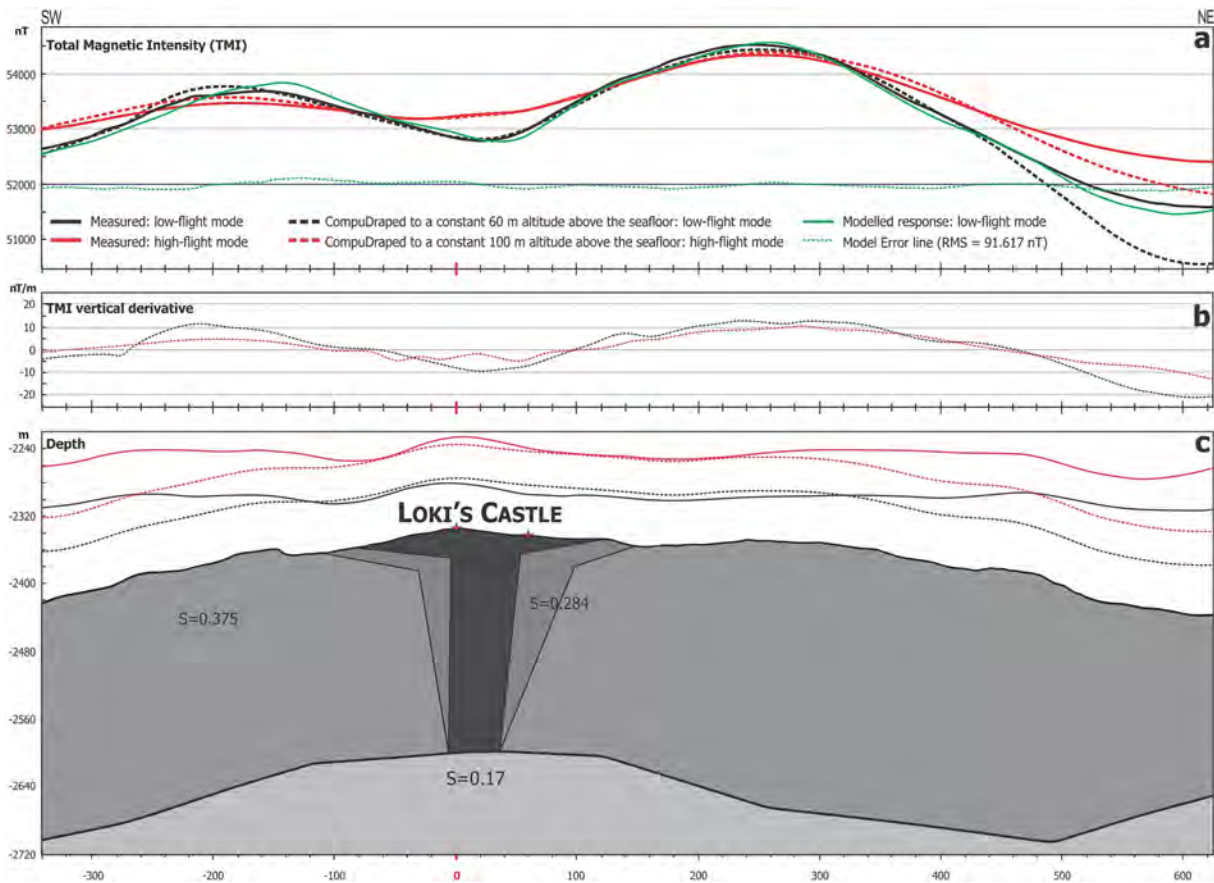


**Figure 6.** Profile across the Loki's Castle deposit, L3 (for location see Figure 5). The red stars denote projections of Loki's Castle mound peaks. (a) Original TMI profiles are denoted by solid lines: Low-flight mode is black; high-flight mode is red. Both modes were acquired with inconsistencies in altitude displayed in c panel. The dashed black and red lines are obtained using a CompuDrape algorithm and correspond to the new constant altitudes above the seafloor: 60 and 100 m. The solid green line indicates the synthetic magnetic response, the dashed green line denotes misfit between the observed and modeled data. (b) TMI vertical derivatives for drape-corrected TMI profiles: low-flight mode in black, high-flight mode in red. (c) Proposed concept of the subsurface structure below the Loki's Castle. Bathymetric profile with original loose drapes for low- and high-flight mode surveys, in black and red solid lines respectively. Dashed lines mark fixed-drape profiles: 60 and 100 m above the seafloor. Magnetic susceptibility values,  $S$ , are provided in SI units. Such high values were required by the model in order to match the observed anomaly amplitudes and indicate the presence of high remanent magnetization in the studied area, which we did not include in this model maintaining a simple approach focused on the geometry and susceptibility contrasts.

3,600 m across it, which almost fully covers the whole rift flank from the crest of a rift-forming fault to the bottom of the axial rift valley, including approximately 500 m west from the crest. Morphologically most of the studied area is a mass-wasting feature resulting from slope failure and landslides. An integrated analysis of the detailed bathymetry, seafloor video observations, and drilling shows that this area is predominantly composed of lithified, semi-lithified and unconsolidated sediments. No volcanic manifestations are observed on the seafloor in this area. Drilling results show that the hard rock observed within the area is a sedimentary rock (claystone), which is commonly exposed by the faults or present as debris sparsely distributed along the slope, and with a distinctive angular shape in contrast to the rounded pillow basalt fragments abundant at the AVR<sub>1</sub> (Figures 3d–3f, photo observations from the area; Figure 7e, drilling site location). A seismic-stratigraphy study approximately 10 km north of the site reports that the sediment layer thickness on the western flank of the rift valley varies between 150 to 800 m (Bruvold et al., 2009). Near-seafloor magnetic exploration registers much lower peak-to-peak dynamic range of the reduced to the pole anomaly values of approximately 3,000 nT (survey area: 17.8 km<sup>2</sup>), compared to the 7,000 nT observed over a much smaller area of Loki's Castle AVR<sub>1</sub> survey (survey area: 1.15 km<sup>2</sup>), and 12,000 nT over the southern AVR<sub>2</sub> (survey area: 28.6 km<sup>2</sup>: 3a; 7.26 km<sup>2</sup>: 3b). This could be explained by the presence of a thick layer of sediments separating basement rocks and the magnetic sensor in addition to possibly different

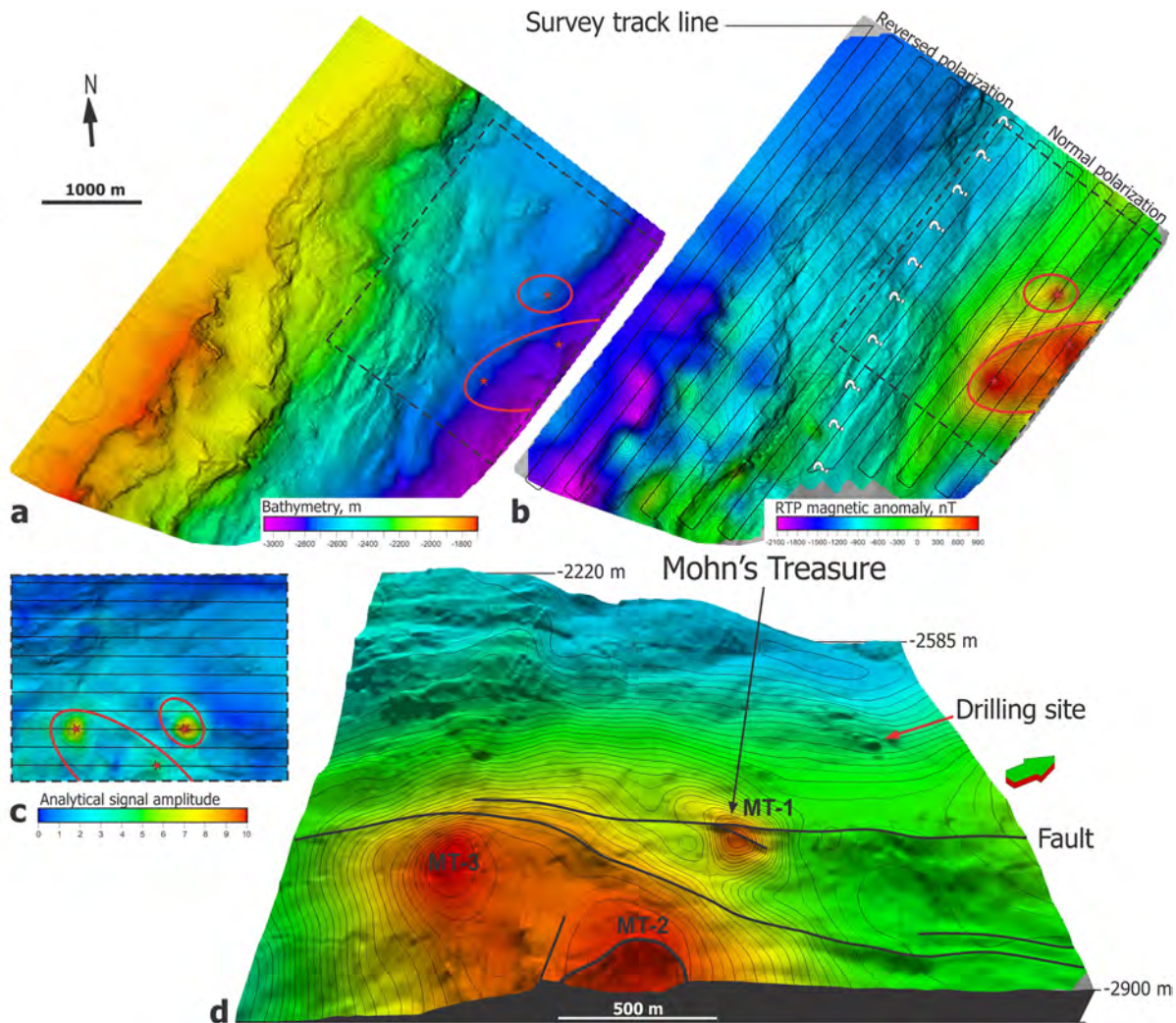


**Figure 7.** Mohn's Treasure survey area in color shaded-relief representation, all illuminated from northwest. All grids are draped over bathymetry grid. Solid black line denotes survey track line with 150 m line spacing. Striped black line marks the extent of panels c and d. (a) Bathymetry resolved at 4-m scale. (b) Draped reduced-to-pole (RTP) total-field magnetic anomaly map gridded at 30 m, isolines drawn every 150 nT. (c) Analytical signal amplitude map. (d) Three-dimensional representation of the (b) panel segment marked by the striped black line. Black arrow tip points at the location of the hydrothermal material exposure documented in Figure 3f and marks the previously reported hydrothermal deposit Mohn's Treasure. Red arrow tip marks the location of the drilling site where claystone core was retrieved. White question mark line denotes the supposed boundary between the normal polarity Brunhes and reverse-polarity Matuyama epochs. Green-red arrow points at the North.

magnetization of the basement rock. Following the assumption that the subsurface structure of the studied rift flank segment is similar to the northern segment of the ridge imaged by reflection seismic (Bruvold et al., 2009), an overall trend of magnetic intensity decreasing in the downslope direction as the thickness of mass waste material increases would be expected. Yet, magnetic data reveals the opposite tendency, suggesting that not only the volume of nonmagnetized material is influencing, but also the change in magnetization of the underlying crustal rocks. Available regional low-resolution aeromagnetic data (10-km line spacing and 300 m altitude survey; Olesen et al., 2010; Ogg, 2012) indicate that this area belongs to a transition zone between reverse Matuyama and normal Brunhes polarity epochs. We believe that the discussed survey covers this transition in high-resolution. Such a topic deserves a separate detailed discussion and tests. For the purposes of the current paper, we infer that the border between the normal and reverse polarity segments lies in parallel with the rift-forming fault presumably as denoted in Figure 7. Therefore, positive magnetic anomalies to the south and east of the assumed reversal border can be attributed to locally elevated magnetization, and vice versa for the upper part of the flank.

The shapes of the positive anomalies depicted in Figures 7b and 7d do not give enough evidence to support a dike or sill intrusion; that is, there is no significant strike extent or localized character to the anomalies. We observe that these observations of two strong positive anomalies correlate with the presence of previously collected sulfide material at the same location (Pedersen, Rapp, et al., 2010) and suggest that these sulfide deposits are creating a magnetic signal. This type of magnetic signature was observed in several locations around the world and is explained by the contrast between nonmagnetic sediments and the massive sulfide deposit usually containing highly magnetized magnetite, pyrrhotite (Gee et al., 2001; Körner, 1994; Pedersen, Rapp, et al., 2010; Tivey, 1994). The interpretation for the smaller anomaly is confirmed by video material and sampling of hydrothermal material composed of pyrite and heterogeneous fine-grained chimney material (Pedersen, Rapp, et al., 2010) and corresponds to the Mohn's Treasure extinct hydrothermal field (MT-1 in Figure 7), as no water column indications of venting are registered at the site. The combination of the total magnetic field intensity data and its derivatives help to delineate the Mohn's Treasure deposit as a causative body of approximately 200 m by 150 m. Euler deconvolution suggests that the depth to the source is around 15 m. This can be interpreted as the depth to the stockwork because the mound was largely weathered, by a combination of physical and chemical destruction of the magnetic minerals, and covered by a thin layer of sediments that leads to the increase of the distance to the source.

The bigger anomaly south-west of the Mohn's Treasure deposit (Figure 7) consists of two smaller-wavelength anomalies approximately 350- and 400-m-long with peaks separated by approximately 800 m. These anomalies are slightly stretched in the downslope direction indicating influence of the dipping slope. All three seem to be separated from each other by faults. While Mohn's Treasure is directly associated with the intersecting faults (Figure 7d), confirming the importance of structural control on the fluid flow by increasing permeability, impermeable faults may act as a seal preventing hydrothermal fluids from lateral migration (Knipe, 1992). The south-western anomalies have not been studied with the ROV during the cruise, and show no particular indications of past hydrothermal activity on the bathymetric data except for being associated with faults. However, the intensity contrast observed over these anomalies and the character of the magnetic signature of the Mohn's Treasure make a strong case for interpreting these anomalies as another fossil hydrothermal deposit. On a larger scale, major rift-forming faults are recognized as major fluid pathways. The most recent electromagnetic data from the Mohns Ridge (Johansen et al., 2019) demonstrates the deep extent of the fluid circulation through such faults and its intensity across the ridge.

Euler deconvolution estimates the depth of the sources to be around 100 m assuming a cylindrical geometry, and twice as much for the spherical shape of the causative body. Since very little is known about the preservation of hydrothermal deposits after the venting activity has ceased and the deposits have been transported away from the ridge axis by seafloor spreading, the subsurface geometry is likely to be far more complex and should not be approximated by simple structures. Overall, close proximity of the anomalies, and their occurrence along one fault suggest that they belong to one plumbing system and share a fluid convection cell. Differences in the shape and intensity of the anomalies, and thus in the resulting depth estimations, their extent and relative position, could be a result of a different age of formation, and possibly reactivation of the hydrothermal activity. The southernmost anomaly MT-2 is adjacent to a deep landslide scarp. Such an extensive avalanche has resulted in a 75 m-deep fault scarp and should lead to the exposure of hydrothermal deposits, yet it is less pronounced in the magnetic intensity data. The analytical signal representation highlights the anomaly MT-3, whereas MT-2 is not resolved against the background. Due to the nature of the analytical signal, such effect can be explained by nonverticality of the source edges and the overall complexity of the shape of this body, also expressed by the scarp. Structural rotation has likely changed the direction of magnetization, which is not accounted for by analytic signal independent of the direction of magnetization. Another factor is the thinning of the magnetic source volume by an avalanche and its redistribution downslope. This relatively deep-seated collapse, with the magnetic anomaly centered on it, strongly supports the interpretation of the anomaly as a fossil hydrothermal deposit, and suggests a high proportion of hydrothermally altered material beneath it that eventually led to a collapse of the hydrothermally altered edifice.

Other anomalies observed in the upper part of the flank, presumably representing reversely-magnetized crust, need more careful analysis for further interpretation and are not discussed within this paper.

*Exploration of AVR<sub>2</sub> and the implications for hydrothermal venting.* For the third study area, we use high-resolution bathymetry and magnetic data along the axial volcanic ridge (AVR<sub>2</sub>) (Figure 8) to investigate



its detailed morphology and the variation of the magnetic field intensity in order to address the following questions: Are there significant anomalies that can be associated with hydrothermal activity? What are the magnetic signatures of the distinctive volcanic features observed in the bathymetry? Are there tectonic features associated with the anomalies? What are the implications of these observations for the hydrothermal venting?

Video footage and detailed bathymetry captures the northern half of the AVR<sub>2</sub> displaying classic features of the neo-volcanic zone associated with the slow spreading. Essentially, the topography is entirely controlled by volcanic processes, and is mostly composed of relatively fresh pillow lava flows with a thin sediment cover (Figures 3g–3i). From video survey observations, and based on the assumption that sediment cover degree is indicative of the lava flow age (Mitchell et al., 1998), the ridge appears to become younger toward the central part of it, as sediment cover thins out. There is a strong correlation between the topographic and magnetic profiles, even after the loose drape geometry was corrected to a constant terrain offset. The magnetic intensity, in this context, could be an indicator of the extrusive lavas thickness and volume of the magnetized material, where the peaks indicate the most recent lava deposition (Schouten et al., 1999; Zhang et al., 2018). The observed along-strike variations in magnetic intensity at the AVRs are consistent with the seismic refraction data from the Mohns Ridge acquired further south, showing an unusually thin, 2–5 km, yet highly variable oceanic crust (Johansen et al., 2019; Klingelhöfer et al., 2000). The dynamic range of the total magnetic field within this area is around 11,000 nT highlighting the volcanic nature of the area (Figure 8b).

Sulfide material discoveries on both sides of the AVR<sub>2</sub> (Figure 1)—western rift flank and the rift valley floor on the east (Pedersen, Rapp, et al., 2010)—indicate the presence of a working plumbing system, that must have been active in the past. The cruise data, however, show no sign of a currently active hydrothermal venting—no water column anomaly was found in the survey area, and no visual evidence was found in the ROV footage. The abundance of fissures and recent lava flows suggests abundant dike intrusions and eruptions, which implies the presence of a magmatic heat source nearby which would drive hydrothermal fluid circulation. On the other hand, eruption events can cause a temporal or even permanent clogging of the hydrothermal vents, as well as cover mature deposits preventing their identification. Moreover, fresh volcanics that have not lost their reactive components are prone to faster clogging (Wolery & Sleep, 1976). Another explanation for the lack of hydrothermal venting at this AVR segment could be the lack of deep high-angle fault populations with diverse orientation, preferably intersecting faults. While downflow of the seawater is attributed to the porous flow mode, venting is mainly associated with the crack zones. Planar faults and fissures are not sufficient to sustain hydrothermal venting at neo-volcanic zones (Sleep & Wolery, 1978), though more likely to form deposits at the sediment-hosted environments where sediment-blanketing aids the process. Also, the cooler crust under the slow-spreading ridges requires an excessive depth of water penetration to harvest the heat. Comprehensive analysis of the area does not provide substantial data to attribute any of the observed magnetic anomalies to considerable hydrothermal deposits of more than 250 m across, given the survey configuration parameters.

However, each anomaly is associated with a distinct volcanic feature, for example, stand-alone volcanic cones or hummocks and their clusters, prominent linear fissure-controlled volcanoes following expected tectonic alignment, but also oblique, or even normal to the AVR edifices. The TDR of the total magnetic field data (Figure 8c) is very instrumental in constraining these features and identifying them in spite of the smaller amplitudes or shorter-wavelength. The deviations of volcanic lineaments and faults in the studied segment (31°NE) from the expected axial trend (39°NE) manifest the obliquity of the rifting, which is common in slow-spreading nontransform offsets and is explained by the oblique shear stress. Curved and sigmoidal faults also suggest the rotation of stresses between the offset spreading segments (Tyler et al., 2007). The stresses surrounding discontinuities and the rotation in the volcanic crust can create more complex cross-cutting fault populations that will grow in both horizontal and vertical direction forming soft-link relay structures, or evolving into hard-link relay structures at the later stages, promoting hydrothermal circulation.

Fissure-fed linear volcanic features are consistent with elongated magnetic highs across the survey, the intensity grows as it gets thicker toward the central part. Short-wavelength circular anomalies correspond to single volcanoes or small agglomerations of several cones, while longer anomalies spreading out from the central volcanic ridge have a smaller intensity and likely represent gravitational features, flows that

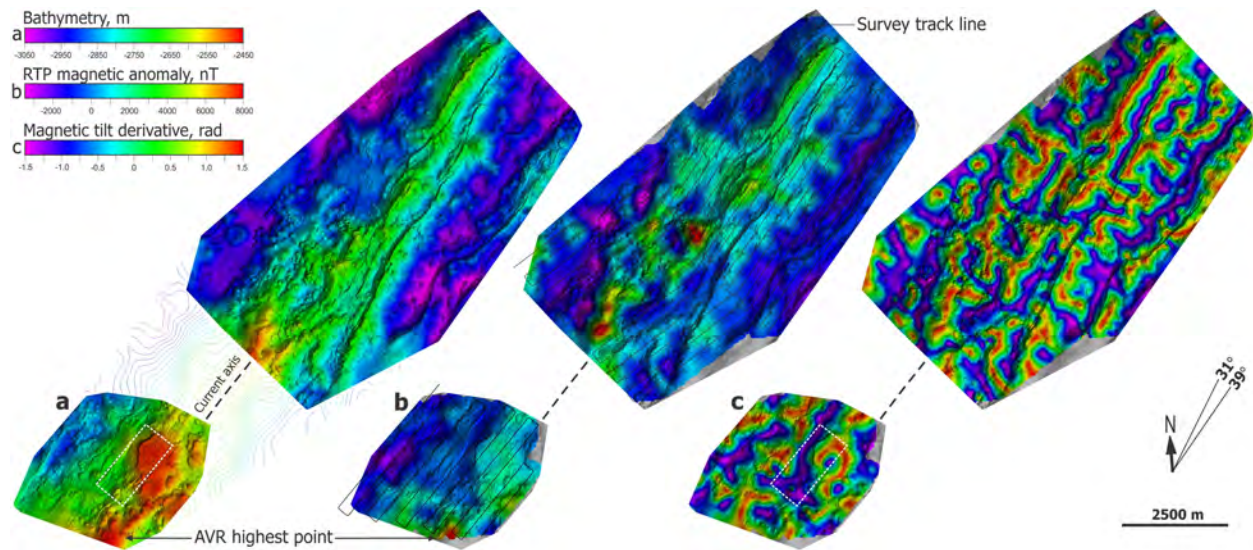


**Figure 8.** Exploration AVR survey area in color shaded-relief representation, all illuminated from northeast. Black line denotes survey track line with 250-m line spacing. All grids are draped onto the bathymetry grid. (a) Bathymetry resolved at 1-m scale. (b) Draped reduced-to-pole (RTP) total-field magnetic anomaly map gridded at 30 m for Survey 3a and 40 m for Survey 3b, isolines drawn at every 150 nT. (c) Magnetic Tilt Derivative (TDR) map. The white striped line box indicates the extent of the data presented in Figure 9.

extend further from its steep-flanked source under gravity. Such flow was observed with the ROV tracing it to its steep-flanked source. Nontransform offsets can explain bigger volcanic features elongated normal to the AVR axis that connects abundant axial ridges with the new one.

A distinctive magnetic signature is observed over a flat-topped volcano identified in the Survey 3b. A ring-shaped feature as outlined in TDR map (Figure 9) with 1,000 nT contrast in intensity between its central part or caldera and a rim perfectly contouring the seamount. This seamount has typical dimensions of a flat-topped volcano (Clague et al., 2000): approximately 1.2 km wide and 200 m high with a central caldera drained inside by roughly 5 m. The detailed bathymetry shows traces of overflowing lava on its steep southwestern slope, with several fissures dissecting it in the NE direction subparallel to the AVR trend, and a small-offset fault (Figure 9). The formation of such a seamount requires the presence of a near-surface magma chamber feeding it through the development of ring-fractures (Simkin, 1973). The TDR signature potentially captures the presence of such circumferential feeders, and a fractured caldera above hot magma chamber in the center. The zero-values define the source edges as they are assumed to be vertical (Figure 9).

A presence of a flat-topped volcano suggests a presence of a shallow magma chamber, known to serve as a primary heat source for many active hydrothermal venting systems found along the mid-ocean ridges. The maintenance of a long-lived eruption is essential to form lava ponds and sustain magma supply creating repeated lava overflows that eventually reach the balance between the outward and upward growth forming a flat-topped seamount (Clague et al., 2000). This also indicates the presence of a sustained magma supply, implying a later adolescent stage of development of the AVR according to Parson et al. (1993). Yet, a small number of such volcanic features and lack of faulting, suggests that the AVR has not yet finalized its volcanic construction stage and has not entered the tectonic stage. The identified magnetic signature of a flat-topped volcano informs our interpretation of the Loki's Castle hydrothermal field. The latter can be recognized as a flat-topped volcano that has been intensively faulted, suggesting that AVR<sub>1</sub> has been subjected to tectonic destruction and is at later development phase than AVR<sub>2</sub> (Parson et al., 1993). Morphological examination of the two AVRs and hydrothermal manifestations, or lack of thereof, suggest that later tectonic destruction phases of AVR development are more likely to sustain hydrothermal venting at the magma-starved ultraslow-spreading ridges than early phases of volcanic construction through increased population and complexity of the faults that weaken the crust and focus hydrothermal flow onto the seafloor.

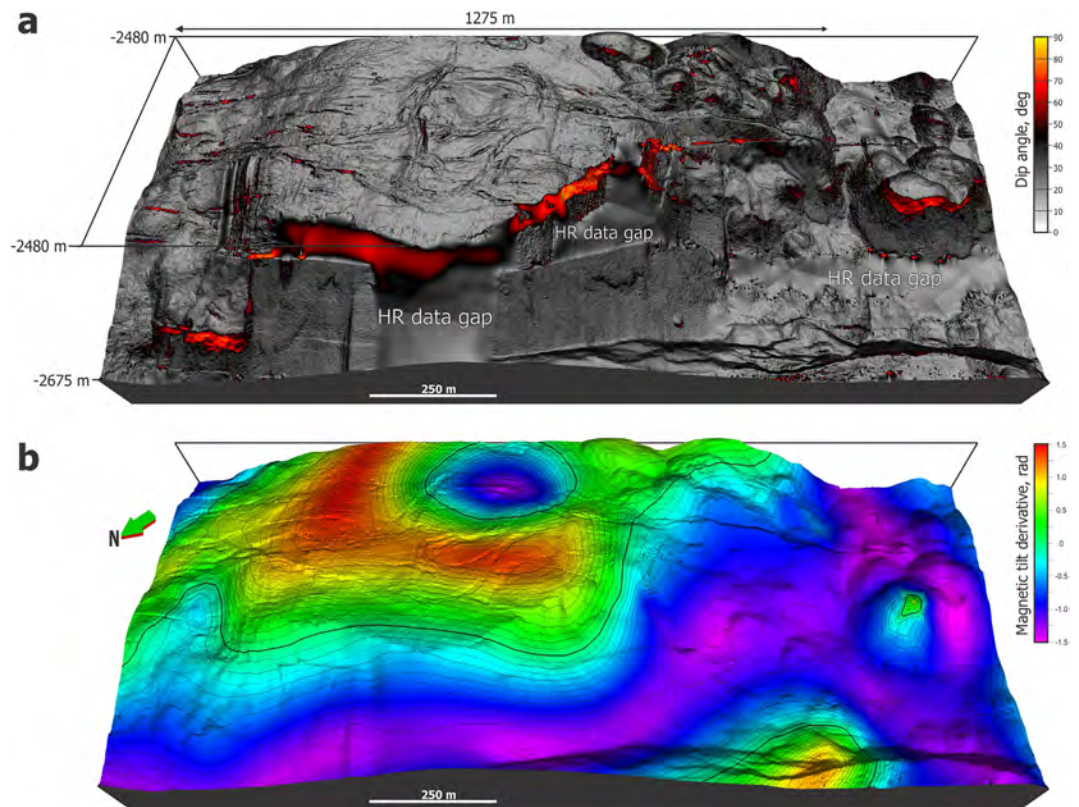


**Figure 9.** A flat-topped volcano in a 3-D view. (a) Color scheme corresponds to the change in the dip angle. This representation highlights volcanic nature of the topography: flat-topped volcano and its crater, overflowing lava lines, fissures and faults well-resolved at 1 m. High-resolution data gaps are interpolated using minimum curvature algorithm and marked by text. (b) Magnetic Tilt Derivative (TDR) draped onto the bathymetry grid with isolines at 0.1. The thick black line marks zero-crossing.

## 5. Conclusions

Near-seafloor magnetic data from the ultraslow-spreading Mohns Ridge is presented for the first time in this paper. Analysis of the high-resolution bathymetry and magnetic data enabled identification of hydrothermal deposits associated with both active and inactive hydrothermal venting sites, providing insights into magmatic and tectonic processes interplay along the axial volcanic ridges.

1. Loki's Castle, an active hydrothermal venting field, consists of two likely interconnected sulfide mounds located on top of a relay structure at the downthrown block of a significantly faulted flat-topped seamount. Rock magnetics and profile magnetic data suggest a negative magnetization contrast associated with the basalt-hosted Loki's Castle deposit. Forward 2-D modeling shows that a localized body having reduced magnetization fit the observed data as one of the concepts. Closer line spacing and stronger control on the altitude of the AUV is required to resolve the deposit in 3-D. Our current investigation can be used as guidelines for further data acquisition.
2. Mohn's Treasure, a fossil sediment-hosted hydrothermal deposit, is associated with a positive magnetic anomaly coincident with sulfide samples recovered from the site. The anomaly is centered at a fault crossing on the slope of a mass-wasting deposit of the western rift flank. It accounts for an approximately 200-m  $\times$  150-m causative body buried by sediments at approximately 15-m depth. The site has enhanced magnetization and produces a clear magnetic signature enabling identification of two new deposits.
3. Two strong positive magnetic anomalies near the Mohn's Treasure (MT-1) reveal new extinct hydrothermal venting sites, MT-2 and MT-3. They exhibit the same magnetic signature as the Mohn's Treasure and structural indications of hydrothermal alteration like a deep fault scarp exposed by the collapse.



4. The increasing prevalence of faulting and its complexity has positive implications for hydrothermal discharge and potentially controls the occurrence of active hydrothermal venting field in the northern AVR<sub>1</sub>, currently undergoing a destructive tectonic stage.
5. In contrast, the southern AVR can be classified as adolescent AVR still going through volcanic construction phase. It is devoid of faulting, shows no indication of on-going hydrothermal activity, even though there are manifestations of the extinct hydrothermalism just outside of it.
6. Potentially, hydrothermal activity along slow-spreading centers follows the cyclicity of the AVR development and is likely to appear and sustain itself during tectonic destruction stages. Structural complexity driven by intensive faulting becomes a major controlling factor on the occurrence of hydrothermal venting within a neo-volcanic zone.

#### Acknowledgments

We thank NTNU Oceans for funding this research. The data used in the paper were collected by MARMINE/NTNU research cruise funded by the Research Council of Norway (Norges Forskningsråd, NFR) Project No. 247626/O30 and associated industrial partners. *Ocean Floor Geophysics* provided magnetometer that was used for magnetic data acquisition and pre-processed the magnetic data. *Geosoft Oasis Montaj* software was used in the preparation of this paper. We thank NGU for providing laboratory services in petrophysical measurements, and Marta Osinska in particular. We thank Maurice Tivey, Jeffrey Gee, and an anonymous reviewer for suggestions that helped to improve the original manuscript. The magnetic data that support the findings of this study are available from NTNU Open Research Data repository <https://doi.org/10.18710/GXMK7K>. Regional-scale bathymetric data are available from Norwegian Mapping Authority (<https://kartkatalog.geonorge.no/meta-data/kartverket/dybdedata-radata/2fe7b56c-334d-4660-ac50-6fc973a0f70>). High-resolution bathymetric data are managed by Norwegian Petroleum Directorate (NPD) and are available from the corresponding author upon reasonable request to NPD at [postboks@npd.no](mailto:postboks@npd.no). All samples used in the paper are assigned International GeoSample Numbers (IGSN).

#### References

- Ade-Hall, J. M. (1964). The magnetic properties of some submarine oceanic lavas. *Geophysical Journal International*, 9(1), 85–92.
- Baker, E. T., Edmonds, H. N., Michael, P. J., Bach, W., Dick, H. J. B., Snow, J. E., et al. (2004). Hydrothermal venting in magma deserts: The ultraslow-spreading Gakkel and Southwest Indian Ridges. *Geochemistry, Geophysics, Geosystems*, 5, Q08002. <https://doi.org/10.1029/2004GC000712>
- Baranov, V. (1957). A new method for interpretation of aeromagnetic maps: Pseudo-gravimetric anomalies. *Geophysics*, 22(2), 359–382.
- Baumberger, T., Früh-Green, G. L., Thorseth, I. H., Lilley, M. D., Hamelin, C., Bernasconi, S. M., et al. (2016). Fluid composition of the sediment-influenced Loki's castle vent field at the ultra-slow spreading Arctic Mid-Ocean ridge. *Geochimica et Cosmochimica Acta*, 187, 156–178.
- Beaulieu, S. E., and K. Szafranski (2018), InterRidge Global Database of Active Submarine Hydrothermal Vent Fields, edited.
- Bloomer, S., P. Kowalczyk, J. Williams, T. Wass, and K. Enmoto (2014), Compensation of magnetic data for autonomous underwater vehicle mapping surveys, paper presented at 2014 IEEE/OES Autonomous Underwater Vehicles (AUV).
- Bruvoll, V., Breivik, A. J., Mjelde, R., & Pedersen, R. B. (2009). Burial of the Mohn-Knipovich seafloor spreading ridge by the Bear Island Fan: Time constraints on tectonic evolution from seismic stratigraphy. *Tectonics*, 28, TC4001. <https://doi.org/10.1029/2008TC002396>
- CEN (2006), EN 1936:2006 Natural stone test methods—Determination of real density and apparent density, and of total and open porosity, European Committee for Standardization, Brussels.
- Clague, D. A., Moore, J. G., & Reynolds, J. R. (2000). Formation of submarine flat-topped volcanic cones in Hawai'i. *Bulletin of Volcanology*, 62(3), 214–233.
- Cordell, L. (1985), Techniques, applications and problems of analytical continuation of New Mexico aeromagnetic data between arbitrary surfaces of very high relief, paper presented at International meeting on potential fields in rugged topography, Institute of Geophysics, University of Lausanne Switzerland.
- Crane, K., Doss, H., Vogt, P., & Sundvor, E. (1999). Morphology of the northeastern Mohns Ridge; results from SeaMARC II surveys in the Norwegian-Greenland Sea. *Exploration and Mining Geology*, 8(3–4), 323–339.
- Cruz, M. I., A. S. Dias, J. M. R. S. Relvas, C. Carvalho, R. Fonseca, R. B. Pedersen, and F. J. A. S. Barriga (2011), Geochemistry of the Arctic Loki's Castle hydrothermal vent products, paper presented at Goldschmidt Conference, Prague, Czech Republic, 14–19 August 2011.
- Dick, H. J. B., Lin, J., & Schouten, H. (2003). An ultraslow-spreading class of ocean ridge. *Nature*, 426(6965), 405.
- Edmonds, H. N., Michael, P. J., Baker, E. T., Connelly, D. P., Snow, J. E., Langmuir, C. H., et al. (2003). Discovery of abundant hydrothermal venting on the ultraslow-spreading Gakkel ridge in the Arctic Ocean. *Nature*, 421(6920), 252.
- Ferraccioli, F., Gambetta, M., & Bozzo, E. (1998). Microlevelling procedures applied to regional aeromagnetic data: An example from the Transantarctic Mountains (Antarctica). *Geophysical Prospecting*, 46(2), 177–196.
- Fisher, C., Rowden, A., Clark, M. R., & Desbruyères, D. (2013). Biology Associated with Sea-Floor Massive Sulphide Deposits. In E. Baker, & Y. Beaudoin (Eds.), *Deep Sea Minerals: Sea-Floor Massive Sulphides, A physical, biological, environmental, and technical review* (Vol. 1A, pp. 19–26). Noumea: Secretariat of the Pacific Community.
- Fossen, H., & Rotevatn, A. (2016). Fault linkage and relay structures in extensional settings—A review. *Earth-Science Reviews*, 154, 14–28.
- Gee, J., Webb, S., Ridgway, J., Staudigel, H., & Zumberge, M. (2001). A deep-tow magnetic survey of Middle Valley, Juan de Fuca Ridge. *Geochemistry, Geophysics, Geosystems*, 2(11). <https://doi.org/10.1029/2001GC000170>
- Géli, L., Renard, V., & Rommevaux, C. (1994). Ocean crust formation processes at very slow spreading centers: A model for the Mohns Ridge, near 72°N, based on magnetic, gravity, and seismic data. *Journal of Geophysical Research*, 99(B2), 2995–3013.
- German, C. R., Baker, E. T., Mevel, C., & Tamaki, K. (1998). Hydrothermal activity along the southwest Indian Ridge. *Nature*, 395(6701), 490.
- Granier, T. (1985). Origin, damping, and pattern of development of faults in granite. *Tectonics*, 7(4), 721–737.
- Gripp, A. E., & Gordon, R. G. (2002). Young tracks of hotspots and current plate velocities. *Geophysical Journal International*, 150(2), 321–361.
- Heirtzler, J., Dickson, G., Herron, E., Pitman, W., & Le Pichon, X. (1968). Marine magnetic anomalies, geomagnetic field reversals, and motions of the ocean floor and continents. *Journal of Geophysical Research*, 73(6), 2119–2136.
- Honsho, C., Ura, T., & Kim, K. (2013). Deep-sea magnetic vector anomalies over the Hakurei hydrothermal field and the Bayonnaise knoll caldera, Izu-Ogasawara arc, Japan. *Journal of Geophysical Research: Solid Earth*, 118, 5147–5164. <https://doi.org/10.1002/jgrb.50382>
- Hopper, J. R., T. Funck, M. Stoker, U. Arting, G. Peron-Pinvidic, H. Doornenbal, and C. Gaina (2014), Tectonostratigraphic Atlas of the North-East Atlantic Region, Geological Survey of Denmark and Greenland.
- Houghton, J. L., Shanks, W. C., & Seyfried, W. E. (2004). Massive sulfide deposition and trace element remobilization in the Middle Valley sediment-hosted hydrothermal system, northern Juan de Fuca Ridge. Associate editor: E. M. Ripley. *Geochimica et Cosmochimica Acta*, 68(13), 2863–2873.
- Humphris, S. E., & Thompson, G. (1978). Hydrothermal alteration of oceanic basalts by seawater. *Geochimica et Cosmochimica Acta*, 42(1), 107–125.
- International Seismological Centre (2018), International Seismological Centre, On-line Bulletin, edited, Thatcham, United Kingdom.

- Johansen, S. E., Panzner, M., Mittet, R., Amundsen, H. E. F., Lim, A., Vik, E., et al. (2019). Deep electrical imaging of the ultraslow-spreading Mohs Ridge. *Nature*, *567*(7748), 379–383.
- Juliani, C., & Ellefmo, S. L. (2018). Probabilistic estimates of permissive areas for undiscovered seafloor massive sulfide deposits on an Arctic Mid-Ocean Ridge. *Ore Geology Reviews*, *95*, 917–930.
- Kent, D. V., & Gee, J. (1996). Magnetic alteration of zero-age oceanic basalt. *Geology*, *24*(8), 703.
- Klingelhöfer, F., Géli, L., Matias, L., Steinsland, N., & Mohr, J. (2000). Crustal structure of a super-slow spreading centre: A seismic refraction study of Mohs Ridge, 72° N. *Geophysical Journal International*, *141*(2), 509–526.
- Knipe, R. J. (1992). Faulting processes and fault seal. In *Structural and tectonic modelling and its application to petroleum geology* (pp. 325–342). Amsterdam: Elsevier.
- Körner, U. (1994). Rock magnetic properties of hydrothermally formed iron sulfides from Middle Valley, Juan de Fuca Ridge, paper presented at Proceedings of the Ocean Drilling Program. Scientific results, Ocean Drilling Program.
- Ludvigsen, M., et al. (2016). MarMine cruise report—Arctic Mid-Ocean Ridge 15.08. 2016–05.09. 2016.
- McCaug, A. M., Cliff, R. A., Escartin, J., Fallick, A. E., & MacLeod, C. J. (2007). Oceanic detachment faults focus very large volumes of black smoker fluids. *Geology*, *35*(10), 935–938.
- Miller, H. G., & Singh, V. (1994). Potential field tilt: A new concept for location of potential field sources. *Journal of Applied Geophysics*, *32*, 213–217.
- Minty, B. R. S. (1991). Simple micro-levelling for aeromagnetic data. *Exploration Geophysics*, *22*(4), 591–592.
- Mitchell, N. C., Allerton, S., & Escartin, J. (1998). Sedimentation on young ocean floor at the Mid-Atlantic Ridge, 29° N. *Marine Geology*, *148*(1–2), 1–8.
- Mosar, J., Lewis, G., & Torsvik, T. (2002). North Atlantic sea-floor spreading rates: Implications for the Tertiary development of inversion structures of the Norwegian–Greenland Sea. *Journal of the Geological Society*, *159*(5), 503–515.
- Nabighian, M. N., Grauch, V., Hansen, R., LaFehr, T., Li, Y., Peirce, J., et al. (2005). The historical development of the magnetic method in exploration. *Geophysics*, *70*(6), 33ND–61ND.
- Norwegian Mapping Authority (2015). Sea shadow relief WMS.
- Ogg, J. G. (2012). In F. M. Gradstein, J. G. Ogg, M. Schmitz, & G. Ogg (Eds.), *Geomagnetic polarity time scale, in The geologic time scale 2012*. Cambridge, UK: Elsevier, Cambridge University Press.
- Olesen, O., J. Gellein, L. Gernigon, O. Kihle, J. Koziel, T. Lauritsen, et al. (2010). Magnetic anomaly map, Norway and adjacent areas. , Geological Survey of Norway.
- Opdyke, N. D., & Hekinian, R. (1967). Magnetic properties of some igneous rocks from the Mid-Atlantic Ridge. *Journal of Geophysical Research*, *72*(8), 2257–2260.
- Pariso, J. E., & Johnson, H. P. (1991). Alteration processes at Deep Sea Drilling Project/Ocean Drilling Program Hole 504B at the Costa Rica Rift: Implications for magnetization of oceanic crust. *Journal of Geophysical Research*, *96*(B7), 11,703–11,722.
- Parson, L., Murton, B., Searle, R., Booth, D., Evans, J., Field, P., et al. (1993). En echelon axial volcanic ridges at the Reykjanes Ridge: A life cycle of volcanism and tectonics. *Earth and Planetary Science Letters*, *117*(1–2), 73–87.
- Paterson, N. R., S. W. Reford, and K. C. H. Kwan (1990). Continuation of magnetic data between arbitrary surfaces: Advances and applications, paper presented at SEG Technical Program Expanded Abstracts 1990, Society of Exploration Geophysicists, 1990/01//.
- Paulsen, E. (2017). Community structure and biodiversity of the benthic megafauna at the inactive hydrothermal site Mohn's Treasure, on the Mohs Ridge, Arctic Mid-Ocean Ridge (AMOR), Master thesis, Norwegian University of Science and Technology, NTNU.
- Pedersen, R. B., Rapp, H. T., Thorseth, I. H., Lilley, M. D., Barriga, F. J. A. S., Baumberger, T., et al. (2010). Discovery of a black smoker vent field and vent fauna at the Arctic Mid-Ocean Ridge. *Nature Communications*, *1*, 126.
- Pedersen, R. B., Thorseth, I. H., Nygård, T. E., Lilley, M. D., & Kelley, D. S. (2010). Hydrothermal Activity at the Arctic Mid-Ocean Ridges. In P. A. Rona et al., (Eds.), *Diversity of Hydrothermal Systems on Slow Spreading Ocean Ridges, Geophysical Monograph Series* (Vol. 188, pp. 67–89). Washington, DC: AGU.
- Pilkington, M., & Roest, W. (1992). Draping aeromagnetic data in areas of rugged topography. *Journal of Applied Geophysics*, *29*(2), 135–142.
- Pilkington, M., & Thurston, J. B. (2001). Draping corrections for aeromagnetic data: Line-versus grid-based approaches. *Exploration Geophysics*, *32*(2), 95–101.
- Rasmussen, R., & Pedersen, L. (1979). End corrections in potential field modeling. *Geophysical Prospecting*, *27*(4), 749–760.
- Reid, A. B., Allsop, J. M., Granser, H., Milllett, A. J. T., & Somerton, I. W. (1990). Magnetic interpretation in three dimensions using Euler deconvolution. *Geophysics*, *55*(1), 80–91.
- Roest, W., Verhoef, J., & Pilkington, M. (1992). Magnetic interpretation using the 3D analytic signal. *Geophysics*, *57*(1), 116–125.
- Schouten, H., Tivey, M. A., Fornari, D. J., & Cochran, J. R. (1999). Central anomaly magnetization high: Constraints on the volcanic construction and architecture of seismic layer 2A at a fast-spreading mid-ocean ridge, the EPR at 9°30′–50′ N. *Earth and Planetary Science Letters*, *169*(1–2), 37–50.
- Simkin, T. (1973). Origin of some flat-topped volcanoes and guyots.
- Sleep, N. H., & Wolery, T. J. (1978). Egress of hot water from midocean ridge hydrothermal systems: Some thermal constraints. *Journal of Geophysical Research*, *83*(B12), 5913–5922.
- Snook, B., Drivenes, K., Rollinson, G., & Aasly, K. (2018). Characterisation of Mineralised Material from the Loki's Castle Hydrothermal Vent on the Mohs Ridge. *Minerals*, *8*(12), 576.
- Szitar, F., Dyment, J., Choi, Y., & Fouquet, Y. (2014). What causes low magnetization at basalt-hosted hydrothermal sites? Insights from inactive site Krasnov (MAR 16°38′N). *Geochemistry, Geophysics, Geosystems*, *15*, 1441–1451. <https://doi.org/10.1002/2014GC005284>
- Talwani, M., & Eldholm, O. (1977). Evolution of the Norwegian–Greenland sea. *Geological Society of America Bulletin*, *88*(7), 969–999.
- Talwani, M., & Heirtzler, J. R. (1964). Computation of magnetic anomalies caused by two-dimensional structures of arbitrary shape. In G. A. Parks (Ed.), *Computers in the Mineral Industries* (pp. 464–480). Stanford, Calif: Stanford Univ. Publ. of the Geol. Sci.
- Thébault, E., Finlay, C. C., Beggan, C. D., Alken, P., Aubert, J., Barrois, O., et al. (2015). International geomagnetic reference field: The 12th generation. *Earth, Planets and Space*, *67*(1), 79.
- Thompson, D. T. (1982). EULDPH: A new technique for making computer-assisted depth estimates from magnetic data. *Geophysics*, *47*(1), 31–37.
- Tivey, M. A. (1994). High-resolution magnetic surveys over the Middle Valley mounds, Northern Juan de Fuca Ridge, Proc. ODP. *Scientific Results*, *139*, 29–35.
- Tivey, M. A., & Johnson, H. P. (2002). Crustal magnetization reveals subsurface structure of Juan de Fuca Ridge hydrothermal vent fields. *Geology*, *30*(11), 979–982.

- Tivey, M. A., Rona, P. A., & Schouten, H. (1993). Reduced crustal magnetization beneath the active sulfide mound, TAG hydrothermal field, Mid-Atlantic Ridge at 26 N. *Earth and Planetary Science Letters*, *115*(1–4), 101–115.
- Tromsø Geophysical Observatory (2018), Geomagnetic Data, edited, University of Tromsø.
- Tyler, S., Bull, J. M., Parson, L. M., & Tuckwell, G. W. (2007). Numerical modelling of non-transform discontinuity geometry: Implications for ridge structure, volcano-tectonic fabric development and hydrothermal activity at segment ends. *Earth and Planetary Science Letters*, *257*(1–2), 146–159.
- Varentsov, I. M., Ryabushkin, P. K., Kazimirov, D. A., Koreneva, E. V., Gendler, T. S., Udintsev, G. B., et al. (1980). The metalliferous sediments of Iceland plateau, North-Atlantic—Geochemical features of formation. *Geokhimiya* (10), 1528–1541.
- Verduzco, B., Fairhead, J. D., Green, C. M., & MacKenzie, C. (2004). New insights into magnetic derivatives for structural mapping. *The Leading Edge*, *23*, 116–119.
- Vine, F. J., & Wilson, J. T. (1965). Magnetic anomalies over a young oceanic ridge off Vancouver Island. *Science*, *150*(3695), 485–489.
- Vogt, P., Kovacs, L., Bernero, C., & Srivastava, S. (1982). Asymmetric geophysical signatures in the Greenland-Norwegian and southern Labrador seas and the Eurasia Basin. *Tectonophysics*, *89*(1–3), 95–160.
- Vogt, P. R. (1986). Geophysical and geochemical signatures and plate tectonics. In B. G. Hurdle (Eds.). *The Nordic Seas* (pp. 413–664). New York: Springer.
- Wolery, T. J., & Sleep, N. H. (1976). Hydrothermal circulation and geochemical flux at mid-ocean ridges. *The Journal of Geology*, *84*(3), 249–275.
- Zhang, T., Gao, J., Xu, M., Shen, Z., & Wu, Z. (2018). Thickness of extrusive basalts dominating the magnetic structure along the ultraslow-spreading Mohs Ridge axis (71.8°–73.7° N). *Tectonophysics*, *742*, 1–14.
- Zhu, J., Lin, J., Chen, Y. J., Tao, C., German, C. R., Yoerger, D. R., & Tivey, M. K. (2010). A reduced crustal magnetization zone near the first observed active hydrothermal vent field on the Southwest Indian Ridge. *Geophysical Research Letters*, *37*, L18303. <https://doi.org/10.1029/2010GL043542>
- Zierenberg, R. A., Fouquet, Y., Miller, D. J., Bahr, J. M., Baker, P. A., Bjerkgaard, T., et al. (1998). The deep structure of a sea-floor hydrothermal deposit. *Nature*, *392*(6675), 485.